HIGH TEMPERATURE FATIGUE CRACK GROWTH BEHAVIOUR OF TIMETAL 21S IN AN OXIDIZING ENVIRONMENT

Jacques Henri Ferreira

Thesis submitted to the Faculty of Engineering, University of Natal, Durban in fulfilment of the requirements of the Degree of Doctor of Philosophy

Department of Mechanical Engineering
University of Natal
Durban
September 1995

DECLARATION

I declare that this thesis is my own unaided work except where due acknowledgement is made to others. It is being submitted for the Degree of Doctor of Philosophy to the University of Natal, Durban. It has not been submitted before for any other degree of examination to any other university.

Jacques Henri Ferreira

15 September 1995

SYNOPSIS

The high temperature fatigue crack growth behaviour of the newly developed, metastable titanium-based alloy, TIMETAL 21S, was investigated in an inert and an oxidizing environment. The investigation adopted a two pronged approached, namely, to initially establish the pure microstructural behaviour under oxidizing and inert environments at various elevated temperatures, and consequently, to establish the environmental effects on the fatigue crack growth behaviour in the various environments at high temperature. The effect of the oxidizing environment on the metastable alloy and on the mechanical and chemical events occurring at the fatigue crack were studied by using optical and scanning electron microscopy, including EDX analysis, x-ray diffraction, and Auger Electron Spectroscopy (AES).

For the microstructural investigation, the TIMETAL 21S samples were exposed for 5 hours to a pure argon and argon + 20% O_2 environment at 300°C to 750°C in increments of 50°C. The results showed that in the oxidizing environment a more homogeneous nucleation of the alpha phase had occurred at higher temperatures and that the oxide TiO_2, in addition to the alpha case, had predominantly formed on the exposed surfaces. AES analysis showed that dissolution of the oxygen into the alloy occurred even at low temperatures.

An LEFM approach was used to investigate fatigue crack growth rate (FCGR) of C(T) specimens at 375°C, 450°C, 550°C and 620°C in the argon and argon + 20% oxygen environment. The crack growth rates were monitored using load-line compliance and the beachmarking method - a method by which beach marks were impressed on the fracture surface to track the progressing crack. The results showed that the crack growth rates were lower in the oxidizing environment and was influenced by a synergistic effect of the temperature, stress intensity at the crack tip and the environment. In addition to the phenomena of crack tip shielding (a process whereby the effective crack tip driving force experienced at the crack tip was locally reduced), other mechanisms such as slip character modification and secondary cracking ahead of the crack tip, leading to crack tip blunting and branching, had to be incorporated to fully explain the crack growth behaviour. The tests conducted in the inert environment effectively excluded the effect of oxygen on the crack growth behaviour and substantiated that various mechanisms ultimately determined the FCGR in TIMETAL 21S at elevated temperatures.

ACKNOWLEDGEMENTS

I would like to thank the following people:

Professor Aghion for his supervision, support and helpfulness.

My fellow PhD student, Sagren Govender, and the other post-grad students and for their helpful suggestions, support and interesting discussions.

John Mahon for writing (several) computer programs under extreme pressure

Paddy for developing the photographs

Mr Bob Blackwell for getting rid the many electronic crises by his tried and trusted process of elimination

The workshop staff at the department for their advice, helpfulness and hard work.

Phil and Fiona at the electron microscope unit for putting up with us, and

My wife Kerry-Lee for her patience and understanding through trying times

My family for their encouragement.

List of Figures

Chapter 1

Chapter 2

List of Tables

Chapter 1

Chapter 2

Chapter 3

CONTENTS

Introduction

It has been stated that for the two centuries following the Industrial Revolution that a "Basic Materials Age" has existed [1]. During this period, the development of materials have lead to the present availability of a multitude of alloys that are able to fulfil most engineering requirements. Amongst these developments, the most significant is the evolution of numerous "high tech" steel alloys, super alloys and light alloys whose mechanical and physical properties have been extensively exploited. Design methods have changed from initial guess work to well-defined methods that are able to predict global stresses in loaded structures. Modern stress analysis techniques are able to not only account for global but also local stresses in components. Present design methods are also able to evaluate intricate stress distributions in components and in the event of a local failure, the design allows for the redistribution of stresses to prevent total and catastrophic failure of the component [1,2]. The advanced analysis and design techniques have lead to materials not only being pushed to handle higher stresses, but also to operate at higher and higher temperatures. The traditional materials of construction have now however reached the upper limit of their useable strength limits. This is particularly evident in components that operate at elevated temperatures. To further improve the efficiency of these components, attention has been diverted to altogether new, engineered materials that will be able to operate under severe conditions. Thus a new materials age is presently being ushered in. The present "Basic Materials Age" has to make way for new innovative concepts in materials and the "Era of Engineered Materials" of the future [1].

The thrust which has lead to increased research activity in the engineered materials field is the aerospace industry. Research programs on systems such as the Integrated High Performance Turbine Engine Technology (IHPTET) - where the goal is to double the performance of the turbine engine while decreasing the fuel consumption by 50% within the next ten years - have lead to the realization that traditional materials of construction have to be replaced with alternate advanced engineered materials in order to cope with the extreme dynamic and environmental conditions under which these materials will operate [1,3]. Another ambitious aerospace project that is currently

underway is the National Aero Space Plane (NASP). The initial goal of the NASP program involved the development of a manned aerospace vehicle capable of cruising at hypersonic speeds and achieve single-stage access to space where the vehicle would rendezvous with an orbiting space station [4-7]. The goal has changed somewhat towards a more commercial approach where passengers will be transported between destinations such as New York and Tokyo - a journey that is expected to last under two hours [6]. The NASP (currently estimated to be the size of a 727 with the weight of an F-15 military plane) will have horizontal take off and land capabilities and the expected speeds of MACH 25 (required to reach low orbit) will generate tremendous temperatures. For the successful development of such a vehicle, it was found that the success of the project evolved around three key technologies, namely, 1. the implementation of computational fluid dynamics for the expected speeds, 2. an appropriate propulsion system capable of spanning the speed range and 3. the development of lightweight, high temperature materials capable of withstanding the expected service conditions [3,8]. In addition, materials that are presently being developed are not to be limited to future applications exclusively, but near term engine and airframe applications will also benefit from these technologies [3].

To increase the performance of the future aerospace systems, improvement in the weight as well as the thermal capability of material systems have to be achieved. Traditionally, monolithic, age-hardenable aluminium alloys have fulfilled the role of lightweight, high specific strength airframe materials of construction. However with an increase in airspeed, heating of the aircraft structure occurs and the aluminium alloy's mechanical properties tend to deteriorate rapidly above 150°C [1]. Titanium-based alloys have shown to be able to operate in this elevated temperature region. After first finding applications in the aircraft turbine engines, titanium alloys have been increasingly used in other aircraft structures. An example of this is the airframe of the high speed MACH 3+ surveillance aircraft, the SR-71, also known as the Blackbird [1]. In other military aircraft, these titanium alloys comprise, on average, nearly 20% of the airframe mass. High-strength titanium alloys have also been extensively used in the advanced YF-12 military aircraft to where 93% of the airframe mass constitutes the titanium alloy [9]. However sustained high temperature use of the alloys have been

limited due to the atmospheric interaction, mechanical property degradation and poor resistance to hot aircraft hydraulic fluid [9,10].

With the development of the titanium aluminides-base alloys (TiAl, Ti_3Al, $TiAl_3$) it was believed that the difficulties experienced with the conventional titanium alloys were about to be overcome. Compared to traditional aerospace materials, the titanium aluminides offered the combination of good high temperature strength and creep capability, improved high temperature (up to 1000°C) environmental resistance and low density [11,12,13]. Thus this class of materials appeared to be candidates for the replacement of conventional titanium alloys and, in some instances, nickel-based superalloys [12]. Experimental studies on titanium aluminides however soon identified undesirable material characteristics which questioned the materials ability to fulfil the required role in the aerospace industry [14,15]. Low ductility and fracture toughness and poor fatigue crack growth characteristics were experienced at ambient temperature and the extremely low impact strength (2-3 J compared to $\pm$ 25 J for conventional titanium alloys) were a major cause for concern in areas where foreign object damage resistance is of high priority, for example in turbine blades [4,14]. Although the low temperature "unforgiveness" of the material were improved somewhat by the use of silicon carbide fibre reinforcing, other detrimental effects of elevated temperatures became apparent [3]. Although further research is currently underway in the titanium aluminide field, the materials selection field has expanded to include other possible candidate materials that show favourable properties for aerospace applications.

Recently a new titanium alloy was developed by the Titanium Metals Corporation (TIMET) in Denver, Colarado, USA, that has been able to overcome some of the problems previously experienced with conventional titanium alloys and titanium aluminides. The alloy, TIMETAL 21S (initially known as BETA 21S), has become the leading candidate material for extensive use in aerospace systems. TIMETAL 21S is said to be the first heat and corrosion resistant titanium alloy that is able to compete with nickel-based alloys up to 595°C [16]. The alloy has excellent oxidation resistance and compares favourably with titanium aluminides and can be used, uncoated, up to temperatures of 800°C [17]. The high corrosion resistance of TIMETAL 21S is on par

with titanium alloys that were specifically developed for use in the chemical industry [16]. Hot hydraulic fluid which severely attacks other aircraft titanium alloys has a limited effect on TIMETAL 21S [18]. The alloy is also to be used by the Boeing Commercial Group, Seattle, Washington to reduce the engine weight of the new 777 jumbo jet by approximately 40%, or 360 kg per engine. The weight saving will have a negligible cost penalty to effect [16].

The ability of TIMETAL 21S to be produced in foil form allows for the manufacture of a metal matrix composite (MMC) with relative ease using the foil-fibre-foil approach [17]. Since TIMETAL 21S has been found to be compatible with SCS-6 silicon carbide fibre, problems that are usually experienced with the manufacture of MMCs have been overcome by using the 21S alloy [19]. Combined with high specific strength, good cold formability, elevated temperature strength, adequate creep resistance and thermal stability, TIMETAL 21S has become the leading candidate for the NASP skin surface and airframe material of construction in both monolithic and MMC form [17]. The alloy has also shown to be able to withstand simulated cyclic exposures similar to both temperature and load excursions that are representative of orbital and cruise missions [17].

While the development of new high temperature materials is critical, the process is only finalized once a full understanding of the material behaviour under various operating conditions is obtained and a desired balance of properties, both physical and mechanical, is achieved. TIMETAL 21S has shown to have the high specific strength and attractive high temperature properties to be used as both monolithic and MMC structural components in advanced aerospace components. However further extensive studies have to be conducted in order for the material to be used in commercial and industrial applications, and with confidence on full-scale aerospace vehicles such as the NASP.

Chapter 1 : Literature Survey

1.1 Metallurgy of Titanium alloys

Role of microstructure

The classification of titanium alloys into two specific groups, the alpha and beta groups, is well documented. Briefly, the crystalline phases of HCP alpha (α) and BCC beta (β) phases observed at room temperature, give rise to the classification. Whereas pure titanium exists as an alpha phase, alloying the metal can result in increased beta phase presence at ambient temperature. The titanium alloys thus can exist as an alpha phase, a beta phase, or a combination of alpha and beta phases (the so-called alpha+beta alloys), each with characteristic and distinct physical and mechanical properties. The alloying elements also effect the beta transus temperature - the temperature above which only a beta phase remains.

Titanium reacts readily with a number of alloying elements to form metallic, covalent or ionic bonds, allowing the opportunity for many alloying possibilities [20]. Alloying additions may have a stabilizing effect on the titanium phases. For example, aluminium, oxygen, nitrogen, gallium and carbon are the most common alpha stabilizing elements, resulting in an increase in the alpha phase field. In contrast, elements such as molybdenum, niobium, vanadium, tungsten and tantalum tend stabilize the beta phase, and sufficient amounts of these alloying elements result in a retained beta structure at room temperature after quenching or air cooling. Mo, Nb and V tend to form isomorphous alloys, while other elements such as Fe and Cr promote the formation of beta-eutectoids [21]. Titanium alloys can also support a mixture of alpha and beta phases simultaneously through various alloying additions. Figure 1.1, the basic pseudo binary phase diagram of titanium and a β-isomorphous stabilizer, shows the effect of increased beta alloying additions and increased cooling rates on the final microstructure of the alloy.

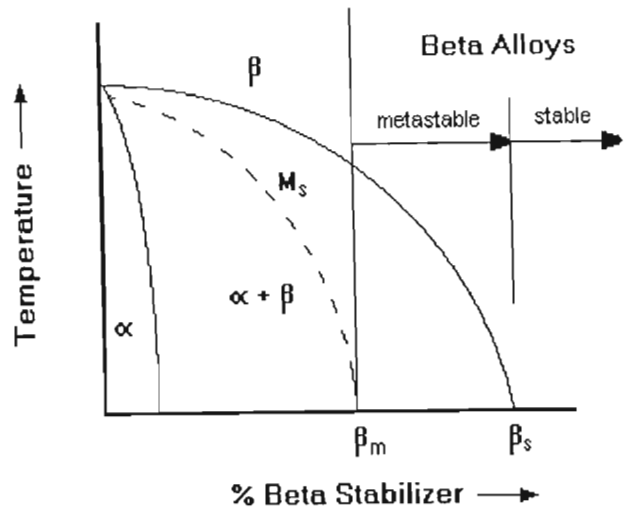

Figure 1.1 : Schematic diagram of the binary titanium phase diagram and β-isomorphous stabilizer

Alpha titanium alloys generally exhibit high strength characteristics even at high temperatures, and with the addition of alpha solid solution strengtheners, the alloys generally posses good high temperature creep capabilities [9,20]. The alpha alloys generally have poor room temperature formability and are mostly hot worked [22]. Heat treating the alpha alloys results in a limited strengthening effect and the properties of the alloys are mostly controlled by alloying [20].

In contrast to the alpha alloys, alpha+beta alloys can be strengthened by solution treatment and aging. The solution treatment is usually preformed high in the alpha + beta phase region, below the beta transus temperature or above the beta transus temperature. The subsequent quenching and aging results in a precipitation of a secondary alpha phase in the beta grains, accompanied by a substantial increase in the strength level [20,22]. These two-phase titanium alloys are often favoured since the alloy achieves a combination of beneficial effects from the various phases. Mostly the retained beta phase promotes an increase in ductility in the alloy [11]. Controlling the size, shape and dispersion of both the alpha and beta phases results in a good balance of properties such as yield and tensile strength, creep, fatigue, SCC and fatigue crack propagation resistance and resistance to oxidation [20,22].

The addition of sufficient beta stabilizing alloying elements to titanium allows for the complete retention of the beta phase during water quenching of thick sections or air cooling of thin sections [22]. The stable beta alloys have found to have good formability, high strength, good corrosion resistance and a low elastic modulus [23,24]. These attractive properties have lead to the extensive use of beta titanium alloys in various industrial applications. However, the alloys generally suffer from problems related to both processing and fabrication [25]. Properties of the binary beta alloys can generally be improved by further careful additions of other alloying components. Small additions of alpha stabilizing elements (with other elements), combined with the sluggishness of the beta to alpha phase transformation during quenching, have resulted in the development of the metastable beta titanium alloys [26]. These alloys are offer improved fracture toughness, corrosion resistance and deep hardenability of relatively thick sections [27]. In addition, the solution treated metastable alloys have good ductility compared to the alpha and alpha+beta alloys' limited ductility at room temperature and can also readily be cold worked, even in the solution treated and quenched condition, resulting in high cold formability [9,24]. The aging treatments mostly result in the precipitation of finely dispersed hexagonal alpha particles in the beta matrix. Further details on the aging response of titanium alloys is described in section 1.5.1.

Although a range of alloying elements exist that have particular influences on the titanium alloy systems, most effects would fall outside the scope of this study and a short discussion pertaining to the more common alloying elements relevant to the investigation is presented herewith.

Effect of alloying additions

The leading beta stabilizer in present titanium alloys is Mo and Nb [20,28]. Initially the Cr and V content as found in the first heat-treatable metastable beta titanium alloys, Ti-13V-11Cr-3Al and Ti-15V-3Cr-3Sn-3Al, presented difficulties due to embrittling precipitates in the alloys (amongst other drawbacks) [28,29]. Although Cr improves the high temperature strength, it lowers the room temperature toughness and raises the

ductile-to-brittle temperature [30]. Alloying with Mo resulted in an increased heat treatment response and hardenability of the alloy that leads to higher alloy strength in the heat treated and aged material [20,28], without the previously mentioned embrittlement occurring. In the surface oxides of Ti some Mo oxides may be present [24]. This has been cited as one of the reasons for the stability of the Ti-Mo alloys, since blocking of the active points on the surface (since Mo oxides may be more stable) retards the dissolution of Ti [24]. Increasing the Mo alloying content results in increased beneficial surface effects, thus the stable Ti-35%Mo alloys are common practice [24]. Furthermore, in two phase alloys, Mo is an important solid solution strengthener and, with Nb, enhance the tensile properties at low temperatures [28,31,32]. Although the alloying additions of Mo in long-term, high creep resistant alloys have been restricted, short-term applications contain higher levels of beta alloying elements [20]. Other benefits of Mo additions include increased corrosion resistance in a variety of environments [18,24,33]. Surface stability, increased oxidation resistance and an increased ductility in brittle phases is obtained by Nb additions which substitutes for Ti atoms and increases the number of slip systems and will generally increase most properties of the alloy except for creep resistance [11,28,32,34]. The tensile and yield strength of the material has been shown to be dependent on the Nb content, however, the optimum content is operating temperature dependent [35]. Low temperature applications favour additions of Nb, combined with low aluminium levels, rather than alloying with Mo [36,37]. Problems can be experienced though with the dissolution of high melting point refractory elements such as Mo, Nb etc. in titanium alloys.

The wide-ranging benefits of aluminium and silicon additions to titanium alloys have long been realized and has been described in various literature [24,28,etc.]. The benefits of aluminium additions span the entire alloy phase range, and the alloying content has been successfully manipulated to achieve optimum mechanical and physical properties. In general, the main effect of aluminium additions is to increase the tensile and creep strength moduli of the alloys and to reduce the density [28,32]. The other important feature of the alloying element is that the age hardening response of the metastable beta alloys is improved [28]. However, additions above approximately 7%

promote the formation of a Ti_3Al phase precipitate which is associated with embrittlement of the alloy [28,38]. In some cases though, higher alloying additions can be tolerated by alloying with the solid solution strengthener, Sn, which suppresses the embrittling phenomena [28]. Relatively small additions of Al (approximately 1.5%) steadies the beta microstructure by suppressing the formation of an athermal embrittling phase, ω [39,40]. Furthermore, solid solution strengthening of the solute lean, low strength alpha phase precipitation in the beta matrix can be achieved by the addition of Al [41].

Silicon is usually present in high-temperature titanium alloys [28]. Small amounts in present in titanium alloys ultimately restricts the mobility of dislocation movement under stress, contributing to the ductility of the alloy and promotes surface stability at higher temperatures [28].

A spontaneous and self healing surface oxide formed on titanium and titanium alloys provides the alloy with superior corrosion resistance in various hostile environments. The tenacious titanium oxide layer is stable even with the inclusion of foreign elements and retains its insulating properties and full corrosion resistance [42]. On the other hand the presence of oxygen in the titanium alloys is not to be confused with the formation of the surface oxide layer. Oxygen is also employed as an alloying element and is most commonly used for the solid solution strengthening of commercially pure titanium [43]. The tensile, hardness (only in the unaged condition though) and ductility values have been shown to be dependent on the oxygen content [44,45]. Variations in the aging response, mechanical properties and the microstructure in different chemistry lots have been traced to irregular oxygen contents [44]. Oxygen contents in the alloy are usually kept low (0.1 - 0.15%) due to the detrimental effects on the alloy strength at long term high temperatures exposures [28]. Oxygen also affects the kinetics of the alpha precipitates in metastable beta titanium alloys due to it being a powerful alpha phase stabilizer [44,45]. The uptake of oxygen in titanium alloys at room temperatures though is limited, and the effects on titanium only becomes apparent at higher temperatures where it plays a major role in influencing the mechanical and physical behaviour of the alloys [22,28].

The microstructure of the titanium alloys are influenced by the processing history and heat treatment [22]. Briefly, the different types of titanium alloys show similar responses to heat treatments. Working of the cast leads to recrystallization, resulting in a more equiaxed structure while further heat treatment can produce a completely equiaxed structure. A varied microstructural response can also be obtained when fast or slow cooling the alloys from above the beta transus temperature. Two types of alpha may be found viz. a primary alpha and a secondary alpha. Primary alpha is that present during hot working or heat treatment, while secondary alpha is obtained from a beta phase transformation, i.e. treatment high in the alpha+beta region or aging of the structure which leads to additional alpha precipitation [22]. The alpha phase may appear as either acicular or lamellar, platelike, serrated or Widmanstätten [20,28,32]. A cluster of the acicular alpha aligned in the same direction is generally referred to as a "colony".

Other phases have also been identified in metastable beta alloys [22,28,31,46,etc.]. In brief, the composition of particular binary or multicomponent beta alloys may lead to the formation of deformation-induced martensite, α'' (or α'), or the liberation of a brittle athermal ω phase. Variants of the ω phase can exist, however, the result of the phase precipitation is, as mentioned previously, an inevitable embrittlement of the alloy. The precipitation of the ω phase is due to, amongst other, the isothermal decomposition of the retained beta ($\beta \rightarrow \beta + \omega$, or $\beta \rightarrow \alpha + \omega$) during low temperature aging and is potentially harmful due to the resultant embrittlement of the alloy. The ω precipitation is in line with the displacement controlled reaction assisted by minor solute redistribution and time dependent growth [31]. The ω phase has been described crystallographically as a diffusionless displacive transition resulting from an ordered movement due to a lattice displacement shift wave [47].

The formation of the martensite in titanium alloys can be produced from the diffusionless transformation of the beta. It is not only directly dependent on the martensite start (M_s) temperature (see figure 1.1), but it is also dependent on the state of stress in the alloy, the alloying elements and can also be deformationally introduced in the alloy. It is sufficient to say that these phase evolutions have mainly been studied

after isothermal aging and quenching from the beta field [39]. Although the martensite is detrimental to metastable alloys in general, the development of the phase can be suppressed by alloying and appropriate heat treatment [22,40]. Incidently, martensite in titanium alloys differs from that found in steels due to the fact that it does not strengthen the titanium alloy [48].

1.2 Development of TIMETAL 21S

The development of the metastable beta titanium alloy, TIMETAL 21S, followed from the primary requirements of a foil formable, highly oxidation resistant titanium alloy for use on the NASP [31,49,50]. Where the highly formable, metastable beta Ti-15V-3Cr-3Sn-3Al (Ti-15-3) had previously been used as a matrix for a fibre reinforced composite, an alternate material was being sought since the oxidation and high temperature characteristics of the 15-3 alloy were extremely poor [31]. The starting point for the investigation for an alloy with improved oxidation resistance remained at the metastable beta titanium alloy systems, since these alloys possessed the cold forming capabilities, the ability to be produced in foil form and the age hardenable characteristics that allow for a higher strength material. Secondary requirements included ease of melting, weldability and other properties such creep, fatigue, etc. [31].

The genesis of the 21S alloy proceeded from the Ti-Mo, Ti-Cr, Ti-Fe and Ti-V binary alloy systems. Since the detrimental effects of vanadium on the titanium alloys' stability and oxidation resistance at high temperatures were well known, further development of these alloys were not considered [36]. Table 1 presents a sample of the results of the initial weight gain trials of the various metastable beta alloys that were capable of a 50% cold working reduction [31]. A Ti-15%wt Mo alloy with small additions of Nb (approximately 5%) was consequently observed to have exceptional oxidation resistance compared to other alloys, even when exposed at 1815°C. Further research was conducted in order to investigate propitious effects (if any) from additional alloying elements. The investigations included alloying Ti-15Mo-5Nb (and also Ti-15Mo-5Fe) with, amongst others, Hf, Ta, Y, Re, Al and Si.

Alloy	% Wt gain	Alloy	% Wt gain
Ti-15Mo-5Zr	7.70	Ti-15Cr-0.2Pd	9.76
Ti-15Mo-3Sn	5.37	Ti-15Cr-5Nb	7.62
Ti-15Mo	2.63	Ti-15Cr-0.5Si	7.00
Ti-15Mo-3Al	2.00	Ti-15Cr-3Al	3.68
Ti-15Mo-5Hf	1.41	Ti-15Cr-5Mo	2.90
Ti-15Mo-0.1Si	1.27	Ti-15Cr	2.27
Ti-15Mo-2Nb	0.98	Ti-15-3	>65
Ti-20Mo-2Nb	0.99	Commercially	
Ti-15Mo-5Nb	0.95	pure Ti	7.70

Table 1.1: Evaluation of alloying additions on weight gain tests on Ti-Mo and Ti-Cr base alloys after 1815°C exposure for 48 hours [31]

The Fe containing alloy was included since this alloying element is added for strength, producibility and for high temperature strengthening [43,51]. High temperature weight gain results concluded that a **Ti-15Mo-2.7Nb-3Al-0.2Si-0.15O_2** displayed the most favourable oxidation behaviour at the expected service temperature.

Table 1.2 shows a weight gain comparison of various titanium alloys and nickel-base alloys with that of TIMETAL 21S, after exposure of 650°C and 815°C for 96 hours [31]. TIMETAL 21S represented roughly a 100 fold improvement in oxidation resistance over the previously used Ti-15-3 although the inferior oxidation resistance when compared to the titanium-aluminide and the nickel-base alloy above 815°C is clearly evident [31,52].

Initially, the alloy was designated as "BETA 21S" since it was a beta titanium alloy, containing 21% of alloying elements, and also contained Si. It has since become known as TIMETAL 21S. In addition to the superior high oxidation resistance, exceptional high strength stability was displayed by the alloy.

Alloy	Temperature (°C)	Weight gain (mg/cm^2)
TIMETAL 21S	650	0.11
	815	2.78
Commercially pure Ti	650	0.53
	815	26.1
Ti-15-3	650	3.18
	815	174.0
Ti-48Al-20Nb	815	0.73
Rene' 41	815	0.32
IN 718	815	0.14

Table 1.2: Comparison of weight gain after 96 hour exposure between TIMETAL 21S, various titanium alloys and a nickel based alloy [31]

Creep tests performed on TIMETAL 21S showed that the alloy had surpassed that of the alpha+beta alloy, Ti-6V-4Al, making it the only metastable beta alloy to achieve this result [31].

TIMETAL 21S is supplied in the solution annealed (SA) condition i.e. solution treated and annealed for four minutes at 845°C. This results in 95% recrystallization of the beta grains in the alloy [31]. TIMETAL 21S can be extensively cold formed in the SA condition, after which a aging treatment can be applied. The cold working process however results in the rapid aging of the material and a re-solution anneal treatment followed by aging is preferred for a predictable aging response [22,31]. TIMETAL 21S has been accepted as the "standard" for the further development of the matrix material of the titanium metal matrix composites. The low diffusivity of elements such as Mo, Nb or Al also lowers the reactivity of the titanium and minimizes the interaction of the alloy with the reinforcing fibre, thus effectively extending the composite stability [11,25,53]. Although the oxide layer which forms on the surface after prolonged exposure to oxidizing environments at elevated temperatures reduces the overall tensile

ductility, the alloy remains metallurgically stable [54]. TIMETAL 21S has been shown to handle high stresses, when the operating temperature remains between 260°C and 425°C, and low stresses up to 540°C [55].

The lattice parameter for the TIMETAL 21S BCC structure is 3.26 Å and with thermal exposure, the BCC parameter changes to 3.24 Å. The precipitated HCP alpha phase structure has a lattice parameter of 2.94 Å and c parameter of 4.74 Å. The thermal coefficient was found to be 9.3 x 10^6 /°C up to 370 °C. The elastic modulus ranges varies between 70 GPa to 80 GPa in the solution annealed condition, and after aging the modulus is typically in the 105 to 115 range. With thermal exposure, the tensile yield strength decreases by 38 % compared to the peak strength obtained during aging. Tests have shown after suitable heat treatment the alloy is stable for at least 1000 hours at temperatures up to 615°C [56].

1.3 Fatigue crack growth evaluation by linear elastic fracture mechanics

With the increasing use of metal alloys during the nineteenth century, the number of unexplained and catastrophic failures increased dramatically. Boiler explosions numbered 50 to 60 a year in the United Kingdom alone, and almost daily railroad related disasters occurred during the late nineteenth century [57]. Other classical catastrophic failures occurred in the early twentieth century [57,58]. At that time, the investigations of these failures were inconclusive and a call for a commission was made to investigate these seemingly inexplicable failures. Primary studies indicated that the probability of inherent material deficiencies and flaws could have lead to the premature failure of these large structures [59]. Further research in order to understand the role of these defects and the mechanisms of these failures were not conducted though. Experiments performed by Griffith in the 1920's on glass fibres with small surface defects gave birth (unsuspectingly) to the concept of fracture mechanics, but not until the legendary failures of the Liberty war ships during the 1940's was Griffith's theories further explored to determine what the effects of pre-existing flaws on the life and fracture characteristics of components under fatigue and static loading conditions were. The concept of fracture mechanics has since tried to relate the combination of a crack

size or any other defect size to the material behaviour on application of a monotonic or cyclic stresses. The fracture mechanics approach, after initially being met with severe criticism, has now globally been accepted to describe the events leading up to, and factors governing, the failure mechanisms. The characteristic brittle fracture appearance that were most common in ships, bridges, pipelines and other large structures, were also termed elastic fractures due to the fact that these failures occurred below the yield level of the material and that no plastic deformation was evident [59]. The investigation of these elastic modes of failure gave birth to what was to become linear elastic fracture mechanics (LEFM). LEFM has since become an important tool in the design, maintenance and life prediction of a variety of structures.

Inglis' paradoxical conclusion that a plate containing a crack is unable to carry any load due to the stresses tending to infinity at the crack front, was resolved by Griffith who used an energy approach based on surface energy [60,61]. Irwin used these research analogies to show that the events occurring near the crack tip could be summarized by a singular parameter, called the stress intensity factor, K. Other complex parameters were later introduced in order to describe different and inherent material behaviour. These included the development of the crack tip opening displacement (CTOD) parameter in ductile materials, the J integral to relate the non-linear energy release rate to the crack tip stress field, the dynamic stress intensity factor to describe dynamic fracture, and, the C-parameters which were derived in order to define the transition from an instantaneous elastic strain field at the crack tip (and thus a stress intensity dominated field), to the occurrence of primary creep leading up to steady state creep. Definitions and details of these terms can be found in various literature [60-62]. Other important practical features that have current applications in modern structures that have evolved from the LEFM research were the leak-before-break, the safe-life and the fail-safe concepts [62].

For the purposes of evaluating the crack movement and crack tip stress fields LEFM defines 3 basic types of relative crack face movements [57-63]. These movements are described by mode I, mode II and mode III loading as shown in figure 1.2.

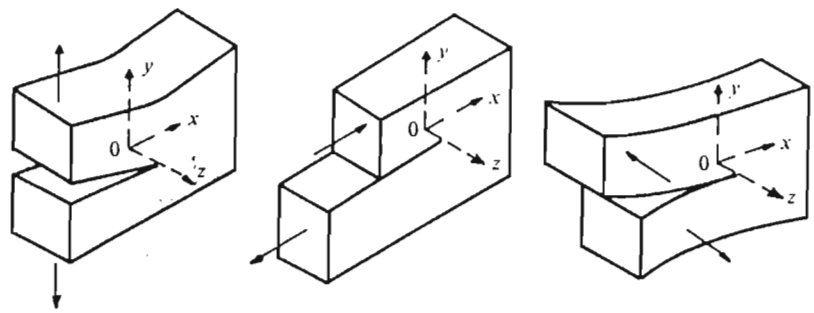

Figure 1.2 : Different modes of cracking described by LEFM [63]

The opening mode, where the crack faces separate normal to the propagating crack faces, is described as mode I loading, mode II loading entails the crack faces sliding over each other and mode III loading is the tearing mode where the crack faces slide over each other in a direction parallel to the crack front. These three different modes of loading set up characteristic stress fields at the crack tips. In order to simulate the events that occur during crack propagation and at eventual failure, standardized specimens are tested in the laboratory environment to gain insight into the various factors and mechanisms affecting the crack propagation rate and final failure, as would be experienced by a component in service. Since mode I cracking is technically more beneficial, most research has been conducted using mode I loaded samples [64].

To summarize the events that occur at the crack tip during the fatigue and fracture of a material the stress intensity factor was introduced. Consider an arbitrary crack front, as depicted in figure 1.3, where σ_{ij} is the stresses experienced on the material element dxdy, a distance r from the crack tip and at an angle of θ. Irwin showed, using linear elastic theory, that the stresses in the vicinity of the crack tip could be expressed by equation 1.1., viz :

$$\sigma_{ij} = \frac{K_I}{\sqrt{2\pi r}} f_{ij}(\theta) \qquad \ldots(1.1)$$

where $f_{ij}(\theta)$ is a function of θ. K_I, which is known as the stress intensity factor for mode I loading, describes the magnitude of the elastic stress field under mode I loading [57-63]. Similarly K_{II} would denote the stress intensity factor for mode II loading, however with a different θ-function. To describe the complete stress field surrounding the crack tip of an infinite plate under uniform tension with a central crack of length 2a, a general form of the stress intensity factor can be found and is given by :

$$K_I = \sigma\sqrt{\pi a} \cdot f(\frac{a}{W}) \qquad \ldots(1.2)$$

where f(a/W) is dependent on the specimen and crack geometry.

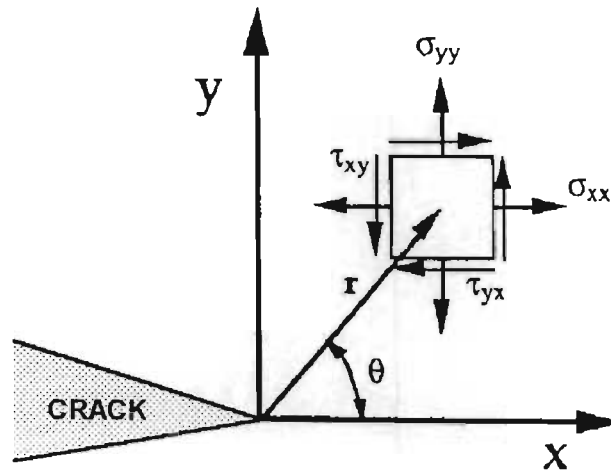

Figure 1.3 : Crack tip and the associated stress field under monotonic loading

To operate within the boundaries of LEFM, finite thickness effects of the sample have to be taken into account and the crack tip stress intensity field description then takes on a different form. Rather than using the remote stress, σ, as in equations 1.1 and 1.2, to describe the stress intensity field, the stress intensity factors are in the form :

$$K_I = \frac{P}{B\sqrt{W}} \cdot f(\frac{a}{W}) \qquad \text{...(1.3)}$$

where P is the applied load, B the specimen finite thickness and W is the specimen width. Various stress intensity factors are assigned to different standard test specimens and these can be found in the ASTM materials testing standards handbook and various fracture mechanics literature [57-64 etc.]. It is possible to calculate the stress intensity factor for almost any body containing a crack [65], as long as certain geometrical constraints are observed, and load conditions at the crack tip are within the scope of LEFM. However, standard test specimens are used in order to establish similar stress fields at the crack tip and to conduct comparative and repeatable tests.

Examining equation 1.1 it can be seen that as $r \rightarrow 0$, the stress at the crack tip theoretically becomes infinite (Inglis' paradox). This however cannot occur since the material has limited strength and it is assumed that a plastically deformed zone ahead of the crack tip is established, thus keeping the stresses finite. By substituting the yield stress, σ_y, into equation 1.1, it can be seen that if the crack tip plastic zone radius along the crack axis ($\theta = 0$) is given by r_p, then,

$$r_p = \frac{K_I^2}{2\pi\sigma_y^2} \qquad \text{...(1.4)}$$

Assuming the validity of such an assumption, it can be seen from equation 1.4 that the size of the plastic zone is dependent on the yield strength and the instantaneous stress intensity factor. Once the size of the plastic zone plays a significant role in the events ahead of the crack tip, elastic plane strain conditions will cease to exist and the K concept will start to lose its significance. These phenomena have also been related to the specimen thickness effect. In the early stages of LEFM testing, variations in the test data were obtained when different sized samples were used. This was due to a finite thickness effect that, in some cases, transformed the plane strain condition to a plastically dominated plane stress condition and hence lead to the data scattering [66]. This implies that the size of the plastic zone ahead of the crack tip has to be kept to a minimum and play a near insignificant role during crack propagation. In general, for

conditions of plane strain to predominantly exist during monotonic load tests, a specimen thickness of more than fifty times greater than the radius of the plastic zone at the crack tip is required [60].

Irrespective of the loading mode, the conditions of plane strain at the crack tip has to be maintained. The American Society for Testing and Materials (ASTM) have accepted the 647 - E88a Standard Test Method for the Measurement of Fatigue Crack Growth Rates to ensure that plane strain conditions exist during fatigue loading of the test sample. This is achieved by recommending suitable test specimen dimensions. The 647 standard covers the recommended test procedure for two standard specimens, namely the compact tension (C(T)) specimen and the centre-cracked tension (M(T)) specimen. Figure 1.4 shows the recommended dimensions of the C(T) test specimen as proposed by the ASTM standard.

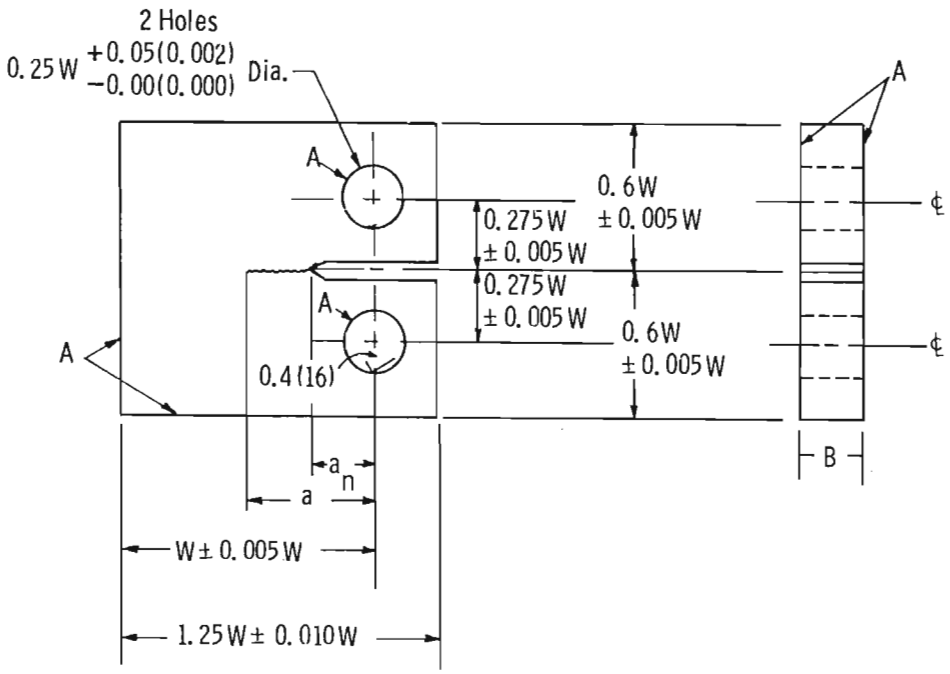

Figure 1.4 : ASTM 647 - E88a recommended dimensions for LEFM compact tension (C(T)) test specimen

Although a minimum thickness is not specified, the only requirement is that during a test the material has to remain predominantly elastic at the crack tip. Thickness may also be varied independently of the rest of the specimen. In order to validate the condition of plane strain during the test, the following condition for the C(T) specimen has to be met :

$$(W-a) \geq (\frac{4}{\pi}) \cdot (\frac{K_{max}}{\sigma_{ys}})^2 \qquad \text{...(1.5)}$$

where (W-a) is the uncracked ligament length, K_{max} is the maximum stress intensity factor experienced during a fatigue cycle, σ_{ys} is the 0.2% offset yield strength determined at the same temperature than what the test will be conducted at [64].

Several expressions for the stress intensity factor for the C(T) specimen have been proposed. The ASTM standard has however accepted the stress intensity factor as proposed by Swraley in 1976 [58,64]. The expression, as given by equation 1.6, covers the entire range of a/W and is accurate to within 0.5%. The use of this expression has also been recommended by other researchers [58,60,67].

$$K = \frac{P}{B\sqrt{W}} \cdot f(\frac{a}{W}) \qquad \text{...(1.6)}$$

where

$$f(\frac{a}{W}) = \frac{(2+\frac{a}{W})}{(1-\frac{a}{W})^{\frac{3}{2}}} (0.886+4.64(\frac{a}{W})-13.32(\frac{a}{W})^2+14.72(\frac{a}{W})^3-5.6(\frac{a}{W})^4)$$

...(1.7)

and P,B,W are defined as in figure 1.4.

Several attempts have been made to relate crack growth rates as a function of a known parameter experienced during fatigue testing. Paris, Gomez and Anderson have shown that the cyclic steady state crack growth can be described by the well known Paris law which states :

$$\frac{da}{dN} = C\Delta K^m \qquad \text{...(1.8)}$$

where da/dN is the fatigue crack length change per load cycle, the terms C and m are scaling factors for the specific material, and the stress intensity factor range, ΔK, is defined as :

$$\Delta K = K_{max} - K_{min} \qquad \text{...(1.9)}$$

where K_{max} and K_{min} are the stress intensity factors corresponding to the application of the maximum and minimum loads during a fatigue cycle. The Paris law is however only applicable to the steady state region of crack growth.

While equation 1.6 describes the stress intensity factor under monotonic loading the equation can be modified to incorporate the stress intensity factor experienced near the crack tip due to cyclic loading, namely,

$$\Delta K = \frac{\Delta P}{B\sqrt{W}} \cdot f(\frac{a}{W}) \qquad \text{...(1.10)}$$

where B and W are defined as previous, and where ΔP is the difference between the maximum and minimum loads applied during the cyclic tests.

$$\Delta P = P_{max} - P_{min} \qquad \text{...(1.11)}$$

The crack length, a, as used in equation 1.10 is now taken as an average length.

Cognisance must be taken of the fact that only tension-tension testing is recommended for C(T) specimens, thus the stress ratio, R, will always be equal or greater than zero. Applying a compressive load on the specimen will introduce uncertainties into the loading experienced at the crack tip [64].

Results of fatigue crack growth rates using the LEFM approach are usually presented in a log da/dN vs ΔK graphical form. This plot reveals three distinct regions, namely stage I, stage II and stage III, as shown in figure 1.5.

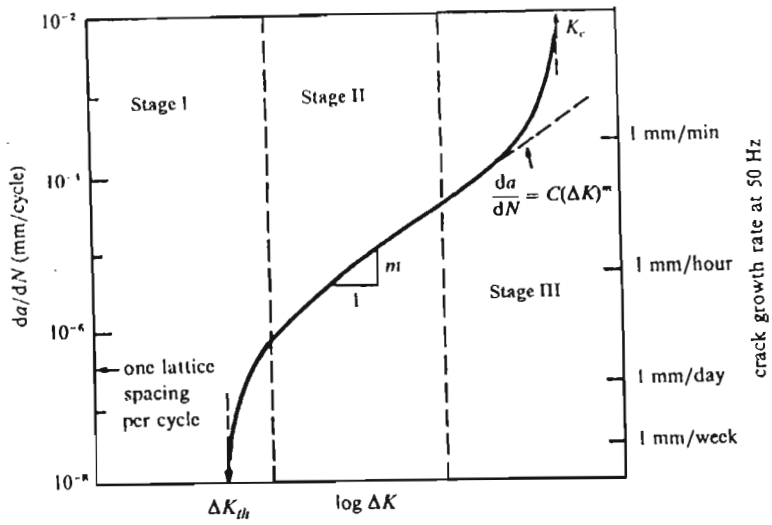

Figure 1.5 : Different stages of fatigue crack propagation

Stage I identifies a stress intensity factor range threshold value ΔK_{th}, below which "long" crack propagation does not exist, or grows at an undetectable rate. Once the loading regime exceeds the ΔK_{th} value there is a rapid increase in the crack propagation rate with increasing ΔK. ΔK_{th} is often used in fatigue design where components have to withstand low load, high frequency vibrations over extremely long periods of time [68]. In stage I crack growth, the threshold value is largely influenced by the slip characteristics of the material, the microstructure, the mean stress and the environment [65,68]. Crack growth occurs mainly by single shear and leads to a zigzag type crack. The plastic zone ahead of the crack tip at this stage is confined to a few grain diameters.

The intermediate level of crack growth, stage II, is the linear region in which the Paris law applies. The crack growth rate in this region has been shown to be insensitive to factors such as the microstructure, the tensile properties and the thickness of the specimen. Environmental effects, mean stress and loading frequency tends to influence the crack growth rate characteristics of a given material to a greater extent [58,65,68]. Stage II is also the region where the characteristic fatigue striations are mostly found. Conflicting evidence to whether striation spacing serve as an indication of crack progression exists, however, under certain loading conditions, correlations have been found between the striation spacing and the experimentally measured fatigue crack

growth rate [58,68]. An infrequent occurrence of the striation marks have been observed in various steels, while in cold worked steels these marks are rarely observed [68]. The plastic zone in the linear region is of the order of many grains and may greatly affect the fatigue crack growth behaviour [68].

Stage III indicates the events leading up to and at final failure. The environment plays a near insignificant role in the rapid crack progression and factors such as the microstructure, stress and stress-state are most influential. At the onset of failure, the maximum stress intensity factor approaches the fracture toughness value, ΔK_{IC}, of the material.

For design purposes, particularly where safety-critical components are involved (for example in the aerospace industry) the da/dN vs ΔK plot is crucial. From laboratory tests using the crack progression and stress intensity factor range data and, where similitude exists, the time or number of cycles to achieve a critical crack length can be estimated in actual components. For non-safety-critical and other applications where the total life of the component is of more of interest, the classical fatigue solution design approach of S-N curves are used [69].

A final point to consider during experimental observations of crack growth rate and ΔK is the effect of the specimen thickness on the propagating crack front geometry. It becomes evident that with increasing thickness, greater curvature of the crack front is experienced. The phenomena, termed crack tunnelling, may introduce large errors into the calculated values of da/dN and ΔK, if severe. The ASTM 647 code recommends taking a number of readings across the crack front to account for the consequences that the tunnelling effect has on the experimental data.

In conclusion, on the use of LEFM and the stress intensity factor, the crack behaviour in practical models can be fairly accurately predicted when similitude exists with experimental work. Violation of the basic principals of LEFM have been shown to exist during fatigue [69], however LEFM is valid as long as the non-linear region is confined to a small region surrounding the crack tip. The importance of LEFM though

is underlined by the fact that although numerous more advanced models exist in order to comprehensively describe material behaviour under loading, LEFM is presently being used by the important aerospace industry in the design of modern aerospace structures [70].

1.4 Methods for determining crack growth rates

Various methods have become available to monitor fatigue crack growth rates. While some methods directly observe the crack progress, indirect methods require calibration curves to predict fatigue crack growth rates. Both direct and indirect methods have their advantages and disadvantages and ultimately a method suitable to the operator and test conditions has to be selected. Consideration should also be given to the test temperature and the restricted working space when, for example, using an environmental chamber. The most widely used techniques will briefly be discussed and their suitability to the anticipated test conditions and temperatures will be evaluated.

Initially, optical methods were the most widely used method to measure the crack progression. A travelling microscope, attached to a vernier, is focused on the crack and the extension tracked. Provided the propagating crack front is relatively straight, reliable readings can be obtained. Although extensions of 0.1 mm are readily detected, the precision of the reading is questionable [2,71]. This can be due to a number of factors, including plastic deformation, poor illumination and high frequency blurring. While certain methods may be used to accentuate the crack, e.g. using a dye penetrant, the effect of these compounds may influence the crack growth rate [2]. While the method is often used at room temperature, higher temperatures present problems due to the specimen being situated inside an enclosed furnace. Furthermore, if a surface oxide is present, accurate detection of the crack becomes increasingly difficult [2]. Some success has been attained though with the use of a travelling microscope of long focal length situated outside the furnace [72], however, distortion of the image and decreasing accuracy of this method have lead to alternative methods to be employed.

Acoustic emissions during fatigue crack progression originate due to stress waves transmitted by the material as it deforms due to an external load or due to phase transformations [2]. Sensors in contact with the surface of the specimen record these emissions, convert them to electrical signals and after rectification these signals can represent the crack growth. Since the emissions occur over a wide range of frequencies and a suitable frequency monitoring range has to be selected. However, the technique is limited to a certain frequency range which has to minimize the intrusion of background noise from the loading fixtures, the loading arrangement, the hydraulic system and other background vibration systems which may mask the signal from the specimen. Apart from the sensors that detect the emission levels from the specimen, a pre-amplifier, a signal conditioning unit, an amplifier, an event detector, an event counter and an appropriate data acquisition system are some of the typical components of the acoustic emission system [2]. The use of this crack monitoring system requires some form of calibration to link the acoustic emissions to crack extension and is mostly used for room temperature tests.

Ultrasonic detection used for fatigue crack detection is similar than what is used for conventional nondestructive testing (NDT). The method involves the transmission and reception of acoustic waves of low intensity and high frequency sound energy which is reflected back to a receiver by the crack or the sample surface [73]. Advantages of this detection method is that it is the only method that can give the internal measurements of the crack as well as the crack profile, however, it is suffice to say that ultrasonic detection has proved to be unsuitable for small, thin specimens, and it cannot be used at higher temperatures [71].

Electrical potential techniques are one of the most widely used methods for measuring the crack growth. The technique can be employed in a variety of situations to monitor various crack velocities, e.g. fast fracture, creep and stress corrosion cracking, etc. [2]. A-c or d-c potential drop techniques can be used. The detection method involves the application of a constant current to the specimen and as the fatigue crack propagates through the specimen, the potential drop across the specimen increases proportionally. The method requires a calibration curve for each particular specimen size and shape

and test temperature, and if corrosion product are present during the test, bridging of the crack during readings may occur and lead to erroneous crack length results [71]. The method is also susceptible to electrical and thermal noise [74]. Furthermore, the specimen needs to be isolated from the specimen grips to avoid current leakage. The particular problem of crack-front curvature is also not addressed by the monitoring method [72].

The compliance method is currently the most versatile and widely used method to study fatigue crack growth rates and other fracture mechanics related topics [2,75-80]. Compliance is defined as the displacement of the specimen per unit load and the method originates from investigations conducted to identify the strain energy release rate at the crack tip per unit thickness of the specimen under constant load or under constant displacement [2]. The compliance method most often uses a double cantilever clip gauge that is attached to the specimen notch mouth. Calibration requires a set of compliance readings to be recorded for various crack lengths up to a crack length that is deemed to be of sufficient final length [2]. The final results of the calibration test can be plotted as a/W vs EBC, where E is the Young Modulus at the test temperature, B is the specimen thickness and C is the compliance. A polynomial is fitted by the statistical method of best curve fitting to obtain a function for a/W vs EBC, i.e a/W = f(EBC). Thus calibration exists between the normalized compliance and the normalized crack length. Obtaining a function of EBC = f(a/W) allows for the determination of an effective Young's modulus at any test temperature, if the instantaneous crack length is known. Increasing the test temperature or using an environmental chamber necessitates the use of expensive strain gauges that are able to withstand the test conditions, or to seek alternate methods of crack opening displacement detection [75]. "Conventional" compliance crack measurement techniques employing a double cantilever strain gauge or back face strain gauges are limited by the test temperature, although capacitive type devices have been able to operate up to 649°C in air [76]. The effect of aggressive environments on these devices are unknown. The use of an environmental chamber inside the furnace furthermore restricts the space available around the test specimen. The compliance method has however been used at high temperature by translating the strain outside the furnace by means of strain

transfer rods [77,78]. This particular setup though was tedious and complicated by having to periodically interrupt the fatigue test, assembling the spring-operated transfer rods, measuring the compliance, de-coupling the rods and then continuing the test [78]. The method is also subject to various translational errors [77]. Although the compliance method uses the notch mouth mounted displacement gauges, the gauges can basically be mounted in various positions [64]. Conventional load-line displacement methods monitor the displacement of the specimen at the point of load application using clip gauge or other devices. Load-line displacement measurement have been found to have the necessary accuracy to describe the fatigue crack growth at elevated temperatures or if the sample is inside an enclosed environmental chamber and has been described as a simple, yet reliable, method to accurately predicted the crack progression [75-77]. With the load line test procedure the displacement gauges can however also be mounted on the actuator piston itself, although it is important to acknowledge the added compliance of the specimen grips in this type of testing [75,77]. At least one visual reading is to be taken after the test to correct for crack curvature. Differences between the actual crack length and the compliance crack length are mostly attributed to the variance in Young's modulus at the test temperature, and all crack length are to be corrected following testing using an effective value [64]. The compliance test is usually done in conjunction with a tensile test at the test temperature to obtain a value for the effective modulus. An added benefit of the compliance method is that it can be easily computerized and accurate *in-situ* monitoring of the progressing crack length is possible [79]. The compliance method is also the most widely used method (thus far) that can monitor the extent of crack closure experienced by the specimen, although it cannot distinguish between the various closure mechanisms [68]. Further discussion on crack closure and its effects is given in section 1.6.

Another fatigue crack growth rate detection method that has recently been favoured is the beachmarking method. In this method, a beachmark is purposely impressed on the surface of the test specimen at regular cyclic intervals, demarcating a block containing a specific number of cycles. The method favours simple loading schemes such as the constant load amplitude, increasing ΔK tests. The beachmarking can be accomplished by either changing the frequency or by changing ΔK, or by a combination of the two

methods, or, by any method that results in significantly reduced rates of crack growth [72]. It is possible to plan, prior to a test, a sequence of blocks of approximately equal width in order to obtain unambiguous evidence of the fatigue crack growth rates. This can be achieved by assigning a block containing a larger number of cycles to a region having a lower ΔK value, and conversely reducing the number of cycles per block as ΔK increases. Although the method provides less data points than with indirect methods, the data obtained is more accurate and additionally provides an exact measure of the degree of crack front curvature, unlike indirect methods [72]. The method is however not sensitive enough to detect the stage I fatigue crack growth and only stage II crack growth can effectively be monitored [72]. Furthermore the crack progression during the test is unknown (unless an additional monitoring method is used) and the crack lengths can only be determined following the test [72]. This results in some trial and error tests before a suitable combination of ΔK/number-of-cycles-per-block/test frequency can be established. Further, other important mechanisms such as crack closure cannot be determined and only the effect thereof verified.

1.5 Effects of high temperature on titanium alloys

Titanium-based alloys have often been used as replacement material were other alloys are unable to maintain their mechanical and physical integrity due to elevated temperatures. Recent advanced titanium-based alloys have pushed the operating limit to temperatures approaching 600°C. The use of these advanced members at high temperatures are limited though due to the severe surface oxidation and the accompanying loss of strength due to the environmental effects [32]. Numerous studies have concentrated on sustaining the high temperature strength with encouraging results, however, the greatest challenge has been to increase and maintain the oxidation resistance when exposed to high temperatures. The use of titanium aluminides and titanium aluminide-based alloys has elevated the temperature limit to 800°C and above [11], however at long exposures to high temperatures the oxidation resistance still is a critical factor [81].

Since the introduction of the titanium alloys as a high temperature material of construction, the elevated temperature capabilities have increased significantly. Table 3 gives an indication of the increasing temperature capability of the alloys. The table is mostly occupied by alpha+beta, alpha and near-alpha alloys since these alloys possess good high temperature capabilities [83]. The limiting operating temperature is due to factors such as the long term surface and bulk microstructural stability [20]. The different types of microstructure of titanium-based alloys play a distinct role in the elevated temperature properties. Existing high temperature structural alloys are mainly two phase alloys with a higher volume fraction of beta phase providing higher short term strength due to the aging characteristics, and high volume fraction of alpha phase are preferable for elevated temperature creep resistance [20,32,84]. Furthermore, the performance of the alloys, in terms of creep, fatigue and fatigue crack propagation rate at elevated temperature, is dependent on the existing morphology [20]. Research for improved high temperature structural titanium alloys has remained with the $\alpha+\beta$ alloy systems since a vast range of microstructure can be obtained through different material processing and heat treatment, providing compromising abilities in the material behaviour. Thus beta alloys have been developed mainly in anticipation of high strength applications, with the Ti 10-2-3 (10V-2Fe-3Al) being the sole "high temperature" beta alloy able to operate at a moderate 315°C [82]. Currently attention is directed to the β alloys which have high formability, are able to maintain their mechanical properties and have a higher oxidation resistance at higher temperatures. In particular, the high strength metastable β titanium alloys have been cited as the material of construction for future (and have also been in the past) elevated temperature use. Although the alloy have a higher density and lower creep strength compared to the alpha and alpha+beta alloys, the sustained high strength capabilities are exceptionally attractive and is being well exploited. An example of the metastable alloy's critical role, and further anticipated use in the aerospace industry, can be found in the development of the SR-71 "Blackbird" which was built in the 1960's. Ninety five percent of the plane consisted of, amongst other titanium alloys, the "original" metastable beta alloy, Ti-13V-11Cr-3Al (Ti-13-11-3) [85]. This alloy, along with its successor, the versatile metastable beta alloy, Ti-15-3 is however a good example of mechanical property degradation and increasing surface instability with increasing temperature [31,86].

Alloy designation	Year of introduction	Useful maximum temperature °C
Ti 6-4	1954	300
IMI-550	1956	400
Ti-811	1961	455
IMI-679	1961	450
Ti-6246	1966	400
Ti-6242	1967	450
IMI-685	1969	520
Ti-5522S	1972	540
Ti-11	1972	540
Ti-6242S	1974	565
Ti-5524S	1976	500
IMI-829	1976	540
IMI-834	1984	600

Table 1.3 : Year of introduction and maximum operating temperature of various titanium alloys [82].

The metastable β alloys have since gained recognition with the introduction of the advanced, high oxidation resistant, high temperature alloys which have sustained mechanical properties over a wide range of temperatures. Since the present investigation is concerned with the conventional titanium-base alloys, the titanium aluminides (intermetallics) fall outside the scope of the current study. To however ignore the plethora of information on titanium aluminides would limit the insight into the general behaviour of the titanium-base alloys and thus comparisons in the typical behaviour of the aluminides and the conventional titanium-based alloys will infrequently be made.

1.5.1 Aging response of titanium alloys

Several factors account for the transformation processes of titanium alloys however, in this study, the most pertinent is the isothermal aging process [41]. It has been shown that the high temperature performance of titanium alloys is as much dependent on the microstructure as on the alloy composition [12]. Generally, alpha and near alpha titanium alloys show superior microstructural stability and have been extensively used

for high temperature applications due to its superior creep resistance [20,31]. Since the alpha alloys do not contain significant amounts of beta stabilizing elements to affect the microstructure, the alpha microstructure is stable at low and at elevated temperatures. The alloys cannot be strengthened by heat treatment and solid solution strengthening by alloying has resulted in increased strength levels. With the increased alloying levels though, in particular silicon (as mentioned previously), the formation of embrittling phases and increased strain localization have resulted in a decrease of the mechanical properties at elevated temperatures [87]. In order to obtain higher strengths and still maintain some high temperature capabilities, alpha+beta alloys have been employed. These alloys can be strengthened by solution treatment and aging, due to the presence of the beta phase in the alloy [19]. The use of these alloys at higher temperatures are limited though due to the inferior creep capabilities of the beta phase [20]. With the expanding use of the metastable titanium alloys, the microstructural behaviour and stability becomes more critical at elevated temperatures. The metastable beta structure tends to precipitate a secondary alpha phase in the matrix when exposed to high temperatures. This precipitation, or aging process, in titanium alloys that contain large amounts of retained phase, lead to a significant change in material mechanical properties [56,88]. The aging response and accompanying distribution of the precipitates is dependent on the nucleation sites, the precipitation kinetics and the driving force for the precipitation and is also strongly influenced by the processing history, i.e. the degree and extent of previous mechanical working of the alloy [56]. The strength, ductility and the toughness of the metastable titanium alloy is dependent on the volume fraction, size and morphology of the of the precipitates in the alloy.

The precipitation hardening process in metastable beta alloys is characterized by the ability to interchange the excellent formability and strength at each manufacturing process e.g. forming of the ductile solution annealed material, followed by aging to high strength. The resulting strength and toughness is superior compared to the alpha+beta alloys [89]. The precipitates are in the form of hexagonal alpha titanium which nucleate inside the BCC beta grains, at the grain (or subgrain) boundaries, also at dislocations and other retained phases [21,27,29,90,91]. The precipitation can occur by either homogeneous or heterogeneous nucleation. The homogeneous nucleation

occurs mainly as the precipitation of fine alpha inside the beta grain [21]. The precipitation that occurs at these high energy sites are known as sympathetic alpha [41]. The heterogeneous process on the other hand occurs mainly at the grain boundaries [92]. While low temperature heat treatment encourages the formation of the alpha phase precipitate at lattice defects inside the beta grains, intermediate temperature exposures promote the precipitation at the grain boundaries and increased grain boundary alpha can be observed at higher aging temperatures [28,56]. These precipitates can exist in several forms, namely that of continuous or semicontinious film-like grain boundary layers or directionally elongated next to the film-like alpha, the so-called allotriomorphic alpha [93,94]. It is interesting to observe that in the metastable beta structure, a precipitation free zone is formed adjacent to the heterogeneous grain boundary nucleation [56]. This has been attributed to the vacancy diffusion to the grain boundaries, effectively eliminating alpha precipitation sites, retarding precipitation or leading to a precipitation free zone, resulting in a non-uniform distribution of alpha [56]. Mechanical property degradation due to the lack of precipitation adjacent to the grain boundaries leads to a locally softer region and potentially a strain localization zone and lower ductility and "intergranular" failure can be expected [27,56,95]. This effect is amplified if a soft, solute lean alpha phase is precipitated [27]. Solid solution strengthening of the precipitates can be accomplished by the addition of alpha solid solution strengtheners such as aluminium to the alloy which also promotes the rapid formation of alpha during aging [28,41]. The preferential grain boundary precipitation results in non-uniform distribution of the alpha phase and increasing the aging time or increasing the aging temperature leads to a more homogenized structure [96]. With increasing aging temperatures, the alpha precipitates become more coarse, which affects the mechanical properties up to a point [56,89]. If the solute lean precipitates are below a critical size, the alpha is coherent and deformable [89]. A shearing type of deformation can occur across the low strength precipitates, which in turn decreases the strength. Strengthening the alpha phase through alloying results in an increase in the strength. The interface between the beta and alpha phases is either an FCC or an HCP structure [97].

The BCC titanium structure allows for higher levels of interstitial elements than the alpha structure. Although the beta alloys appear to be more tolerant to these elements, the effect of these elements on the transformation kinetics, aging behaviour and mechanical properties need to be studied further [90].

In some cases, the solution treated and aged condition does not result in sufficiently high strength level [98]. This is due to the relatively limited availability of homogeneous nucleation sites. In annealed alloys, where these sites are even more restricted, precipitation mainly occurs at the grain boundaries [27]. To affect the age hardening response of the alloys, homogeneous nucleation sites have to be created. It has also been noted that upon partial aging of hot worked metastable titanium alloys, the un-recrystallized zone etched darker that the surrounding matrix [19,64]. This was due to the accelerated aging of these zones since these contained a number of defects or greater dislocation substructure (stored energy), resulting in a more rapidly aged grain [64,94]. This is a similar process that is used to accelerate the aging process in certain titanium alloys. To illustrate this, consider the selection of the metastable titanium alloy, Ti-13-11-3, for the SR-71. The use of the alloy was due to its high strength ability and its stability (in particular weld stability) at moderate elevated temperatures. However the alloy required aging times in the order of 100 hours before an appreciable response was obtained [88]. One of the "tricks" to increase the aging response then was to hot and cold work the material prior to aging, thus resulting in an improved aging response. In order to obtain the required strength from the metastable beta alloys in general though, the homogeneous precipitation processes needs to be controlled [99]. This can be achieved as follows: 1. when the beta phase stability is too high, the alpha will preferentially precipitate at the grain boundaries but this can be improved by adjusting the alloy stability, 2. the preferential precipitation can be retarded by grain refinement, 3. the growth rate of the alpha can be retarded by selecting as low an aging temperature as possible, 4. homogeneous precipitation can be controlled by tailoring the aging process, and/or, 5. homogeneous precipitation is enhanced by the control of the dislocation structure [89]. Controlling the dislocation structure by either cold working, cold working and recovery treatment or warm working has proved to be most effective in controlling the fine and homogeneous

precipitation of the alpha phase [89]. In particular, a better balance between the strength and ductility has been achieved by warm working [47,89]. Thermo-mechanical treatments have been used to improve the balance of strength and ductility by controlling the morphology of the alpha precipitates [94]. Combinations of thermo-mechanical treatment has resulted in titanium alloys with a tensile strength of 1900 MPa and an elongation of 10% [89]. In this case a combination of grain size control, solution treatment to control the dislocation structure and a moderate recovery of the structure produced the result. The relative advantage of metastable beta titanium alloys are that they are highly formable in the solution treated condition and parts can readily be cold formed, and after forming, direct aging can be applied. The cold worked material ages to an appreciably higher strength [50,87]. In some instances re-solution annealing is recommended because of the rapid aging response of the deformed material [31,87]. Two stage aging processes, i.e. precipitation of the low temperature ω phase followed by a high temperature age to aid in the precipitation of alpha, or a high temperature age followed by a low temperature age to precipitate fine alpha around the larger alpha precipitates, also results in attractive combinations of strength, ductility and toughness [41,47,89,92,98]. It should be noted though that even with the thermo-mechanical structure modification processes the grain boundaries are still preferential sites for alpha nucleation [94].

Low aging temperatures can only be used in some cases due to the rapid diffusivity of elements such as V and Fe [41]. Long term, low temperature exposure are generally avoided for solution annealed and cold worked alloys, and high temperature applications require that the material be used in the fully aged condition [31]. The stability of the metastable titanium alloys also becomes an issue if the alloy is used near its aging temperature [31].

1.5.2 Effects of oxidizing environment

Key areas of importance can be established with regard to the successful implementation of titanium alloys at elevated temperatures, namely that of resistance to oxidation, microstructural stability at elevated temperatures and sustained,

predictable mechanical properties at elevated temperature. Other properties such as post exposure mechanical properties, compatibility with hydrogen at elevated temperatures etc. also have to be considered in some cases [31]. The resistance to oxidation and microstructural stability at elevated temperatures are two phenomena that occur concurrently and are interrelated and synergistically control the alloy's performance. Furthermore, the oxidation resistance concept can be divided into two categories. That of the resistance to surface oxide formation, and that of resistance to the ingress and diffusion of oxygen within the bulk of the alloy.

Generally the upper temperature limit of titanium alloys are defined by the onset of excessive surface oxidation and material wastage [86]. This definition is misleading though since it does not provide tangible information regarding the extent of diffusion of interstitial oxygen near the surface and migrating into the bulk of the material. Removing the oxide layers have in some cases restored the original mechanical properties, verifying the detrimental effects of these oxide layers. While the oxide layer formation in titanium alloys is dominant at low temperatures, the oxygen dissolution in the alloy at elevated temperatures dominates the oxidation kinetics [100]. The migration of oxygen ions (also nitrogen) through the surface oxide leads to the alpha phase stabilization - the well known alpha-case - and hence interstitial hardening and embrittlement and the accompanying mechanical property deterioration can directly be attributed to an oxygen uptake [100,101]. It has been shown that large weight gains do not necessarily imply mechanical property degradation, but that the surface has actively been forming oxides while restricting the influx of oxygen [100]. The hardness values of the alloy in fact serves as a good measure of the extent of oxygen diffusivity in the alloy [102]. Further evidence of the presence of interstitial oxygen in the metastable titanium alloys can be inferred from the distribution of the alpha phase within the alloy [100]. In particular, larger amounts of alpha near the alloy surface that has been exposed to an oxidizing environment, signify the presence of the alpha stabilizer, oxygen. Due to the natural aging characteristics, and hence precipitation of the alpha phase in the beta grains, a distinction has to be made between the precipitated alpha and the stabilized alpha. For an exposed component a simple procedure would be to heat the alloy to just above the beta transus temperature in an inert environment. Since

the alpha stabilizers raise the beta transus temperature, the "uncontaminated" alpha would transform to the original beta structure, leaving the stabilized alpha unchanged [54]. Where comparison is possible, samples can heated in an inert environment or in a vacuum furnace allowing for the natural transformation to occur. Beta titanium alloys are however notorious for oxygen pickup even when "vacuum" treated [52].

The oxidization of titanium and its alloys at elevated temperatures, in particular the formation and characteristics of the surface oxide layer, have been extensively studied. The oxidation behaviour depends mainly on three variables, namely, the temperature, the duration and nature of the atmosphere and the properties of alloying elements and their amount [35]. Exposure of commercially pure titanium alloys reveals that the surface oxide consists of mainly TiO_2 with lesser amounts of TiO [4]. Although the oxide has poor mechanical properties, a continuous layer is formed on the metal surface which acts somewhat as a diffusion barrier against the ingress of oxygen ions into the alloy [101]. The severity of the oxidation alone can be reduced through alloying, by applying coating systems etc., however, the effectiveness of the oxide layer in preventing the diffusion of oxygen into the material can only be enhanced through alloying of the metal. Although surface enhancement to improve oxidation resistance has increased the titanium alloy working capability up to 800°C, the effect of the embrittlement due to diffused oxygen still presents problems in the 550° to 600°C range [86]. Furthermore, the diffusion coefficient of oxygen in the beta alloys at approximately 550°C is substantially larger than that of other titanium alloys at the same temperature [86]. Usually the first sign that oxygen interstitials have formed is the loss of ductility which can however be restored once the contaminated surface layers have been removed [54,100]. Although most studies have concentrated on the effect due to oxygen with exposure to high temperature air environments, the possible reaction of nitrogen with titanium in the presence of oxygen is presently not clear [100]. However, the diffusion of both elements and thus the formation of both interstitials are to be avoided for sustained mechanical properties and microstructural stability at elevated temperatures [100].

The improvement of the oxidation resistance of new titanium alloys over that of pure titanium is partly due to the improvement in the diffusion barrier properties of the surface scale [102]. Alloying elements "commonly" found in these titanium alloys influence the formation and integrity of the surface oxide layer. For example, elements which have been found to significantly increase the oxidation resistance are Nb, Mo, Al, Si, Pd and Ta [86,90]. On the other hand, elements which are generally avoided in titanium alloys operating at elevated temperatures and which inhibit the surface oxide formation and accelerate the oxidation rates, are (amongst others) V, Fe, Sn and Zr [36,86]. This is partly due to the rapid diffusivity of the elements in titanium, thus the poor elevated temperature performance of the Ti-15-3 and Ti-13-11-3 alloys. The alloying elements that promote surface stability have been optimized in a Ti-Mo alloy and this has lead to the development of TIMETAL 21S [86]. Relevant alloying additions will further be discussed.

The addition of aluminium, whose oxidative properties promote the formation of Al_2O_3, offers greater resistance against continuing oxidation and element migration [100]. Low aluminium alloying levels shows a pronounced decrease in weight gain compared to unalloyed titanium and increased quantities offers up to 100% improved oxidation resistance [4]. A minimum quantity of aluminium is needed at the surface to continuously form a self-healing alumina layer though [4]. Coating systems employing this system have successfully been used on titanium alloys and this will be discussed later in more detail. Along with aluminium, other alloying additions have shown to exhibit a synergistic effect by the development of complex oxide layers that are able to resist the extensive formation of oxides and restrict the migration of oxygen into the bulk of the material. In particular, additions of Mo, Nb and Si to titanium alloys have shown to significantly decrease the weight gain and oxygen diffusion by forming complex oxides in addition to Si oxides, Al oxides and Ti oxides [31,101]. Mo has replaced Cr as the main metastable alloying element for elevated temperature use once it was observed that no other alloying additions significantly increased the oxidation resistance of the Ti-Cr systems [31]. Synergistic effects on the oxidation resistance were observed with the addition of other elements to the Ti-Mo alloys, in particular when alloying with Si, Nb and, to some degree, Al [31].

The exact mechanism by which Nb participates in the oxidation resistance process is not well established [4]. Pure Nb oxides are very porous and offer little oxidation resistance, however increased additions of Nb to titanium alloys significantly increase the surface stability and oxidation resistance at elevated temperatures by forming dense and protective oxides with titanium, silicon and aluminium oxides [35,89,101,102]. Nb also accelerates the formation of the protective Al_2O_3 and it slows down the diffusion of various elements in the beta phase alloys [101,103]. Although only trace amounts of Nb have been detected in the TiO_2 and Al_2O_3, it is speculated that the Nb ions in the TiO_2 lattice displace the vacancies available for oxygen and thus are able to reduce the diffusivity of the oxygen ions [102]. The combination of oxides in the form of TiO_2, Al_2O_3 and SiO_2 at the surface enhances the oxidation characteristics by inhibiting further oxidation and decreasing the oxygen flux through the oxide layer [101]. The position of these oxides in the oxide layer "stack" will also determine the integrity of the surface scale. A surface coating of Al_2O_3 with the titanium oxides in a "secondary" subsurface position can be expected to perform better than an oxide layer where the TiO_2, or even combinations of TiO_2 and Al_2O_3, is the primary oxide layer. Although the Al_2O_3 initially forms during exposure, if a relatively high concentration of titanium is present, the titanium diffuses through the Al_2O_3 and nucleates as TiO_2 which leads to inferior oxidation protection. On the other hand, when abundant aluminium is present, such as in an Al_3Ti-base alloy, a continuous formation of Al_2O_3 is obtained, offering an improved oxidation resistance [104]. In general, titanium alloys exhibiting higher oxidation resistance, in terms of the quantity of oxide layer formed, have been observed to possess a surface layer of Al_2O_3 with the titanium oxides in a subsurface configuration [100,102,104]. It has also been shown that TiO_2 and Al_2O_3 do not form stable complex compounds between themselves to enhance the oxide layer oxidation resistance properties [105].

The additions of Si to high temperature titanium alloys appears to be the norm. The advantageous effect of Si can be seen from the Ti-6242 and Ti-6242-Si alloys. By increasing the Si content of Ti-6242 by 0.1%, the alloy temperature range was extended by 30°C. A modified version of the Ti-6242-Si alloy containing further increases in Si content (and slightly lower beta formers) was recently developed, the

result being the Ti-1100 titanium-based alloy. The Ti-1100 alloy is capable of operating close to 600°C [31,38]. Si provides beneficial effects in terms of oxidation resistance, solid solution strengthening and increased creep capability. However, parallel to a higher silicon content and an increase in oxidation resistance, the chance of silicide formation increases with higher levels of Si which leads to a reduction in mechanical properties [90]. The silicide formation is mainly found in titanium alloys containing Zr though [28]. Relatively high concentrations of silicon found at the metal-oxide interface has also lead to speculation that SiO_2 plays a significant role in the spalling of the oxide layer at high temperatures [38,101,102].

The inward diffusion of oxygen and the formation of a non-protective oxide layer on the surface can be controlled by the application of a surface coating. The oxygen can be either trapped by forming an oxide or prevented from being transported into the bulk of the material by means of a barrier coating, or by a combination of the two methods [100]. Studies suggest that by forming Al_3Ti on the surface the oxygen diffusion can be effectively retarded and the oxidation rate significantly be reduced [86,100,104]. The weight gain experienced by these alloys was found to be concentrated in the surface oxide layer, demonstrating the effectiveness of the coating in reducing the interstitial oxygen uptake [100]. The silicophosphate glass (sol-gel) barrier coating has shown to significantly decrease the interstitial element concentration, resulting in higher ultimate tensile strength values after exposure [100]. Other coating systems involves ion plating of the surface with noble metals like gold and platinum [32,45]. Benefits of this process includes improved adherence of the coating to the substrate and high coating ductility leading to improved creep the life [32].

1.5.3 Mechanical Properties at Elevated Temperatures

Bigger forgings are lately being made of metastable titanium alloys to limit the number of post-forging welds and fasteners [106]. The wide range of microstructures that are produced during the forging of such large parts and the ability to predict the high temperature microstructure-property relationships are important, in particular the long

term microstructural behaviour [23,90]. Once the chemistry of the titanium alloys has been selected, the mechanical properties have to be optimized by controlling the size, shape and dispersion of the individual phases since it has been shown that the mechanical properties are microstructurally dependent [20,21,81]. The analysis of the metastable titanium alloys microstructures are often difficult due to the complex, fine microstructures that develop after elevated temperature exposures [90]. Limited information is also available on the high temperature deformation of metastable titanium alloys [23].

Moderate amounts of Mo and Nb enhance the tensile properties at lower temperatures and higher temperatures [35,89]. The tensile behaviour has been shown to be dependent on the strain rate and type of alloying elements, and are dependent on the relative atomic sizes between the titanium and the solute atoms [23]. Generally with metastable titanium alloys the high temperature stress-strain curve shows an initial drop in flow stresses followed by a steady state region [23]. This particular behaviour of the alloys is due to the dynamic recovery and declustering of the solute atoms as well as the multiplication of mobile dislocations, subsequently leading to dynamic recrystallization [23]. The formation of the alpha case and interstitial embrittlement at higher temperatures produced localized sites for crack initiation and reduction in tensile strength [95]. Diffusion of an embrittling species along the grain boundaries are often the cause of weakened boundaries and subsequently lead to intergranular failure [95]. Where a grain boundary alpha is present, the ductility is severely reduced although the toughness has been shown to remain relatively unaffected [21].

Al, along with Si, Sn and Zr, increases the resistance to creep at low and intermediate temperatures [20,27,38,89]. However, increasing the Al content to above 6% may lead to the decomposition of the alpha phase to alpha + Ti_3Al which is associated with embrittlement [28]. The additions of Si increase strength at all temperatures but tend to form silicides which creates localized concentrations of Si and lowers the ductility, in general, as well as the post-creep ductility [20]. While Sn promotes the alloy stability, Zr increases the strength at low to intermediate temperatures, although additions of more than 5-6% may reduce the ductility and the creep strength.

Rosenberg deduced the following empirical formula, given in equation 12, for optimum creep and tensile properties in high temperature alloys [28].

$$Al + \frac{1}{3}Sn + \frac{1}{6}Zr + 10O_2 \leq 9 \qquad \text{...(1.12)}$$

It can be seen that the oxygen content has the most profound influence on the high temperature properties. Although oxygen is used as an solid solution strengthener at low temperatures, the beneficial effects disappear at intermediate temperatures, and the ductility, toughness and long term stability suffer. The creep performance is dependent on the alpha phase morphology and lenticular or lamellar alpha performs better than equiaxed structures [20,38,89,107].

In the titanium aluminides the beta content is generally kept low since this has a detrimental effect on the high temperature mechanical performance [11,20]. However the alpha+beta structure provide a degree of ductility in an otherwise brittle structure [11]. The volume fraction of the beta is kept to a minimum and the beta phase can be hardened by adding other beta refractory stabilizers [27]. Tensile tests on these alpha+beta alloys show that the failures initiate near the alpha/beta interfaces [108]. Under quasi-static crack growth at intermediate temperatures, the ductile beta phase has been shown to bridge the main crack, and the phase has been found to increase fracture toughness by crack deflection and blunting [108]. At elevated temperatures though the beta phase contribution diminishes, and ineffective deflection and bridging ensues. There is also a definite correlation between the environmental effects and the high temperature tensile behaviour. Tests have shown that in an oxidizing environment sharp crack originate at the surface of the material, lowering the tensile strength and the ductility, while test conducted in a vacuum showed increased strength and produced higher moduli as well as higher elongation and percentage area reduction. This phenomena was attributed to the surface contamination experienced during the oxidizing environment exposure, pointing to the correlation between the mechanical properties and the environmental effects [95].

1.6. Fatigue crack growth in titanium alloys

1.6.1 Fatigue crack closure

In order to develop reliable fatigue design methology, the crack growth rate of the material has to be quantified in terms of the intrinsic resistance of the material to the fatigue crack growth for different conditions of loading, environment and specimen and crack geometry [68]. As pointed out in section 1.2, the stress intensity factor range ΔK summarizes the events occurring at the crack tip, if the plastic deformation ahead of the crack tip is small. To further recap, ΔK is defined as :

$$\Delta K = K_{max} - K_{min} \qquad \ldots(1.13)$$

where K_{max} is the maximum stress intensity factor and K_{min} the minimum stress intensity factor. The driving force for the fatigue crack growth has also been defined as the portion of the fatigue cycle where the crack remains fully open [68].

Experiments by Elber in the 1970's showed that the fatigue crack can close even at far-field tensile loads [68]. Elber argued that the plastic deformation at the crack tip resulted in a residual tensile field in the wake of the crack tip. As the fatigue crack progressed the extent of the plastic deformation increases, developing an envelope of plastic zones and resulting in the premature contact between the crack faces. This phenomena has been termed plasticity-induced closure. The closure mechanism leads to a reduction in the driving force required for the fatigue crack advance [68]. This phenomena has been experimentally verified by means of monitoring the load-displacement curve of a specimen during a fatigue cycle. To illustrate this, consider a typical load-displacement curve of a material containing a fatigue crack as shown in figure 1.6. The constant slope region A-B typically exhibits the same stiffness as a specimen containing a saw cut of the same length as the fatigue crack, implying that the crack is fully open until the load is reduced to P_{op}. As the load is reduced from point B to point C, the effect of the premature closure becomes apparent, and from point C to D the slope of the load-displacement curve is similar to that of a identical notched specimen without a fatigue crack (the straight line OE), indicating that the crack is fully closed.

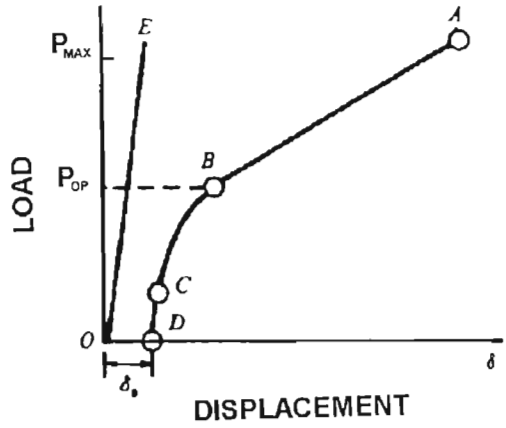

Figure 1.6 : Typical load-displacement curve of a LEFM specimen containing a fatigue crack

From the hysteresis curve of the stress intensity factor vs displacement, as shown in figure 1.7, two important stress intensity factors can be identified, namely the opening stress intensity and the closing stress intensity, K_{op} and K_{cl} respectively. Important points should be noted regarding these two values, namely, that there is no unique definition for the closure stress intensity since the crack closes gradually, and, that the opening and closure points are not necessarily similar due to the compressive interference, such as frictional and deformational contact, induced during the crack closure [68]. For discussion purposes, no distinction will be made between the opening and closing data. "Closure" will be regarded as either mechanism, unless otherwise specified. A method to effectively accentuate the opening and closure stress intensities is provided in chapter 2, section 2.3.2.

Since the driving force for the fatigue crack propagation has been defined as the portion of the fatigue cycle where the curve remains fully open, a "new" definition of the driving force in light of Elber's experiments can be defined.

The "effective stress intensity factor" takes into account the effect of the partially open crack, thus,

$$\Delta K_{eff} = K_{max} - K_{op} \qquad \text{...(1.14)}$$

where K_{op} is defined in figure 1.7.

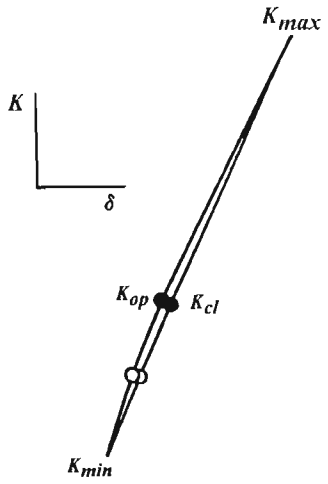

Figure 1.7 : Hysteresis curve for a full fatigue cycle in terms of stress intensity factor and displacement

This implies that :

$$\Delta K_{eff} = U(\Delta K) \qquad \text{...(1.15)}$$

where U $\leq$ 1. The value of U is strongly influenced by factors such as specimen geometry, the stress intensity factor range and the environment [68].

Further research into the crack closure phenomena lead to the identification of several fatigue crack closure mechanisms. Apart from Elber's plasticity-induced crack closure, additional sources of closure originate from 1. corrosion layers formed within the fatigue crack, 2. microscopic roughness of the fracture surfaces, 3. viscous fluid penetration inside the crack, and, 4. stress- or strain-induced phase transformations at the crack tip [68,69]. These retardation processes can be summarized as :

1. oxide-induced crack closure
2. roughness-induced crack closure
3. viscous-induced crack closure, and
4. transformation-induced crack closure.

Other mechanism have also been identified in advanced metallic, non-metallic and composite materials. These include crack deflection, crack-bridging or trapping and

crack-shielding due to microcracking, phase transformations and dislocations [68,109]. Figure 1.8 schematically illustrates these mechanisms.

More than one of the closure mechanisms may be present and microstructural and/or environmental behaviour may combine with, or dominate over, the plasticity-induced closure mechanism to effectively determine ΔK_{eff}. In general, the more dominant closure mechanisms have been identified as plasticity-induced closure, roughness-induced crack closure and the oxide-induced closure [110,111].

The oxide-induced crack closure has evolved from irregularities found due to the environment on the near-threshold crack growth rates in aluminium and steel alloys [68,109,112]. References have been made to the possibility of the increased effect of surface oxidation during fatigue on the crack closure values at ambient and at elevated temperature, at near threshold and higher fatigue crack growth rates [68]. By repeated surface fretting in the wake of the propagating fatigue crack, the existing oxide layers are broken down and fresh, thicker oxide layers are reformed, promoting the closure effect. At higher R ratios the influence of surface oxidation decreases markedly since the crack face contact is minimized and fatigue crack growth rates the crack growth is too rapid to allow substantial surface oxide build up [68].

The roughness-induced crack closure has provided explanations for many irregularities on the fatigue crack growth due to microstructural variations [68]. For example, it has generally been establish that although coarser grained materials exhibit greater resistance to fatigue crack initiation, fine grained materials show greater resistance to fatigue crack propagation [68]. In both instances plastic deformation and slip, either single shear as found in stage I growth or irreversible slip produced during unloading from peak stresses, induce a fracture surface mismatch and premature contact of fracture surface asperities [69]. Although the roughness-induced crack closure is dependent on the extent of the surface roughness, the absolute magnitude would depend on the slip reversibility at the crack tip due to reversible crack tip sliding [111]. The resultant mixed-mode type sliding of the crack faces and premature contact of the asperities provides an enhanced mechanism of roughness-induced crack closure.

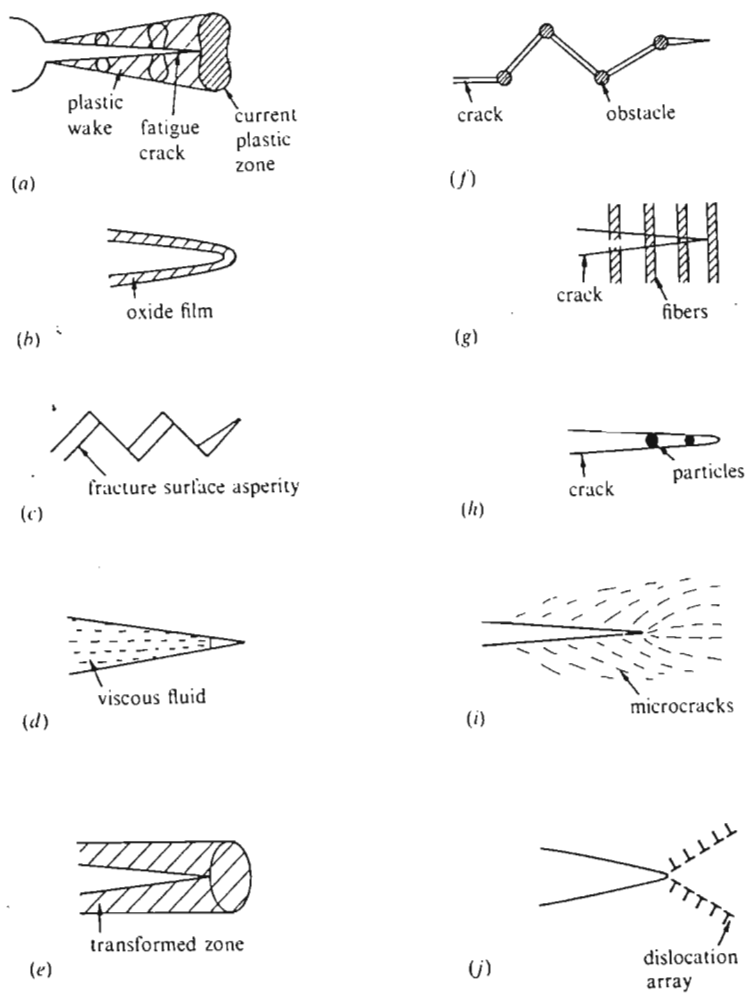

Figure 1.8 : Schematic illustration of crack closure mechanisms that retard fatigue crack growth rate **a.** plasticity-induced closure, **b.** oxide-induced crack closure, **c.** roughness-induced crack closure, **d.** fluid-induced crack closure, **e.** transformation-induced crack closure, **f.** crack deflection, **g.** crack-bridging by fibres, **h.** crack-bridging by particles, **i.** crack-shielding by microcracks, **j.** crack-shielding by dislocations [68].

Furthermore, if fatigue crack deflection is also present, the closure effect can be magnified [68,109]. The roughness-induced crack closure is generally promoted by low ΔK and R ratios.

To summarize the features of the closure mechanisms, it can be said that the closure levels are strongly influenced by the microstructure, the environment and the mechanical loading parameters. The level of closure is specific to the experimental conditions and its magnitude is influenced by synergistic effects of the microstructure and the environment [68].

The closure is mainly produced by events occurring in the wake of the advancing crack, as well as at the crack tip. Furthermore, the crack closure is more dominant at low ΔK levels and low R ratios which in turn encourages smaller crack opening displacements and thus enhanced probability of fatigue fracture surface interference. Thereafter the crack closure may become independent of the crack length after an initial saturation level. Measurement of the crack closure by regular compliance methods do not render the exact closure mechanism(s), but rather verifies and quantifies the existence of such events. In addition, near tip closure mechanisms may also be identified from the compliance curves [113].

1.6.2 Effect of closure on fatigue crack growth rate

The closure mechanism is primarily responsible for the crack-size dependence of da/dN-ΔK data in titanium alloys under elastic fatigue [69]. Plotting values of the effective stress intensity factor, ΔK_{eff}, (which can also been defined as $\Delta K_{eff} = K_{max} - K_{cl}$, assuming that $K_{cl} = K_{op}$ [114,115]) demonstrates that the effects of the material variables and crack size are reduced and similar curves under various test conditions can be obtained [69,76]. Consolidating the values in such a manner excludes the surface (e.g. roughness, plasticity) and surface-environmental (e.g. oxide) induced effects, demonstrating the effects of the slip character and other intrinsic mechanisms on the fatigue crack growth resistance. Furthermore, when accounting for the crack closure the fatigue crack growth rate has been shown to be relatively insensitive to e.g. heat treatments [109,115].

Studies have shown that in certain alloys the closure loads in titanium alloys might be as high as 90% of K_{max} [69]. For long cracks the closure loads are mostly independent of K_{max} and the closure effects can be reduced or magnified by altering R [69]. Tests using stress ratios of 0.5 showed that actual and closure-corrected data were similar once the minimum load approached the closure load while stress ratios of 0.7 produced no notable differences between the actual and corrected fatigue crack propagation [76]. In the event of closure loads being significantly above the minimum loads, the fatigue crack growth rate is notably affected by the closure. Further studies of the dependence of K_{cl} on the crack length might explain certain anomalies in the fatigue crack growth rate [69,111]. Although the far-field closure has been the focus of numerous studies, near-tip closure, or closure immediately behind the crack front, have been found to control load-interaction effects. The near-tip closure can be estimated from the regular compliance curves, as demonstrated by Ward-Close *et al* [113]. The contact near the crack tip in these studies were found to have a much greater influence on the fatigue crack growth driving force than the remote contact [113].

Stage 3 fatigue crack growth rates were not affected by the corrected and non-corrected data and reversible loading has been hypothesized to neutralize the beneficial closure effects [76,116].

In general, fatigue crack propagation of titanium alloys tested in air at ambient temperature was accelerated compared to that found in a vacuum over the entire range of ΔK. Closure loads in a vacuum have been higher possibly due to (although partly unexplained) rewelding of the fracture surfaces, resulting in slower growth rates. Fracture surface oxide formation prevents the rewelding from occurring [116].

1.6.3 Additional factors influencing fatigue crack growth rate

Recently greater attention has diverted to the presence and propagation of small fatigue cracks [68,69,109,114]. The small cracks (also termed short cracks), are essentially described as a crack of size comparable to microstructural dimensions, physically small cracks (shorter than a millimetre) and cracks for which the near tip plasticity is

comparable to the actual crack length [68]. At low stress levels the crack tip plastic zone becomes negligible which implies that the linear elastic methology can be used to describe the crack behaviour [114]. The crack length required to comply to the LEFM description are typically designated as long cracks and the behaviour of these long cracks will mainly be considered. Furthermore, effects on the threshold values, $\Delta K_{th,}$ will only be briefly referred to.

In numerous studies have the identification of single mechanism to describe and/or predict the fatigue crack growth rate under various environmental, microstructural, compositional and loading conditions been attempted, but inconsistencies in the titanium alloys' behaviour have yet to identify such a mechanism [117]. Fatigue crack growth rates have been shown to depend significantly on various factors such as the degree of alloying, the phase composition, the microstructure on the dislocation and metallographic levels, the grain size and the quantity and distribution of interstitial impurities [110,118,119]. And the other hand, considering the loading, it is the stress ratio, the frequency, the maximum cycle stress and the shape of the wave form that has been found to mainly influence the crack growth rates [118].

The fatigue crack growth rate in metastable titanium alloys have been of interest since the alloys have been used in fatigue critical aircraft components [120]. Controlling the crack growth rate by microstructural manipulation has remained elusive though and the crack growth characteristics are thus more predictable in the metastable titanium alloys in contrast to the alpha and alpha+beta alloys. However structures containing abundant finely precipitated alpha in the matrix have shown marginal improvements in fatigue crack growth rate [28,121,122]. The microstructure that delivers the highest resistance to fatigue crack growth in alpha and alpha+beta alloys is well documented. In near alpha or alpha+beta alloys, the lenticular or Widmanstätten structures containing elongated alpha structure, leads to repeated rerouting the propagating crack along alpha/beta grain interfaces, resulting in greater crack path tortuosity and higher fatigue crack growth resistance. These microstructures however exhibit poor fatigue crack initiation resistance but compromising microstructures have however been achieved [20,28,38,48]. The lack of any of the significant aligned alpha/beta interfaces have

been touted as the reason for the lack of meaningful changes in the fatigue crack growth rate of beta titanium alloys [120].

In the alpha and alpha+beta titanium alloys the roughness induced closure is particularly predominant due to intrinsically coarse microstructure such as Widmanstätten colonies and inherent slip localization in fatigue as a result of planar deformation character [111]. It has been suggested that due to this intrinsic behaviour that only modifications to the chemistry and microstructure will increase the resistance to crack propagation in the various alloys. Thus far both alpha and beta stabilizing elements have been shown to affect the fatigue crack growth rate [20,81]. Appropriate thermo-mechanical treatment can also significantly improve fatigue crack nucleation [48]. Although in most structural steels a strong microstructural influence is observed in the stage I region and a weaker influence in the Paris region, the effect of the microstructure is strongly felt throughout the entire range of crack growth in the alpha and alpha+beta titanium alloys [120]. Contrary evidence is also available though [111,117]. The most noticeable features of fatigue crack propagation in the titanium alloys containing both alpha and beta phases is that there is a definite change in fatigue propagation mechanism observed at the alpha/beta interfaces [116]. Fracture toughness tests have demonstrated that the propagating crack will follow the path of least energy [27]. Fatigue crack growth rate tests in metastable beta alloys aged to produce a continuous grain boundary alpha show similar trends. The fatigue crack propagated along the grain boundaries in a classical intergranular failure manner [120]. Although this manner of propagation is distinctly different from the transgranular type of propagation, the fatigue crack growth rates were found to be unaffected. This has also been reported by other investigators that only observed minor effects of the aging treatments on the fatigue crack growth rate [121]. Duerig *et al* concluded the following regarding fatigue crack growth rate in metastable beta titanium alloy, Ti-10-2-3 :

1. no significant effect on the fatigue crack growth rate was found due to the various aged microstructures in high strength alloys, in contrast to the alpha and alpha+beta alloys.
2. no apparent variation in fracture surface roughness were found in the various aged structures, and,

3. high fatigue crack growth rate were affected by the microstructural (alpha and beta) variations [120].

Points 1 and 2 further substantiated the premise that the roughness-induced closure mechanism is dominant in the titanium alloys [120]. However, point 2 had resulted due to the alloy containing primary alpha structures, providing a virtually continuous path through the matrix, leading to a smoother fracture surface.

Mostly alpha and alpha+beta alloys have been used to try and correlate the effects of alloying with oxygen on the fatigue crack growth rate, however the inconsistencies in the growth rates could be attributed to the overriding effect of the microstructure that could have masked the oxygen effects [117]. The fatigue fracture related properties in the titanium alloys are dependent on the deformation characteristics, in particular slip character and slip length. Oxygen intrinsically influences the slip characteristics, inhibiting dislocation relaxation thereby necessarily influencing the crack growth rate [117].

Fracture surfaces indicate that fatigue crack propagation is dependent on the microstructure (e.g. alpha and beta structure), crystallographic orientation and the degree of alloying [111,117,120,etc.]. Numerous evidence also indicates to different propagation mechanisms that operate in the beta and the alpha phase regions with the beta phase exhibiting more ductile behaviour while cleavage type fracture features are observed in the alpha phase regions [36,114,116].

1.7 Effects of environment and high temperature on the fatigue crack growth rate in titanium alloys

Studies concerning fatigue crack growth rates in metastable beta titanium alloys have been primarily concerned with the microstructural influences on the room temperature fatigue growth characteristics and limited work has been conducted in order to investigate crack propagation at elevated temperatures. With the advent of various new beta alloys that are proposed for structural components operating at higher

temperatures, a better understanding of the complex synergistic influences of cyclic loads, creep and environmental effect on the crack growth rate have to be gained. Although further studies are required in this field, the most prominent closure mechanisms prevalent at elevated temperature have been identified. These mechanisms are (the now well known) plasticity-induced closure, roughness induced closure and oxide-induced crack closure [76,115,116]. These mechanisms ultimately control the high temperature crack growth performance. Furthermore, the processed microstructure plays an important role in the crack path orientation and slip characteristics [111].

At elevated temperature, the oxygen effects on the crack growth behaviour of the alloy becomes more pronounced. The oxygen effects can be divided into two categories - that which is detrimental to the crack progression, and that which retards the crack growth rate, i.e. the detrimental oxygen embrittlement which produces a less crack resistant material at the crack tip, and, for example the surface oxide build up that retards the growth by a closure mechanism. These two processes are dependent on the oxidation characteristics of the material. The environment, in particular the influx and saturation of the crack tip with oxygen, influences the crack propagation mechanism by modifying the slip character, ultimately modifying the crack propagation rate [111,116]. While the concept of closure is able to account for the effects of temperature and/or stress ratio, the higher fatigue crack growth rate that are generally experienced at higher temperature is mostly due to the oxygen-assisted crack propagation [76,116]. Increasing the stress ratio reduces the influence of the closure mechanisms on the crack propagation and increases the driving force for propagation. In this manner the plastic zone ahead of the crack tip is penetrated by oxygen and thus the microstructural resistance to fatigue crack growth can be isolated [76,111,115,117,123].

Oxide thickening on the fracture surface leads to a wedging effect and thus a reduction in K_{eff} [123]. Petit *et al* have concluded in their study on Ti 6-4 that the detrimental influence of oxygen could explain the rapid crack growth at 300°C, and that when operating at low R, the oxide-induced closure by oxide thickening can compensate for the detrimental effect of the oxygen embrittlement [123]. The increasing oxide thickness can be attributed to either the repeated fracture and reformation of the oxide

due to closure crushing, or "natural" spalling of the oxide or the poor resistance of the titanium alloys to oxygen penetration, all of which enhances the oxide-induced closure [124]. Experiments conducted on Ti_3Al-base alloys showed that similar results were obtained in high and low frequency tests at 700°C [125]. This also could indicate the limited effect that the environment has on the material, prior to mechanical advance of the crack since oxides may possibly limit the oxygen diffusion. Further reduction in loading rate did not produce intensified environmental effects. In a more conventional titanium alloy the effects of oxidation is much more rapid and thus crack growth rate is only weakly dependent on the cycle frequency [102]. In the case of aluminides, the crack tip that has been saturated with oxygen has been shown to be more susceptible to creep though [48,125]. A threshold frequency exists below which creep and/or mechanical events influence the crack growth, and above which the effects of creep, and possibly oxidation effects play a major role [25]. Although the crack tip oxidation is a major damage mechanism, the effect of creep at low cyclic frequencies should be considered if anomalies in crack growth data are observed [25].

Closure cannot always account for the temperature effects on fatigue crack growth rate [125]. Other microstructural effects, the extent of which is dependent on the environment, may account for the behaviour that cannot be explained by the additional oxide-induced crack closure effects. These features include secondary cracking and crack front branching [76].

Lower crack growth rates have also been observed in Ti 6-4 at increased temperatures. In this case the retardation has been attributed to a dynamic strain aging process [116]. A typical drop off the fatigue crack growth rate at elevated temperature is also likely due to increased effects of plasticity-induced and oxide-induced closure [126]. Salivar *et al* though found that the same numerical value of closure exists at room temperature and at 260°C [76]. This similar value was observed although increased oxidation and surface roughness was present. In spite of this, the fatigue crack propagation increased at the higher temperature and the effects of oxidation was believed to account for this behaviour. Various near-threshold fatigue crack propagation studies indicate that the fatigue crack growth rate increases with increasing temperature [123].

While the alpha phase still exhibits cleavage fracture (and the beta phase a ductile fracture) at higher temperatures, other slip systems are activated and the basal cleavage dominance is reduced [111,127]. Increased secondary cracking has noticed at the alpha/beta interface and has been attributed to higher available energy and probably also due to the aggressive environmental effects [76]. The cracking has also shown to correlated well with the type of microstructure [116]. Microcreep at the crack tip leading to crack tip blunting reduces the stresses at the crack tip and thus reduces the fatigue crack propagation rates [116]. On the other had the effect is opposed by the creep damage ahead of the crack tip as well as the environmental interaction [116]. If the activation energy for the creep is higher than that of the environmental effect, the creep mechanism becomes dominant and tends to control the propagation rates [116].

Oxygen has also been found to promote the internal stress concentrations and evidence of this is the distinct difference in propagation mechanism and slip character, resulting in a particular fracture surface appearance [117].

Chapter 2. Experimental Systems and Procedure

2.1 Test Specimen

The C(T) test specimen design was based on the ASTM 647 - 88a Standard Test Method for Measurement of Fatigue Crack Growth Rate code. The ASTM standard has been outlined in chapter 1, section 1.2. A schematic of the specimen geometry and dimensions are shown in figure 2.1.

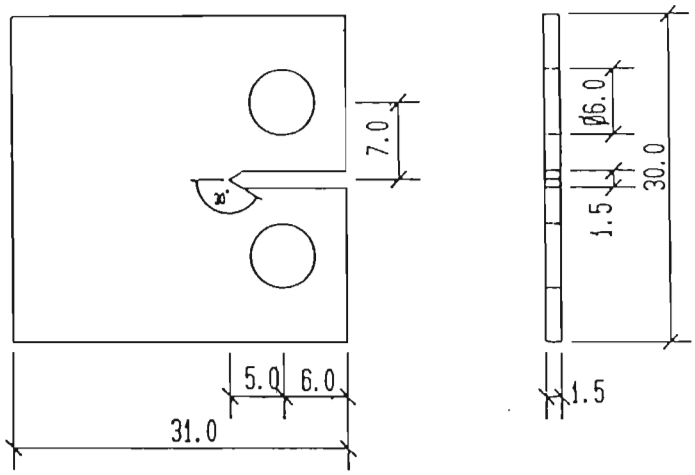

Figure 2.1 : C(T) test specimen dimensions

The specimens were of the T-L type, as per ASTM notation for specimens extracted from rolled plate or forgings. This configuration features the notch machined parallel to the rolling direction and is recommended for general material characterization [64].

The 1.55 mm thickness of the as-received samples limited the overall dimensions of the test specimen. Although the ASTM standard is not rigid with respect to the minimum material thickness requirements for the C(T) sample, the final design could be accommodated within the recommended guidelines.

The machined notch conformed to the minimum length requirements and the notch tip geometry featured the 60° convergence option [64]. Although the use of a machined

sharp start on the notch tip is recommended for fatigue precracking purposes to ensure that the precracking starts at the correct position and not at a corner, careful observation of the developing crack during precracking operations indicated that the thickness of the as-received material did not necessitate the use of such a starter tip. The sharp starter notches are most often used in relatively thick samples where corner cracking is most probable and could result in irreproducible, curved crack fronts which may invalidate the test data [64].

2.2 The Thermo-mechano-chemical test system

2.2.1 High-temperature fatigue loading apparatus

The high-temperature fatigue test system consisted mainly of an Universal MTS closed-loop electro-hydraulic system and a split tube furnace. The ability to produce various fatigue cycling waveforms and effectively control the hydraulic actuator response provided the MTS system with a wide variety of fatigue test capabilities. The control system featured a digital data display unit, a frequency controller and an electro-hydraulic control unit. The split tube furnace was attached the MTS load frame upright. An overall view of the test apparatus is shown in figure 2.2.

The digital display unit displayed values such as load and hydraulic piston displacement. Provision was also made on the unit for an external input. Resolution of the displayed values was 0.001 Volt, which is equivalent to a load value of 1 N. The frequency controller was capable of providing a variety of waveforms with a wide range of frequency settings.

The control unit was able to control the piston movement by either displacement feedback control or by load feedback control. For load control the affixed loadcell provided the necessary feedback signal, while the displacement feedback signal was obtained from a displacement transducer connected to the actuator piston. The load control was particularly useful during heating of the test specimen to the required test temperature to avoid the possibility of compression due to the increasing temperature.

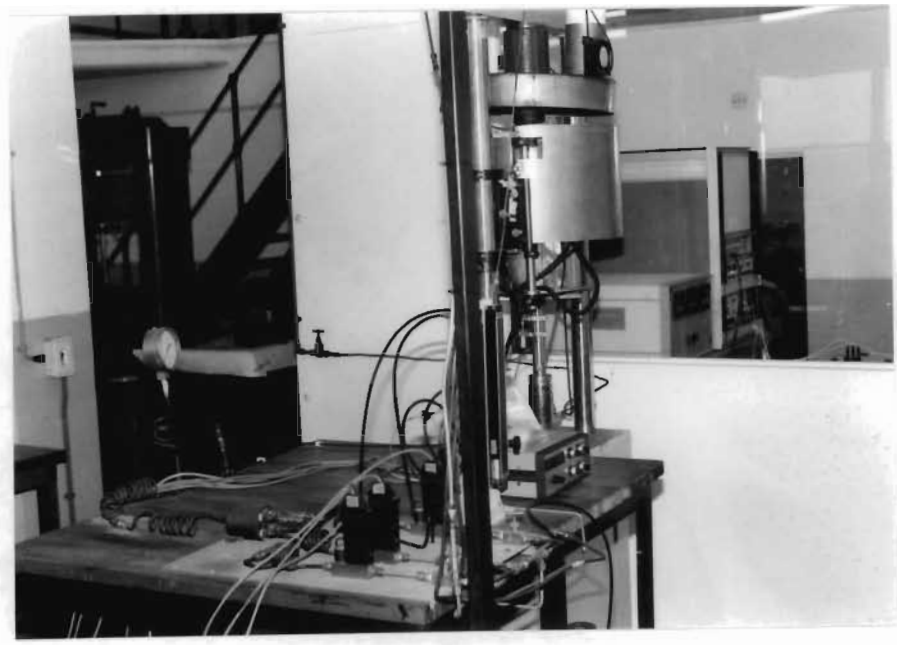

Figure 2.2 : Overall view of high-temperature, fatigue loading apparatus

The cycle counter was linked to a cycle interrupt function. The test program could be interrupted once a predetermined number of cycles were reached and the operator would then resume control. The cycle-interrupt feature was used when high frequency tests were conducted for a specific number of cycles.

A tension-compression 10 kN loadcell was used to conduct the tests. The loadcell specifications indicated a combined error (linearity and hysteresis) of 0.03% and repeatability error of 0.01%. Calibration by National Calibration Service of the South African Bureau of Standards showed an maximum error of 0.9%. Attached to the loadcell and the hydraulic piston were a top and a bottom grip. To accommodate the C(T) specimens, dedicated clevis grips were attached to the two grips. The design of the clevis grips, as shown in figure 2.3, were based on the ASTM 647 standard for the design of the clevis assembly for gripping the C(T) test specimen [64].

The clevis grips ensured that only in-plane rotation of the specimen was possible. The pins used to hold the C(T) specimens were made from MAR-M 002 nickel-based superalloy. The pins were finished to an extremely smooth surface finish and prior to each test a high-temperature lubricant was applied to the pins to further reduce friction. The high strength of the superalloy at elevated temperatures was particularly attractive and the resistance to oxidation at all tests temperatures ensured that the surface smoothness was maintained during testing.

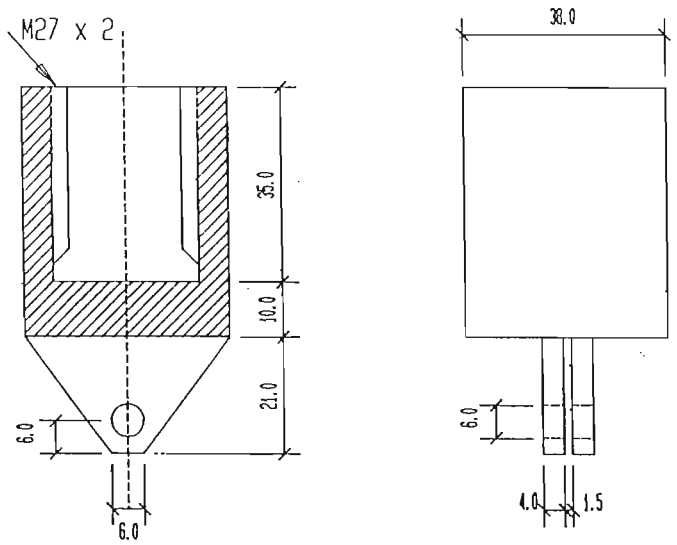

Figure 2.3 : Clevis design for C(T) specimens

A cooling water jacket positioned in the top grip prevented the unnecessary transfer of heat to the loadcell and hence eliminated the possibility of temperature drift.

The split tube furnace was used to heat the specimen and maintain the desired test temperature. The resistive type heating elements in the furnace were arranged into three zones, namely, the top zone, the centre zone and the bottom zone. This element arrangement ensured even heating of the specimen and eliminated the possibility of thermal gradients. The three elements were controlled via thermocouple feedback by 815S controllers which maintained the element temperatures to ± 1°C. The top and bottom openings on the furnace were covered with refractory material during the tests to ensure maximum temperature stability within the furnace with the minimum of heat loss.

A stainless steel outer housing connected to an extraction fan unit enclosed the split tube furnace. This enclosure ensured a constant flow of cooling air around the furnace, extracted "spent" gasses from the furnace and further isolated the loadcell from possible temperature effects.

2.2.2 Compliance monitoring system

A computerized compliance-based crack growth monitoring system was developed specifically for the investigation. The compliance was calculated using the load-line displacements obtained from a transducer mounted on the actuator/bottom grip. A schematic representation of the computer-based compliance monitoring system used is shown in figure 2.4. The system incorporated a multiplexer, an analog-to-digital converter (ADC) circuit and a personal computer.

The multiplexer is basically used as an analogue switching device, allowing for the connection of several analogue signals to a device that has only one input. For this application, the computer controlled multiplexer alternately switched between the load and the displacement transducers, allowing a single analogue to digital converter (ADC) circuit to alternately read both transducer values. The multiplexer was operated at a frequency of approximately 280 Hz and roughly 140 load and displacement transducer readings per second were obtained.

The load values were read directly from the load cell and the displacements were read from a linear variable displacement transducer (LVDT) that was attached to the bottom grip with the LVDT sensor rod fixture mounted via the MTS upright, as shown in figure 2.5. The LVDT sensitivity was approximately 8 V/mm over a range of ± 10 V. The ADC circuit used a 12 bit converter, resulting in a resolution of ± 5 mV for ± 10 V range device. This translated into an actuator piston displacement resolution of ± 0.61 μm and a load resolution of ± 5 N. Further details on the ADC circuitry and operation can be found elsewhere [128].

Considering the overall size of the specimens and that maximum loads of approximately 700 N were anticipated, the compliance of the grips at maximum test temperature was calculated and found to be significantly less than the LVDT resolution, and hence was considered negligible.

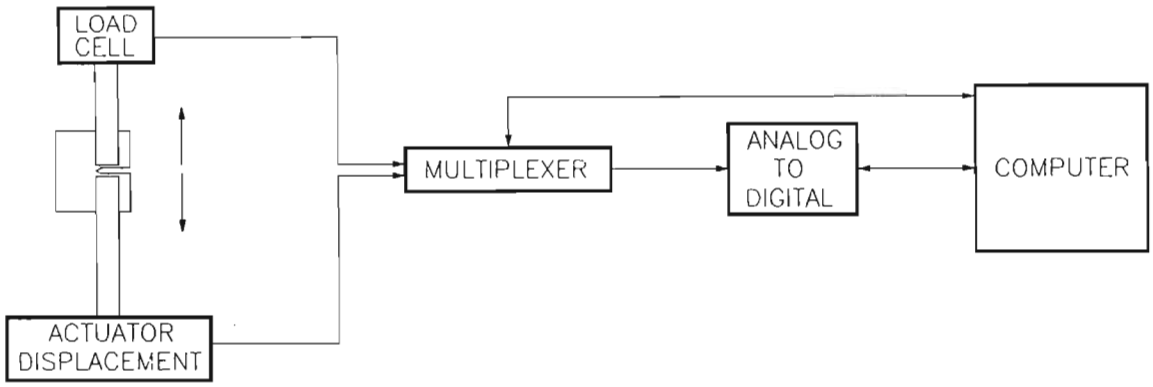

Figure 2.4 : Schematic representation of compliance monitoring experimental system

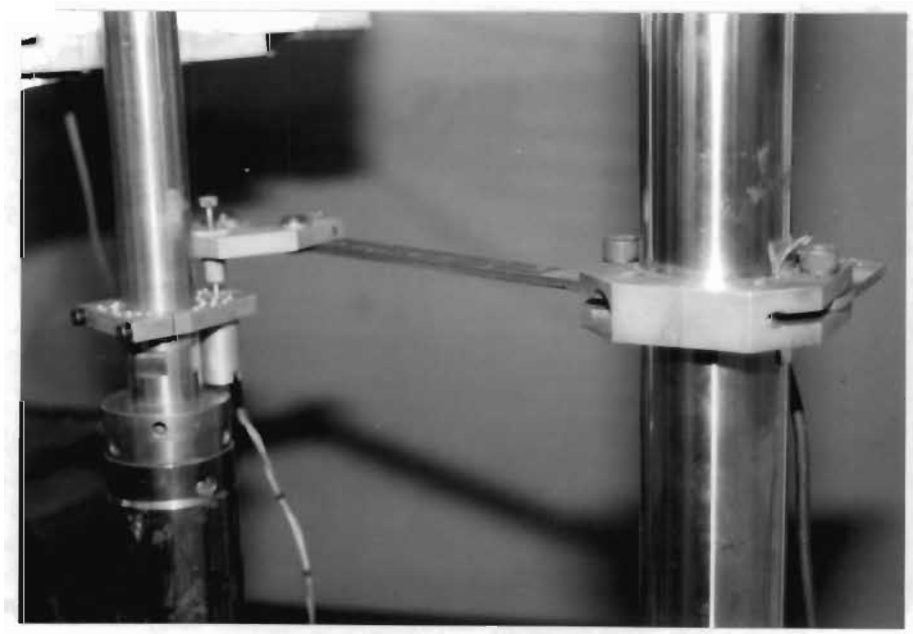

Figure 2.5 : Position of the LVDT on the actuator piston to monitor load-line displacement

The computer-based system systematically extracted relevant information regarding the specimen geometry and tests parameters from the user. Upon start-up, after selecting a relevant file name to store the data, values such as precrack length, specimen thickness, specimen width, the anticipated Young's Modulus and test frequency were requested. Several test cycles were then initiated and the compliance and the resultant effective Young's Modulus determined. This value was required to be within 10% of the anticipated value. The effective Young's Modulus at the specific test temperature was thus obtained and this value was used to determine position of the propagating fatigue crack.

During the test, the computer continuously displayed values of cycle number, reading cycle increment, last read cycle, compliance calculated crack length, normalized crack length, compliance at last reading and crack growth rate. The latter was simply determined by the difference between the present crack length and the previous crack length and only served as an indication of the variance of the crack growth. The program featured the ability to change the cycle number and the incremental number of cycles at which readings were to be taken.

Compliance of the specimen was determined by the inverse of the slope of the linear regression (using the least squares method) performed through 40% to 80% of the increasing load portion of the load-displacement curves. Values of cycle number, crack length, compliance and maximum and minimum load were stored in a relevant file and this data could be imported into a data base package after the tests for further data manipulation.

The load line displacement method has been cited to represent the closure values more accurately [112]. The fatigue crack closure data was automatically calculated during the tests using a method similar to the offset method described by Suresh [68]. The values of load, displacement and offset displacement were stored in a separate file and following the test, the data could be imported into a data base package where the closure data could be plotted and scrutinized. The offset method will be elaborated on in section 2.3.2.1.

2.2.3 Gas delivery system

In order to deliver and maintain the desired gaseous environment around the test specimen, a gas mixing and delivery system was constructed. The system was able to effectively isolate the test specimen from external environmental contamination during fatigue testing. A schematic of the gas mixing and delivery system is shown in figure 2.6.

Gas cylinders situated remotely from the mixing system supplied the system with the various gases. The flow of these gases were controlled by means of either two rotameters or a bank of electronic controllers. The rotameters were the Brookes SHO-RATE 1357 models, types R-2-25-A and R-6-25-A, capable of a maximum flow of approximately 3 l/min and 26 l/min of gas respectively. In addition to the rotameters, a bank of Matheson electronically controlled flow meters were also available. These flow meters were able to supply a maximum flow rate of up to 1 l/min or 3 l/min of gas, depending on the meter selected. The meters were controlled by means of an electronic controller which was capable of managing up to four different electronic meters simultaneously.

After passing through a unidirectional valve, a conical mixing chamber and coiled tubes situated downstream from the flowmeters ensured thorough mixing of the gases. The pressure gauge which indicated that the gas was being delivered and maintained at a positive pressure. Provision was made in the refractory material covering the top of the furnace to introduce the gas line into the furnace, however, before being delivered to the environmental chamber, the gas line was coiled around the top grip several times to ensure that the delivered gas was heated to the correct test temperature. Figure 2.7 shows the overall gas mixing and delivery system setup.

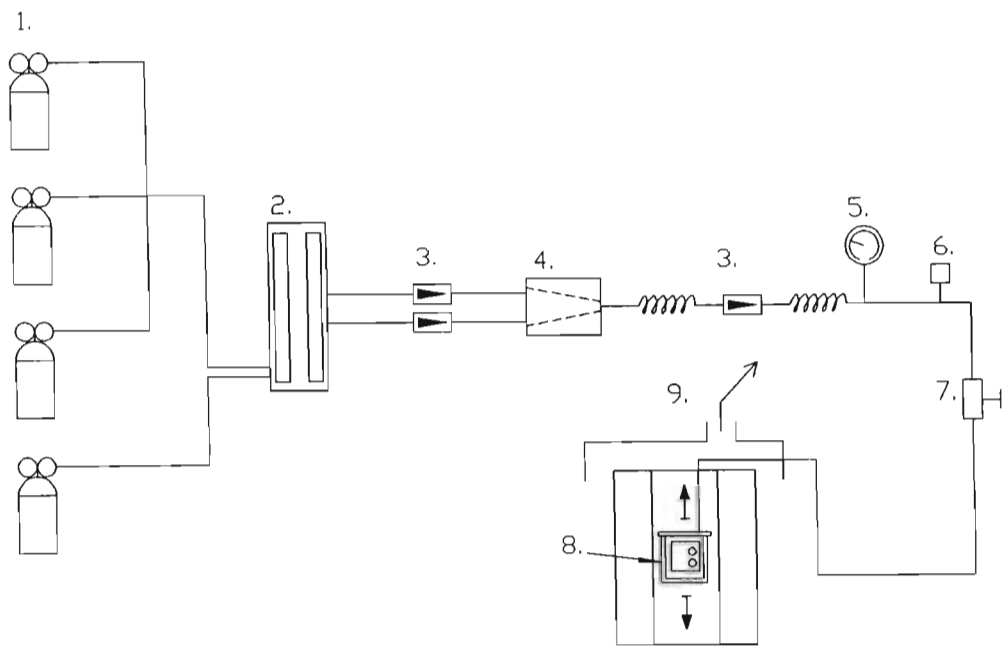

1. gas cylinders
2. flow meters
3. unidirectional valve
4. conical mixing chamber
5. pressure gauge
6. safety valve
7. shut-off valve
8. environmental chamber
9. exhaust system

Figure 2.6 : Schematic view and key of the gas mixing and delivery system

Figure 2.7 : Overall view of the gas mixing and delivery system

An environmental chamber, which was affixed to the top grip inside the furnace, enclosed the C(T) specimen in the grips, was used to concentrate the desired gaseous test environment around the specimen during high temperature fatigue testing. The environment was introduced into the chamber at an above atmospheric pressure to prevent possible extraneous environmental contamination. The position of the gas entry line on the chamber was to direct the gas flow at, and concentrate the gas around, the test specimen. A hole, slightly larger in diameter than the bottom grip, was made in the base of the environmental chamber to allow for unrestricted movement of the bottom grip while the small clearance between the chamber and the grip minimized the gas loss. Provision was also made to insert a thermocouple into the environmental chamber to monitor the internal chamber temperature and serve as a guide for the furnace element temperature setting. Figure 2.8 shows the environmental chamber in position in the grips, inside the furnace, with the gas entry line and the thermocouple attached.

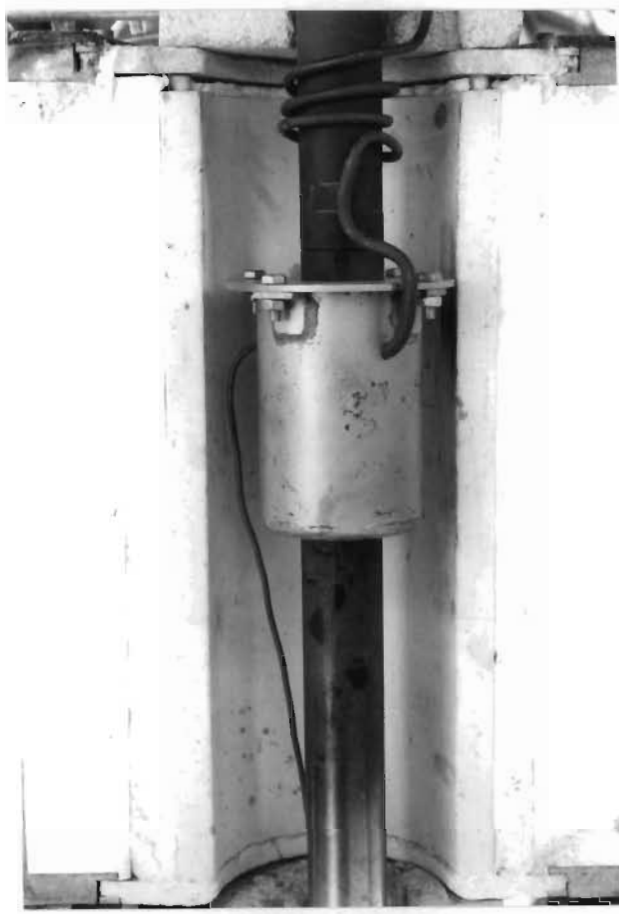

Figure 2.8 : Environmental chamber with thermocouple and gas line positioned in the furnace

2.2.4 Corrosion Chamber

In order to isolate the effects of the environment at elevated temperatures on unstressed TIMETAL 21S samples, a corrosion chamber was employed.

The corrosion chamber comprised of two sections, namely, a base which contained a specimen platform, and a covering top lid that could be affixed to the base. A TIMETAL 21S test piece of approximately 15 x 15 mm^2 was placed on the platform, the lid of the chamber was bolted onto the base and the whole assembly placed on the bottom grip inside the furnace. The desired test environment was then introduced into the chamber via the gas line entering through the top of the furnace, positioned in the side of the corrosion chamber. On the opposite side of the lid, provision was made for the positioning of a thermocouple to monitor the corrosion chamber internal

temperature and to serve as a guide for the furnace element settings. A positive environmental pressure was maintained inside the chamber during testing and a small opening in the top of the chamber lid allowed for the continuous flow of "fresh" gas through the chamber. The TIMETAL 21S corrosion specimens were prepared by progressively grinding to a 600 grit finish after which it was ultrasonically cleaned and washed in ethanol. The sample was placed on the specimen platform on the corrosion chamber base with the ground surface facing the incoming gas flow. Figure 2.9 shows the position of the test specimen in the corrosion chamber while figure 2.10 shows the corrosion chamber containing the test specimen positioned in the furnace with the gas line and the thermocouple attached.

The corrosion chamber was heated to the test temperature, and once the required temperature was reached, the exposure in the environment was maintained for approximately five hours. Upon completion of the test, the furnace was switched off and a large argon gas flow introduced into the corrosion chamber to prevent any further reaction of the specimen with the environment as the chamber and specimen cooled. Once the assembly had cooled sufficiently, the lid was unbolted, the specimen taken out and rapidly transferred to a cooling fixture to assist in the final cooling of the specimen to room temperature. Contamination of the ground surface was avoided at all costs. As a precautionary measure, the specimens were washed in ethanol after final cooling. X-ray diffraction was then performed on the specimens in order to determine the environmental consequences of the exposure on the microstructure.

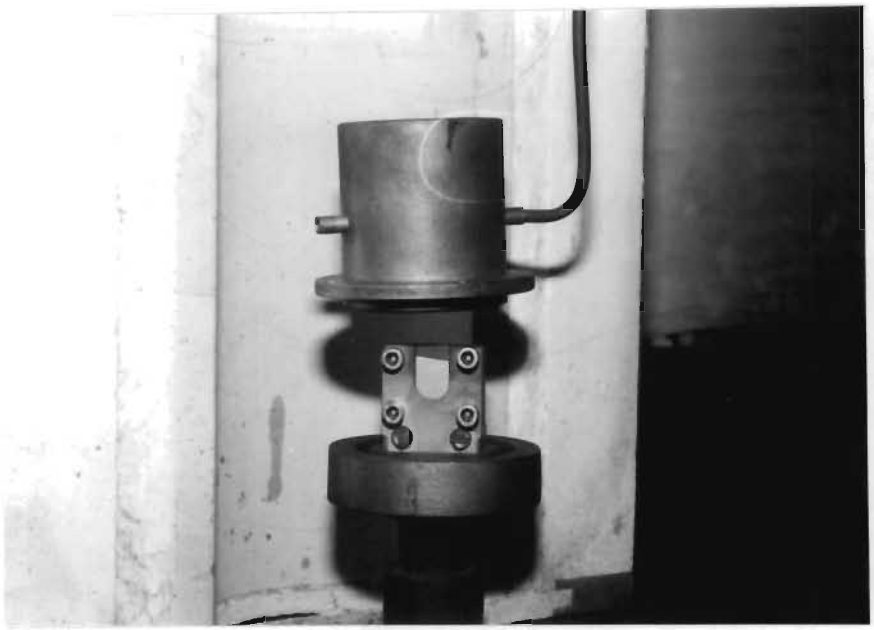

Figure 2.9 : Test specimen positioned in corrosion chamber

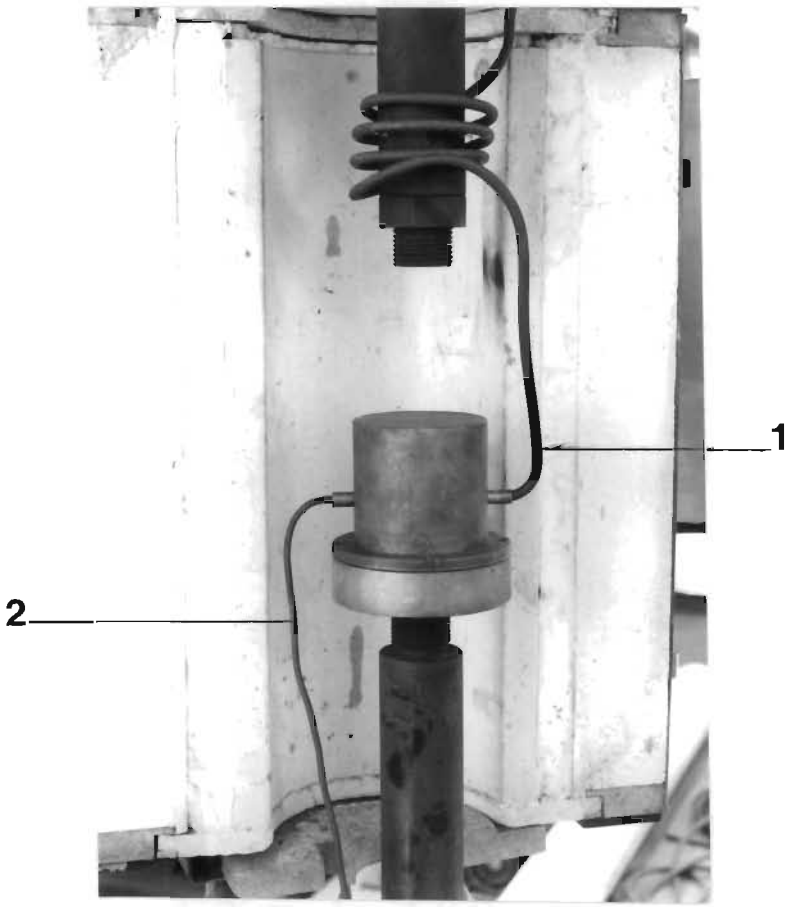

Figure 2.10 : Corrosion chamber positioned in the furnace
1. gas entry line
2. thermocouple

2.3 Parameters for the experimental systems

2.3.1 Corrosion tests

Controlled aging of metastable titanium alloys is typically performed in an inert environment in order to exclude any environmental effects. While the inert atmosphere effectively isolates the sample from any environmental effects, investigations on the role and effect of oxygen on the microstructural response and the surface oxide behaviour has to exclude any environmental assistance from the nitrogen, which is a known alpha phase stabilizer. Considering this, tests were conducted in two different environments, namely, an inert argon atmosphere and argon + 20% O_2 atmosphere which isolated the effect of oxygen. For all the tests, the argon flow was kept constant at approximately 6 *l*/min.

Due to the fact that TIMETAL 21S is susceptible to aging at elevated temperatures (precipitation of the alpha phase), the role of oxygen in the transformation of the microstructure could be observed.

The corrosion tests were conducted at the following temperatures : 300°C, 350°C, 400°C, 450°C, 550°C, 600°C, 650°C, 700°C and 750°C. As mentioned previously, the duration of the tests was approximately five hours, the interval being taken from the time the specimen reached the desired test temperature.

2.3.2 Fatigue crack growth rate measurement

2.3.2.1 Compliance method

For fatigue crack growth monitoring rate by compliance, the specific specimen geometry was firstly calibrated. A geometrically similar sample manufactured from Ti 6Al-4V was used for this process. The anticipated crack path along the width of the specimen was electropolished using 5% H_2SO_4, 95% ethanol mixture to facilitate in the optical crack length measurement. A calibration curve of dimensionless crack length,

a/W, versus dimensionless compliance, EBC (terms defined in chapter 1, section 1.3), was obtained by progressively extending a fatigue crack into the sample and determining the compliance at a series of known crack lengths, using the computer-based system. The crack length was measured using an optical travelling microscope with a resolution of 1 μm.

The calibration sample was precracked following recommended ASTM procedure to a dimensionless crack length of approximately a/W = 0.25. The crack length was optically measured and approximately five compliance measurements were taken at this point by using relatively high stress intensity range ΔK at low cyclic frequency. The crack was then extended by cycling at a higher frequency and at a lower ΔK after which the crack length was again measured, after which another set of compliance readings were taken. This process of low frequency-high ΔK and high frequency-low ΔK was repeated until sufficient crack length and accompanying compliance readings were obtained in the range $0.25 \leq a/W \leq 0.7$. After the tests the fracture surface was examined and the optically measured crack lengths corrected for crack tunnelling. The MATLAB mathematical package was used to obtain a best fit fifth order polynomial of EBC = f(a/W) and a/W = f(EBC). The resultant calibration curve obtained is shown in figure 2.11.

Fatigue Crack Propagation Parameters

Prior to testing the TIMETAL 21S samples were aged at 593°C for 8 hours in an inert argon environment to stabilize the microstructure. This aging treatment is typical of a fully aged condition likely to be used in commercial applications [31,54]. The 620°C samples were not aged since aging at this temperature requires only approximately 2 hours [31].

Fatigue crack growth rate tests were conducted at temperatures of 375°C, 450°C, 550°C and 620°C in the various environments. The tests were conducted at a frequency of 0.1 Hz and a stress ratio of R=0.1. The frequency allowed the maximum environmental interaction while still negating the effect of creep [25]. The tests were

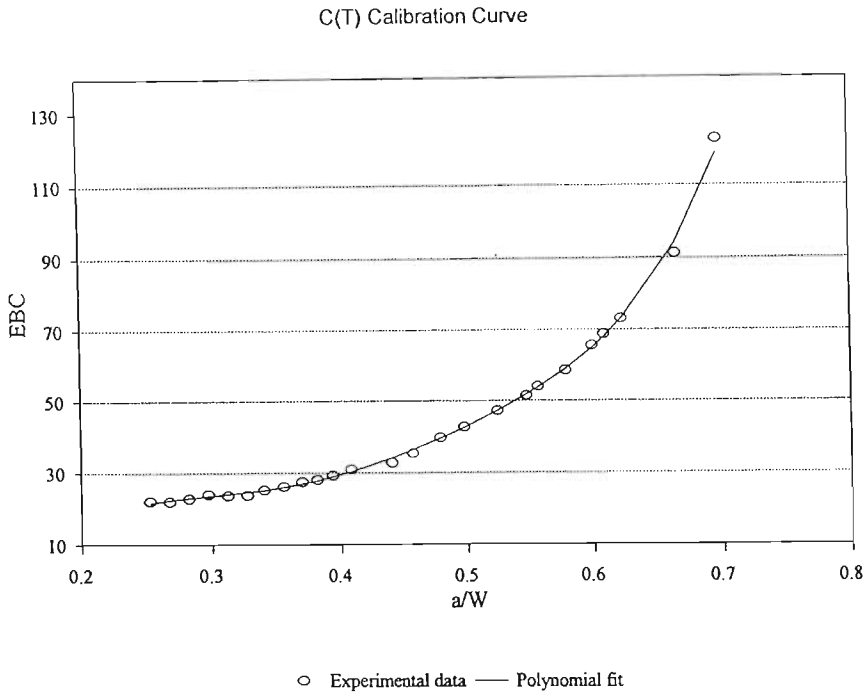

Figure 2.11 : EBC vs a/W calibration curve obtained for the particular C(T) specimen

conducted by systematically increasing the mean load until a small but persistent crack growth/increase in LVDT span was detected over a number of cycles. This allowed the crack growth to be detected from the near-threshold region. An increasing ΔK test was then conducted up to a/W = $\pm$ 0.68, at which point the sample was beachmarked by reducing the mean load to approximately 50% of the previous value and increasing the cyclic frequency to 10Hz. The beachmarking was then employed up to failure of the specimen. The actual and compliance measured crack lengths specimen crack length could thus be calibrated and an effective Young's modulus for the specific test temperature established.

The validity of the linear elastic stress intensity factor was verified using the criterion stipulated by ASTM E647. This validity criterion was presented in chapter 1, equation 1.5. In the all the tests this criterion was satisfied.

The FCGR data was plotted using either the 7-point incremental method, as recommended by the ASTM 647 standard, or by polynomial fit using the MATLAB package.

Offset Displacement Procedure

The "offset displacement method" is often used to magnify the opening and closing loads from the load-displacement hysteresis curve. To illustrate this procedure, consider a typical load-displacement hysteresis curve, in which a closure mechanism is apparent [68], as shown in figure 2.12a. From the figure it is clear that there is a deviation from linearity at higher loads. This deviation indicates the region where the opening and closing load, P_{op} and P_{cl} respectively, are active.

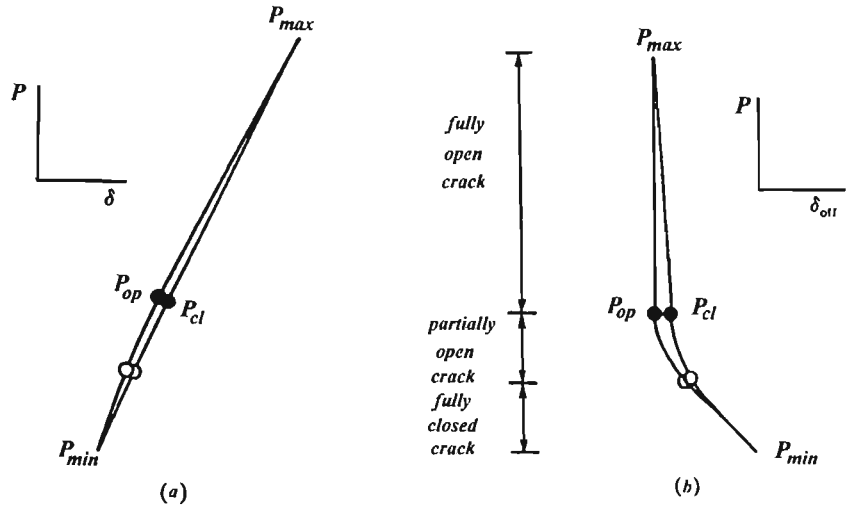

Figure 2.12 : a. Typical complete fatigue cycle load-displacement hysteresis curve containing a closure mechanism
b. Offset displacement curve indicating opening and closing loads - see text for interpretation

The displacement, δ, (as shown in fig. 2.12a), can be given by :

$$\delta = \alpha P + C \qquad \ldots(2.1)$$

where C is a constant, and α is the compliance between P_{op} and the maximum opening load, P_{max}, and P, any load between P_{min} and P_{max}. The offset displacement, δ_{off}, can thus be given by :

$$\delta_{off} = \delta - \alpha P \qquad \ldots(2.2)$$

Plotting δ_{off} versus load results in figure 2.12b from which the magnitude of P_{op}, and similarly P_{cl}, can clearly be identified. Similarly, to determine the closure load, P_{cl}, the analysis can be performed between P_{cl} and P_{max}. It can however be seen that to produce this result from experimental data, a prior knowledge of the value of P_{op} (or P_{cl}) is necessary to obtain the compliance between closure load and P_{max}. To bypass this apparent impasse, linear regression was performed between 60% and 90% of P_{max} on the loading portion of the curve, as previous work has shown this interval to be sufficient in effectively excluding P_{op}, or P_{cl} [110,123,129]. In the event of apparent anomalies when scrutinizing the opening/closure graphs, regression was performed between 75% and 90% of the loading/unloading portion of the hysteresis curve.

The compliance method was used for all temperatures except 620°C, in which case the beachmarking method was used.

2.3.2.2 Beach marking method

The approach that was found to produce appreciable results on the TIMETAL 21S samples at 620°C was to cycle at a relatively high mean load at a frequency of 0.1 Hz for a specific number of cycles to form a "block". The mean load was then reduced to approximately 70% of the previous mean, the frequency increased to 10 Hz and cycled for a specific period of time to produce a beachmark. In both cases the stress ratio was kept constant at R = 0.1. Each block was thus separated by a beachmark and the crack propagation rate could be calculated from the block. Each crack length was measured at three specific points across the breadth of the specimen to account for the crack front curvature. Details of the loading regimes used to produce the blocks and beachmarks in the argon + 20% O_2 and argon environments at 620°C is shown in tables 2.1 and 2.2. To avoid unnessary use of the limited TIMETAL 21S alloy available to establish the beachmarking parameters, the method was not used at lower temperatures.

Mean Load [N]	cycles/time
210	2000 cycles
150	10 min
210	1000 cycles
150	10 min
210	1000 cycles
150	10 min
210	1000 cycles
150	7.5 min
210	500 cycles
150	10 min
repeat to failure	

Table 2.1 : Loading regime used to beachmark TIMETAL 21S C(T) sample tested at 620°C in an argon environment.

Mean Load [N]	cycles/time
210	2000 cycles
150	10 min
210	1000 cycles
150	10 min
210	1000 cycles
150	10 min
210	1000 cycles
150	7.5 min
210	500 cycles
150	10 min
repeat to failure	

Table 2.2 : Loading regime used to beachmark TIMETAL 21S C(T) sample tested at 620°C in an argon + 20% O_2 environment.

2.4 Metallurgical research methods

To completely describe the microstructure, concentration of elements and the chemical state of the elements, optical microscopy, scanning electron microscopy (SEM) with Energy Dispersive X-ray (EDX) analysis, X-ray diffraction analysis and Auger Electron Spectroscopy (AES) were used.

2.4.1 Optical Microscopy

For general purpose analysis e.g. fracture surface appearance and fatigue crack profiles, low magnification (up to approximately x50) an Olympus SZ-PT stereo microscope was used. For higher magnifications up to x400 a Nikon Epiphot microscope was used.

2.4.2 Scanning Electron Microscopy with EDX detector

The SEM's were used for general metallographic and fractographic investigations and EDX analysis.

A HITACHI S520 Scanning Electron Microscope fitted with a energy dispersive X-ray (EDX) analyzer, KEVEX 7000/77 mainframe and the Macintosh Desk Spectrum Analyzer (DTSA) program was used. The system was used for metallographic and fractographic observations, and secondary electron as well as backscattered electron imaging were employed. The 6μm beryllium window on the EDX detector prevented the detection of elements with atomic mass lower than that of sodium.

For general material characterization (fractography and metallography) and for EDX analysis, a 15 kV acceleration voltage was used. Backscattered electron investigations was conducted at 17 kV.

A JEOL JSM-6100 SEM fitted with a windowless EDX detector and a Noran Voyager 2100 analysis system was used for quantitive analysis. Acceleration voltage of 25 kV was used which proved to be sufficient to obtain an appreciable output signal from the higher atomic mass elements. The spatial resolution of the system is approximately 1 μm.

2.4.3. X-ray diffraction analysis

The X-ray diffraction analysis was used to identify the existing phases in the as-received material and also to monitor the evolution of the phases that occurred during the corrosion tests. The diffraction analysis used Cobalt K_{α}-radiation (λ = 1.7902 Å) and was conducted with a scanning angle (2θ) ranging between 20° and 110°. The diffraction analysis was conducted on the as-received samples as well as on the specimens that had been exposed to various temperatures and to the inert and oxidizing environments in the corrosion chamber.

Specimen preparation for the x-ray diffraction analysis is similar to that described in section 2.2.4.

2.4.4 Auger Electron Spectroscopy

Auger Electron Spectroscopy (AES) was used for the detection, identification and quantitization of elements at the surface or in near-surface regions. AES is able to detect light elements, including oxygen, and is thus particularly suited to the detection of oxides. Although AES is mainly used for qualitative analysis, particular oxides have been shown to have characteristic AES profiles [130,131], thus qualitative analysis of certain compound to some degree, can be obtained.

The AES analysis was performed at MATTEK, a division of the CSIR in Pretoria. A PHI 595 Auger Electron Microprobe was used with a beam voltage of 5kV and a beam current of 2 μA.

AES line scans were performed on the transverse section of the samples tested in the corrosion chamber in the oxidizing environments, while point analysis was performed on the fracture surface of some of the C(T) specimens tested in the oxidizing and inert environments at 620°C.

Due to titanium's ability to spontaneously form a protective surface oxide layer in the presence of oxygen, sputtering was performed *in-situ* on the samples prior to analysis., using Ar ions at 3 kV and a beam current of 30 $\mu A/cm^2$. Carbon complexes formed on the sample surface indicated the extent of any surface contamination. The carbon residues were sputter-removed to an acceptable level prior to a full analysis of the sample surface.

Standard depth profiling procedures using the AES system involves the ion bombardment of the surface resulting in an eroded region of specific depths. The element analysis is then performed at this level. This process is fairly tedious though and long bombardment times may only yield low penetration depths [7]. A different approach to depth profiling of the fracture surface of the C(T) specimens has been adopted. This approach involved the partial grinding of the fracture surface at an angle of approximately 20° (see figure 2.13), allowing analysis to be performed on the fracture surface (point F), adjacent to the fracture surface (point I) and at a location remote from the fracture surface (point B) - the relatively "unaffected" bulk material. This configuration allowed for the analysis of the elements at various locations, giving an indication of their relative amounts present at the different sites.

The C(T) specimen preparation for AES analysis involved the progressive grinding of the angled surface to 600 grit paper finish, after which a 6 μm ,1 μm and 0.05 μm colloidal silica final polishing ensued. The specimens were then washed in acetone, cleaned in de-ionized water and dried. Sputtering was performed on the samples prior to AES analysis to remove any surface residue and also for the aforementioned reasons.

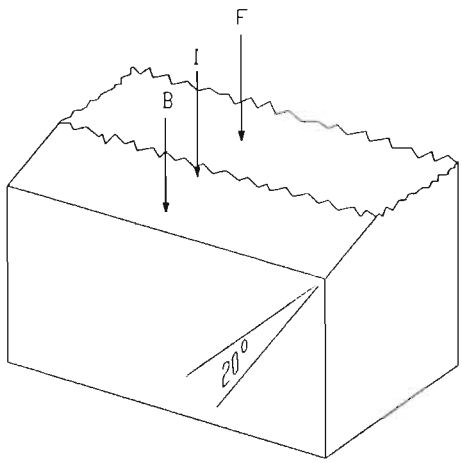

Figure 2.13 : Schematic of partial grinding of the C(T) specimen fracture surface for AES depth analysis (see text for details)

Chapter 3 : Results

3.1 Characterization of TIMETAL 21S

The development of the TIMETAL 21S metastable titanium alloy was described in chapter 1, section 1.2.

The chemical analysis of the as-received TIMETAL 21S alloy is given in table 3.1.

Element	Mo	Al	Nb	Si	Ti
wt%	14.4	1.71	2.1	0.24	rem

Table 3.1 : Chemical analysis of as-received TIMETAL 21S

The TIMETAL 21S material was obtained in plates of thickness 1.55 mm from Heat G 1664, Test H 499, GA 060. X-ray diffraction was performed on the as-received material and the analysis revealed the presence of the beta structure, as shown in figure 3.1.

Transverse and longitudinal samples of the materials were prepared to examine the as-received microstructure. The samples were prepared according to the Buehler preparation method for titanium alloys [132]. The process involved grinding to a 180 grit finish in deionised water, followed by grinding for approximately 12 minutes on the Buehler Minimet system using a Metlap 4 platen, charged with 9μm diamond suspension. Final polishing for approximately 10 minutes followed using a Texmet polishing cloth and 0.05μm colloidal silica. This preparation method proved to be far superior compared to "standard" cloth preparation methods for maintaining surface integrity and flatness and for minimizing edge rounding.

Examination of the as-polished metallographic samples showed no inclusions in the alloy and the etched longitudinal metallographic samples shows an equiaxed structure

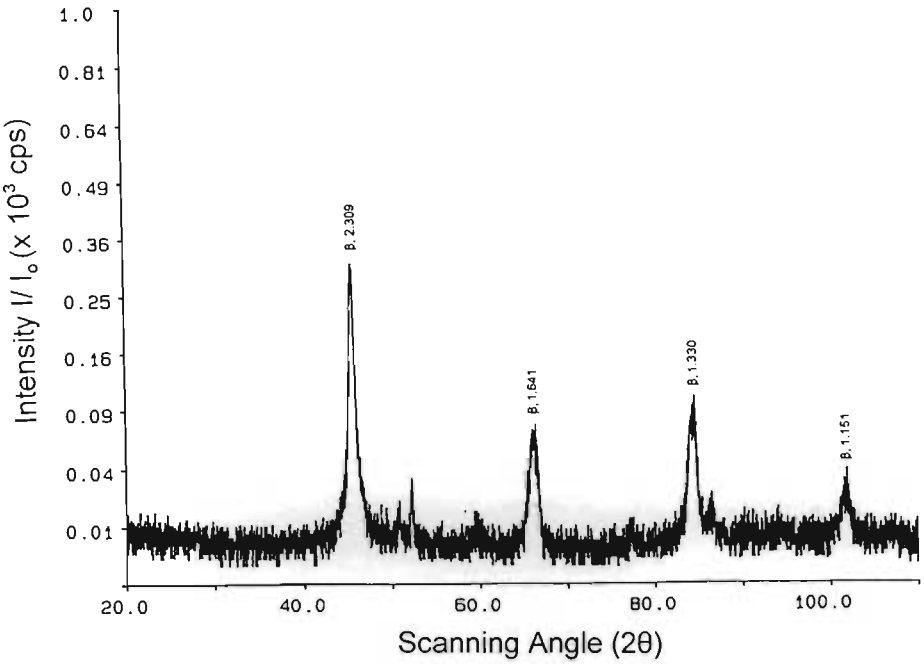

Figure 3.1 : X-Ray diffraction analysis of as-received TIMETAL 21S

consisting of beta grains (figure 3.2a), with a grain size number of approximately 6. The transverse metallographic samples showed non-crystallized regions towards the centre of the sample in addition to the equiaxed beta grains. These non-crystallized regions are due to incomplete formation of beta grains during a post hot rolling recrystallization-annealing treatment. The transverse view of the sample is shown in figure 3.2b.

The as-received samples were etched in a solution of 85 ml H_2O, 25 ml HCl, 12 ml Hf and 10 ml HNO_3. The apparent appearance of small precipitates in the etched samples can be attributed to pitting during the etching process.

3.2 Corrosion tests on TIMETAL 21S at various temperatures

Transverse metallographic samples were prepared from the specimens tested in the corrosion chamber in pure argon and argon + 20% oxygen environments at various temperatures to examine the extent of the microstructural transformation and reveal the oxide layer, if present, using optical microscopy, SEM and X-ray diffraction analysis.

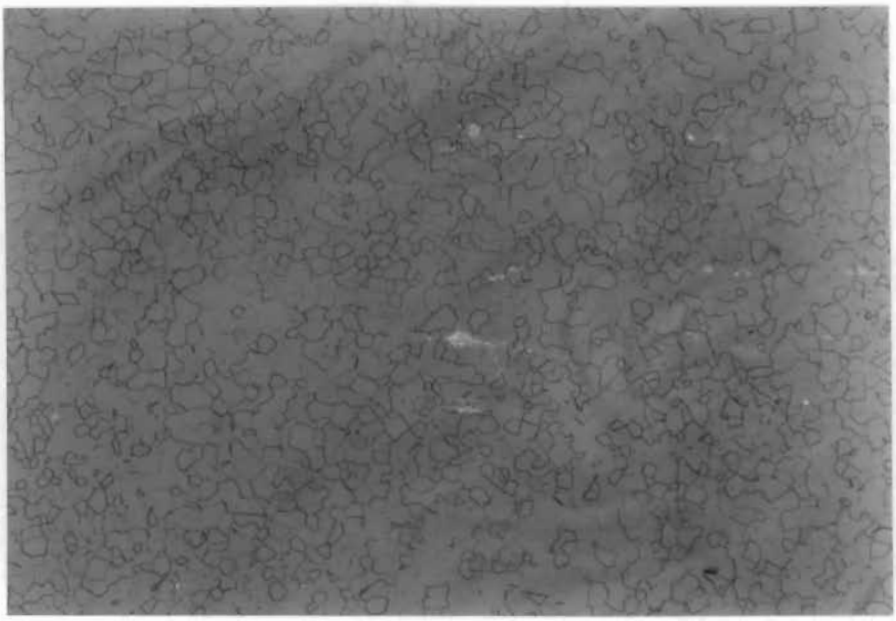

a.

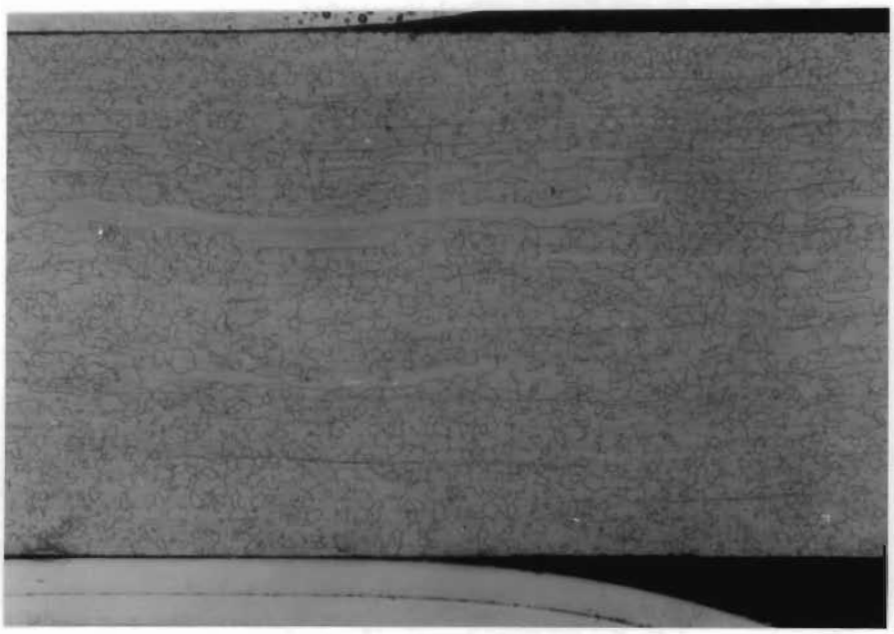

b.

Figure 3.2 : Microstructure of the as-received TIMETAL 21S in the etched condition
a. Longitudinal view, x100
b. Transverse view, x50

EDS point analysis was performed on a transverse cross section of the material to establish which elements actively participated in the material high temperature protection mechanism. A more detailed EDS point and area analysis was also conducted on some of the samples exposed to higher temperatures in order to determine the extent of element migration.

Preparation of the samples were similar to that given in section 3.1, and the samples used in electron microscopy were carbon coated. Due to the evolution of different microstructures during the exposure tests, it was noted that certain test temperatures required specific etchants to more effectively reveal the microstructures. Table 3.2 details these etchants.

Exposure temperature	**Etchant**
as-received	85ml H_2O, 12ml Hf, 10ml HNO_3, 25ml HCl
300°C	85ml H_2O, 12ml Hf, 10ml HNO_3, 25ml HCl
350°C	as for 300°C
400°C	as for 300°C
450°C	as for 300°C
500°C	as for 300°C
550°C	77ml H_2O, 20ml HNO_3, 3ml Hf
600°C	250ml H_2O, 3ml HNO_3, 2ml Hf
650°C	250ml H_2O, 3ml HNO_3, 2ml Hf
700°C	85ml Glycerol, 10ml Hf, 10ml HNO_3, 25ml HCl
750°C	85ml Glycerol, 10ml Hf, 10ml HNO_3, 25ml HCl

Table 3.2 : Etchants used for TIMETAL 21S exposed at various temperatures

3.2.1 Argon + 20% O_2 environment

Microstructural observations

The microstructure of the TIMETAL 21S samples tested at 300°C and 350°C in the oxidizing environment is shown in figure 3.3. No apparent microstructural changes were observed when compared to the as-received specimen. A slight accelerated aging response could however be detected in the samples tested at 400°C, manifested by the overetching of the non-recrystallized regions (figure 3.4a). Fine alpha precipitation within the beta grain can also be seen from the greyish appearance of the grain interior of the sample and a slightly precipitation depleted region at the grain boundaries indicates that precipitation has initiated at the grain boundaries as shown in figure 3.4b.

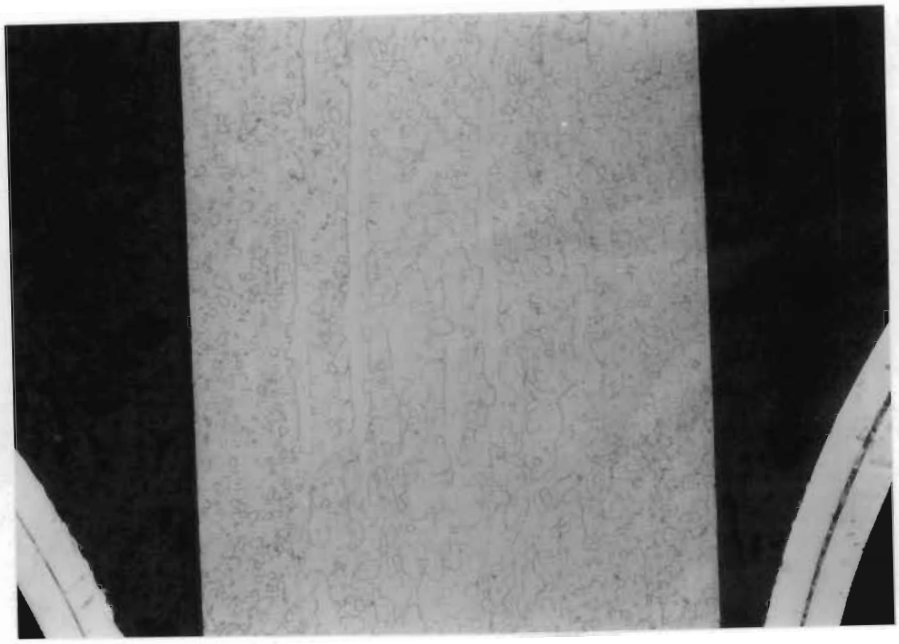

a.

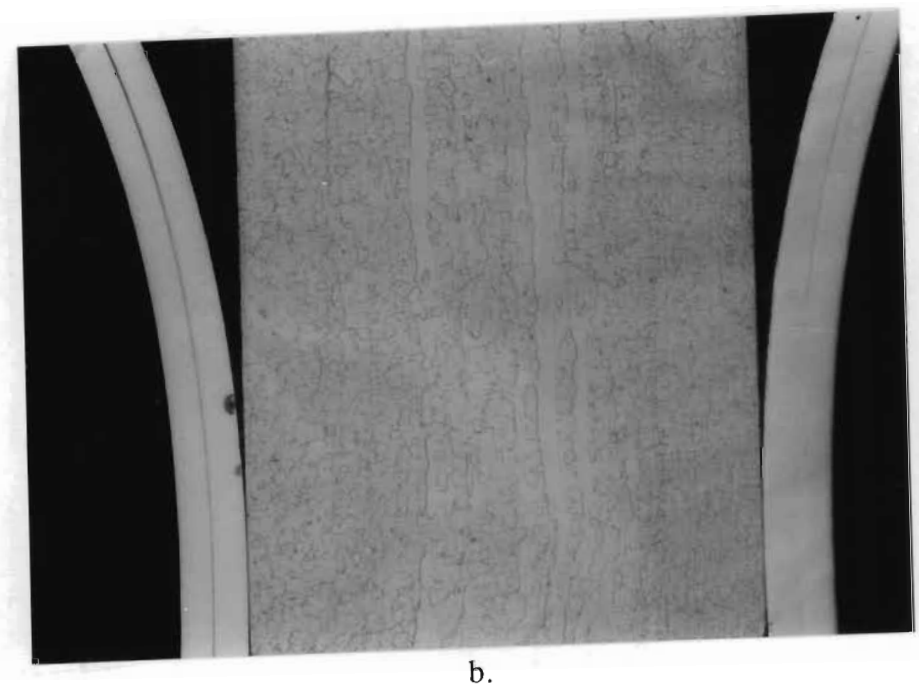

b.

Figure 3.3 : Transverse view of TIMETAL 21S samples tested in argon + 20% O_2 at :
a. 300°C, x50, **b.** 350°C, x50

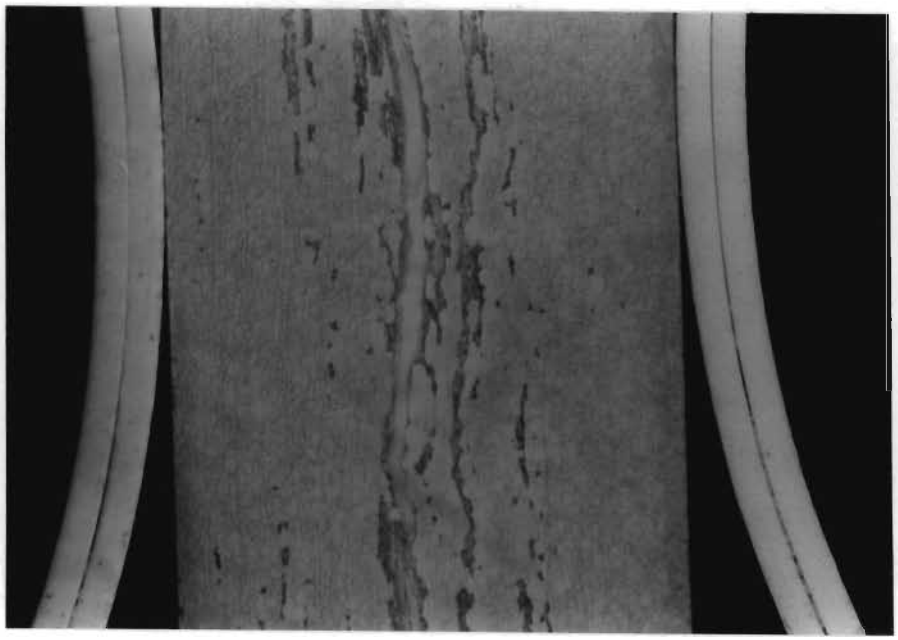

a.

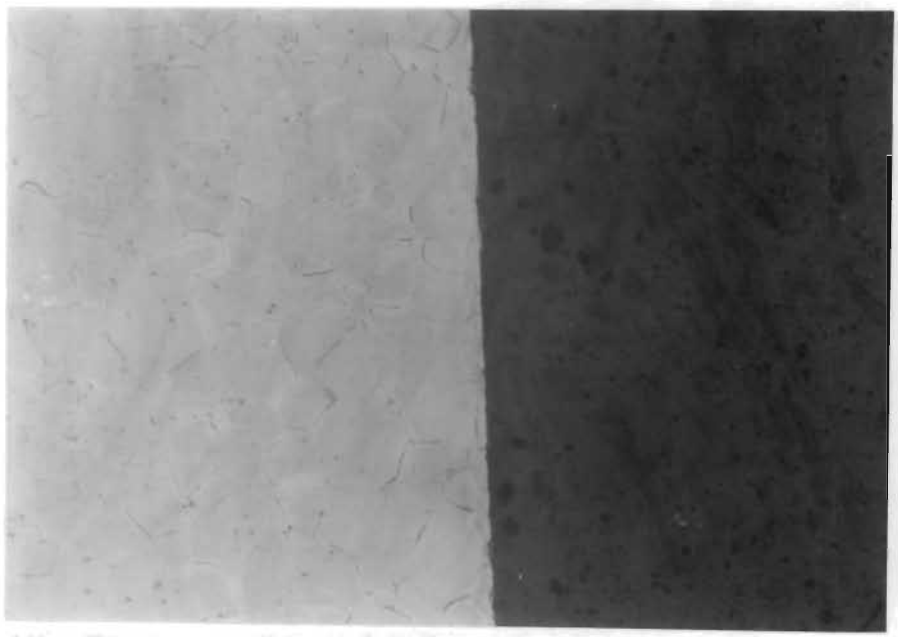

b.

Figure 3.4 : Microstructure of TIMETAL 21S after exposure at 400°C in argon + 20%O_2 environment
a. Accelerated aging of un-recrystallized regions, x50
b. Precipitation depleted region at the grain boundary regions, x400

The x-ray diffraction analysis performed on the 300°C, 350°C and 400°C samples showed negligible changes of the material and no apparent oxide scale formation. The results of the x-ray diffraction analysis performed on the samples is shown in figure 3.5a,b and c.

The TIMETAL 21S sample tested in temperatures of 450°C indicated that the precipitation of the alpha phase at the grain boundaries was more pronounced. Examination of the samples under optical microscopy shows a fine precipitate within the beta grains, while a precipitation-free area adjacent to the grain boundaries can be seen from figure 3.6.

The presence of the evolving surface oxide layer, TiO_2, and the gradual reduction from a predominantly beta phase near-surface region is evident from the x-ray diffraction analysis of the sample tested at 450°C as shown in figure 3.7.

Figure 3.8 shows the surface region and the accompanying results of EDS point analysis performed in this area. There appears to be a correlation between the oxidation resistance of the material and the relative quantities of Al, Si, Nb and Mo at this temperature. Higher concentrations of these elements are experienced towards the exposed surface. Note that the apparent elevation of the grain boundary regions is an optical artifact and by inverting the micrograph, an elevated grain interior can be observed.

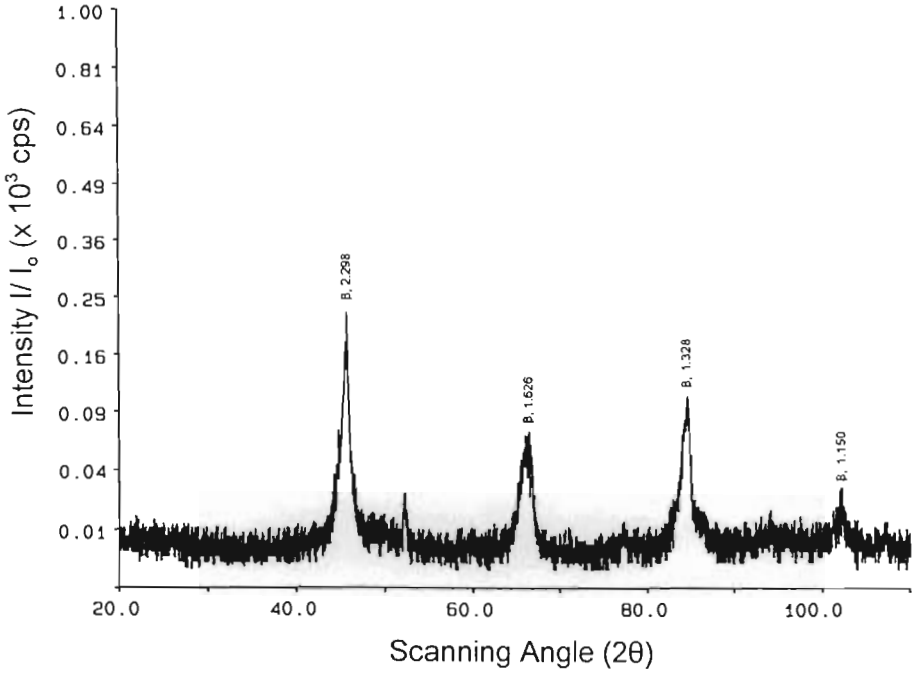
1.00
0.81
0.64
0.49
0.36
0.25
0.16
0.09
0.04
0.01
Intensity I/ I$_o$ (x 10^3 cps)
β, 2.298
β, 1.626
β, 1.328
β, 1.150
20.0
40.0
60.0
80.0
100.0
Scanning Angle (2θ)

a.

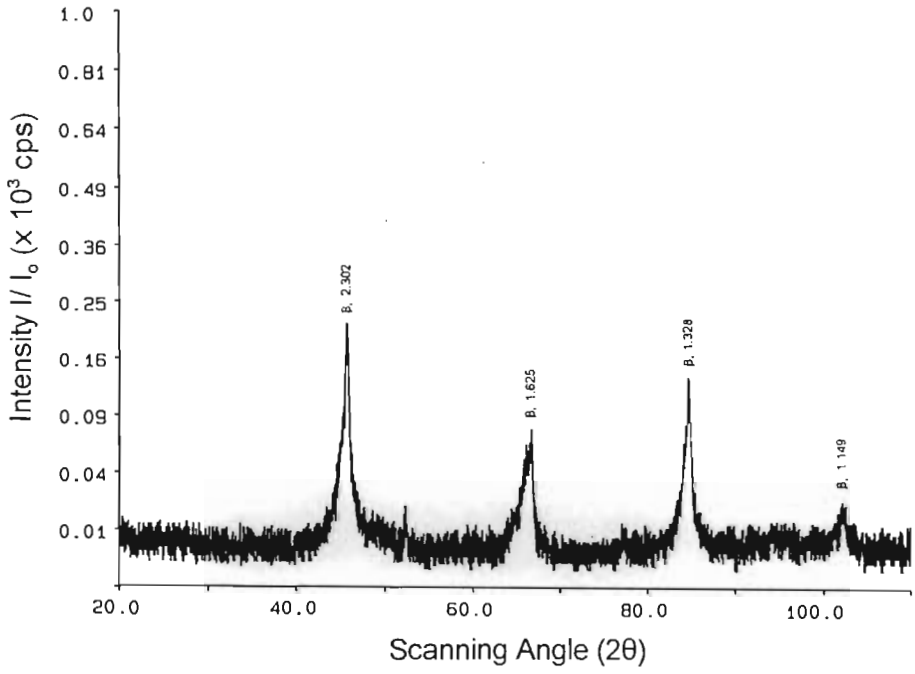
1.0
0.81
0.64
0.49
0.36
0.25
0.16
0.09
0.04
0.01
Intensity I/ I$_o$ (x 10^3 cps)
β, 2.302
β, 1.625
β, 1.328
β, 1.149
20.0
40.0
60.0
80.0
100.0
Scanning Angle (2θ)

b.

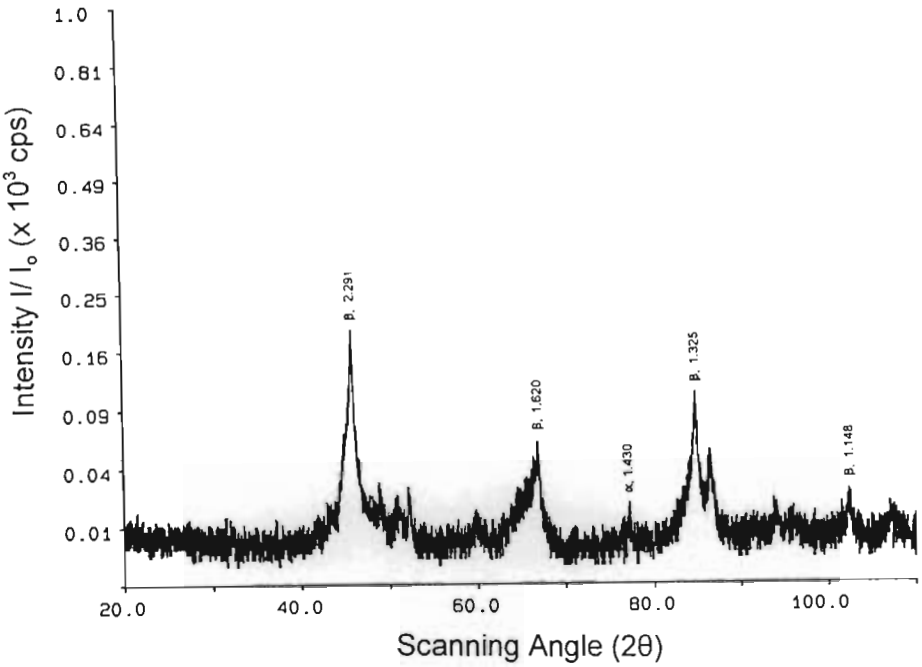

c.

Figure 3.5 : X-ray diffraction analysis of TIMETAL 21S samples tested in argon + 20% O_2 at :
a. 300°C
b. 350°C, and
c. 400°C

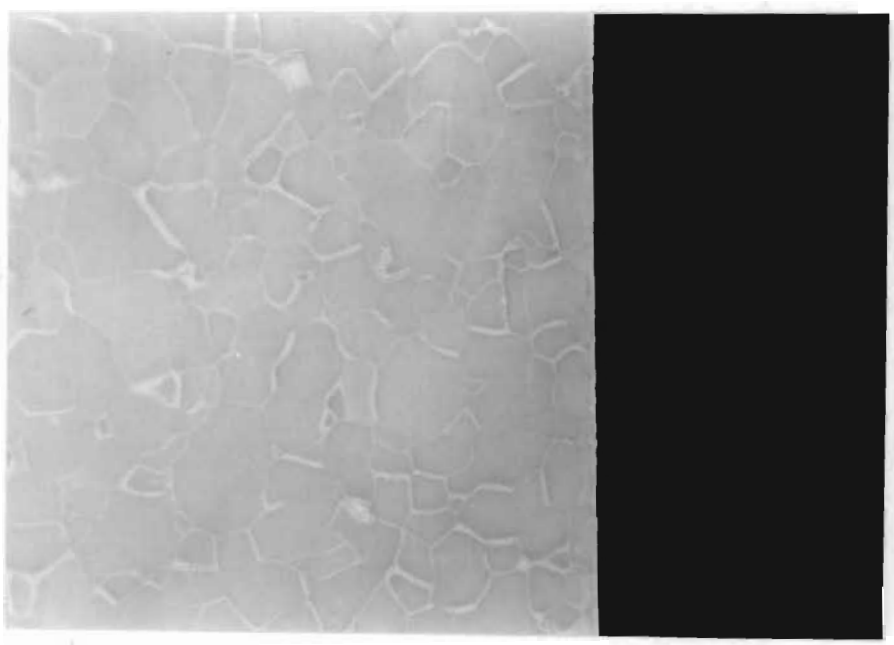

Figure 3.6 : Microstructure of the TIMETAL 21S sample tested at 450°C in argon + 20% O_2 environment; grain boundary precipitation highlighted using the DIC technique, x400

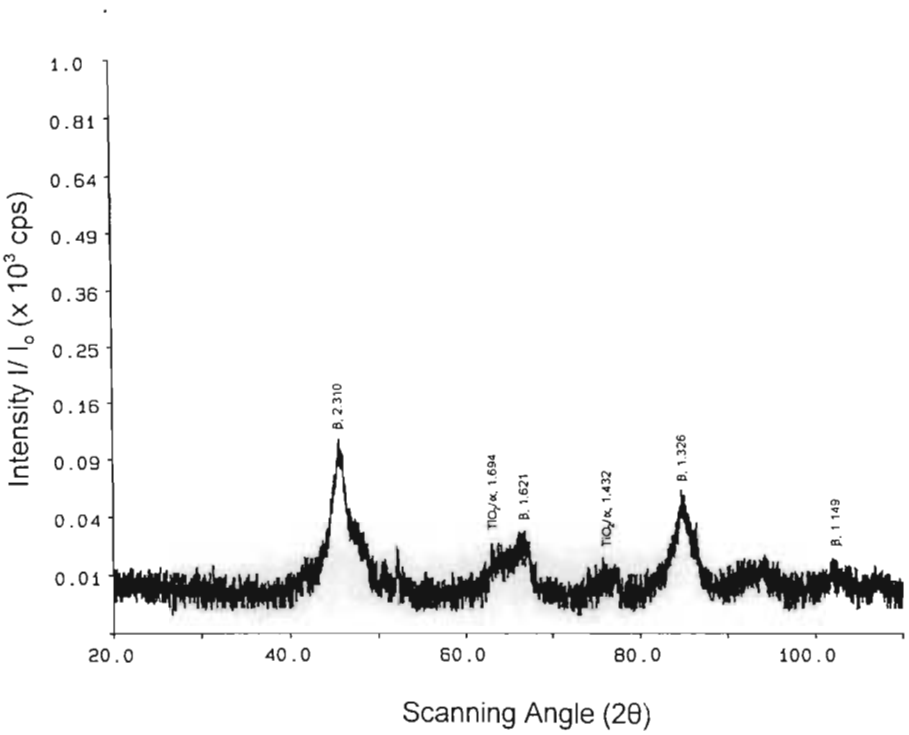

Figure 3.7 : X-ray diffraction analysis results of the TIMETAL 21S sample exposed to argon + 20%O_2 at 450°C

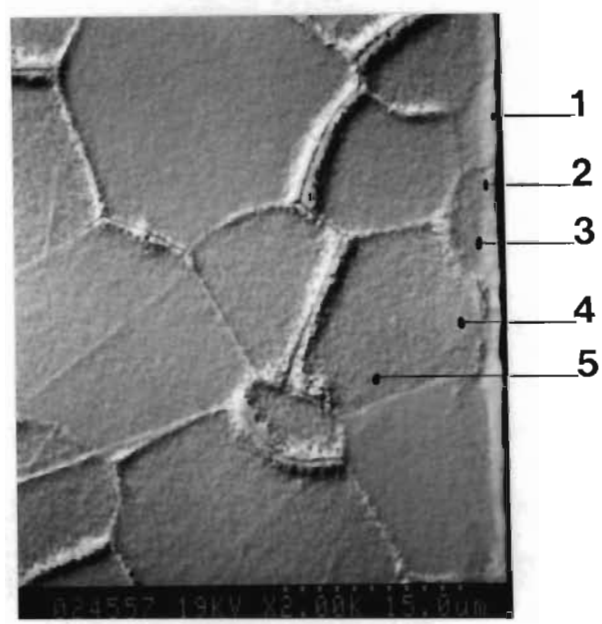

Position\ Element	1	2	3	4	5
Al	4.31	3.56	2.39	2.47	2.38
Si	0.44	0.26	0.21	0.12	0.20
Nb	2.82	2.49	2.18	2.33	2.46
Mo	14.72	14.53	12.97	13.20	13.41
Ti	77.71	79.16	82.25	81.88	81.56

Figure 3.8 : EDS analysis of the surface region of the TIMETAL 21S sample tested in argon + 20%O_2 at 450°C

In the TIMETAL 21S sample tested at 500°C, the fine alpha precipitation is still noticeable inside the beta grains, but a coarser precipitation of the alpha phase near the grain boundaries has occurred. This is accompanied by a larger precipitation-free zone adjacent to the grain boundaries as evident from figure 3.9. The surface oxide layer is also clearly evident as a white edge layer.

The x-ray diffraction analysis performed on the 500°C tested sample (figure 3.10) reveals the stronger presence of TiO_2 at the surface. In addition, the alpha phase has become more prominent while there is a reduction in the intensity of (110) beta phase peak.

Tests performed at 550°C in the argon + 20% O_2 environment revealed a similar microstructure to that obtained for 500°C (figure 3.11a). However the alpha precipitation inside the grains and at the grain boundaries appeared somewhat coarser. Figure 3.11a also shows that the surface oxide layer thickness has increased marginally over that of the 500°C sample, and slight increases in the oxide thickness of the 600°C and 650°C samples is evident from figure 3.11b and c.

The SEM micrograph as shown in figure 3.12 details the resultant microstructure of the sample tested at 650°C. The area adjacent to the grain boundary region contains the needle-like alpha precipitates, while the finer precipitation is evident more towards the centre of the grain. Grain boundary precipitation of the alpha phase is not clearly visible, however this may be due to masking by the etching process itself. Also shown are the different types of alpha precipitation common to titanium alloys i.e. (A) fine internal precipitation, (B) needle-like precipitation in an otherwise precipitation-free region adjacent to the grain boundaries, (C) grain boundary precipitation and, (D) directionally elongated precipitation originating from the grain boundaries.

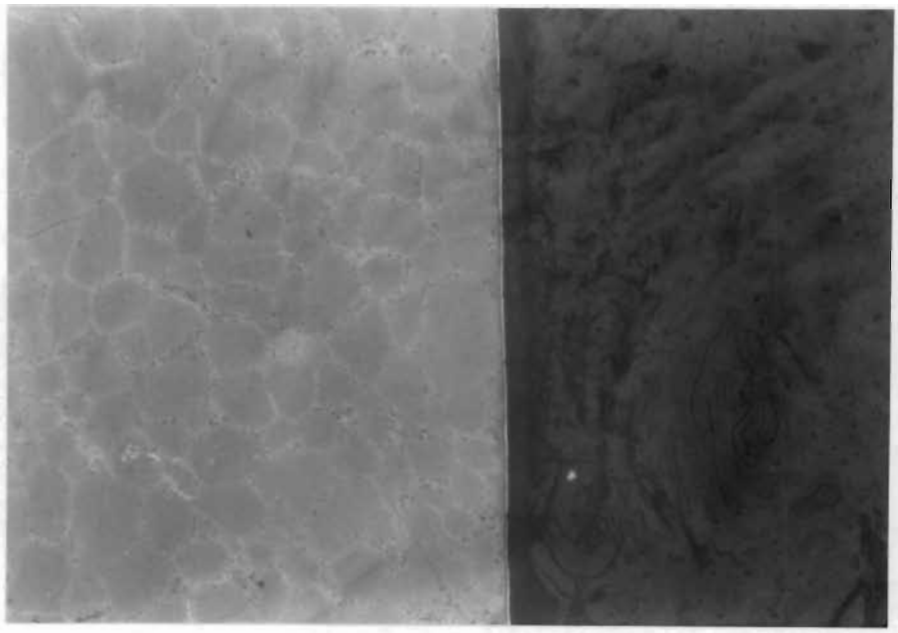

Figure 3.9 : Surface oxide layer and microstructure of TIMETAL 21S after exposure to 500°C in argon + 20% O_2, x400

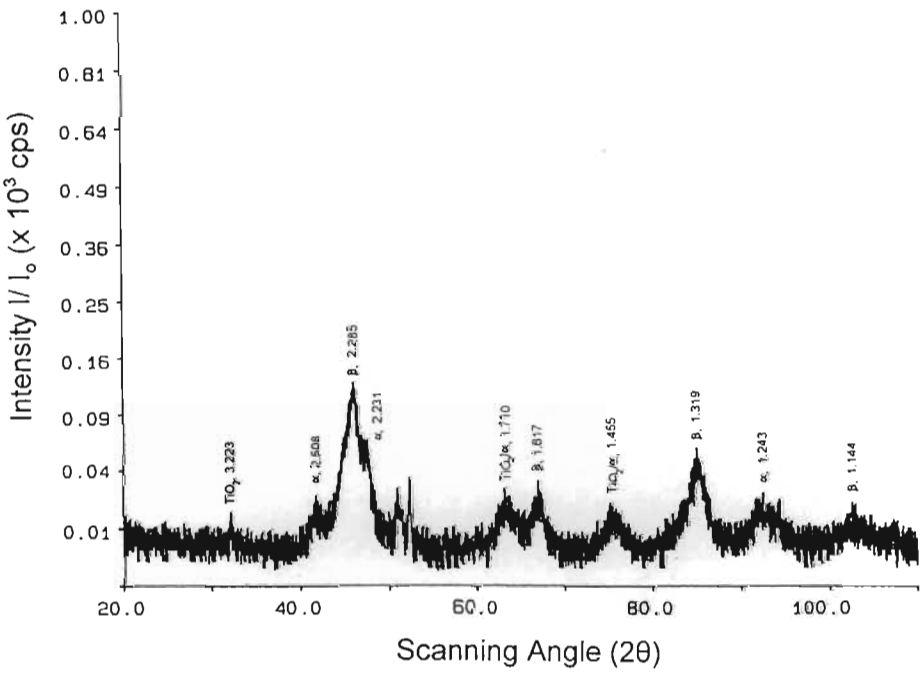

Figure 3.10 : X-ray diffraction analysis of TIMETAL 21S sample tested at 500°C in argon + 20%O_2 .

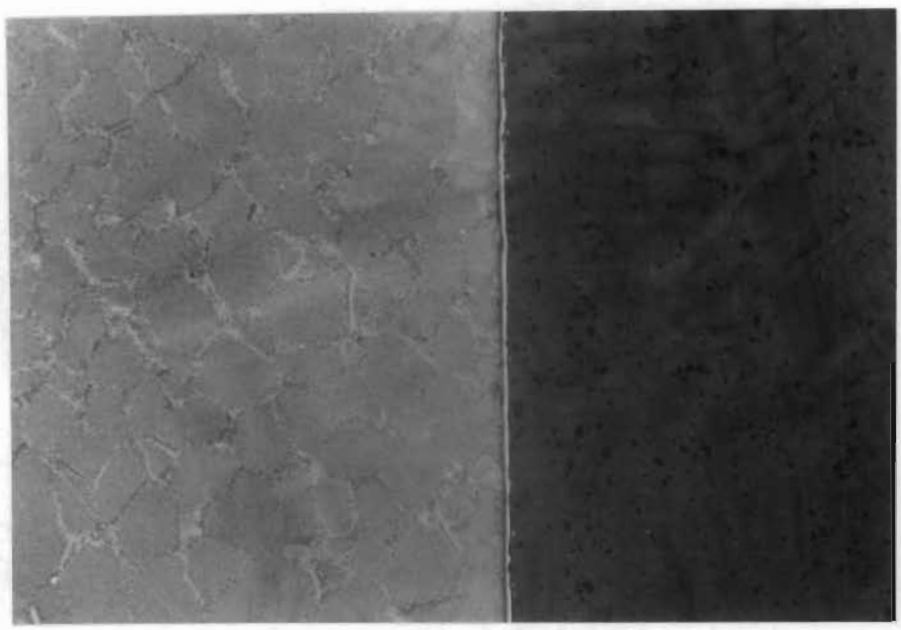

a.

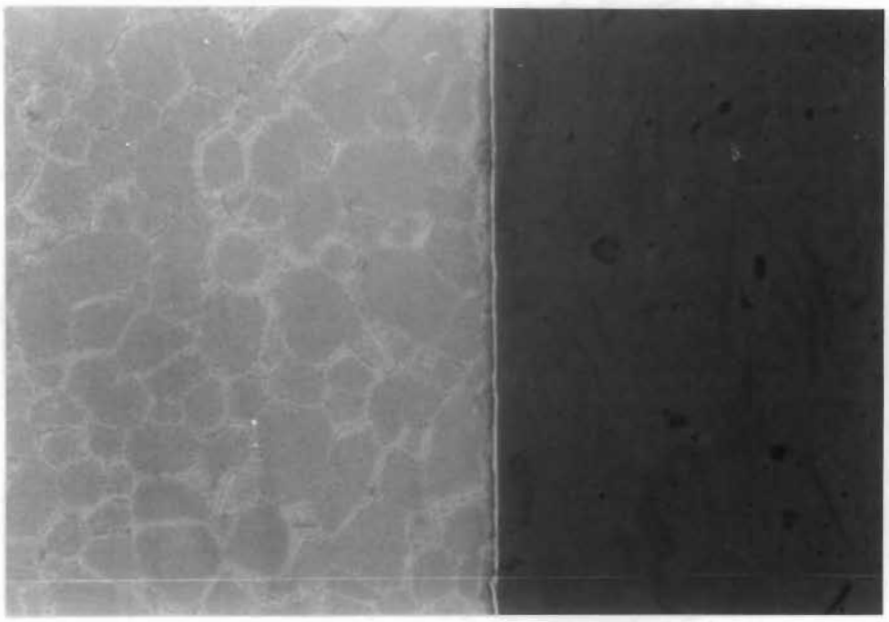

b.

c.

Figure 3.11 : Microstructure and surface oxide layer of the TIMETAL 21S sample tested in argon + 20% O_2 tested at :
a. 550°C, x400 **b.** 600°C, x400 **c.** 650°C, x400

The EDS analysis performed on the 650°C surface region is presented in figure 3.12. There appears to be local areas of high element concentrations, viz. relatively high Al and Si contents at the exposed surface and a high Si content at the interface of the oxygen affected region and the bulk material. It also appears that Nb plays an important role in the oxidation resistance at this temperature due to the increased quantities found towards the exposed surface of the sample. A small variation in the Mo content at this point is also evident.

Comparing the 600°C x-ray diffraction analysis result to that obtained for the 550°C sample, it is evident that the various peak heights are similar, however the (101) alpha peak has become dominant over the principal (110) beta peak (see figure 3.13a and b). The x-ray analysis of the sample tested at 600°C shows the small increase in the oxide peaks.

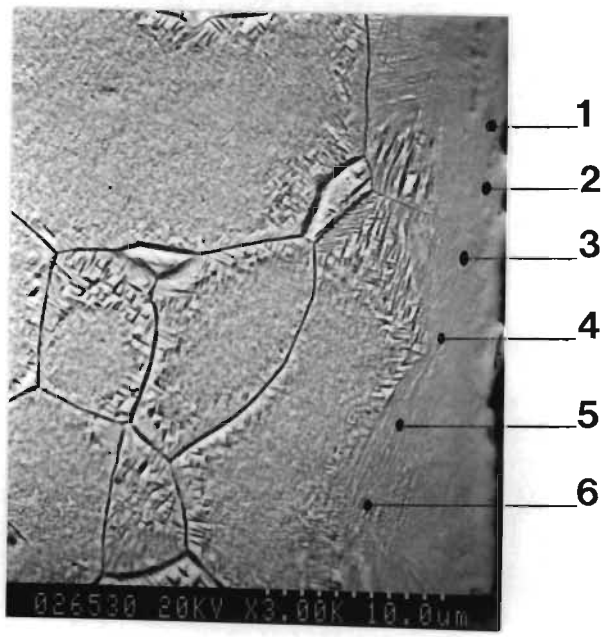

Position Element	1	2	3	4	5	6	Centre area analysis
Al	3.92	2.35	2.57	2.25	2.26	2.28	1.98
Si	0.94	0.59	0.76	1.22	1.06	0.76	0.24
Nb	3.08	2.79	2.75	2.51	2.34	2.51	2.32
Mo	14.99	14.51	15.31	14.79	14.25	14.12	14.19
Ti	77.06	79.76	78.61	79.23	80.09	80.34	81.28

Figure 3.12 : Characteristic precipitation (see text for details) and EDS analysis of surface region of the TIMETAL 21S sample tested at 650°C in argon + 20% O_2

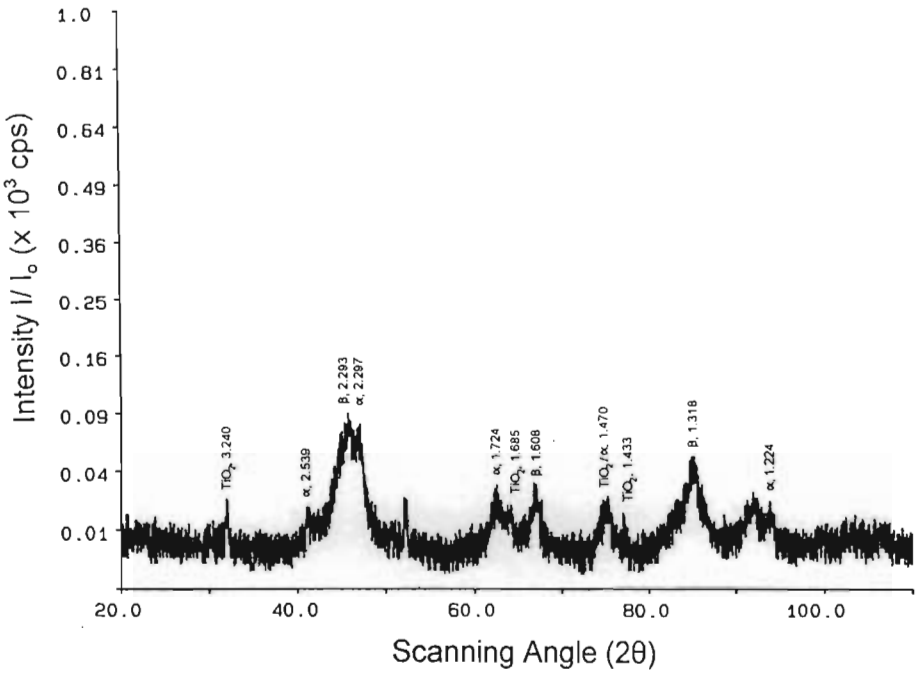
1.0
0.81
0.64
0.49
0.36
0.25
0.16
0.09
0.04
0.01
Intensity I/ I$_o$ (x 10^3 cps)
TiO$_2$ 3.240
α, 2.539
β, 2.293
α, 2.297
α, 1.724
TiO$_2$, 1.685
β, 1.608
TiO$_2$/α, 1.470
TiO$_2$, 1.433
β, 1.318
α, 1.224
20.0
40.0
60.0
80.0
100.0
Scanning Angle (2θ)

a.

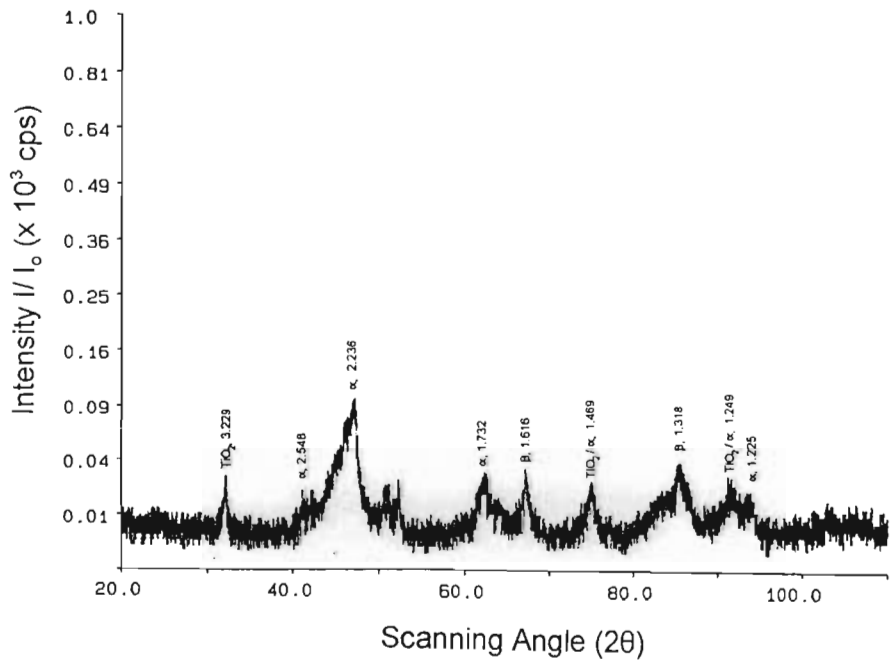
1.0
0.81
0.64
0.49
0.36
0.25
0.16
0.09
0.04
0.01
Intensity I/ I$_o$ (x 10^3 cps)
TiO$_2$ 3.229
α, 2.548
α, 2.236
α, 1.732
β, 1.616
TiO$_2$/α, 1.469
β, 1.318
TiO$_2$/α, 1.249
α, 1.225
20.0
40.0
60.0
80.0
100.0
Scanning Angle (2θ)

b.

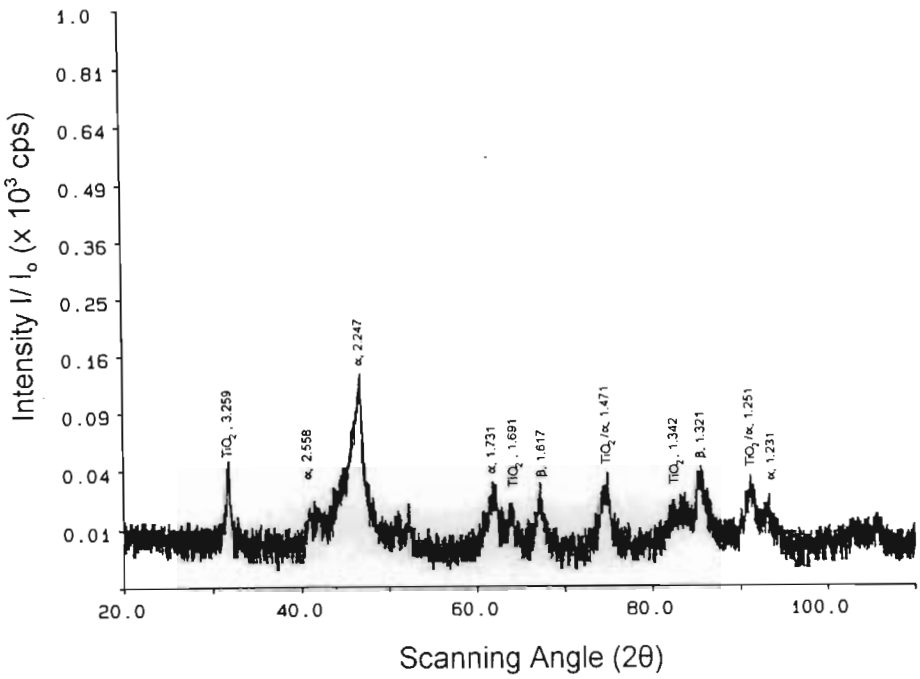

c.

Figure 3.13: X-ray diffraction analysis of the TIMETAL 21S sample exposed in argon + 20% O_2 environment at :
a. 550°C, **b.** 600°C, **c.** 650°C

For the 650°C exposure, the diffraction analysis shows the gradual increase in the oxide peak intensities and an increase in the alpha phase prominence (see figure 3.13c).

At 700°C and 750°°C the TIMETAL 21S samples appear to have run out of oxidation resistance. The x-ray diffraction analysis of the two samples, shown in figure 3.14a and b, indicates a sharp increase in the intensities of the various TiO_2 peaks through the entire analysis range. While the surface oxide and the alpha phase are both significant in the 700°C tested sample, the oxide peaks dominate the x-ray diffraction analysis for the 750°C sample, and there is only a minor contribution from the alpha and beta phases.

Figure 3.15a shows the increased oxide layer thickness experienced during the 700°C exposure test. The backscattered electron micrograph shown in figure 3.15b and c shows the alpha precipitation at the grain boundaries. Generally coarser precipitation of the alpha phase can be seen in the region closer to the exposed surface (fig 3.15b), while finer precipitation is evident towards the centre of the sample (fig. 3.15c).

Figure 3.16 shows the sample microstructure after exposure to 750°C. Noticeable is the increased oxide thickness, as well as the coarser alpha precipitates inside the alpha grains. There also appears to be a variation in the amount, shape and distribution of the precipitates from the near-exposed region towards the centre of the sample. This is also evident from the SEM micrographs presented in figure 3.17a and b. The figure also shows the EDS analysis performed at the edge and at the centre region of the sample which was performed in order to investigate which elements actively participated at the material/environment interface as well as the solute redistribution in the grains.

The EDS analysis of the surface region shows that mainly the aluminium and silicon contents are higher near the metal/environment interface region.

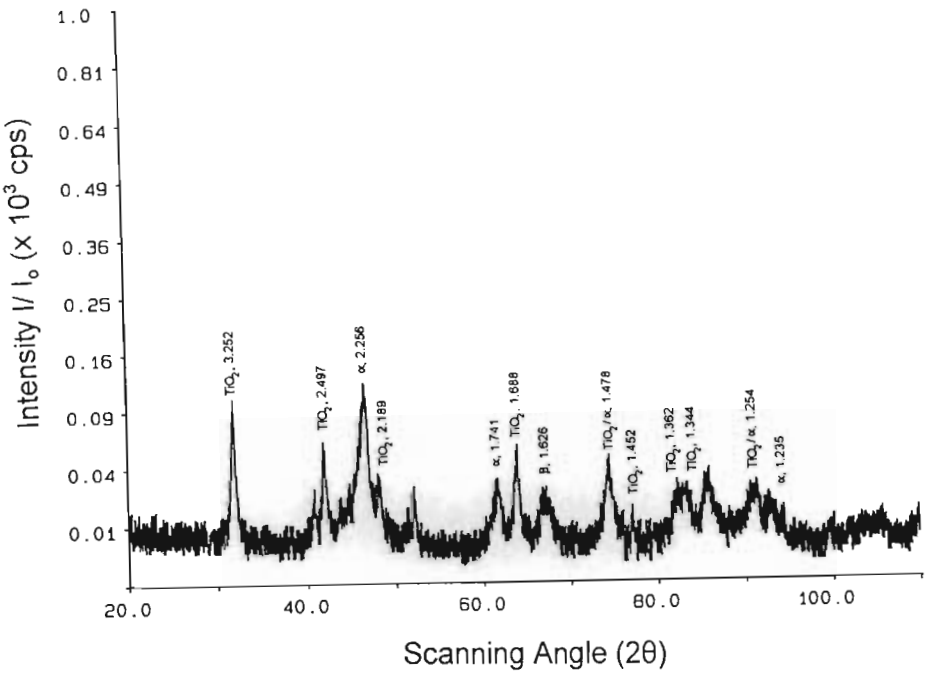

a.

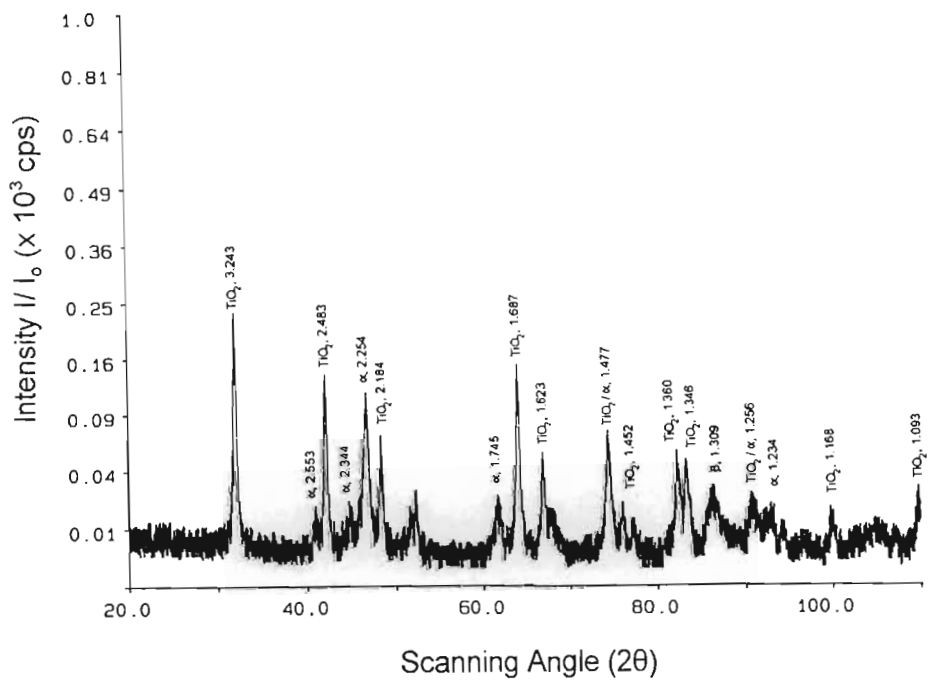

b.

Figure 3.14 : X-ray diffraction analysis of TIMETAL 21S samples tested in argon + 20%O_2 at :
a. 700°C, **b.** 750°C

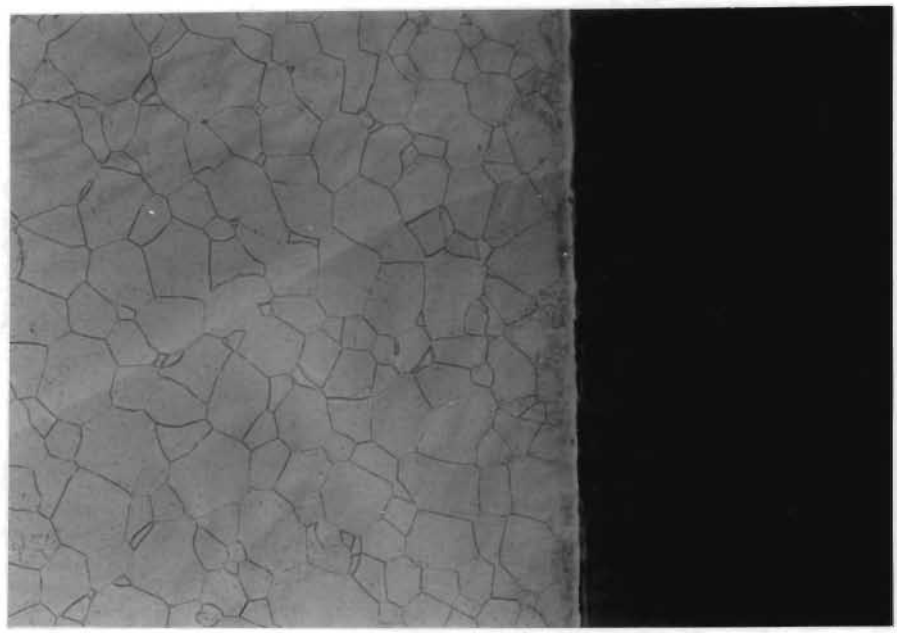

a.

b.

c.

Figure 3.15 : Microstructure and surface oxide layer of TIMETAL 21S samples exposed in argon + 20% O_2 environment at 700°C .
a. optical microscopy, x400
b. SEM near exposed surface region
c. SEM towards centre of specimen

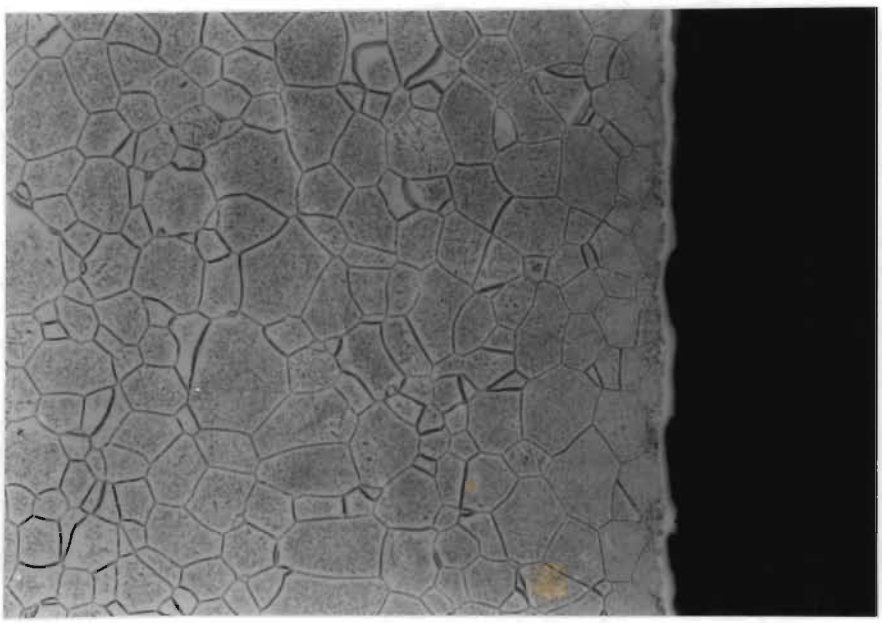

Figure 3.16 : Microstructure and oxide layer formation on TIMETAL 21S exposed to argon + 20%O_2 environment at 750°C, x400

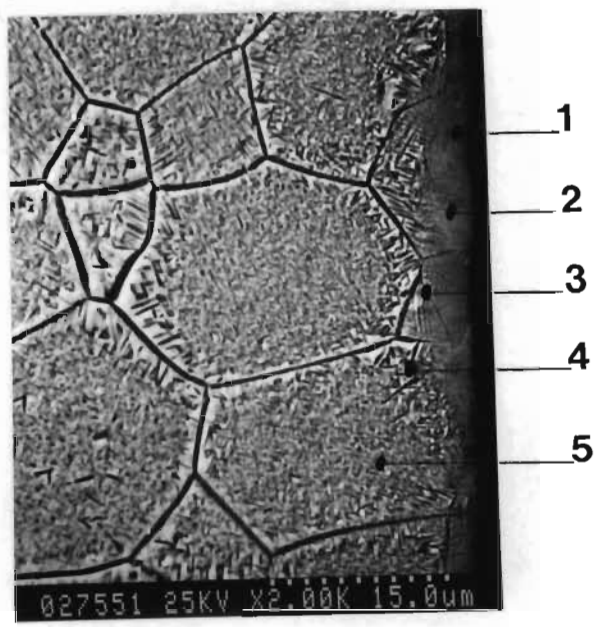

Position Element	1	2	3	4	5
Al	3.14	2.82	2.60	2.66	2.74
Si	0.73	0.26	0.25	0.25	0.34
Nb	2.63	2.73	2.38	2.18	2.44
Mo	14.08	13.28	12.40	13.07	12.66
Ti	79.43	80.92	82.36	81.83	81.82

Figure 3.17 a : Microstructure and EDS analysis of the near-surface region of the TIMETAL 21S sample tested at 750°C in argon + 20% O_2 environment

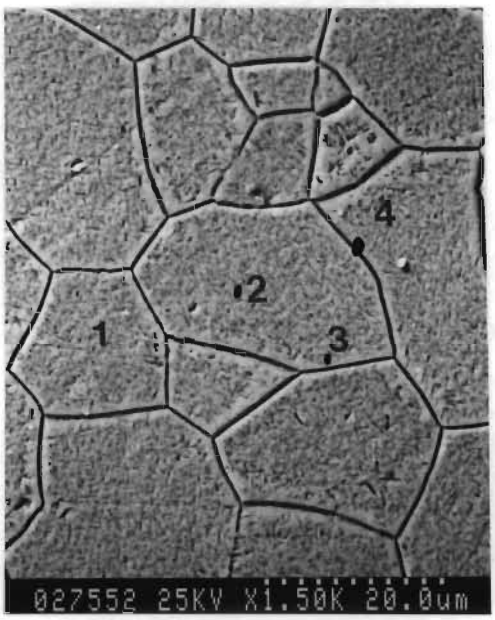

Position Element	Overall Area 1	Grain Interior 2	Grain Edge 3	Grain Bndry 4
Al	2.50	2.53	2.65	2.69
Si	0.38	0.20	0.38	0.26
Nb	1.99	1.79	2.64	2.98
Mo	13.18	13.39	13.18	13.21
Ti	81.96	82.08	81.15	80.86

Figure 3.17 b. : Microstructure and EDS analysis of the interior region of the TIMETAL 21S sample tested at 750°C in argon + 20% O_2 environment.

Exposed Surfaces

The exposed surfaces of the samples tested at elevated temperatures in the oxidizing atmosphere were investigated using SEM. The results, as shown in figure 3.18, showed that fine surface "particles" had evolved during the exposures. An increase in these particles occurrence was particularly noticeable at higher temperatures.

Oxide Thickness

The oxide layer thickness was optically measured. The layer was assumed to constitute only the white surface layer (e.g. as shown in figure 3.11, 3.15 and 3.17). Figure 3.19 shows the oxide thickness obtained after exposure to the various temperatures and oxidizing environments.

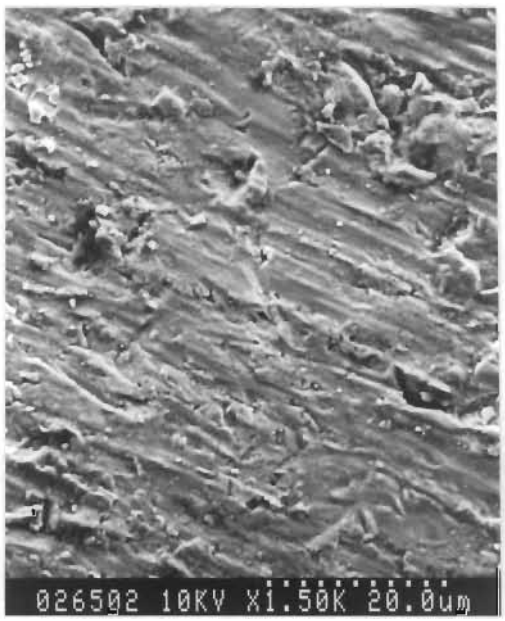

a.

b.

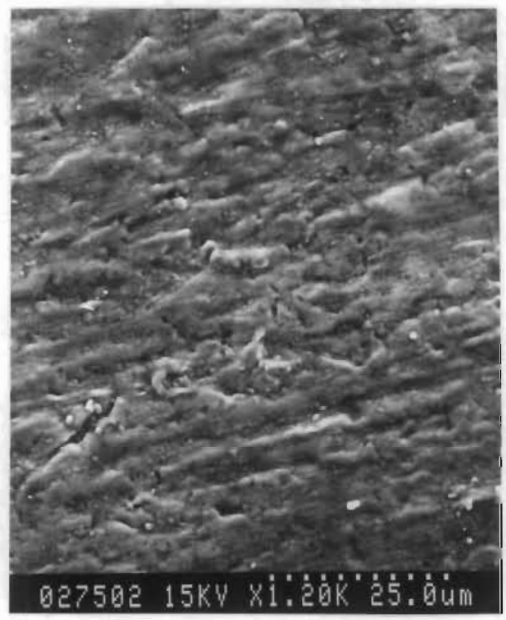

c.

Figure 3.18 : Exposed surface of TIMETAL 21S samples tested in argon + 20% O_2 environment at
a. 650°C, **b.** 700°C, **c.** 750°C

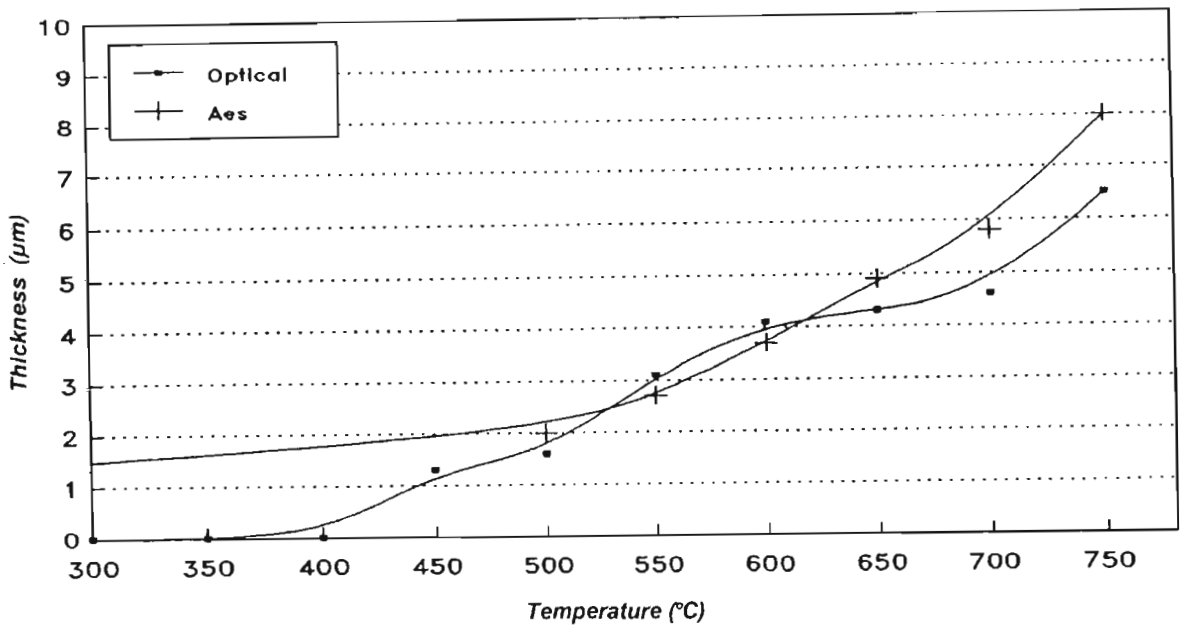

Figure 3.19 : Comparison of the visually observed and AES oxide effective thickness after 5 hour exposure in argon + 20% O_2 environment

AES line scans

AES line scan were performed transversely on the samples tested in the argon + 20%O_2 environment to determine the profile and extent of oxygen penetration. The analyses were performed from the exposed surface to a depth of approximately 100 μm. Figure 3.20 shows the AES results obtained for a 5 hour exposure to temperatures of 400°C, 500°C, 550°C, 600°C, 650°C, and 750°C.

An effective oxide penetration thickness was also determined by measuring the thickness at approximately 80% of the peak-to-average oxygen content as given by the AES line scans. The results are also shown in figure 3.19.

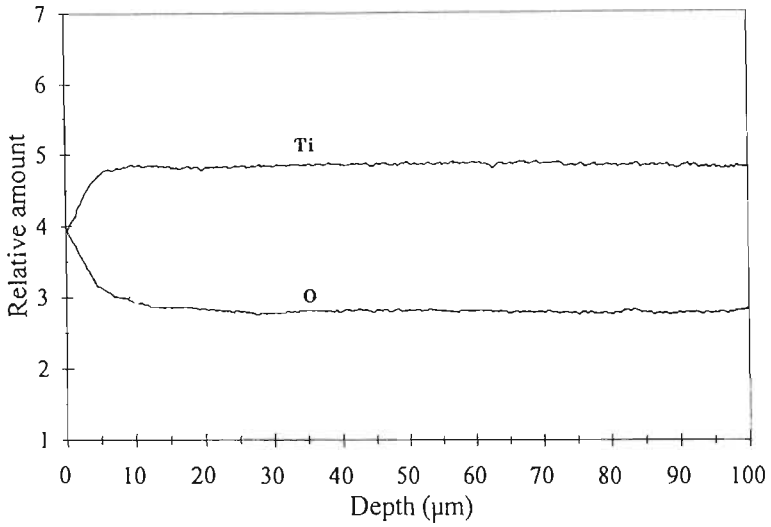
Relative amount
Ti
O
Depth (μm)
1
2
3
4
5
6
7
0
10
20
30
40
50
60
70
80
90
100

a.

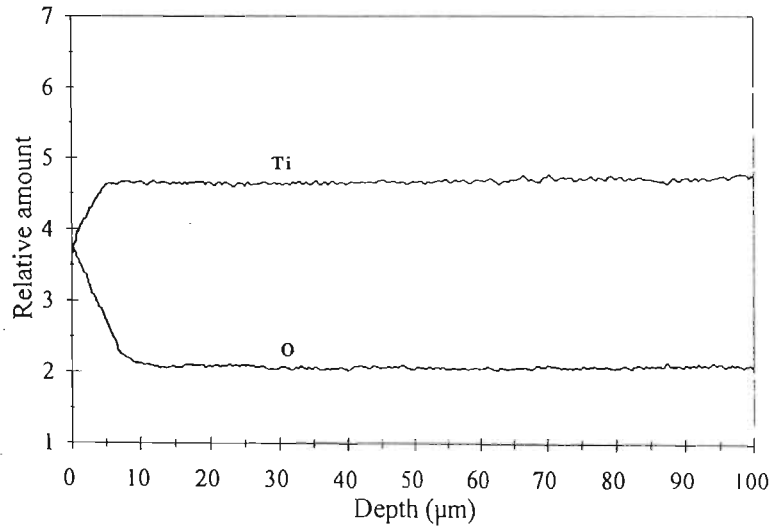
Relative amount
Ti
O
Depth (μm)
1
2
3
4
5
6
7
0
10
20
30
40
50
60
70
80
90
100

b.

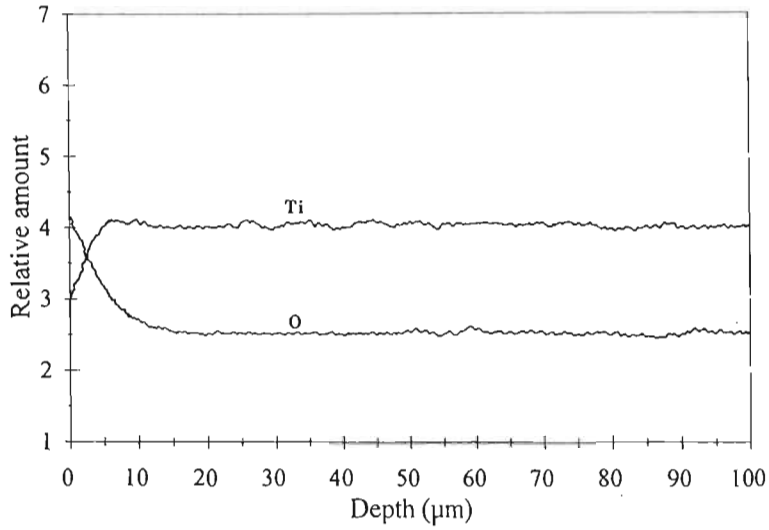

c.

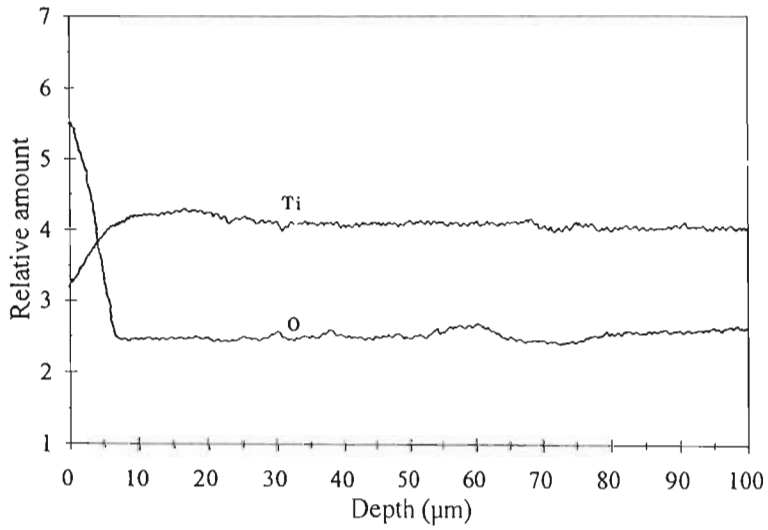

d.

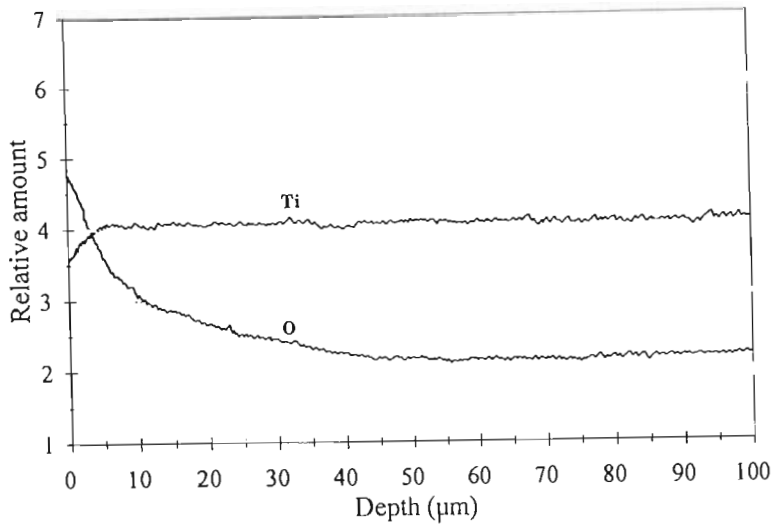

e.

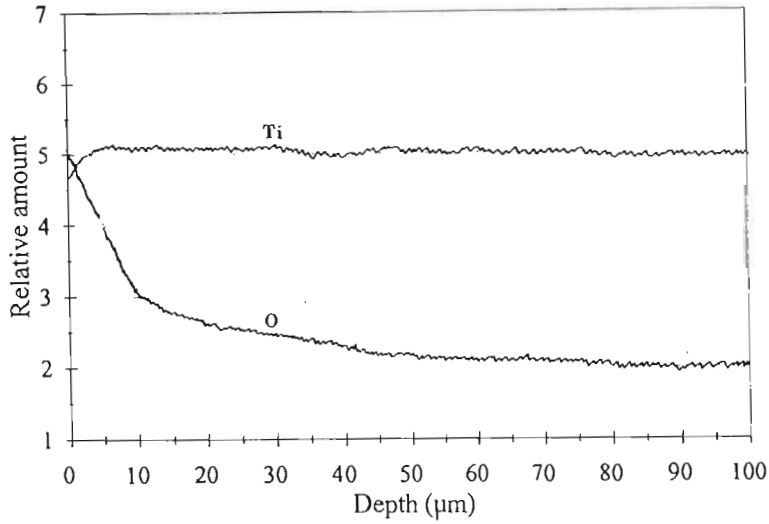

f.

Figure 3.20 : AES line profiles of samples exposed in argon + 20%O_2 environment at :
a. 400°C, **b.** 500°C, **c.** 550°C, **d.** 600°C, **e.** 650°C, **f.** 750°C

Hardness Tests

A comparison of the hardness tests performed on the samples tested in the oxidizing and inert environment is presented in the summary of results, section 3.4.2, figure 3.59.

3.2.2 Argon environment

The corrosion tests in the inert argon environment were conducted in order to compare the resultant microstructures to those exposed to the oxidizing atmosphere, and to evaluate the contribution of the alpha phase precipitation due to only the high temperature exposure.

The emergence of the alpha phase in the beta matrix with the increase in exposure temperature in the argon environment is summarized in the x-ray diffraction analyses shown in figure 3.21.

The transforming microstructures of the samples tested in an inert environment show a similar trend to those tested in the argon + 20% O_2 environment, however a more homogeneous distribution of a coarser precipitates was evident. Typical evolving microstructures (as presented in figure 3.22), in which the internal alpha phase precipitation as well as the near grain boundary precipitation-free regions are found, are evident up to temperatures of 600°C. At higher temperatures the structure is more homogenized with a general distribution of coarser alpha precipitation (figure 3.22e and f).

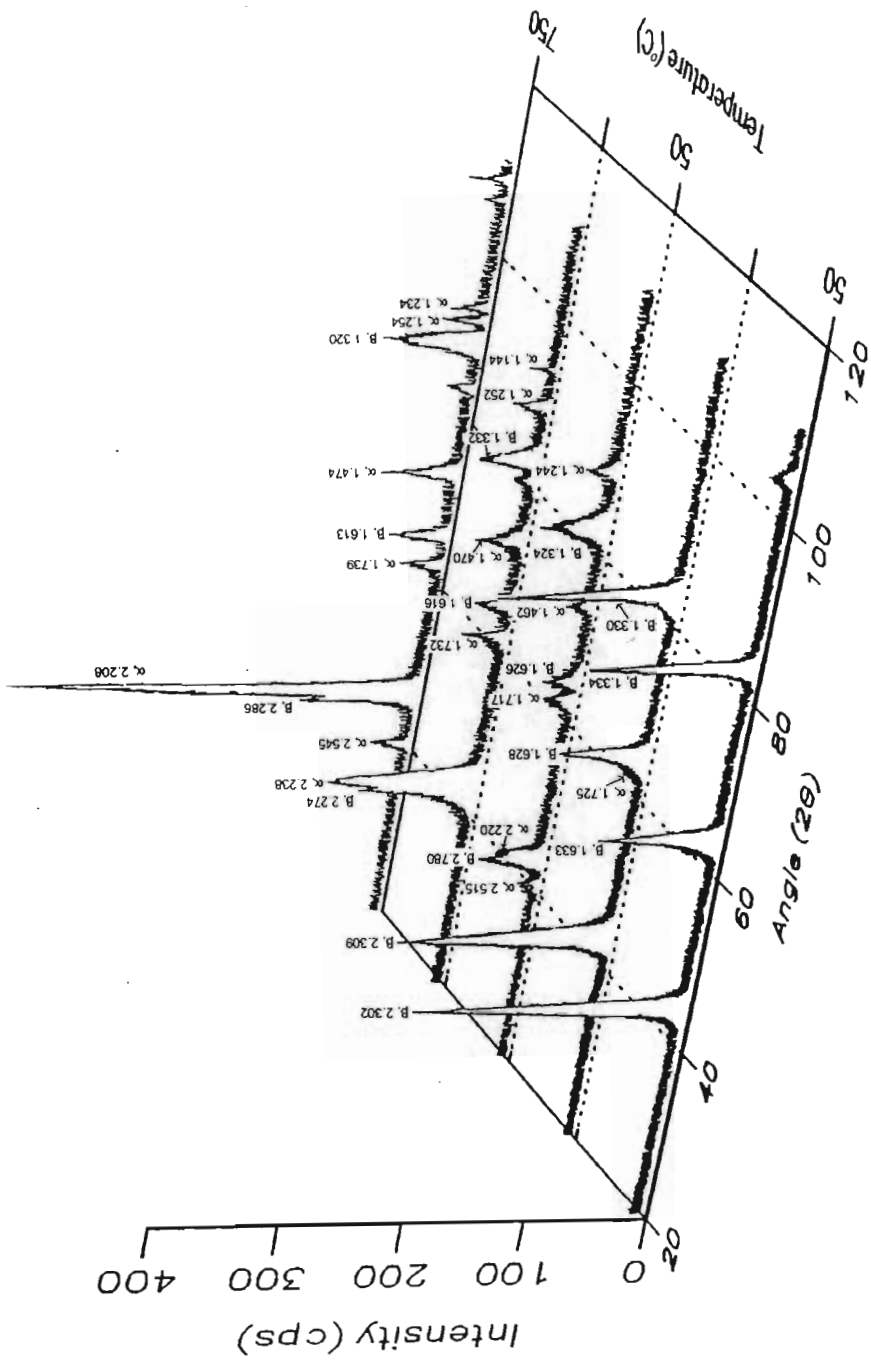

Figure 3.21 : X-ray diffraction analyses of TIMETAL 21S samples tested in an argon environment at various temperatures

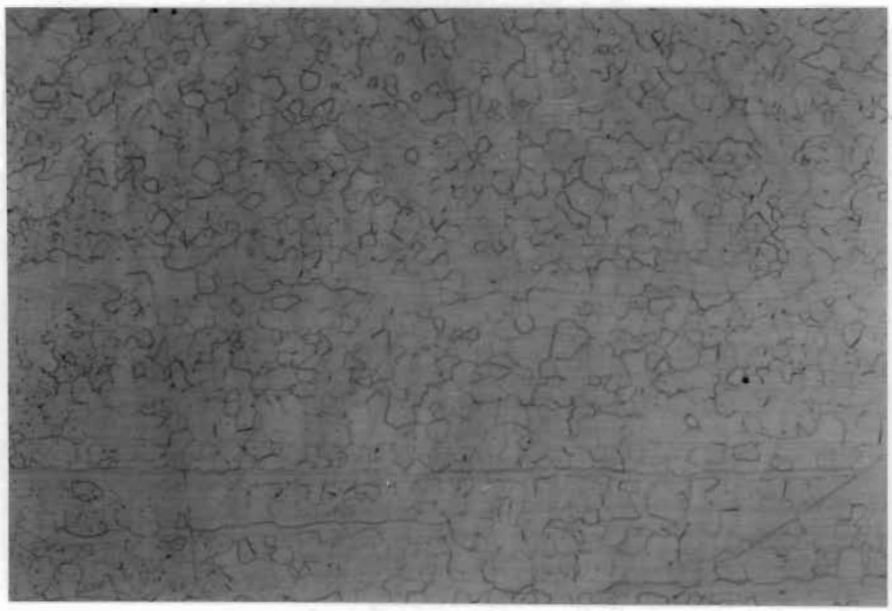

a.

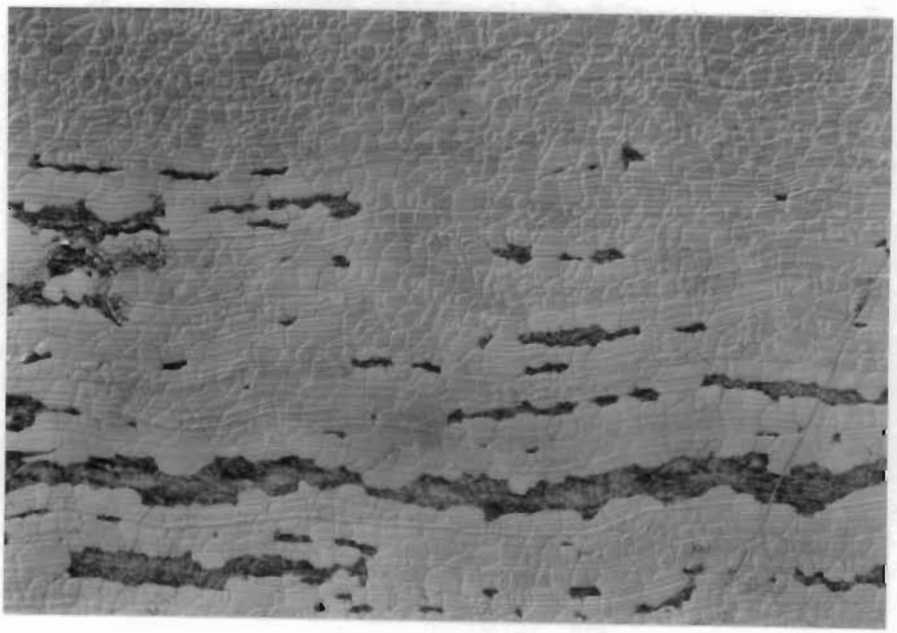

b.

c.

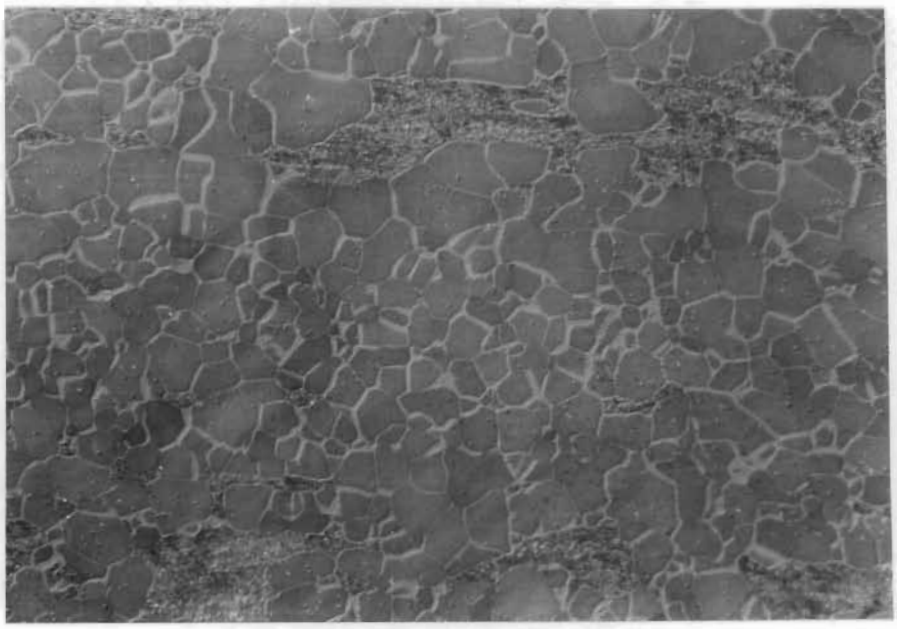

d.

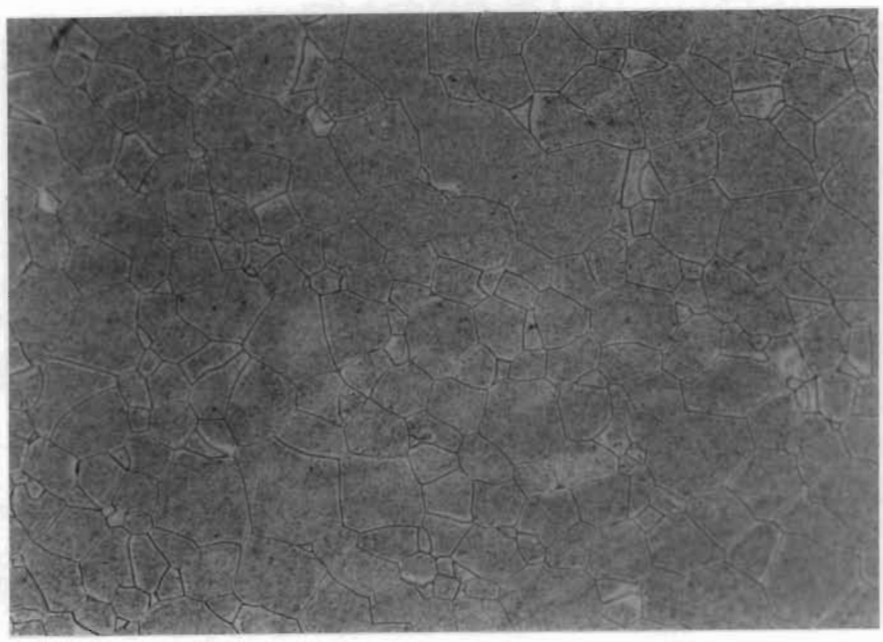

e.

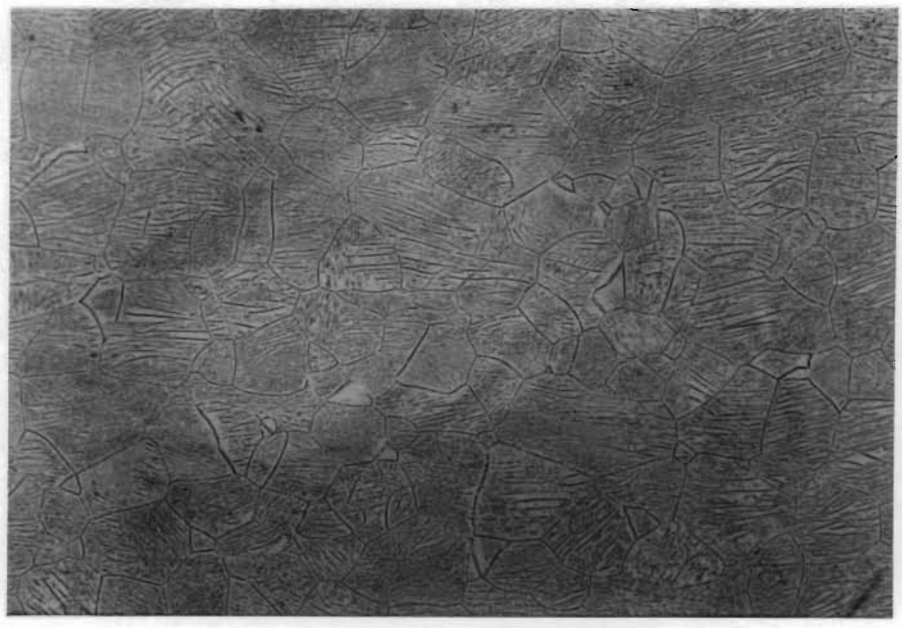

f.

Figure 3.22 : Typical microstructures of TIMETAL 21S obtained after exposure in argon environment at :
a. 300°C, x100 **b.** 400°C (DIC), x100 **c.** 450°C, x200 **d.** 600°C (DIC), x200 **e.** 700°C, x400 **f.** 750°C, x400

3.3 Effect of an oxidizing environment on the fatigue crack growth rate at various temperatures

The curve of dimensionless crack length (a/W) vs number of cycles was the starting point in order to determine the fatigue crack growth rates at the various temperature and in the different environments. The initial data obtained from the tests were first examined for obvious errors, and the "corrected" data were used to determine the relevant fatigue crack growth rate (FCGR) values.

Figure 3.23 shows a typical curve of dimensionless crack length vs number cycles obtained during fatigue crack growth tests conducted at the various temperatures and in different environments.

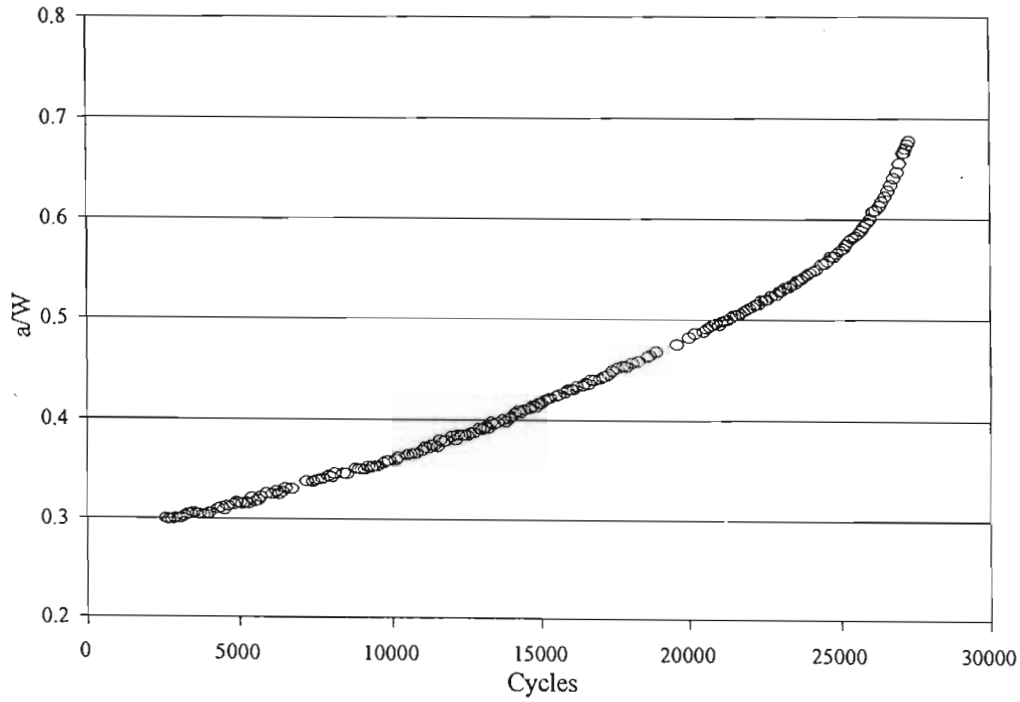

Figure 3.23 : Typical data of a/W vs number of cycles obtained during FCGR tests at elevated temperature on TIMETAL 21S

A typical load vs displacement curve is also shown in figure 3.24. Evident from this curve is the deviation from linearity at lower loads, indicating that a closure mechanism was operative. It would also appear that the curve deviates in the opposite direction to that presented in section 2.3.2.1, figure 2.14a, i.e. an apparent hysteresis exist with

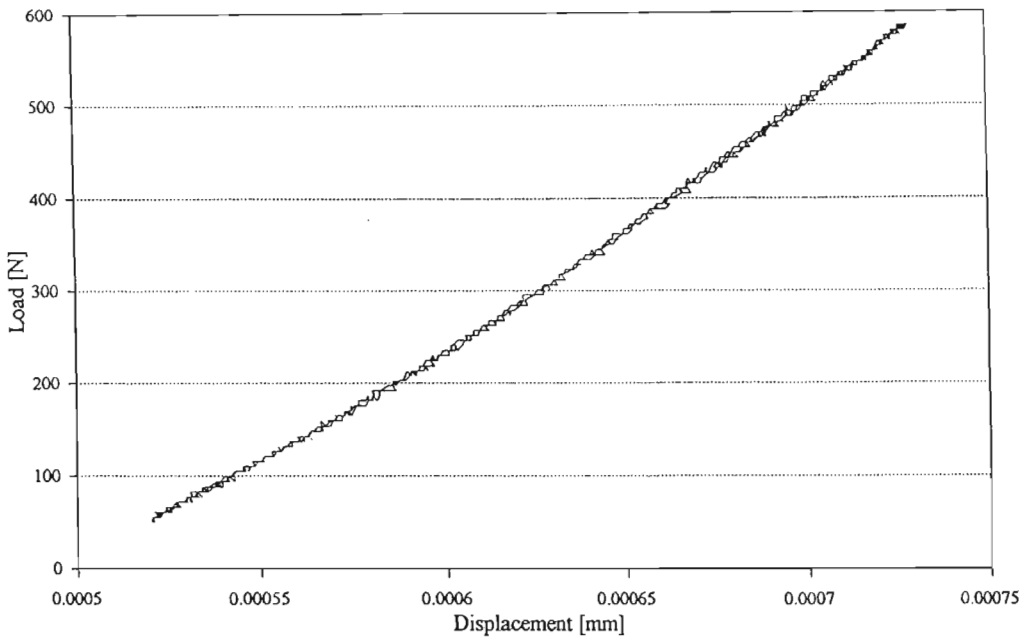

Figure 3.24 : Typical load vs displacement curve obtained during FCGR testing at elevated temperature

respect to load rather than the displacement. This type of behaviour though is an artifact of the load-line displacement monitoring method. The procedure for calculating the closure/opening loads however remained unaffected though. The load vs offset displacement data is shown in figure 3.25 and the two curves shown (one obtained for the closure data and the other for the opening data), demonstrate the effectiveness of the offset method in identifying the distinct values of P_{op} and P_{cl}. Due to the relatively restricted resolution obtained from the displacement monitoring system, the opening and closure loads values were identified visually rather than by statistical methods. A clear indication of the deviation from linearity can however be observed, as seen from figure 3.25.

NOTE: In all the fractographic micrographs, the crack propagation direction proceeds left to right, unless otherwise indicated.

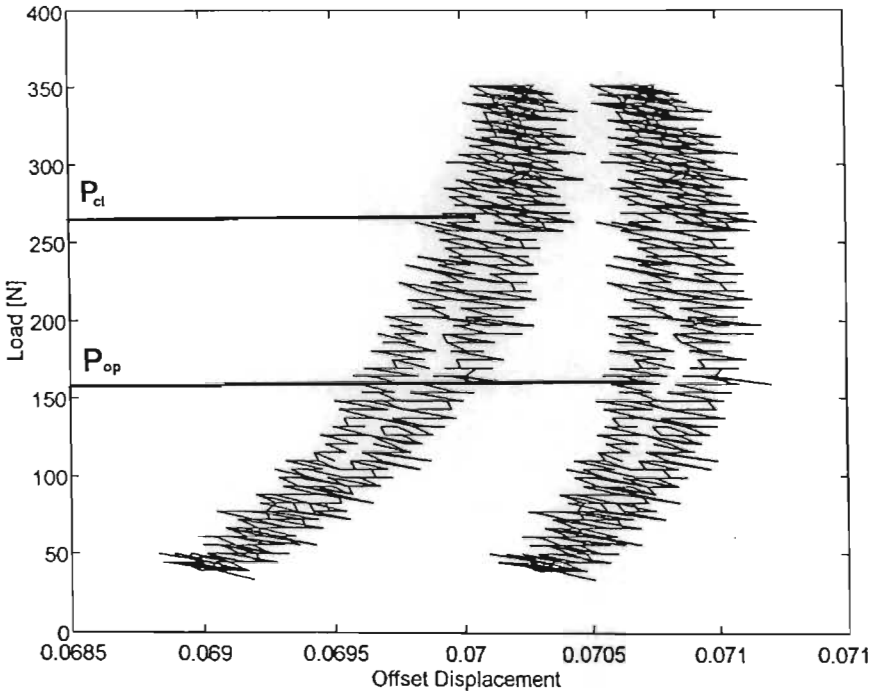

Figure 3.25 : Example of load vs offset displacement graph obtained for opening and closure data at elevated temperature in various environments

3.3.1 Characterization at 375°C

3.3.1.1 Fractography

Argon environment

The fracture surface at different ΔK on the TIMETAL 21S sample tested in the argon environment at 375°C is shown in figure 3.26a and b. The tilting type of transgranular crack propagation (fig. 3.26a) was found to sustain throughout the entire crack growth. Increased plastic deformation is evident in the latter part of the crack propagation (fig. 3.26b). In addition to the fracture surface deformation, **surface cracking** perpendicular to the crack propagation direction appears to have occurred in selected areas between striations. This is shown in figure 3.26a and figure 3.26c. A type of surface ripping effect is also apparent from figure 3.26d.

A gradual increase in surface roughness with increasing stress intensity was also evident, as shown in figure 3.27. This increase in roughness at higher ΔK was evident in most samples.

A longitudinal metallographic sample of the failed C(T) specimen was prepared to observe the extent (if any) of secondary cracking. In the inert environment significant cracking was not observed.

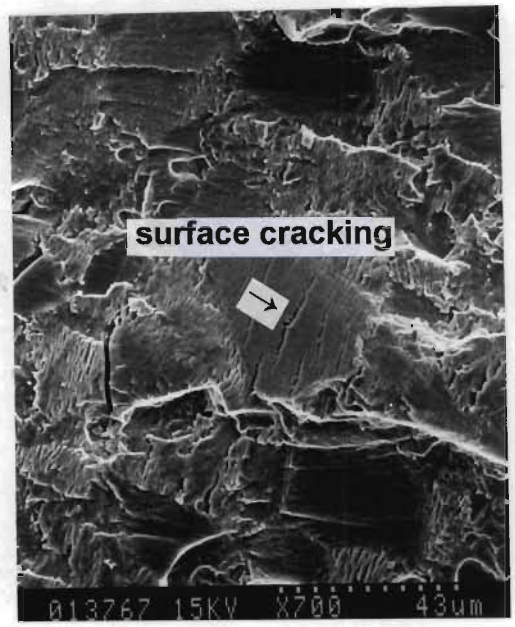

a.

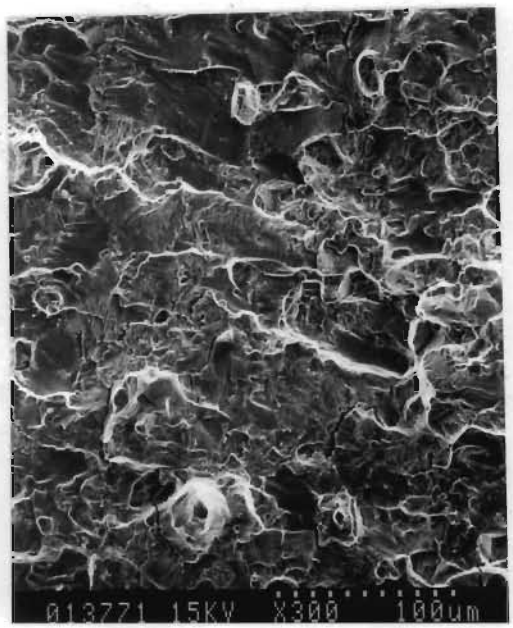

b.

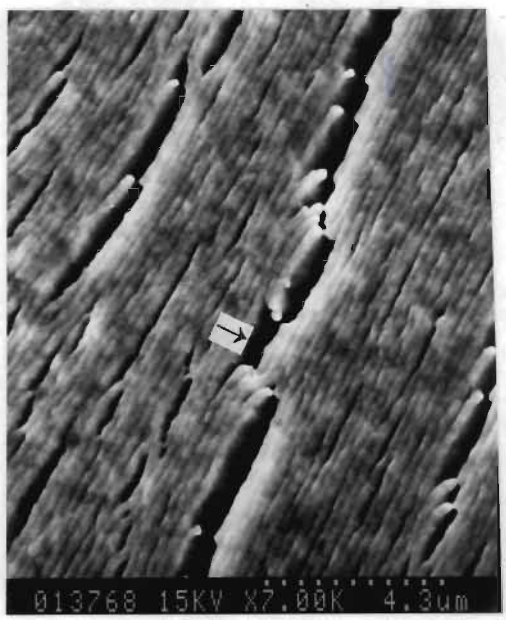

c.

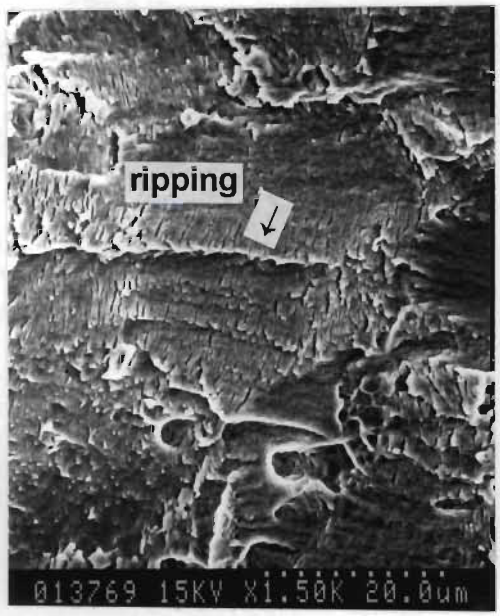

d.

Figure 3.26 : Fracture surface of TIMETAL 21S tested at 375°C in an argon environment
a. $\Delta K \approx 15$ MPa.$\sqrt{m}$ **b.** $\Delta K \approx 45$ MPa.$\sqrt{m}$
c. cracking at striation interface ($\Delta K \approx 15$ MPa.$\sqrt{m}$)
d. surface ripping effect ($\Delta K \approx 15$ MPa.$\sqrt{m}$)

a.

b.

c.

Figure 3.27 : Increase in surface roughness of TIMETAL 21S tested at 375°C in an argon environment
a. $\Delta K \approx 15$ MPa.$\sqrt{m}$ **b.** $\Delta K \approx 22$ MPa.$\sqrt{m}$
c. $\Delta K \approx 40$ MPa.$\sqrt{m}$

Argon + 20% O_2 environment

Fractography of the fracture surface of the sample tested at 375°C indicates that a similar type of crack propagation mechanism was operative in the argon + 20% O_2 environment. Regions of transgranular crack propagation was complemented by areas containing surface and secondary cracking (cracking perpendicular to the crack propagation direction) as well as general surface deformation, as shown in figure 3.28a and b. The surface ripping effect is also visible (see figure 3.28c) and appears only to be evident in selected areas.

The longitudinal metallographic sample showed that minor intergranular secondary cracking had occurred. This is shown in figure 3.29.

3.3.1.2 FCGR at 375°C

The comparison of the FCGR between the specimens tested in the argon and the argon + 20% O_2 environment is shown in figure 3.30. Similar crack growth rates were observed in the different environments.

3.3.1.3 Crack Opening/Closure Data

Argon Environment

A comparison of the opening loads, P_{op}, and closure loads, P_{cl}, as a percentage of the maximum load, P_{max}, vs ΔK values in the argon environment is shown in figure 3.31. P_{op} and P_{cl} appear to be independent of ΔK.

Argon + 20% O_2 Environment

The behaviour of the sample in the argon + 20% O_2 environment however differed from that in the argon environment. Although the P_{op} and P_{cl} were initially at similar loads to that found in the argon environment, the values tended to decrease with increasing ΔK. This is illustrated in figure 3.32.

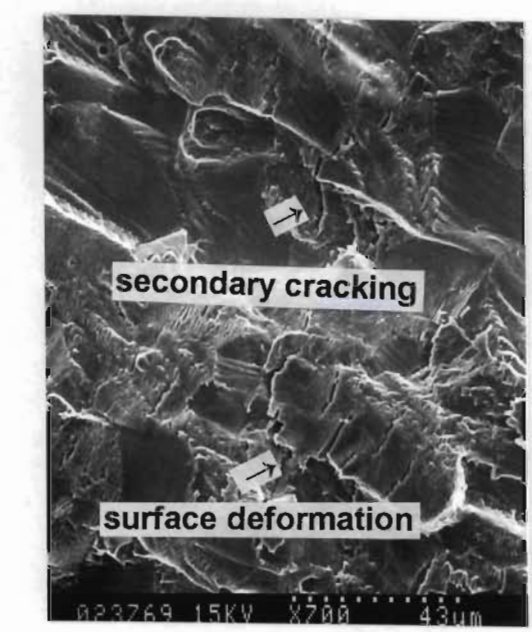

a.

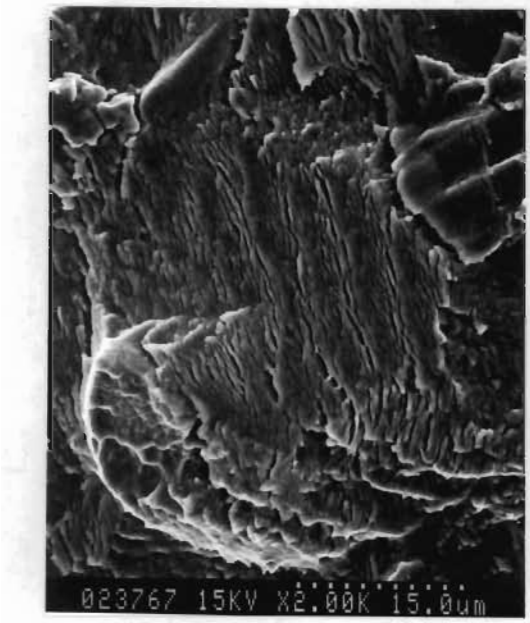

b.

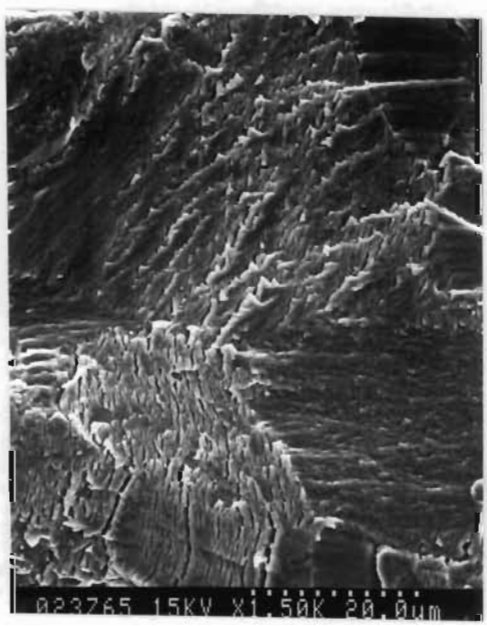

c.

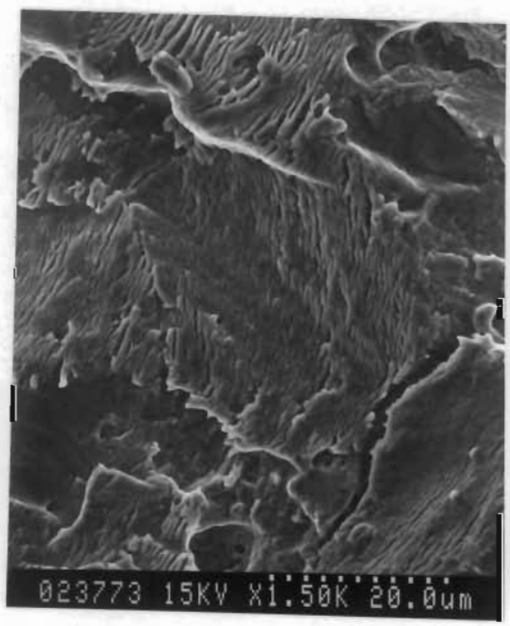

d.

Figure 3.28 : Fracture surface of TIMETAL 21S tested in argon + 20% O_2 environment at 375°C
a.,b.,c. $\Delta K \approx 15$ MPa.$\sqrt{m}$ **d.** $\Delta K \approx 26$ MPa.$\sqrt{m}$

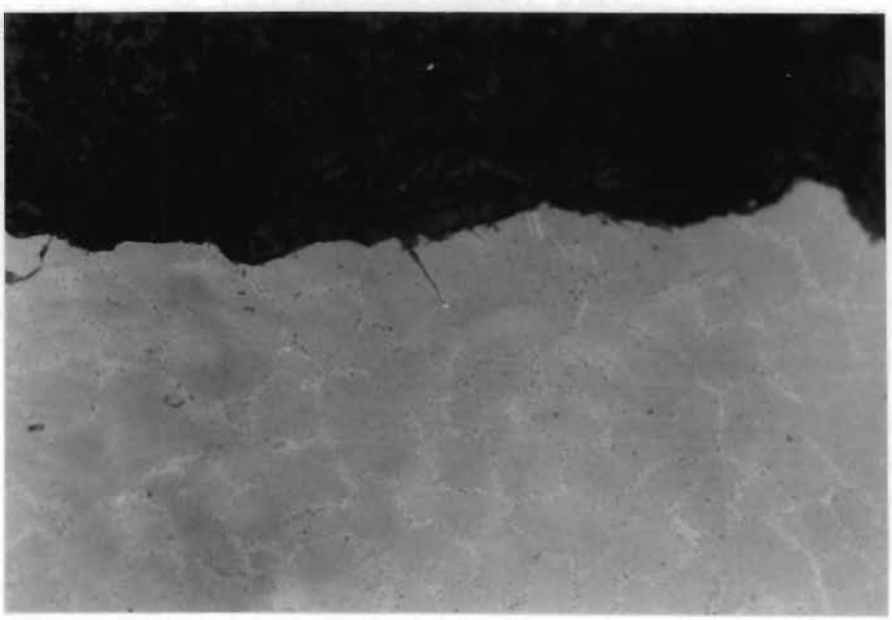

Figure 3.29 : Longitudinal metallographic sample showing secondary cracking as experienced in the argon + 20% O_2 environment at 375°C

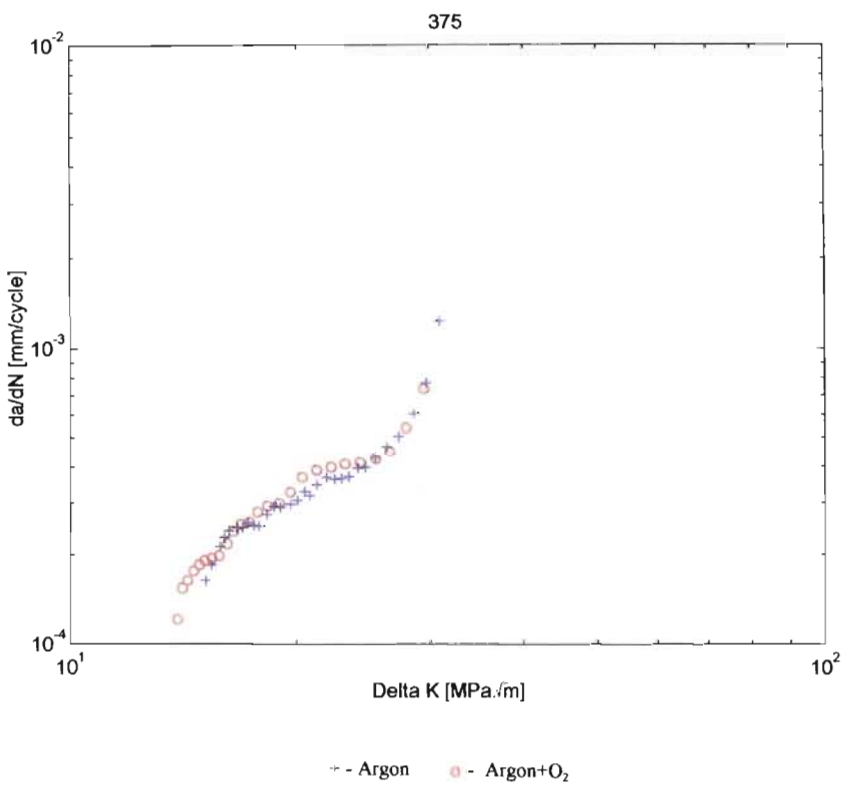

Figure 3.30 : Comparison of FCGR of TIMETAL 21S at 375°C in an inert and an oxidizing environments

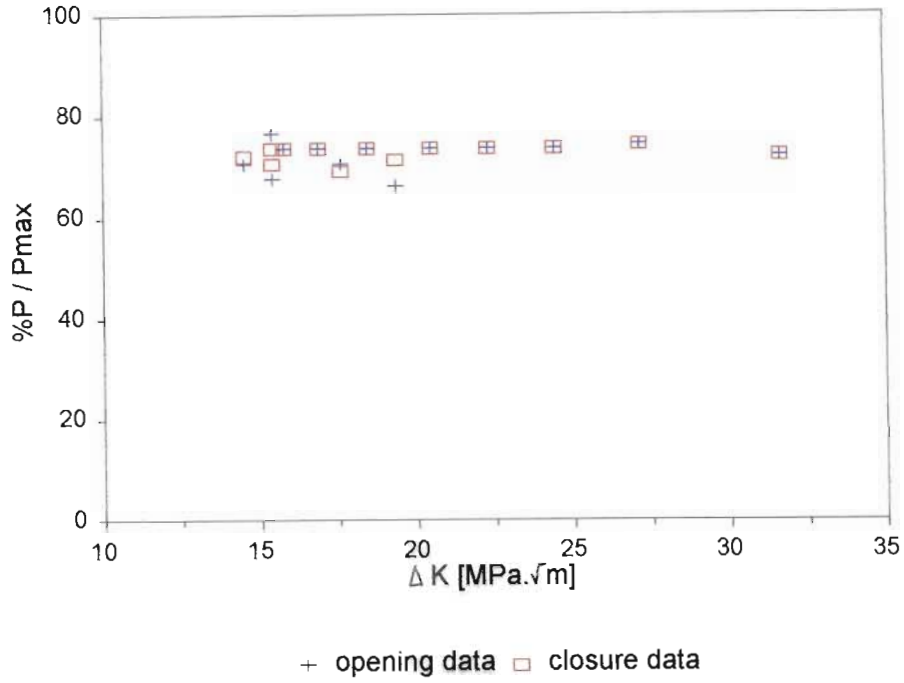

Figure 3.31 : Comparison of opening and closure loads vs ΔK in TIMETAL 21S tested at 375°C in an argon environment

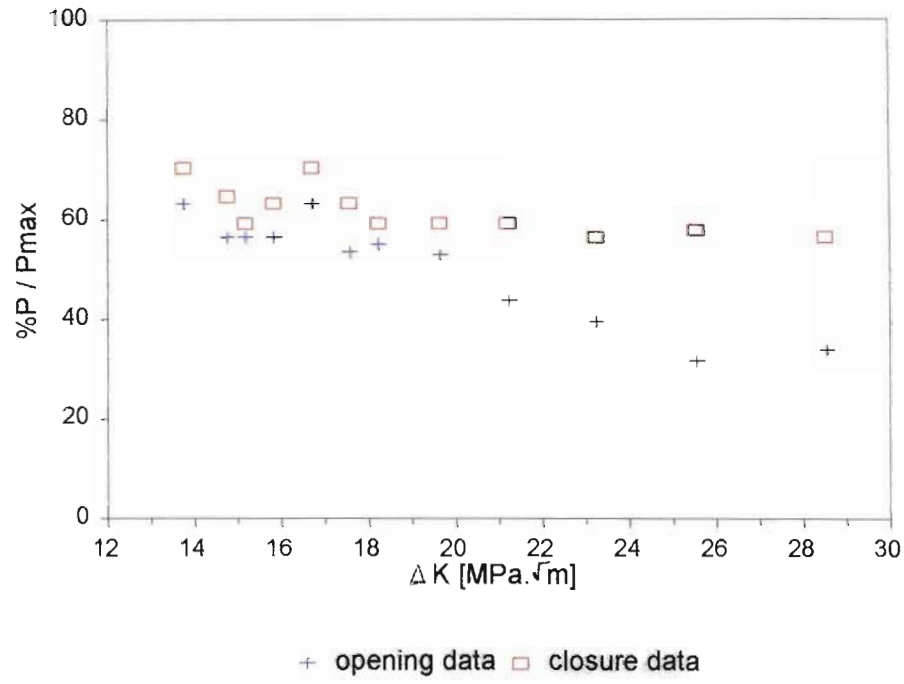

Figure 3.32 : Comparison of opening and closure loads vs ΔK for TIMETAL 21S tested at 375°C in an argon + 20% O_2 environment

3.3.2 Characterization at 450°C

3.3.2.1 Fractography

Argon environment

The transgranular type of crack propagation was also found in the TIMETAL 21S sample tested in the argon environment at 450°C, however, in addition to the tilted type crack growth, twisting now also occurred at the grain boundaries, as shown in figure 3.33. The secondary cracking and surface cracking increased at higher ΔK values (compare figures 3.33b, d, e and f). In figure 3.33e, in addition to the fatigue striations, the extensive surface deformation, increased secondary cracking and surface cracking can be observed.

The longitudinal metallographic sample showed that isolated intergranular secondary cracking had occurred in the inert environment, as shown in figure 3.34.

Argon + 20% O_2 environment

While the transcrystalline fatigue crack progression is still prominent in the specimen tested at 450°C, further surface damage, in terms of the ripping effect and surface deformation is evident, as shown in figure 3.35a and b. With increase in crack length, the ripping effect has been significantly reduced (see figure 3.35c and d) but secondary cracking and surface cracking was prevalent.

The metallographic sample of the C(T) sample showed that some branching of the secondary cracking was experienced in the argon + 20% O_2 environment as shown in figure 3.36.


twisting
014561 15KV X700 43um

a.

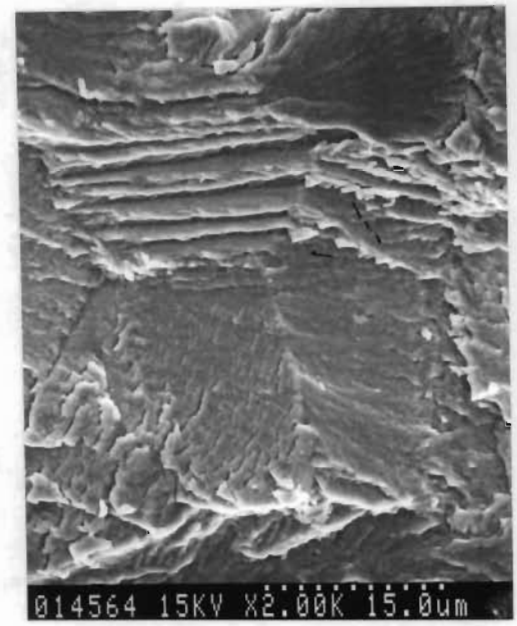
014564 15KV X2.00K 15.0um

b.


014568 15KV X1.00K 30um

c.

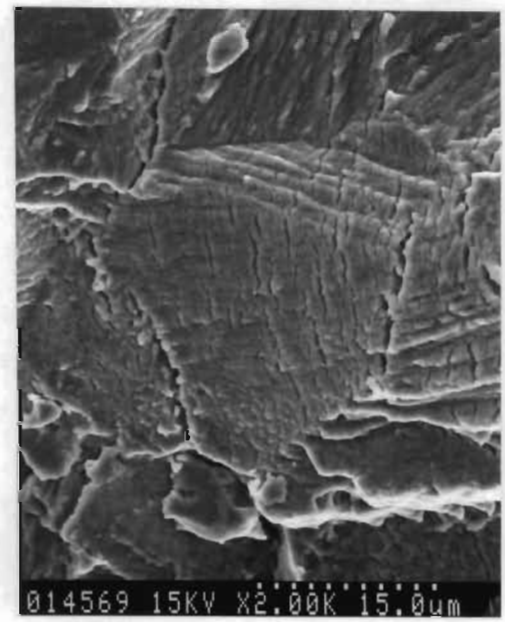
014569 15KV X2.00K 15.0um

d.

P.T.O.

e.

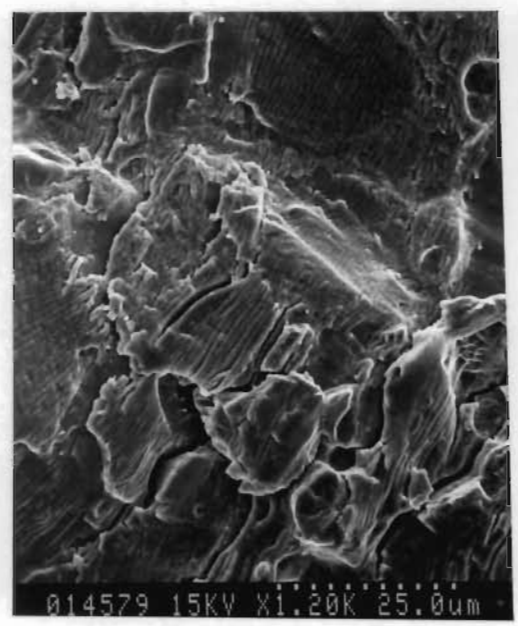

f.

Figure 3.33 : Fracture surface of TIMETAL 21S tested at 450°C in argon environment
a,b. $\Delta K \approx 13$ MPa.$\sqrt{m}$, **c,d.** $\Delta K \approx 17$ MPa.$\sqrt{m}$,
e. $\Delta K \approx 20$ MPa.$\sqrt{m}$, **f.** $\Delta K \approx 32$ MPa.$\sqrt{m}$

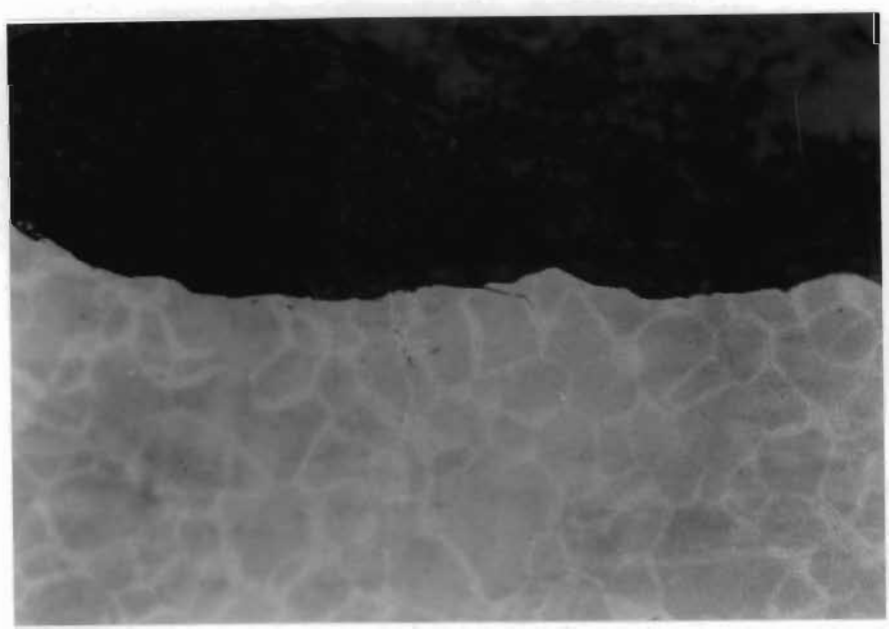

Figure 3.34 : Secondary cracking experienced in the argon environment at 450°C, x400

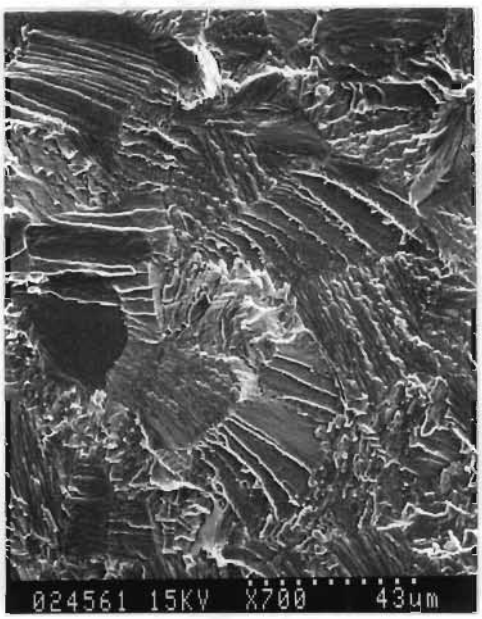

a.

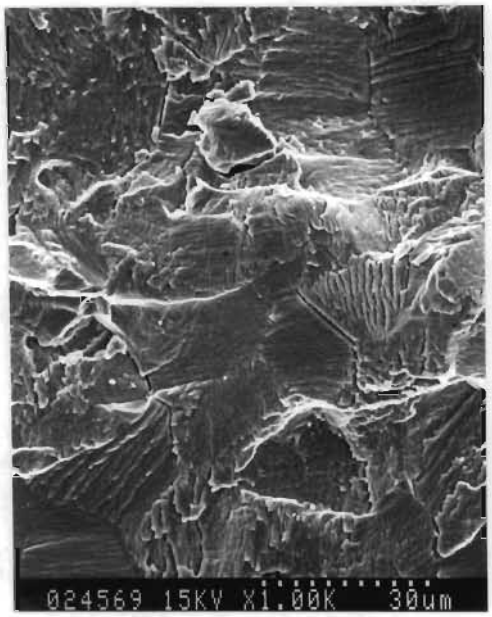

b.

c.

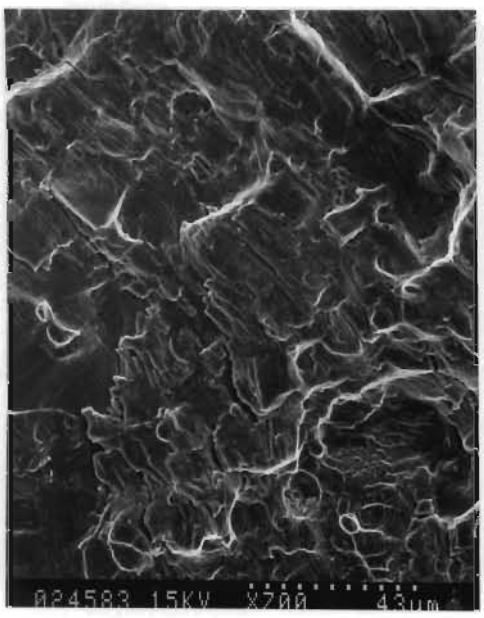

d.

Figure 3.35 : Fracture surface of TIMETAL 21S tested in argon + 20% O_2 environment at 450°C
a. $\Delta K \approx 13$ MPa.$\sqrt{m}$, **b.** $\Delta K \approx 17$ MPa.$\sqrt{m}$,
c. $\Delta K \approx 22$ MPa.$\sqrt{m}$, **d.** $\Delta K \approx 32$ MPa.$\sqrt{m}$

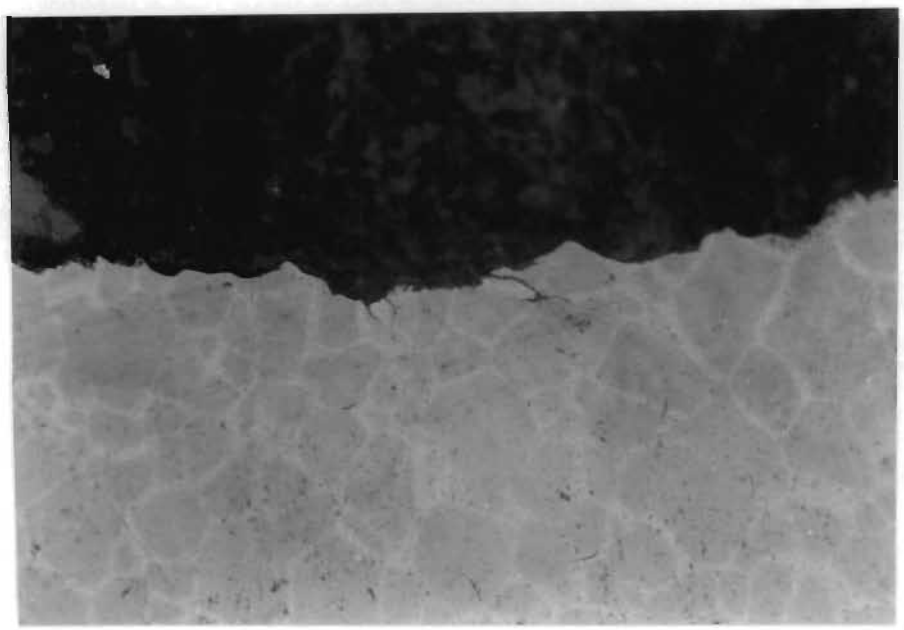

a.

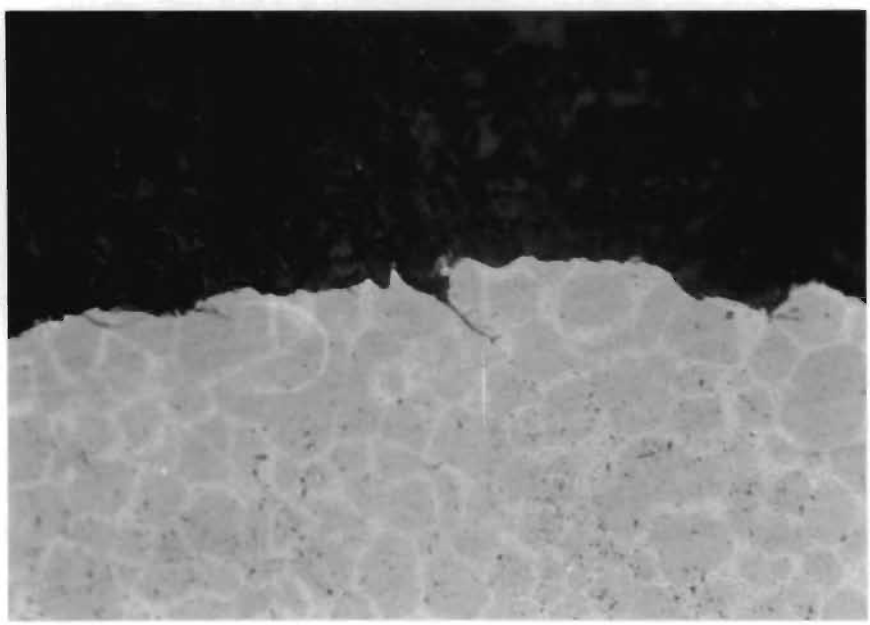

b.

Figure 3.36 : Branched secondary cracking experienced in the argon + 20% O_2 environment at 450°C, x400

3.3.2.2 FCGR at 450°C

The da/dN vs ΔK curve (figure 3.37) shows that the environmental influence has significantly affected the crack growth rate. The crack growth rate in the oxidizing environment has been retarded compared to that found in the inert environment.

In the latter stages of crack growth (i.e. stage III) the environmental effect had apparently been reduced and the growth rates were found to be similar.

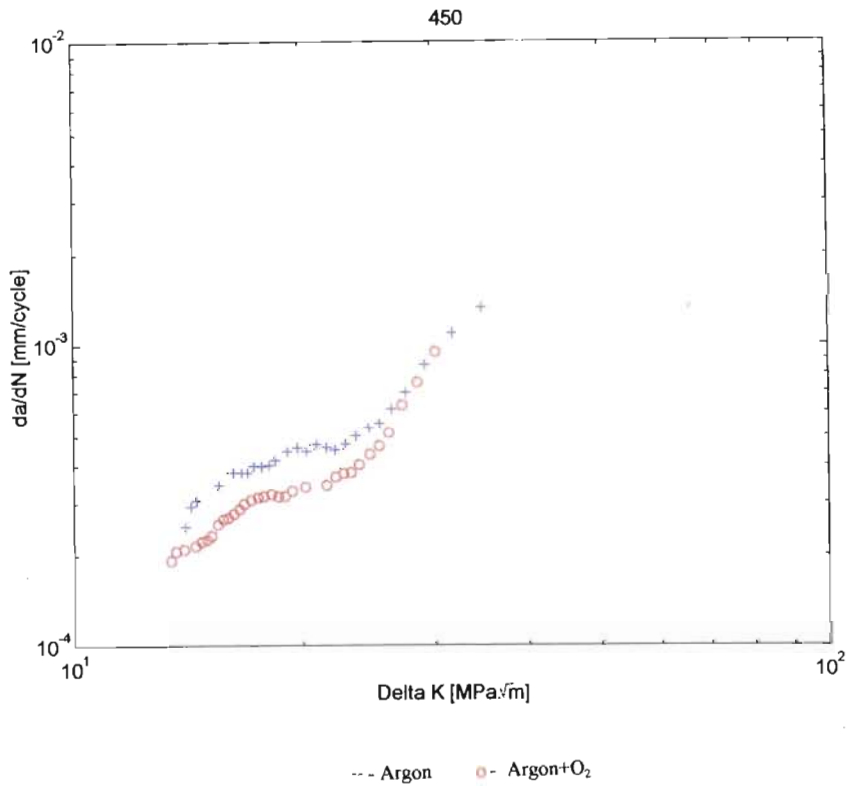

Figure 3.37 : FCGR in TIMETAL 21S in inert and oxidizing environment at 450°C

3.3.2.3 Crack Opening/Closure Data

Figures 3.38a and b show the variation of P_{op} and P_{cl} with ΔK in the different environments. In general the closure loads were higher than the opening loads and although the opening and closure loads remained fairly constant in the argon environment, the sample tested in argon + 20% O_2 environment showed a near constant P_{cl} after an initial increase, while the opening load in the oxidizing environment tended to decrease with increasing ΔK.

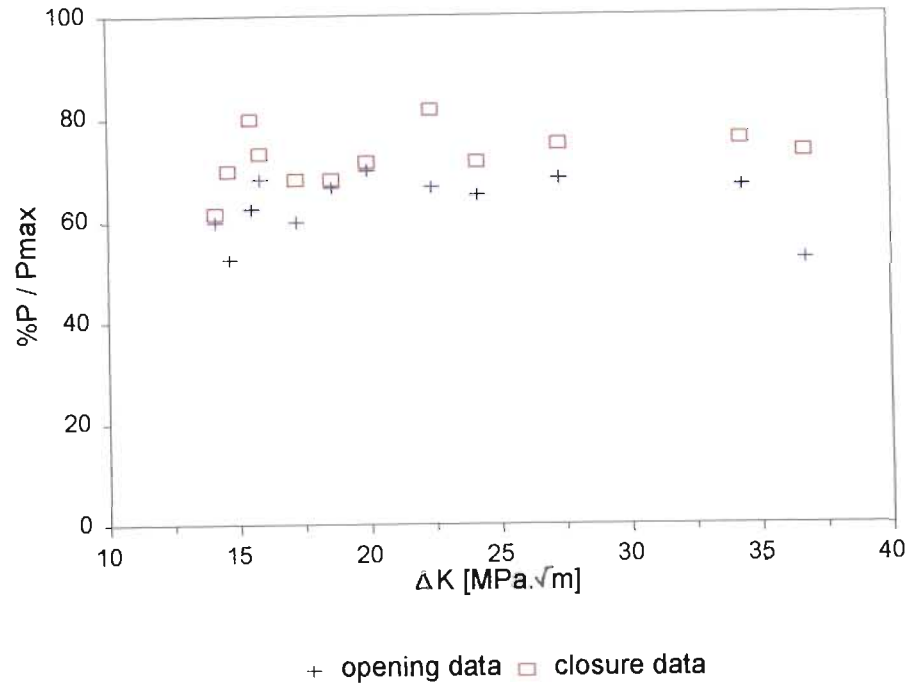

a.

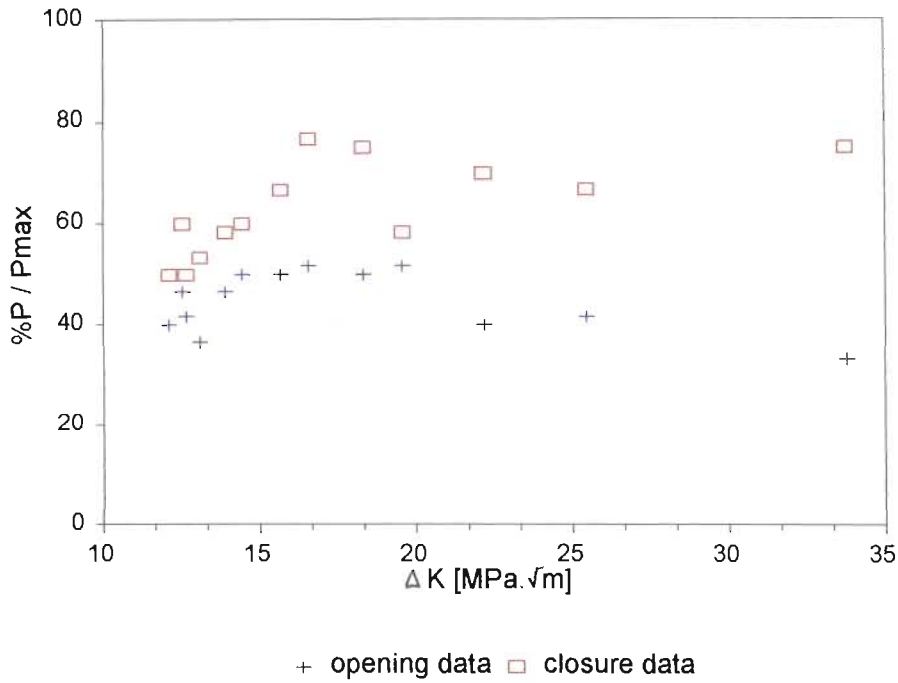

b.

Figure 3.38 : Trends in P_{op} and P_{cl} with increasing ΔK of the sample tested at 450°C in the :
a. inert environment
b. oxidizing environment

3.3.3 Characterization at 550°C

3.3.3.1 Fractography

Argon environment

The fractography performed on the samples tested in the inert environment at 550°C showed that the crack progressed in a transcrystalline mode. At low ΔK the fracture surface was devoid of the severe surface deformation as previously found at lower temperatures and in different environments. Cleavage-type lines are the most prominent feature of the fracture surface at this stage as shown in figure 3.39a and b.

At higher ΔK values, areas of local of surface fracturing becomes more evident, while more surface damage and deformation is visible. Fatigue striations are also visible at this stage (see figure 3.39c and d).

Further advancement of the crack lead to increasing fracture surface deformation, and in addition to the transgranular type failure and local areas of fracture on the surface, minor surface cracking, as well as cracking at the grain boundaries has also appeared, as shown in figure 3.40.

a.

b.

c.

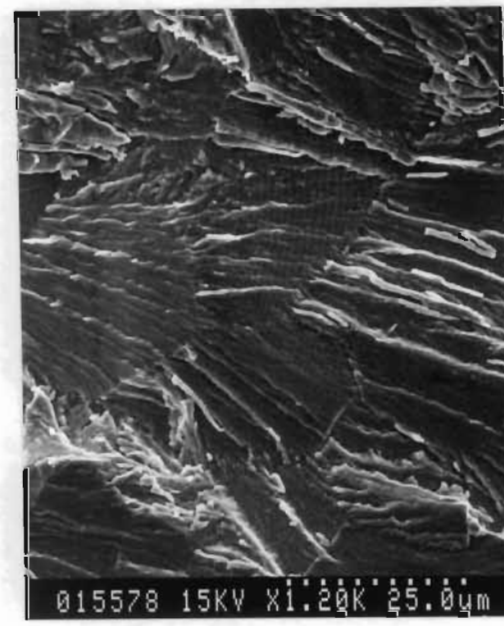

d.

Figure 3.39 : Fracture surface of TIMETAL 21S in argon environment at 550°C showing transgranular crack propagation, areas of local fracture, characteristic fatigue striations and secondary cracking
a., **b.** $\Delta K \approx 8$ MPa.$\sqrt{m}$ **c.**, **d.** $\Delta K \approx 12$ MPa.$\sqrt{m}$

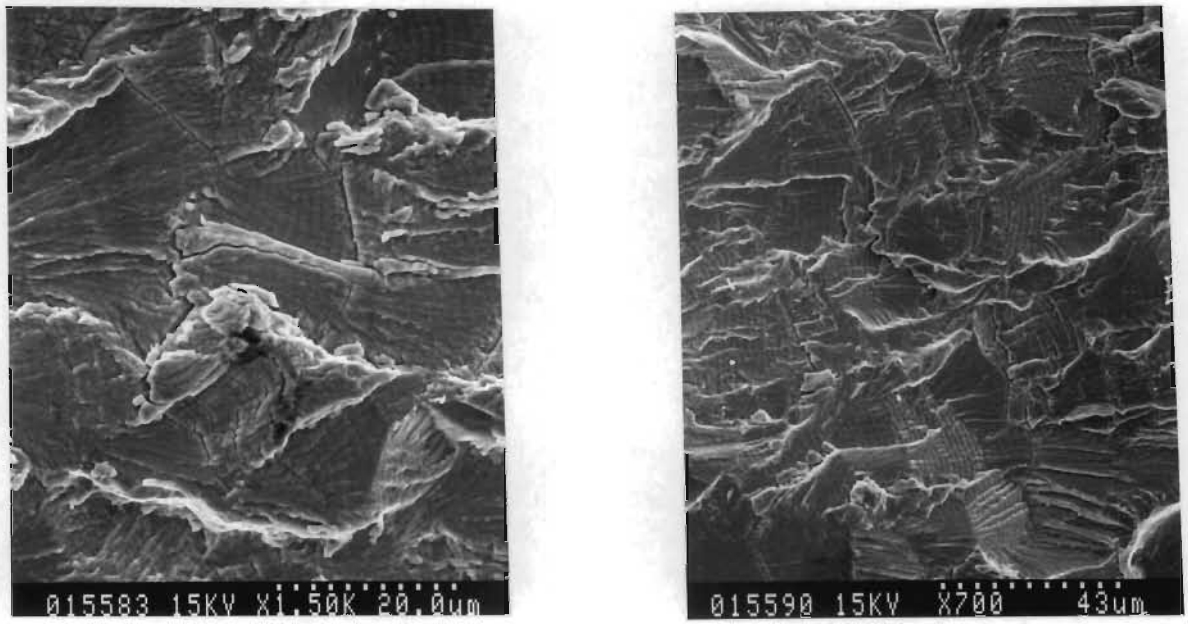

a. b.

Figure 3.40 : Fracture surface in argon environment at 550°C showing surface cracking
a. $\Delta K \approx 14$ MPa.$\sqrt{m}$, **b.** $\Delta K \approx 16$ MPa.$\sqrt{m}$

Figure 3.41 also shows that some secondary cracking has also occurred during the latter part of the crack propagation, however, examination of the longitudinal metallographic sample failed to reveal the significant secondary cracking penetrating into the material.

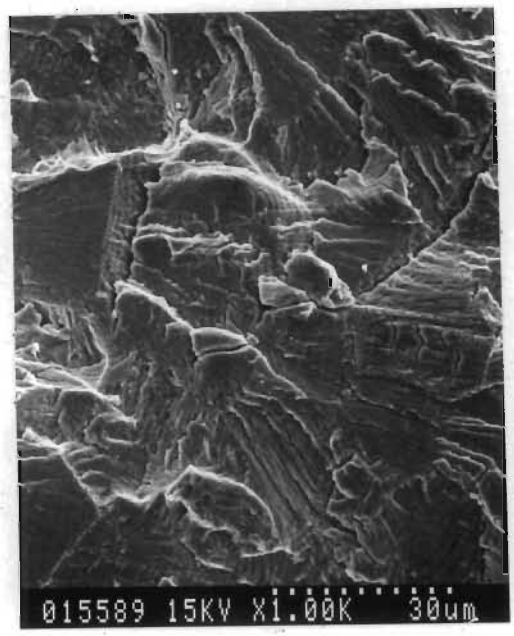

Figure 3.41 : Fracture surface in argon environment at 550°C showing general fracture mode and onset of secondary cracking ($\Delta K \approx 20$ MPa.$\sqrt{m}$)

Argon + 20% O_2 environment

While the principal transcrystalline mechanism of crack propagation was still evident in the specimens tested at 550°C, a distinct environmental influence on the fracture surface appearances was noticeable. Moreover, the fracture surface appearance in the various environments at similar ΔK values were distinctly different. Figure 3.42a shows the fracture surface at low ΔK values. With the dulled surface appearance, fine particles distributed over the fracture surface can be observed as in figure 3.42b. While coarser particles appeared to be distributed in discrete areas on the fracture surface, a close up view shows the general distribution of the fine particles on the surface as shown in figure 3.42c and d.

At higher ΔK values, the amounts of coarse particles decrease, but there is still an even distribution of fine surface particles (see figure 3.43a and b). Secondary cracking and surface cracking also appear with further increases in ΔK (figure 3.43c and d). At these ΔK values a "collapse" or fracture of some surface features can also be seen. Figure 3.43 b and d show these phenomena.

In the latter part of the crack growth, the brittle nature of the surface is demonstrated by the fracturing of the surface features as shown in figure 3.44a and b. The characteristic fatigue striations are also evident at this stage of crack growth. Figure 3.44c, showing the general fracture surface appearance, also shows the extent of secondary cracking experienced at this stage of the fatigue crack growth. In addition, there is a fair distribution of fracture surface fragments over the area, as indicated by the arrows in figure 3.44c. A close up of the surface cracking effect is shown in figure 3.44d.

The longitudinal metallographic examination of the sample revealed some branched secondary cracking and corrosion product which has filled these cracks (see figure 3.45).

a.

b.

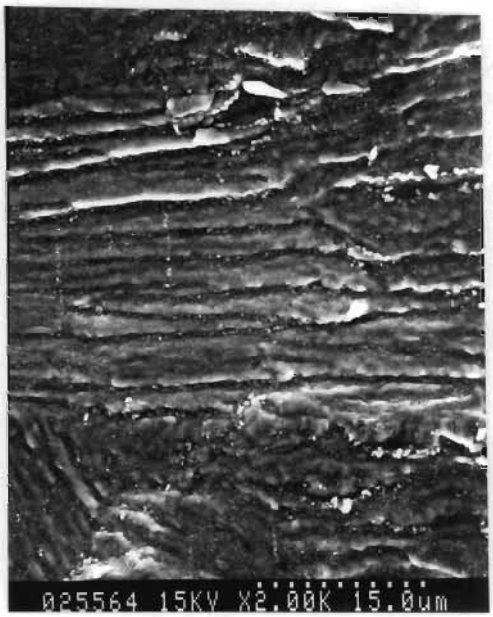

c.

d.

Figure 3.42 : Fracture surface of TIMETAL 21S in argon + 20% O_2 environment at 550°C ($\Delta K \approx 12$ MPa.$\sqrt{m}$)
a. General fracture surface appearance
b. Distribution of particles on the fracture surface
c,d. Close up of fine particles on the fracture surface

a.

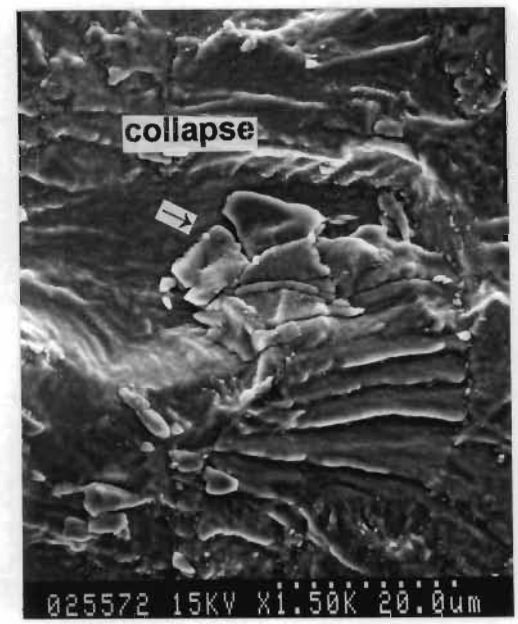

b.

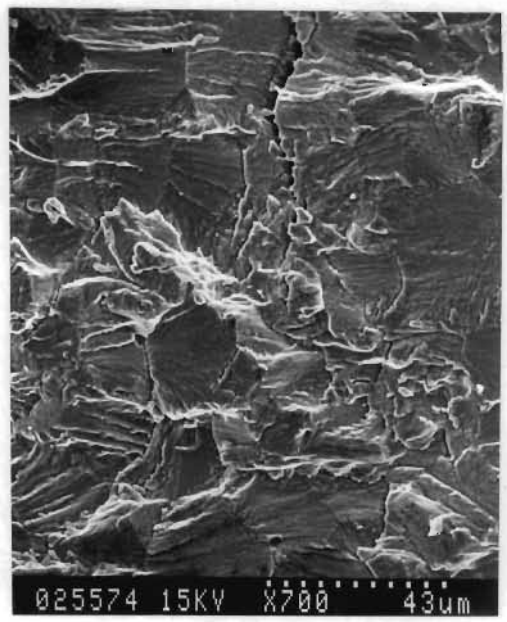

c.

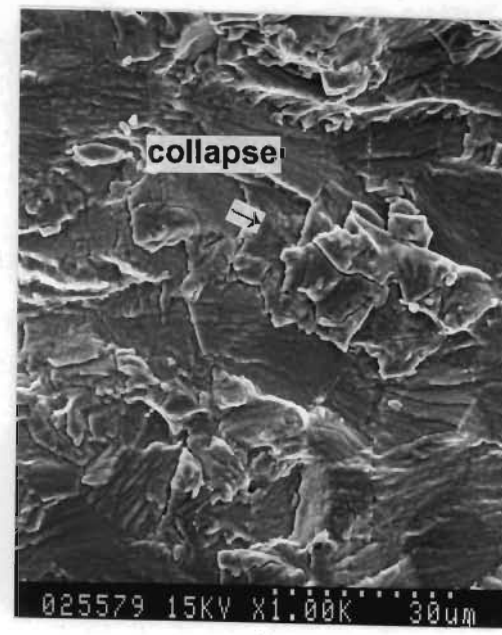

d.

Figure 3.43 : Fracture surface of TIMETAL 21S in argon + 20% O_2 environment at 550°C

a. Decrease in coarse particle distribution

b. Distribution of fine particles and collapse of surface features (**a.,b.**: $\Delta K \approx 12$ MPa.$\sqrt{m}$)

c. Onset of secondary and surface cracking

d. Showing collapse of surface features (**c.,d.**: $\Delta K \approx 16$ MPa.$\sqrt{m}$)

a.

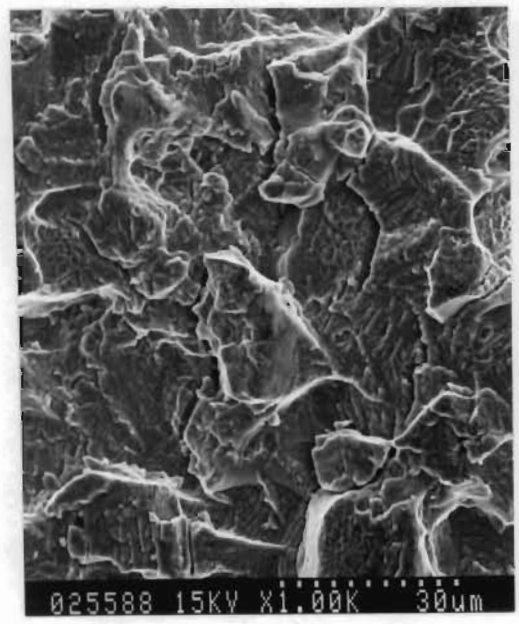

b.

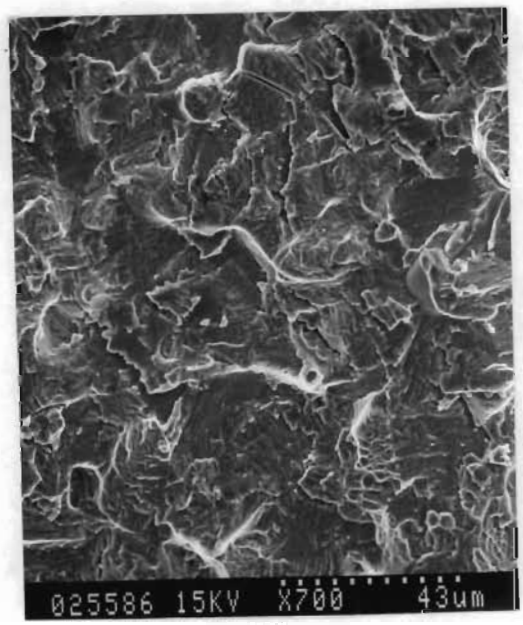

c.

d.

Figure 3.44 : Fracture surface of TIMETAL 21S in argon + 20% O_2 environment at 550°C showing :
a,b. brittle cracking of surface ($\Delta K \approx 20$ and 27 MPa.$\sqrt{m}$ respectively)
c. Fragments on the fracture surface
d. Surface cracking (**c.,d.** $\Delta K \approx 27$ MPa.$\sqrt{m}$)

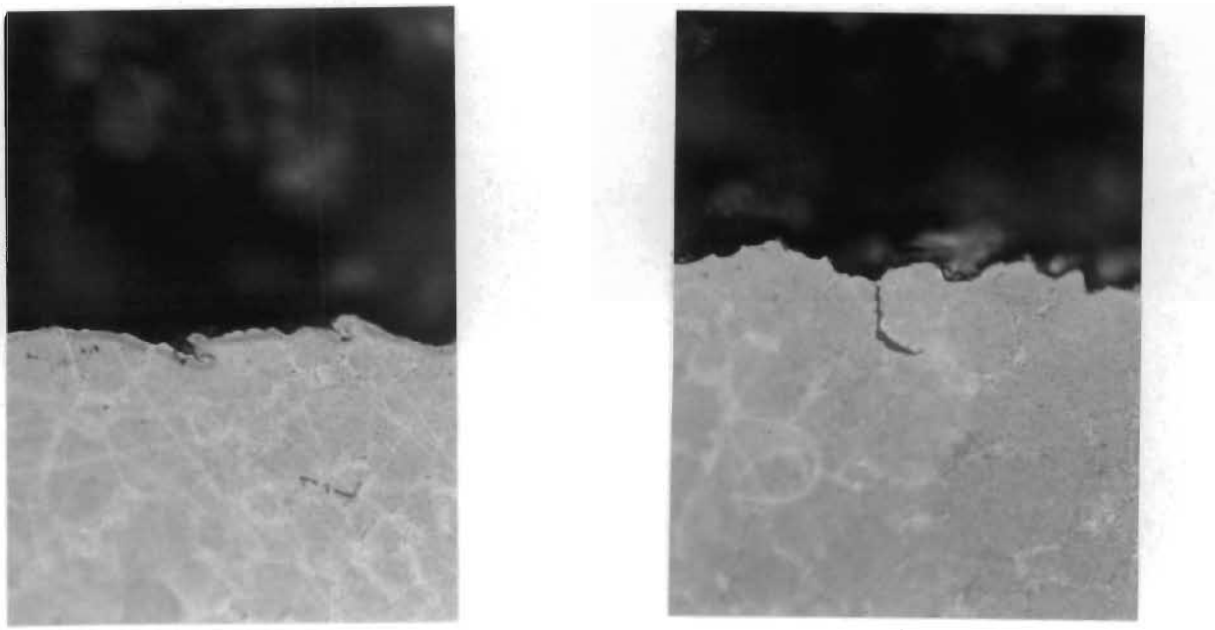

a. b.

Figure 3.45 : Longitudinal sample of TIMETAL 21S tested in argon + 20% O_2 environment at 550°C showing secondary crack branching and cracks filled with corrosion product, x400

3.3.3.2 FCGR at 550°C

The comparison of the fatigue crack growth rates is given in figure 3.46. The accelerated crack growth rate in the inert environment compared to the oxidizing environment shows the severe effect of the environment on the fatigue crack propagation properties at this temperature. The crack growth rate was found to be up to three times faster in the inert environment.

3.3.3.3 Crack Opening/Closure Data

P_{op} and P_{cl} in the different environment was found to be fairly constant throughout the crack growth range. The normalized values are shown in figure 3.47a and b.

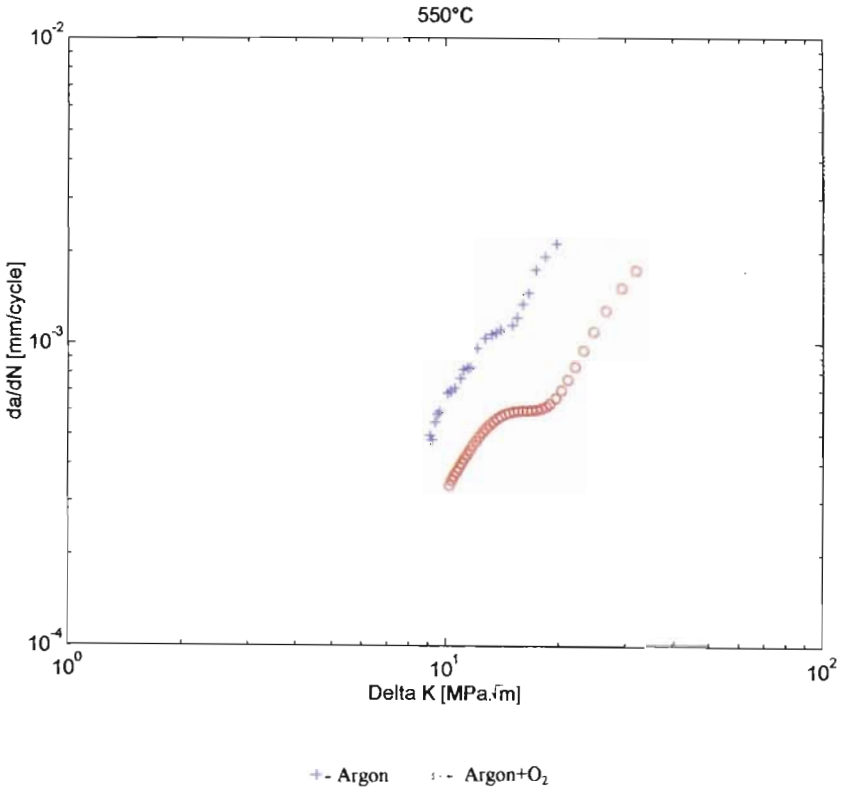

Figure 3.46 : FCGR of TIMETAL 21S in the inert and oxidizing atmosphere at 550°C

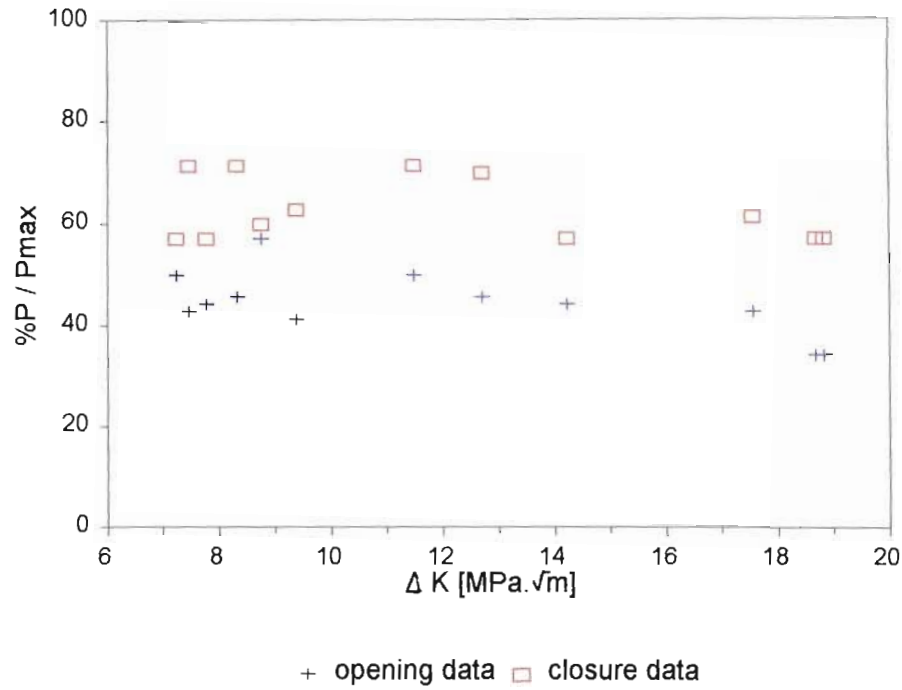

a.

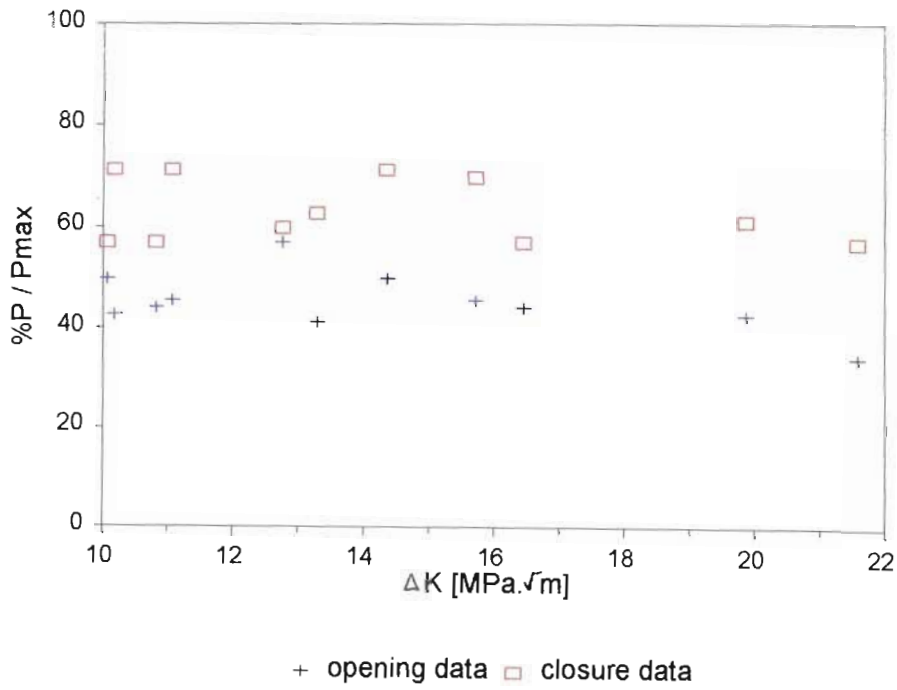

b.

Figure 3.47 : Opening/Closure normalized values obtained at 550°C in :
a. argon environment
b. argon + 20% O_2 environment

3.3.4 Characterization at 620°C

3.3.4.1 Fractography

Argon environment

The beachmarking method was successfully applied to the specimen tested in the argon environment and produced approximately 15 - 18 beachmarks which was deemed to be sufficient to produce the fatigue crack growth rate vs ΔK curve. Figure 3.48 shows the fracture surface and the resultant blocks and beachmarks can clearly be distinguished.

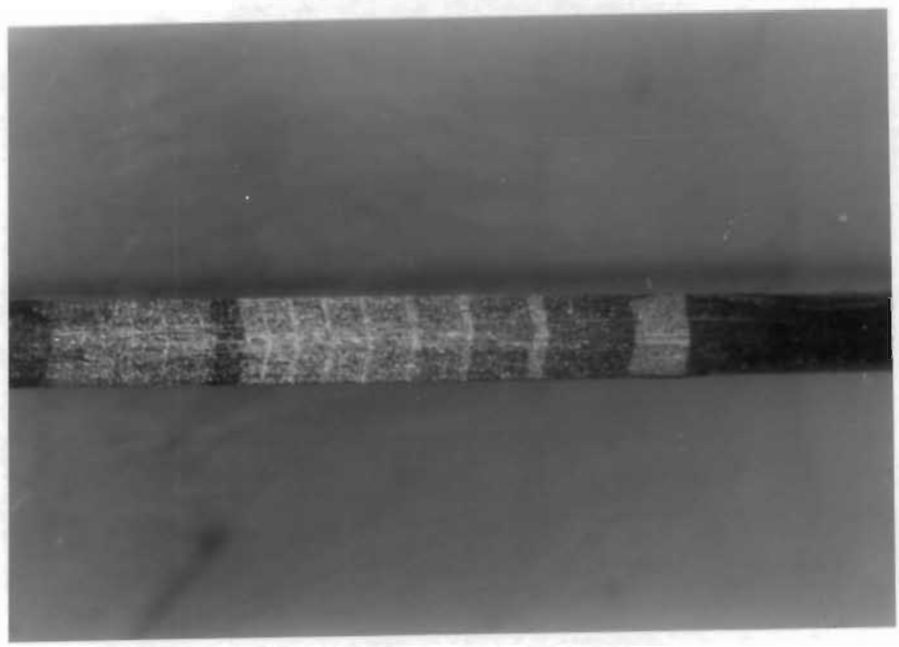

Figure 3.48 : Fracture surface of C(T) specimen obtained in argon environment at 620°C showing beachmarks and blocks, x7

SEM examination of the fracture revealed that the transgranular crack propagation mechanism was still present in the inert environment, with cleavage-like fan features in the grains (see figure 3.49). Fragments of fracture surface, distributed over the surface, are also shown in the figure. While the "smooth" fracture surface, as shown in figure 3.49a and b, is present at low ΔK, an increase in surface deformation can be observed at higher ΔK values. This deformation includes secondary cracking, increased separation at the grain boundaries and a general more coarse fracture surface appearance. Fatigue striations can also be seen on the fracture surface viz. figure 3.49c and d. The longitudinal metallographic sample did not reveal significant secondary cracking in the inert environment.

a.

b.

c.

d.

Figure 3.49 : Fracture surface of TIMETAL 21S at 620°C in argon environment for increasing ΔK showing :
A. surface fragments, **B.** secondary cracking, **C.** grain boundary separation.
a. $\Delta K \approx 8$ MPa.$\sqrt{m}$, **b.** $\Delta K \approx 10$ MPa.$\sqrt{m}$
c. $\Delta K \approx 13$ MPa.$\sqrt{m}$, **d.** $\Delta K \approx 18$ MPa.$\sqrt{m}$

Argon + 20% O_2 environment

An overall view of the beachmarked fracture surface is shown in figure 3.50. The beachmarks were not as defined as the sample tested in the argon environment. The dull fracture surface appearance also showed the extent of the environmental interaction with the alloy.

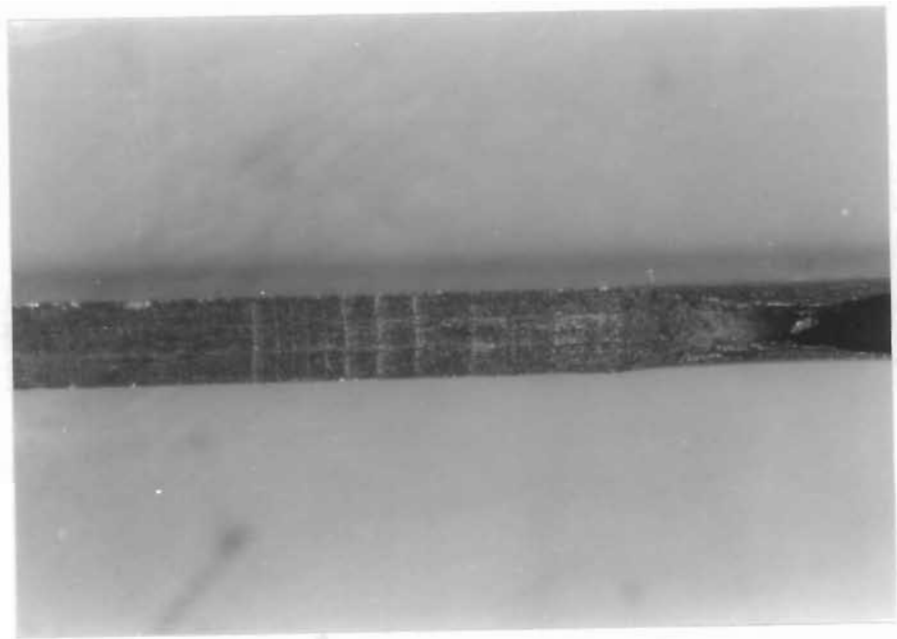

Figure 3.50 : Fracture surface of the C(T) specimen obtained in argon + 20% O_2 environment at 620°C showing beachmarks and blocks, x7

As with the samples tested at 550°C, the specimen tested at 620°C in the oxidizing environment also showed fracture surface features distinctly different from that obtained in the inert environment. Whereas the specimens tested at 620°C in the inert environment also showed a smooth, "clean" fracture surface, the specimen tested in the oxidizing environment showed coarse and fine particles distributed over the fracture surface, as well as a severe blunting of the fracture surface features. Figure 3.51 shows the general fracture surface appearance and the particle distribution over the surface at a low ΔK value.

At higher ΔK values the number of coarse surface particles appeared to decrease. Local collapse of certain surface features, particularly as shown in figure 3.52a and d, was evident. Surface fragments were observed over the total fracture surface area. The extent of secondary cracking also steadily increased with increasing ΔK.

a.

b.

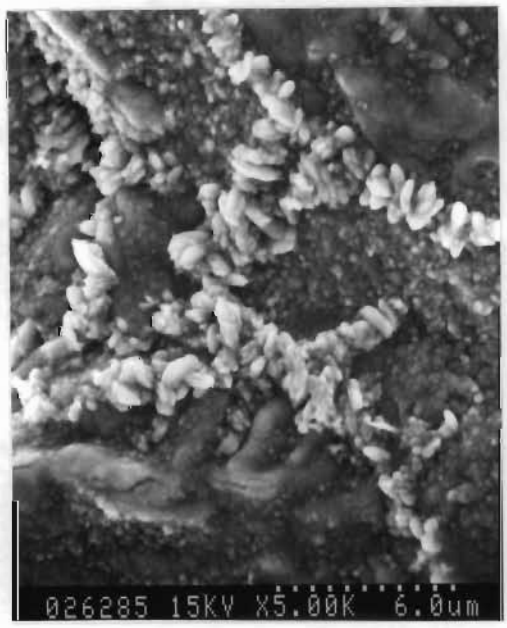

c.

Figure 3.51 : Fracture surface of TIMETAL 21S at 620°C in argon + 20% O_2 environment $\Delta K \approx 8$ MPa.$\sqrt{m}$:
a. General fracture surface appearance
b. Distribution of particles on fracture surface
c. Close-up of coarse surface particles

a.

b.

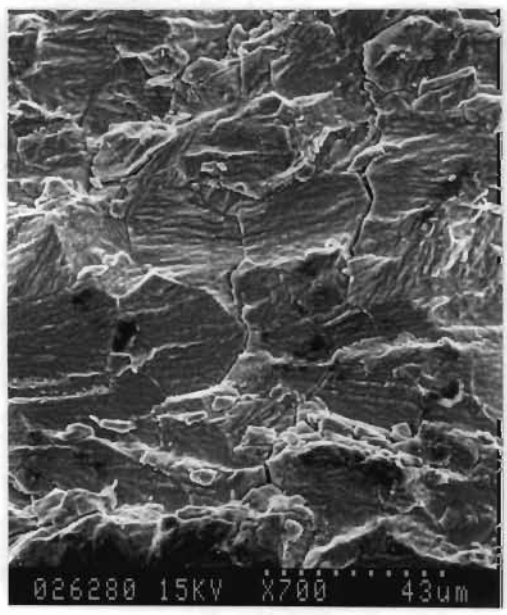

c.

d.

Figure 3.52 : Fracture surface of TIMETAL 21S at 620°C in argon + 20% O_2 environment showing :
A - local collapse **B** - surface fragments
C - secondary cracking
a. $\Delta K \approx 12$ MPa.$\sqrt{m}$, **b.** $\Delta K \approx 15$ MPa.$\sqrt{m}$
c. $\Delta K \approx 18$ MPa.$\sqrt{m}$, **d.** $\Delta K \approx 20$ MPa.$\sqrt{m}$

Only in the latter part of the crack growth, at relatively high ΔK values, can the fatigue striations be observed, as shown in figure 3.52d.

Metallographic samples prepared from the failed C(T) samples revealed frequent secondary cracking, extending to just below the fracture surface. These cracks also contained an abundance of corrosion product as shown in figure 3.53

Interrupted tests

While the beachmarked samples tests were conducted to failure, other tests performed in the different environments at 620°C were prematurely interrupted to compare the propagating crack profiles. Figure 3.54 shows the propagating crack obtained during these tests. The tests were interrupted at $\Delta K \approx 9$ MPa.$\sqrt{m}$.

SEM investigation of the crack profiles obtained showed a significant variance in the crack propagation mechanism in the inert and oxidizing environments. Comparing the crack characteristics it is evident that the test conducted in the inert environment produced a relatively straight crack propagation (figure 3.55a and b) while the crack in the oxidising environment experienced a more tortuous and zigzag type of propagation and the mismatch of the fracture surface asperities are clearly evident (see figure 3.55c and d).

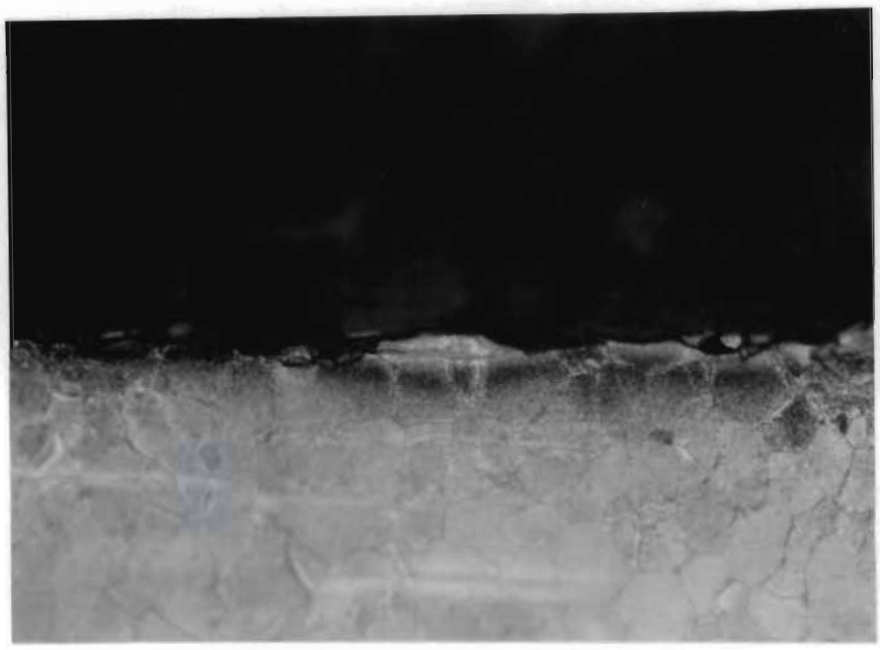

a.

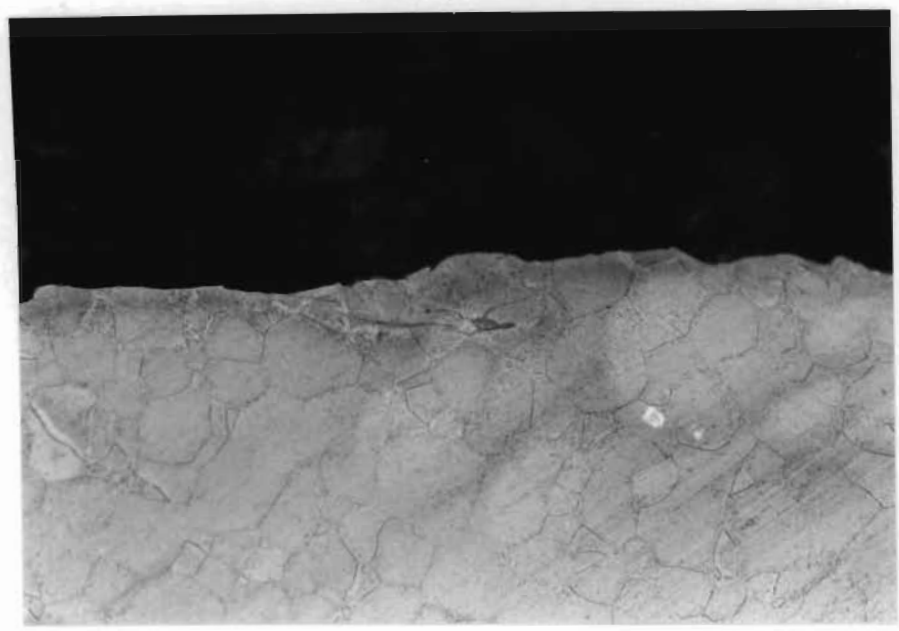

b.

Figure 3.53 : Secondary cracking containing corrosion product of TIMETAL 21S tested in argon + 20% O_2 environment at 620°C, x400

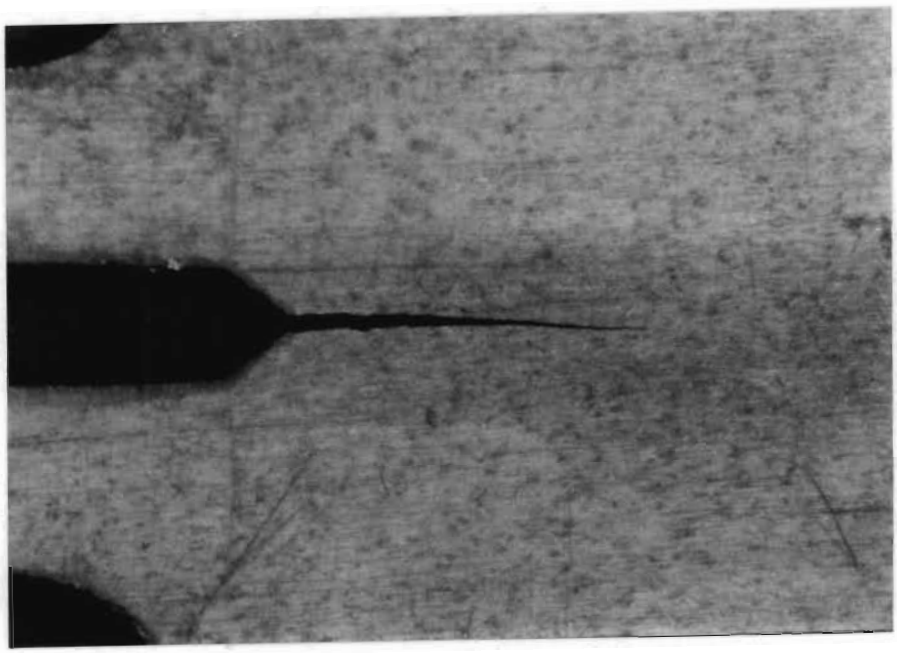

Figure 3.54 : Crack path of interrupted tests of the C(T) specimen representing argon and argon + 20% O_2 environments at 620°C, x12

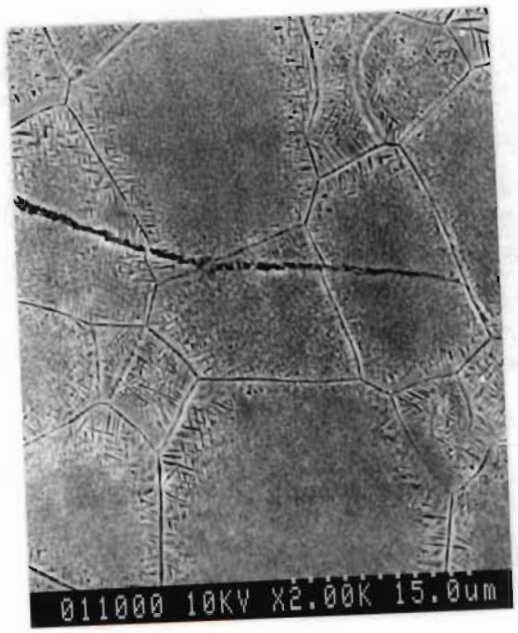

a.

b.

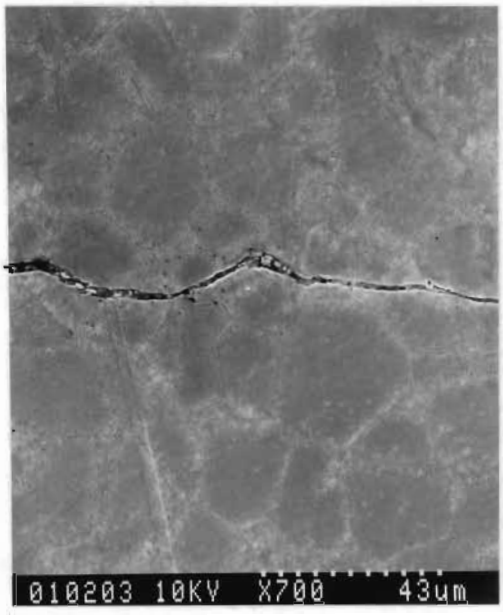

c.

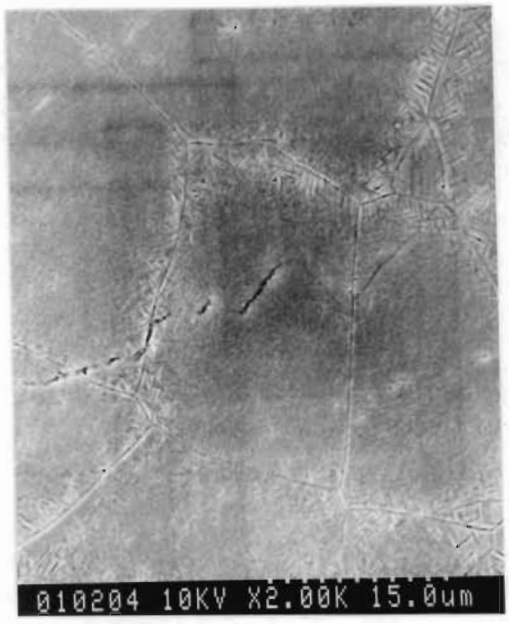

d.

Figure 3.55 : **a., b.** Relatively straight crack propagation in argon environment
c. General tortuous crack propagation, and,
d. zigzag crack propagation path at crack tip in argon + 20% O_2 environment

3.3.4.2 AES Analysis

The AES analysis was performed on the C(T) specimen in the regions described in chapter 2, section 2.4.4.

Argon environment

The results of the point scan performed on the sample tested in the argon environment is shown in figure 3.56. Minor changes in element distribution was noted.

Argon + 20% O_2 environment

Figure 3.57 shows the results of the scans performed on the C(T) specimen tested in the argon + 20% O_2 environment. There is a significant increase in the Al, Si and Mo content on the fracture surface. The Nb content also appears to have decreased significantly, compared to the analysis performed at positions 2 and 3.

3.3.4.3 FCGR at 620°C

The fatigue crack growth rate in the inert and oxidizing environments at 620°C was found to be, as previously, retarded in the oxidizing environment. The comparison of the FCGR is shown in figure 3.58.

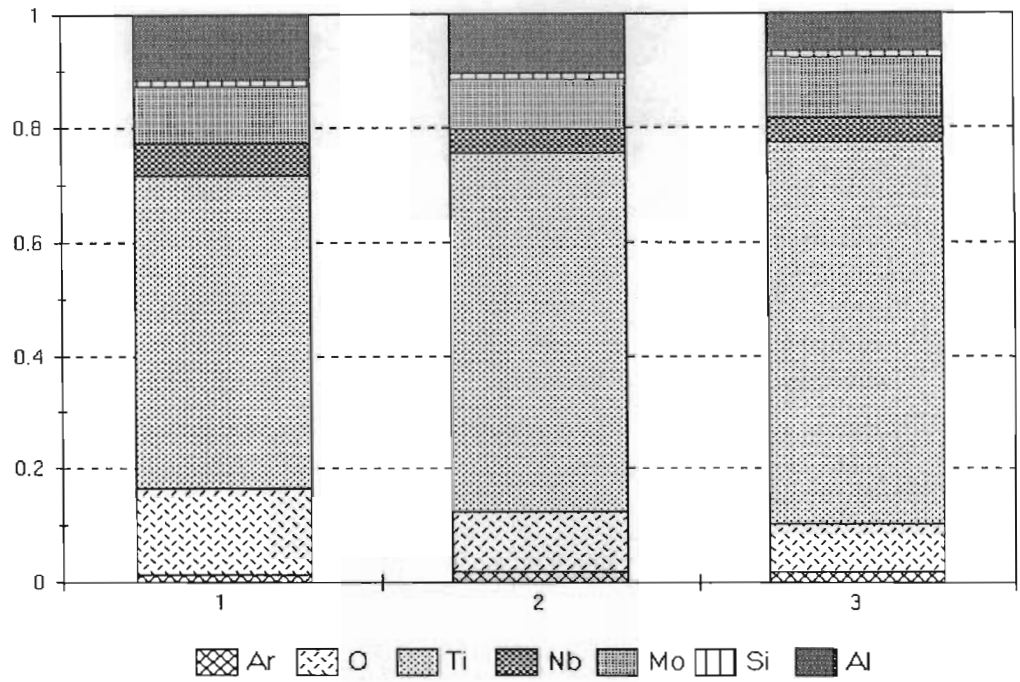

Figure 3.56 : AES point analysis performed at various locations on the C(T) specimen tested in argon environment at 620°C

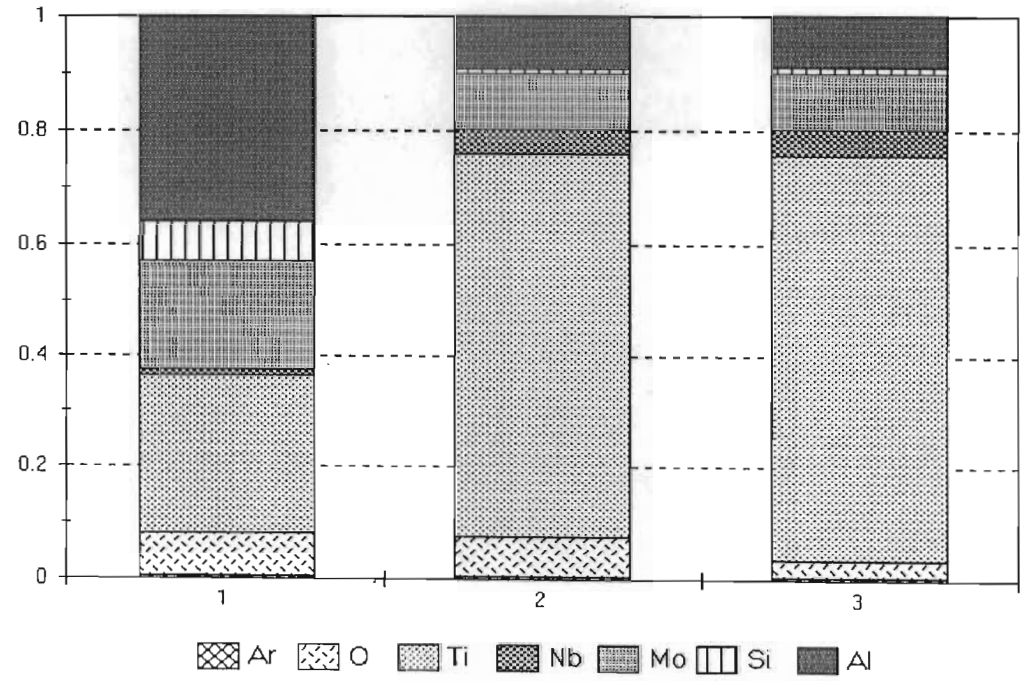

Figure 3.57 : AES point analysis performed at various locations on the C(T) specimen tested in argon + 20% O_2 environment at 620°C

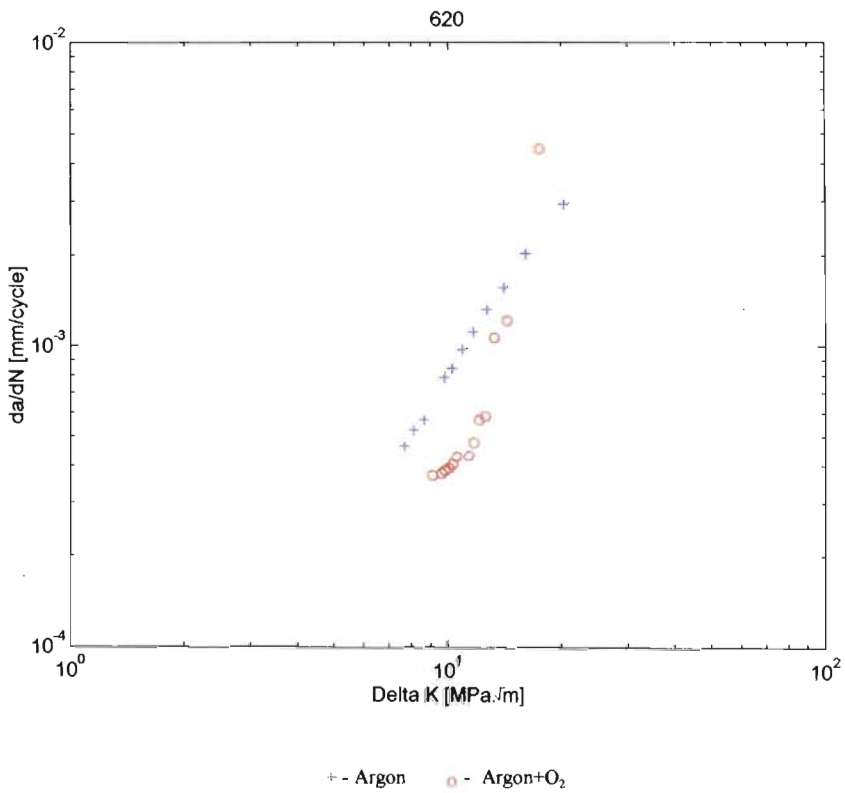

Figure 3.58 : FCGR of TIMETAL 21S in the inert and oxidizing atmosphere at 620°C

3.4 Summary of Results

3.4.1 Corrosion tests

In both inert and oxidizing environments, significant changes in the microstructure after a 5 hour exposure was initially restricted to an accelerated aging response in the non-recrystallized regions up to approximately 400°C. While fine alpha precipitated within the beta grains from approximately 400°C, grain boundary precipitation was observed from 450°C. A precipitation depleted zone was also found to be established immediately adjacent to the grain boundaries, and a region of coarser alpha precipitation separated the depleted region from the beta grain interior which contained a finer alpha precipitation. The fine precipitation became more coarse with increasing test temperature. At temperatures of 700°C and 750°C a more homogenized structure occurred towards the centre of the sample with the alpha occurring as a uniform, evenly distributed precipitate. Increased grain boundary precipitation at higher temperatures was also observed.

Although, in general, the precipitation at the elevated temperatures was more uniform, a distinct influence of the oxidizing environment on the microstructure near the exposed surface at higher temperatures could be observed. This difference entailed the variation in the amount, size and distribution of the alpha phase precipitation.

Visual observation of the white surface oxide layer in the oxidizing environment was achieved from 450°C. A fairly linear increase of the oxide layer thickness ensued with increasing test temperature up to approximately 700°C, whereafter a rapid increase in the oxide thickness was observed. AES line scan of the samples showed a similar trend in the oxygen content compared to the visually determined layer at the surface. The analysis also showed that there was some oxygen diffusion into the alloy in the temperature range 300°C - 450°C.

SEM conducted on the samples tested in the argon + 20% O_2 environment showed that fine oxide particles had evolved on the exposed surface during the high temperature exposure.

EDS Analysis

In the argon + 20% O_2 environment substantial increases in the amounts of Al and Si were found near the exposed surface while slight increases in Mo and Nb contents were also evident.

Analysis performed in an interior region of the samples tested in both the inert and oxidizing environments showed only minor changes had occurred in element redistribution at the grain boundaries, adjacent to the boundaries and in the grain interior.

X-ray diffraction analysis

In the argon + 20% O_2 environment the gradual emergence of the alpha phase, and corresponding decrease in the beta phase intensity at increasing temperatures, were evident. Up to 650°C the oxide formation was slight, while at 700°C and 750°C a rapid increase in the detected oxide intensities were observed. From the x-ray diffraction analysis the surface oxide was identified as mainly TiO_2.

In the inert environment the alpha phase evolution was slightly retarded as compared to that found in the oxidizing environment.

Hardness tests

A comparison between Vickers hardness of the samples tested in the inert and oxidizing environments is shown in figure 3.59. The tests were performed in the centre region of the samples and the hardness values do not indicate a significant environmental influence of the oxidizing atmosphere.

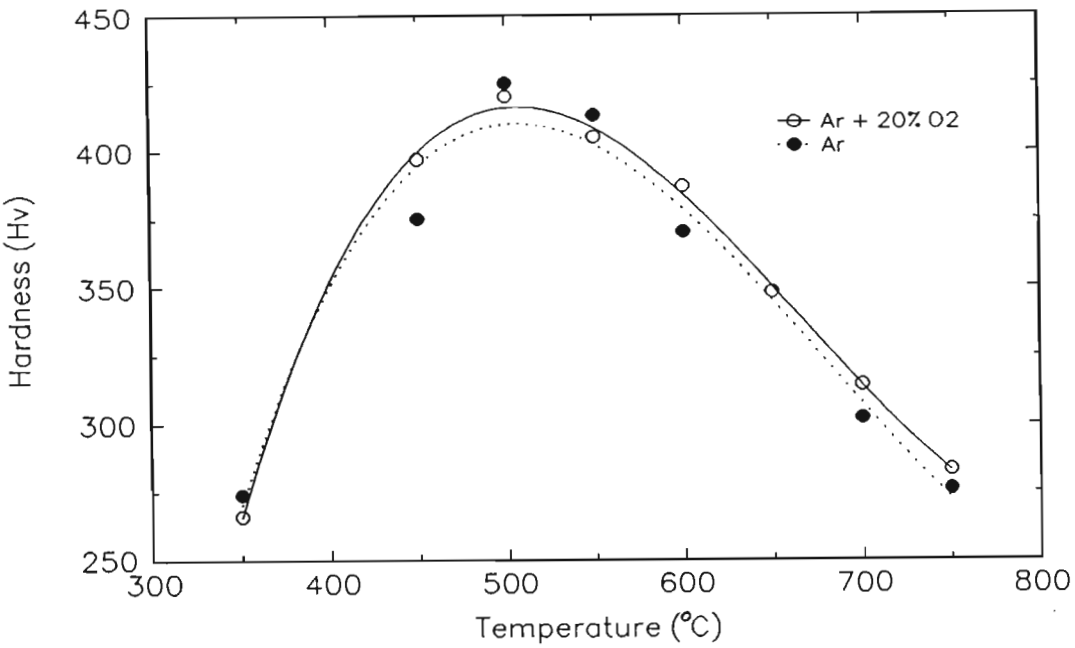

Figure 3.59 : Vickers hardness of samples exposed to argon and argon + 20% O_2 environment at various temperatures

3.4.2 FCGR at various temperature and in different environments

FCGR Comparison

At 375°C the FCGR in the inert and oxidizing environments were found to be similar. However, at the higher test temperatures of 450°C, 550°C and 620°C the effect of the environment became more pronounced and retarded crack growth rates were experienced in the oxidizing environments. Figure 3.60 summarizes the FCGR as found at the various temperature and in the different environments.

Closure Data

Opening and closure loads ($P_{op/cl}$) of up to 85% of P_{max} were experienced at higher temperatures, while at lower temperatures the values fell within the range 50% - 82% of P_{max} (see figure 3.61). P_{max} here is defined as the maximum load applied during a specific test.

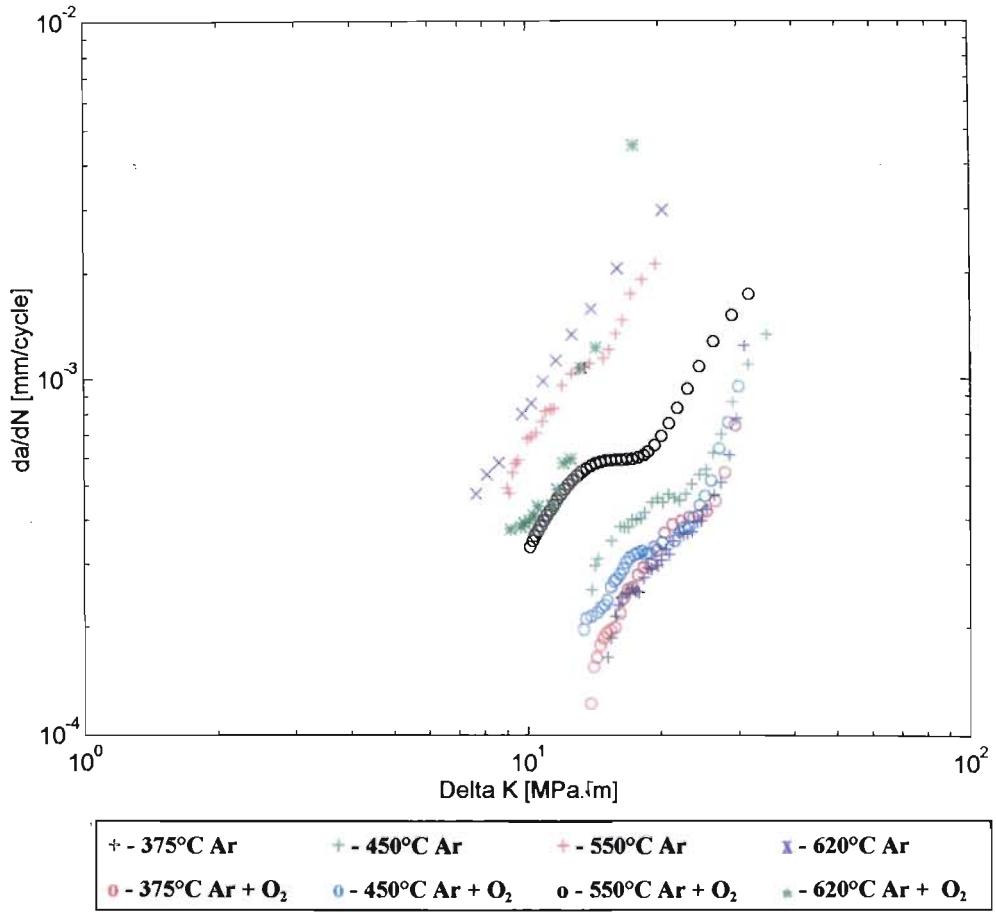

Figure 3.60 : Comparison of the FCGR of TIMETAL 21S in a inert and oxidizing environments at various temperatures

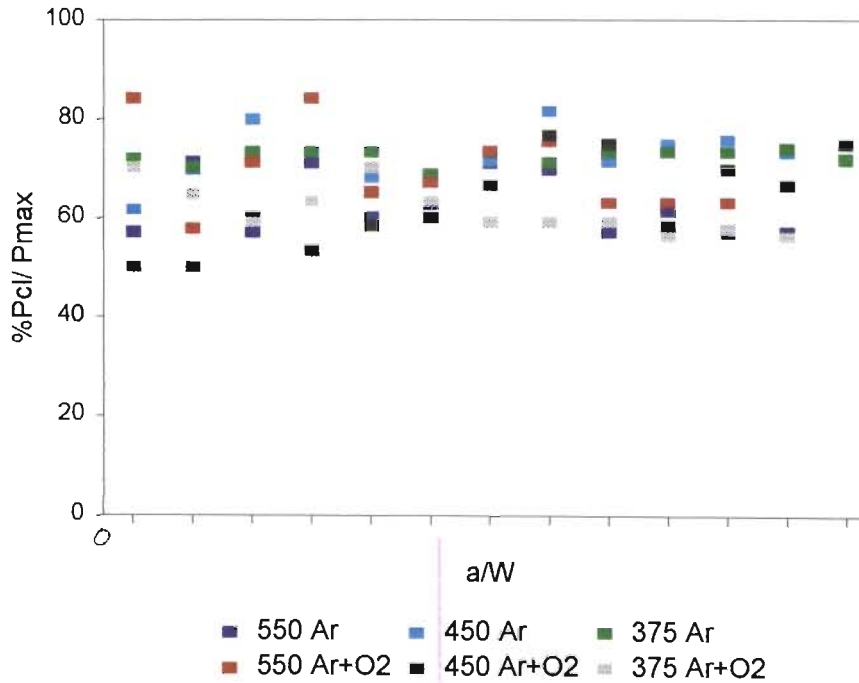

Figure 3.61 : Comparison of P_{cl}/P_{max} in the inert and oxidizing environments

The $P_{op/cl}/P_{max}$ values was found to fairly independent of ΔK, however, a small decrease in $P_{op/cl}$ values occurred at higher ΔK values. In general, the magnitude of $P_{op/cl}$ tended to decrease with increasing test temperature.

Fractography

375°C

The sample tested at 375°C in both the inert and oxidizing environments showed similar fracture surface features albeit a slightly different transgranular type of crack propagation. The crack propagation contained cracking and deformation between the striations, secondary cracking and a surface "ripping" effect, while the longitudinal metallographic samples showed insignificant secondary cracking in both environments.

450°C

At 450°C surface cracking and secondary cracking were again experienced, with increased amounts of secondary cracking experienced in the sample tested in the argon + 20% O_2 environment. The transgranular crack progression now included twisting at the grain boundaries in both the inert and oxidizing environments.

On the longitudinal metallographic sample, minor secondary cracking was observed in the inert environment, while branched cracks were observed on the sample tested in the argon + 20% O_2 environment.

550°C

Fine surface particles was evident on the fracture surface of the sample tested at 550°C in the argon + 20% O_2 environment and the surface features in the oxidizing environment were dulled compared to that obtained in the inert environment.

The transgranular crack propagation mechanism was prevalent in both environments, however, whereas the fracture surface appeared "smooth" in the argon environment, a more tortuous crack propagation path was evident in the oxidizing environment. Increased secondary cracking on the fracture surface was also evident in the oxidizing environment. The surface cracking of the samples had been significantly reduced compared to the samples tested at the lower temperatures. Surface fragments and a local collapse of surface regions were increasingly observed in the argon + 20% O_2 environment.

Evidence of the secondary cracking on the longitudinal metallographic sample of the C(T) specimen tested in the inert environment could not be found, while in the oxidizing environment some branching of the secondary cracks could be seen. These cracks also contained a significant amount of corrosion product.

620°C

In the oxidizing environment and at low ΔK, the environmental reaction comprised the evolution of large and finer surface particles and the dulling of the surface features. In addition, surface cracking, increased secondary cracking and increased occurrence of surface fragments were evident.

In the inert environment the transgranular, cleavage-type of crack propagation was well defined. Surface fragments and secondary cracking were evident to a lesser extent.

On the longitudinal metallographic samples, some crack deviation was found in the specimens tested in argon + 20% O_2 environment. These cracks contained significant amounts of corrosion product.

Interrupted Tests

The metallography performed on the interrupted tests showed that a zigzag type of crack propagation was experienced in the oxidizing environment. A relatively straight crack propagation was found in the inert environment.

Chapter 4 : Discussion

4.1 The Environmental Effect on TIMETAL 21S at various Temperatures

Microstructural Transformations

The evolving microstructure of TIMETAL 21S with increasing temperature was found to be typical of metastable beta titanium alloys. Alpha precipitation proceeded both homogeneously and heterogeneously. Mahoney *et al* [56] has previously extensively studied TIMETAL 21S aging behaviour at various elevated temperatures under inert conditions. Comparing Mahoney *et al*'s result to the microstructures obtained in the argon and argon + 20% O_2 environment indicated that generally a similar precipitation sequence had resulted. In the present study though finer internal alpha precipitation was present in the samples tested in both the inert and oxidizing environments. The microstructures in the inert and oxidizing environment were generally similar and some disparity in microstructural appearance between the samples could be attributed to a slight different in response to the etchant. However, a perceptible difference had occurred in the sample tested in the argon + 20% O_2 environment in the 700°C - 750°C range. Whereas a coarser, more homogeneously distributed precipitate developed more rapidly in the inert environment, a sustained presence of the fine internal alpha was evident in the sample tested in the oxidizing environment. This would seem to indicate that the diffusion of oxygen had occurred (even towards the centre of the specimen) leading to the increased availability of homogeneous nucleation sites in the grain interior, allowing finer and more numerous alpha precipitation to endure. The oxygen dissolution also explains the difference in precipitation location and appearance as found near the exposed surface in the sample tested in the 750°C oxidizing environment.

Oxide formation

Optical detection only perceived the oxide formation at approximately 450°C. Below this temperature an oxide layer (if present) could not be resolved by optical microscopy or SEM. The fairly linear increase of the oxide shows the predictable oxidation behaviour of TIMETAL 21S up to approximately 650°C. At higher temperature the oxidation resistance deteriorated rapidly as seen by the increase in the oxide layer thickness. Similarly in the x-ray diffraction analysis revealed the initial indication of an oxide formation occurring at 450°C.

Analysis of phases

The evolving alpha phase observed in the x-ray diffraction analysis performed in the argon + 20% O_2 environment consisted of the "natural" alpha phase precipitation due to the aging characteristics and the oxygen stabilized alpha titanium (alpha case). Not considering the titanium oxide formation, the x-ray diffraction analysis performed on the specimens tested in the different environments were similar up to 550°C, whereafter the alpha phase was more prominent in the argon + 20% O_2 environment than in the inert environment. This phenomena can be attributed to the formation of the oxygen enriched alpha case at the alloy surface or the increased alpha phase precipitation due to the oxidizing environment.

The TiO_2 peak intensities rapidly developed with the exposure at 700°C and 750°C in the argon + 20% O_2 environment. This behaviour is analogous with that of the measured oxide thickness were the oxidation resistance was shown to run out above 650°C.

The peak broadening and splitting effect experienced in the samples tested in the inert and oxidizing environments suggested a phase separation reaction in the beta structure [41].

Oxygen Dissolution and Alpha Precipitation

The effect of the oxygen dissolution in TIMETAL 21S tested in high purity **air** in the 600°C - 800°C range has been shown by Wallace *et al* to be appreciable - the oxide formation consistently accounted for approximately 70% of the total weight gain [100]. The influence of the diffusing oxygen in the argon + 20% O_2 environment became apparent at the higher temperatures. An increase in the shape, distribution and amount of alpha near the exposed surface compared to the centre of the specimen had occurred. Closer to the exposed edge the structure contained extremely fine internal alpha, increased acicular alpha adjacent to the grain boundaries, distinct precipitation free zones and grain boundary precipitation, while the sample tested in the inert environment displayed a more uniform, homogeneous precipitation in addition to the grain boundary alpha, indicating that the oxidizing environment had a unequivocal effect on the microstructure. Wallace *et al* attributed the increased alpha near the exposed surface in TIMETAL 21S to the dissolution of oxygen into the bulk material, and, in fact, used the precipitation content to model the oxygen content profile from the exposed surface into the alloy. Direct comparison to Wallace *et al*'s results to verify if any significant differences were evident between the air and the argon + 20% O_2 environment could not be made due to the variation in specimen exposure time. In general though, the air atmosphere appeared to produce a much coarser structure.

The effect of nitrogen on the total weight gain and the transformation kinetics was neglected in the Wallace *et al*'s study.

External surface exposure

The SEM of the exposed surface of the sample tested at 650°C, 700°C and 750°C showed the presence of fine "particles" on the surface which appears to be an artifact of high temperature exposure. The surface appearance did not exhibit any indications of local rupturing and indicated a more compact and less porous surface film [133].

Chemical composition modifications

In general, increased amounts of Al, Mo, Si and Nb were found near the exposed surface of the samples tested at 550°C, 650°C and 750°C. This result was anticipated since numerous studies have shown active participation of these elements in the oxidation protection mechanism of titanium alloys at the metal/environment interface. Although increased amounts of these elements were noted, oxides of the elements were not revealed by x-ray diffraction analysis. Wallace *et al* showed that only weak Al_2O_3 peaks were obtained after exposure of TIMETAL 21S to up to 100 hours at 600°C to 800°C in air. Figure 4.1 shows the thermodynamic free energy vs temperature for the oxidation of different metals at various temperatures. From the figure it is evident that for high temperature exposure of TIMETAL 21S, the Al would form the most stable oxide, rather than Ti and/or Si. The Al content of TIMETAL 21S however has been found insufficient to sustain the formation of a continuous and dense Al oxide, thus only limited protection is offered.

Similar thermodynamic data for Mo and Nb could not be located. Although the exact role of Nb and Mo in the high temperature protection mechanisms is unclear, Maki *et al* [101] has shown that particularly Nb synergistically increases the oxidation resistance of titanium alloys by accelerating the formation of Al_2O_3. Increased amounts of Nb and Mo were also found in the surface oxide of TIMETAL 21S. Since these elements have been found to form non-protective oxides, it may indicate that the elements synergistically participate in the oxidation protection mechanism.

The AES line scans showed that even without a detectable surface oxide formation, an appreciable dissolution of oxygen had occurred. This was evident from the samples tested at the lower temperatures e.g. up to 450°C . The scans also showed the dissolution of oxygen into the bulk of the material at higher temperatures. As the surface oxygen content gradually increased with increasing temperature, the dissolution of oxygen similarly increased. This dissolution did not show abrupt changes with the increasing temperature, rather a gradual increase occurred.

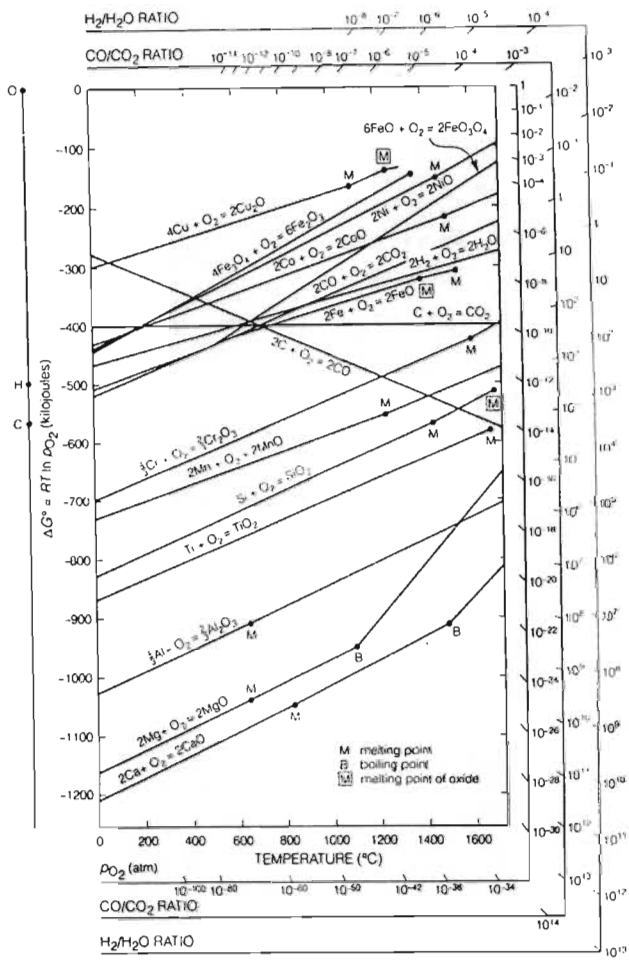

Figure 4.1 : Thermodynamic free energy vs temperature for the oxidation of metals [133]

Hardness evaluations

Although the extent of diffusing oxygen in titanium alloys can be identified from the hardness tests, an expected increase in the hardness of the samples tested in the argon + 20% O_2 environment did not occur. It is believed that the exposure time of five hours was not sufficient to allow for an significant environmental influence on the centre hardness. Both environments showed that after the initial increase in hardness with increasing temperature, the hardness curve peaked and the hardness dropped off at high temperatures. This is indicative of the overaging process where the coarser precipitates are unable to further strengthen the alloy.

4.2 Fatigue Crack Growth Rate Characteristics in Argon and Argon + 20% O_2

The fatigue crack growth rates were successfully monitored using the compliance method and the beachmarking method. In particular, the application of the load-line compliance testing technique used in this study proved to be particularly successful. The method can be described as an innovative means whereby crack progression can accurately be tracked at high temperatures and within a confined space such as when an environmental chamber is used. The method can also be used for low temperature tests. It is foreseen that this particular test method will be increasingly used for other fatigue crack growth tests conducted under similar experimental conditions.

Although less fatigue crack growth data was obtained using the beachmarking method, a sufficient number of values were collected in order to conduct meaningful comparison with the other test data. The method provided unambiguous data of the crack growth rates, however, to establish the required ΔK/number-of-cycles-per-block/test frequency combination proved to be a time consuming practice.

4.2.1 375°C

The fracture surface of TIMETAL 21S tested at 375°C in the inert and oxidizing environment was characterized by a transgranular mode of crack propagation with ductile striations, containing surface cracking, secondary cracking and a surface "ripping" effect. Further examination indicated that the surface cracking, which was mainly found at the striation "interfaces", appeared to be due to a surface deformation. Although this type of deformed striation has been classified as ductile striations, the possibility exists that a combination of the effects of roughness-induced closure mechanism and a plasticity-induced crack closure mechanism in which mismatching surface asperities are prematurely brought into contact, resulting in the crushing and deformation of these contact areas, can account for these type of striations. Further substantiation of the surface contact is that the surface cracking is orientated primarily perpendicular to the crack propagation direction which would indicate a fretting-type contact. The general occurrence of lower opening loads, compared to the closure loads,

could have resulted due to the initial mismatch and ensuing deformation of the surface asperities during the crack closing cycle, resulting in lower release loads. If this is the case, it would indicate the ductile nature of the fracture surface and the ever present crack path tortuosity. Furthermore, the surface ripping effect may also have resulted from the fretting contact.

Generally, surface cracking has also been found to initiate secondary cracking [127], however only minor secondary cracking was observed at this temperature in both the inert and oxidizing environments.

The similar appearance of the fracture surfaces obtained in the inert and oxidizing environments indicated an insignificant environmental influence at 375°C. The x-ray diffraction results has also shown that the surface oxide evolution at this temperature are virtually non-existent, however, AES analysis has shown that there is a small dissolution of oxygen into the alloy at this temperature. It would appear though that the environment has been unable to significantly influence the crack propagation rates.

While the opening and closure loads level remained fairly constant for the duration of the test in the argon environment, the loads tended to decrease slightly with increasing ΔK in the argon + 20% O_2 environment. Although Vesier *et al* [116] attributed this decreasing loads phenomena to the increased plastic constraint experienced at the crack tip, it was observed that the change from the inert argon environment to the argon + 20% O_2 environment had resulted in the difference of the loads. Vesier *et al* also commented that the amount of plastic constraint found in an inert environment is higher than that in air. The reason for this behaviour is not well understood, however, evidence has shown that the plastic zone ahead of the crack tip and in the wake of the propagating crack can be modified due to an environmental interaction.

4.2.2 450°C

In the 450°C sample, a more cleavage like crack propagation was evident. This is manifested by the fan shaped facets and steps in the transgranular region at low ΔK values in both the inert and oxidizing environments - although the effect was more pronounced in the oxidizing atmosphere. Gray *et al* [46] has reported an increased incidence of these cleavage-like facets during fatigue, as well as a change in slip planarity in titanium alloys alloyed with increasing oxygen content. The presence of roughness-induced and plasticity-induced crack closure was manifested at higher ΔK values where the faceted occurrence decreased and an increased surface fretting was observed.

Examination of the opening and closure loads obtained in the different environments, showed that the loads were essentially similar - the data obtained in the inert environment being slightly higher than in oxidizing environment. Considering that the crack propagation can only effectively occur when the crack is fully open [68], it can be seen that the opening/closure data could not explain the retarded crack growth experienced in the oxidizing environment and thus the additional effect of the material's modified behaviour due to the oxidizing environment interaction has to be considered. In spite of the x-ray diffraction analysis indicating a detectable oxide formation at 450°C, the fracture surface appearances essentially had remained similar in the different environments. Furthermore, although in the argon + 20% O_2 environment a slight oxide formation was anticipated on the fracture surface to encourage a retarding oxide-induced crack closure mechanism, the closure related data did not indicate the formation of such an oxide. However, an increased incidence of secondary cracking on the fracture surface was found in the oxidizing environment and is believed to contribute to the retarded crack growth rate. Metallography performed on the longitudinal samples had showed the occurrence of branched secondary cracking (intergranular as well as transgranular) in the oxidizing environment, as opposed to the minor straight intergranular cracks experienced in the inert environment. Other researchers have observed an increased incidence in secondary cracking due to an aggressive oxidizing environment which has lead to crack tip blunting and branching

of fatigue cracks [116,134,135]. The branched secondary cracking has been shown to affect the load distribution at the crack tip by activating a mixed mode type of crack propagation, resulting in changes in the effective driving force necessary for the crack advance. This translates into a lower ΔK experienced at the crack tip, during fixed amplitude far field loading fatigue crack growth, and this effectively lowers the crack growth rates [68,113].

4.2.3 550°C

At 550°C a marked increase in the crack growth rates over the lower temperatures were observed in both the inert and oxidizing environments. Similarly, Ghonem *et al* [25] found in comparative FCGR tests conducted in air on TIMETAL 21S laminate at 23°C, 482°C, 650°C and 760°C, that the two lower temperatures produced similar results, while the 650°C and 760°C tests produced similar, yet significantly increased growth rates compared to the two lower temperatures. No closure values were monitored during their study and hence the acceleration was simply attributed to a crack tip oxidation damage mechanism.

The transgranular crack growth was present in the inert and oxidizing environments at lower ΔK values, however the cleavage-like propagation, as found at the lower temperature tests, was absent. Smith *et al* [136] has shown that at elevated temperature, the propagating crack slip character can be modified, resulting in a different mode of fatigue crack growth. This could partly explain the initial "smoother" fracture found in the inert environment (and to some extent in the oxidizing environment) and the markedly accelerated growth rates obtained in both the inert and the oxidizing environment at the higher temperature. Furthermore, substantially lower opening and closure loads were observed at 550°C showing that the effective crack driving force has increased, thus accelerated crack growth rates were experienced at this temperature. However, the effect of the surface oxidation in retarding the FCGR was observed from the crack closure data, where relative to the inert environment, the closure loads in the oxidizing environment were higher. This would suggest an oxide-induced crack closure effect due to fracture surface oxide formation. Additionally, in the oxidizing

environment, the extensive secondary cracking was evident on the fracture surface, as well as branched secondary cracking (on the metallographic sample) containing substantial corrosion product. As mentioned previously, the secondary cracking results in an increase in the crack tip shielding, whilst the crack driving force is locally reduced, rendering a retarded crack growth.

While the fracture surfaces of the specimens tested at 550°C showed a similar mode of crack propagation, the effect of the oxidizing environment was clearly visible. The effect was manifested by the appearance of fine "particles" on the fracture surface. These particles have been shown to originate from the high temperature exposure in the oxidizing environment. The origin of the coarser particles is however unknown. It can be postulated that the particles have evolved due to a continued alpha precipitation at the grain boundaries since the specimens were tested close to the aging temperature. The dwindling occurrence of the particles with increasing ΔK indicates also that a free surface and a prolonged environmental interaction is required for the emergence of these coarse particles. Mahoney *et al* [56] has proposed an aging temperature of approximately 650°C for up to 48 hours for maximum microstructural stability of TIMETAL 21S for elevated temperature use.

As mentioned previously, the closure and opening loads were in general lower at 550°C in both the inert and oxidizing environments than at the lower test temperatures. This is manifested on the fracture surface by the lack of prominent compressively deformed areas, although some fretting contact was still visible. While compressive loading and (resultant) fracturing of the fracture surface features was observed at higher ΔK, the effect was more pronounced in the oxidizing environment, indicating the embrittled nature of the fracture surface.

4.2.4 620°C

A transgranular fatigue crack propagation, similar to that found at 550°C, was evident in the 620°C environment and at higher ΔK values and more extensive secondary cracking was evident on the fracture surface of the sample tested in the argon + 20%

O_2 environment. Metallography on the longitudinal section showed that the secondary cracking in the inert atmosphere was insignificant, however, in the oxidizing environment several branched secondary cracks containing substantial corrosion product, were evident. This cracking, as elaborated on previously, partakes in the retardation of the crack growth rates in the argon + 20% O_2 environment. An acceleration of the crack growth rate at higher ΔK values in the argon + 20% O_2 environment can be attributed to the embrittling damage mechanism ahead of the crack tip exceeding the ability of the closure-induced crack retardation mechanisms to restrain the crack growth effectively.

The interrupted tests clearly indicated the presence of an environmentally assisted crack growth mechanism. Whereas the test conducted in the inert atmosphere contained a relatively straight crack propagation, the crack in the oxidizing environment experienced a retarded crack growth as manifested by the zigzag type propagation. This type of crack path appearance has been found to indicate a roughness induced crack closure mechanism experienced at near-threshold conditions. This occurs due to the plastic zone ahead of the crack tip at this point being small compared to the microstructural dimensions such as the grain size, resulting in a promotion of a crystallographic-dependent fracture path [68,69,109,136,138]. However, in addition to the roughness-induced crack closure, it is believed that some degree of environmental influence was indeed present in this region since oxide-induced crack closure has been cited to have the most profound effect on the crack growth behaviour in the near-threshold region. Although the physical characteristics of oxide-induced crack closure is difficult to identify, the presence of the oxides was confirmed by the AES results which showed an increased oxygen content at the fracture surface. If the effect of the oxidizing environment had been insignificant and unable to influence the crack propagation, similar crack paths should also have been observed in both the inert and oxidizing environment, since then the crack propagation will be solely dependent on the crystallographic orientation and the crack propagation will then be affected by the roughness-induced crack closure alone. However, the different crack propagation profiles obtained in the inert and oxidizing environments indicates that there exists a strong association between the crack propagation mode and the environment. This

raises an important question as to whether the roughness-induced crack closure is purely a microstructural effect, or whether it can be stimulated or repressed by the environment.

Although the oxidizing environment has been shown to increase the formation of the alpha phase, increased alpha precipitation was not observed in the area surrounding and ahead of the crack tip. However further investigations need to be conducted in order to verify the presence of such precipitates as it is believed that a strong environmental influence, which determines the FCGR and crack propagation path, exists ahead of the crack tip.

The AES results showed that the thermodynamically stable Al and Si oxides, in addition to the Ti oxides, had copiously formed on the fracture surface of the sample tested in the argon + 20% O_2 environment. This finding supports the theory of an oxide-induced crack closure mechanism present during the fatigue crack growth. Increased fracture surface oxide layer thickness may also have been artificially created due to the repetitive contact between the fractures surfaces by means of the repeated fracturing and reformation of the oxide layer as reported by Suresh [68]. This would result in the further impediment of the effective crack driving force and therefore further retard the crack propagation rate. The oxide thickness along the crack path was not directly investigated though.

Actual closure loads were not available due to the beachmarking method used however the fractured surface regions was believed to be evidence of the compressive closure-inducing mechanism.

While the AES analysis of the fracture surface accounted for the events occurring immediately after and in the wake of the propagating crack, the AES analysis performed adjacent to the fracture surface (point I, figure 2.15) characterized the chemical events occurring ahead of the crack tip. From this analysis a slight increase in the oxygen content, compared to the bulk material analysis (point 3), was observed. This was accomplished without the other elements showing particular activity. It would

thus appear that the main environmental mechanism ahead of the crack tip in the oxidizing environment was the formation of the oxygen enriched zone. However, the embrittlement ahead of the crack tip is either 1. insignificant, or 2. completely overshadowed by the closure mechanisms since retarded crack growths were experienced in the argon + 20% O_2 environment. Since AES line scans showed substantial oxygen diffusion into the alloy at these temperatures, it would appear that the closure mechanisms such as the roughness-induced closure mechanism, the plasticity-induced closure mechanism and oxide-induced closure mechanism dominates the FCGR behaviour as found in TIMETAL 21S.

Combined FCGR Data

Figure 3.60 showed a comparison of the crack growth rates obtained in the argon and argon + 20% O_2 environment at the various temperatures. It can be seen that in both environments at 375°C and at 450°C in the argon + 20% O_2 environment the crack growth rates were fairly similar. Relative to these values, the crack growth rate in the argon environment at 450°C was accelerated, showing the earliest discernible indication of an environmental influence. The FCGR obtained from the 550°C and 620°C tests were distinctly different from the 375°C and the 450°C results. The two higher temperatures showed significantly accelerated crack growth rates. As previously reported, Ghonem *et al* [25] found similar accelerated rates in TIMETAL 21S in air at higher test temperatures.

Consolidation of Closure-Related Data

The induced crack closure mechanisms have extensively been used to rationalize anomalies in the fatigue crack growth data in various environments and at various temperatures. It has become a convenient tool to normalize external and intrinsic material effects such as alloy composition, microstructure, environment and loading conditions [46]. This is achieved by establishing an effective stress intensity factor, ΔK_{eff} as previously defined in chapter 1, section 1.5. In this study, consolidation was attempted using the opening loads to determine $\Delta K_{eff,}$ as stated in equation 1.14.

The consolidation process could not be applied to the 620°C-beachmarked samples.

Figure 4.2 shows the consolidated data for the specimens tested in the argon and in the argon + 20% O_2 environment at 375°C, 450°C and 550°C. Data for the test temperatures of 375°C and 450°C in the **argon** environment could effectively be merged, showing that ΔK_{eff} can account for some of the temperature effect in the inert environment. However, the data obtained from the 550°C inert environment could not be consolidated into the same region as the two lower temperatures. It would appear that a purely temperature effect could not account for the higher crack growth rate in the inert environment. Other mechanisms which yield an accelerated crack growth rate for the effective applied driving force are operative at this temperature. However, such a mechanism could not readily be identified, and the origin of the accelerated growth is mostly unexplained.

While the consolidation was able to effectively merge the data obtained from the argon + 20% O_2 environment at 375°C and 450°C into a specific region, the data obtained at 550°C could not be reduced into the same region (see figure 4.2). This would indicate that simple consolidation could not account for the high temperature behaviour under oxidizing conditions. Salivar *et al* [76] attributed the inability of the consolidation process to effectively reduce the crack growth data in titanium alloys to the elevated temperature oxidation effects. Since a balance of factors governing the crack growth behaviour exists in titanium alloys, namely that of the damaging oxygen embrittlement ahead of the crack tip leading to an accelerated crack growth, and that of the induced closure mechanisms which retards the growth, the diffusion of the oxygen at the higher temperatures appears to have tipped the balance of factors in the favour of the damage mechanism. This phenomena has lead to the inability of the consolidation process to effectively collapse the 550°C data. Even though an increase in P_{cl}/P_{max} was observed in the 550°C specimen tested in argon + 20% O_2, as compared to the inert environment, P_{op}/P_{max} values in both tests were shown to be fairly similar. These similar values still resulted in the same effective crack driving force (ΔK_{eff}) leading to an accelerated crack growth rate in the argon + 20% O_2 environment. Subsequently higher consolidated crack growth rates are observed. The inadequacy of the

consolidation process in reducing the data can thus directly be attributed to the effect of the oxidizing environment.

The consolidation is also seen to partly discriminate between the data obtained in the inert and in the oxidizing environments. While all the data for the two lower temperatures of 450°C and 375°C from the inert environment was collapsed into a specific region, data from the oxidizing environment for the same temperatures was also reduced to a similar yet separate region. Although consolidation of the 550°C oxidizing environment data did fall in the 375°C /450°C inert environment region, the 550°C argon environment yielded values which did not fit either region. Thus similar trends in the crack growth rates were observed for the different environments, however, these trends were clearly separated.

As mentioned previously, different plastic constraints experienced in a vacuum and in air and was found to be responsible for the difference in crack growth rates in titanium alloys. Although the consolidation process may take into account the microstructural effects and the formation of an oxide layer on the fracture surface, it does not consider the additional environment-material interaction ahead of the crack tip which directly affects the material physical and mechanical properties and modifies the amount plastic constraint surrounding the crack. This modification of constraint consequently influences the crack growth rate.

Further observations concerning opening/closure data

1. The opening and closure loads in the 375°C and 450°C inert environments were somewhat higher compared to that found in the oxidizing environment, and therefore could not be used to explain the fatigue crack growth rates at these temperatures.

Considering the data obtained in the inert and oxidizing environments at 375°C and especially at 450°C, a weak presence of a surface oxide was expected to be revealed by the closure data - especially since the x-ray diffraction analysis showed the slight

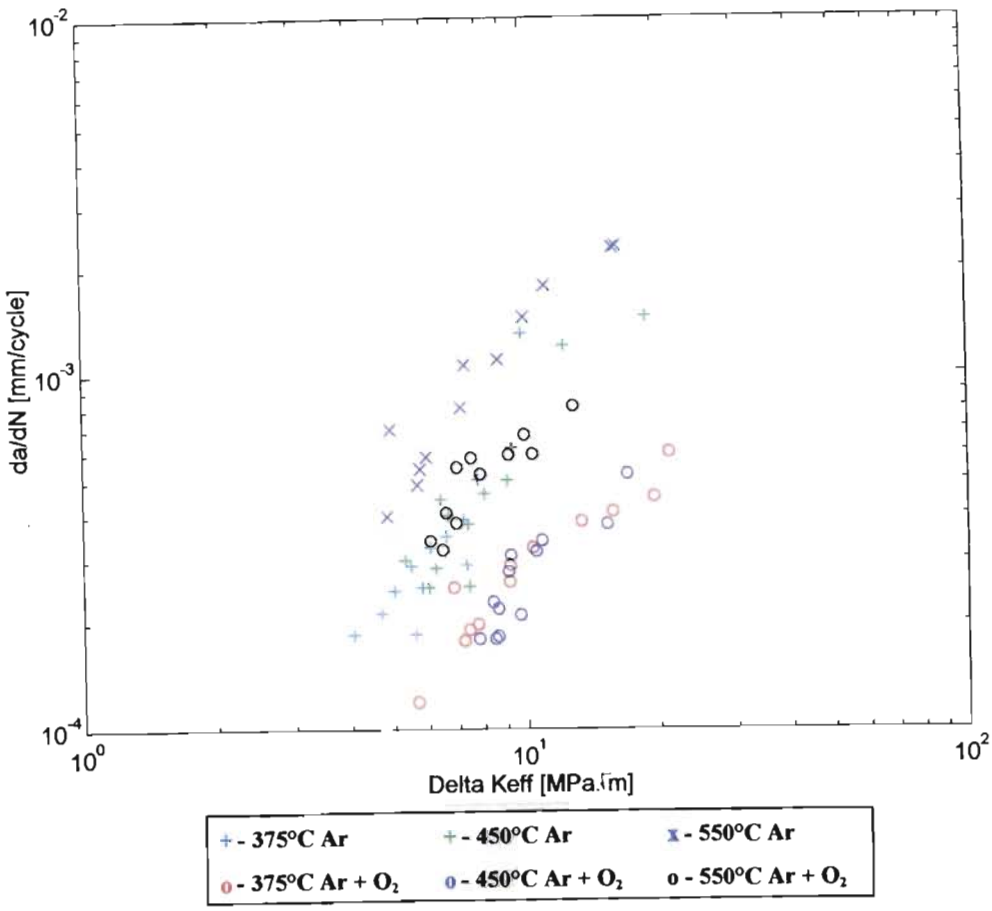

Figure 4.2 : Consolidated data for ΔK_{eff} at various temperatures in the argon environment and argon + 20% O_2 environment

formation of such an oxide. However, the opening/closure data was consistently higher in the inert environment. Although consolidation of the data was achieved, the actual fatigue crack growth rates has to be explained by additional environmentally assisted mechanisms.

2. It was observed that, on average, the magnitude of the opening and closure loads decreased with increasing temperature, showing a correlation between the gradually accelerated fatigue crack growth rate and the closure-induced mechanisms. Figure 4.3 shows the normalized opening and closure loads relative to the absolute maximum applied load.

Larsen *et al* [110] has shown that the level of closure can significantly be influenced by the variation in titanium alloy slip character. It is thus believed that with the

increasing test temperature other slip systems were activated, leading to a different type of crack propagation and hence also can partially account for the markedly accelerated fatigue crack growth rates as found in both the inert and oxidizing environments at 550°C and 620°C. This modification in the slip character was also manifested by the different fracture surface appearances observed in the various environments and at the various temperatures.

3. The ratio $P_{op/cl}/P_{max}$ was fairly constant for the different temperatures and environments (see figure 3.61). Thus the closure loads depended on P_{max} applied at the respective test temperatures.

The fairly similar ratios of P_{op} and P_{cl} to P_{max} at all the test temperatures was somewhat surprising, considering that $P_{max\ 550°C} \approx \frac{1}{2}P_{max\ 375°C}$. This phenomena would indicate that the closure loads progressively decreased with increasing temperature since a lower P_{max} was applied at the higher test temperatures. The lower fracture surface interference observed with the increasing temperature verifies the phenomena. In the inert environments, where the effect of the oxidizing environment is excluded, the decreased opening and closure loads can only be attributed to either a decrease in the surface roughness and/or the amount of plastic constraint surrounding the propagating crack. It can thus be postulated that either a different fatigue crack path, due to other slip systems being activated at higher temperatures, has lead to an overall lower surface roughness and thus resulted in lower closure levels, and/or, a lower P_{max} has had less plastic constraint to effect and hence reduced the level of closure by lesser amounts of plasticity-induced crack closure. With the added effect of the oxidizing environment, it can be stated that the environmentally modified plastic constraint and the environment-metal interaction additionally contributed to the anomalous closure-related data behaviour.

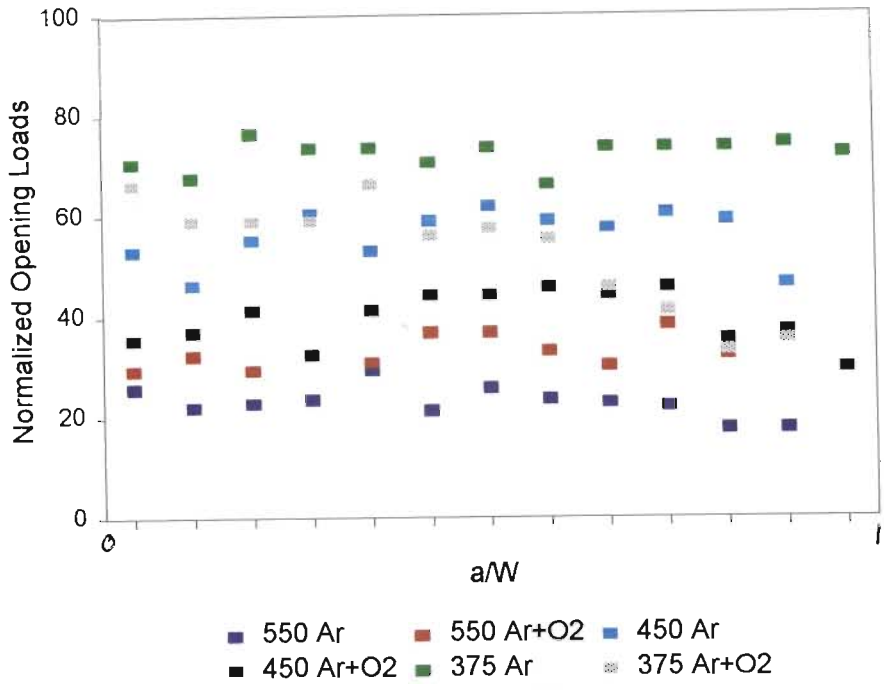

a.

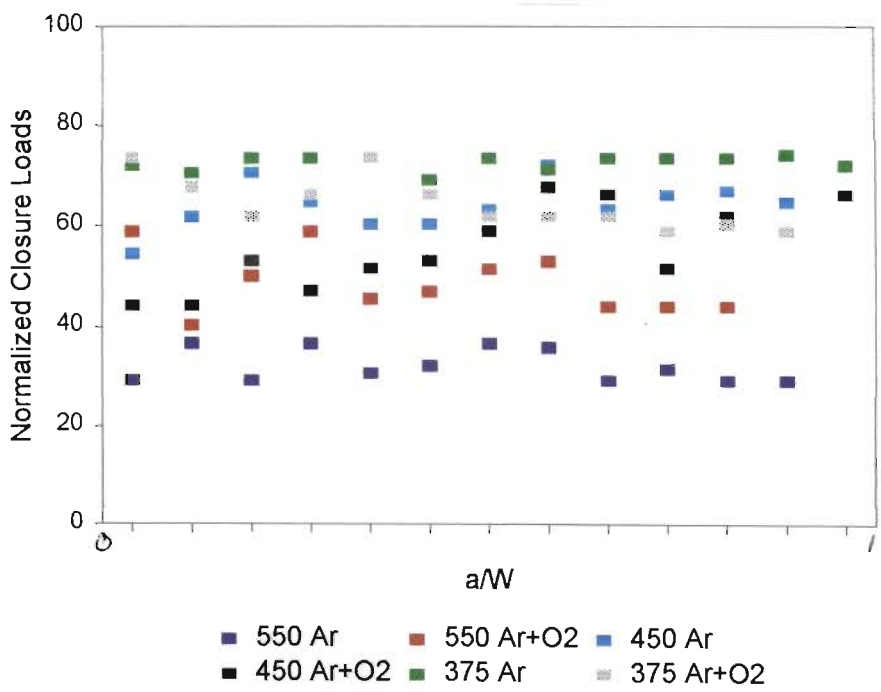

b.

Figure 4.3 : Comparison of closure-related data obtained at the different test temperatures and in the argon and argon + 20% O_2 environment :
a. opening loads
b. closure loads

4.3 Mechanisms of Corrosion and Fatigue Crack Growth Behaviour

4.3.1 Corrosion characteristics

The corrosion tests in the argon and argon + 20% O_2 environment showed that the aging response of TIMETAL 21S was analogous with other metastable beta titanium alloys. However, whereas the inert environment generally produced a coarser precipitation of the alpha phase in the beta grains, the oxidizing environment encouraged a finer alpha precipitation at higher aging temperatures. The oxidizing environment also influenced the appearance and accelerated the formation of the alpha precipitation near the exposed surface of the sample.

From the alpha precipitation appearance at higher temperatures, the effect of the oxidizing environment could be observed in the centre of the specimen. This effect did however not significantly influence the hardness of the allow.

AES analysis detected an appreciable the dissolution of oxygen into the alloy even below 400°C. Optical microscopy and x-ray diffraction analysis confirmed that the initial detectable surface oxide formation occurred only at 450°C.

X-ray diffraction analysis indicated the increased the prominence of the alpha formation in the argon + 20% O_2 environment at an earlier stage than observed in the inert environment. This was due to the formation of the alpha case, and/or the promotion of alpha precipitation due to the oxidizing environment.

Fine particles observed on the TIMETAL 21S surfaces was an artifact of high temperature exposure in the oxidizing environment.

The EDS analysis performed near the exposed surface in the argon + 20% O_2 environment showed that complex oxides consisting of Ti, Al, Si, and possibly Mo and Nb may have participated in the overall oxide formation, however x-ray diffraction analysis did not reveal oxides other than TiO_2 after the 5 hour exposure.

The oxidation resistance of TIMETAL 21S in the argon + 20% O_2 environment was seen to run out above 650°C, whereafter a rapid increase in the formation of TiO_2 occurred.

4.3.2 Fatigue Crack Growth Behaviour

Similar fatigue crack growth rates were obtained at 375°C in the inert and oxidizing environments. This was attributed to the environment having an insignificant effect on TIMETAL 21S at this temperature. The fracture surface showed a transgranular crack propagation with ductile striations which was believed to be evidence of roughness-induced and plasticity-induced crack closure. Figure 4.4 schematically shows the factors controlling to the fatigue crack growth rates at 375°C in both the inert and oxidizing environments. An environmental interaction was also seen to affect the closure-related loads when comparing the inert and oxidizing environment results. The closure loads could not sufficiently explain the similar crack growths rate in both environments.

At 450°C, a retarded crack growth was experienced in the argon + 20% O_2 environment. The crack closure data indicated that the induced crack closure mechanisms were unable to entirely account for the retarded growth rates. Metallographic examination of the samples revealed that branched secondary cracking was experienced only in the oxidizing environment, and that this crack tip blunting and branching phenomena promotes a mixed mode crack propagation. This can effectively reduce the crack driving force, and hence partly offer an explanation for the slower fatigue crack growth rates in the oxidizing environment. The lower closure loads found in the oxidizing environment was attributed to the dissolution of oxygen ahead of the crack tip which could have affected the amount of plastic constraint in the wake of the propagating crack. A modification in the slip character and hence the crack propagation mode was also attributed to the higher temperature.

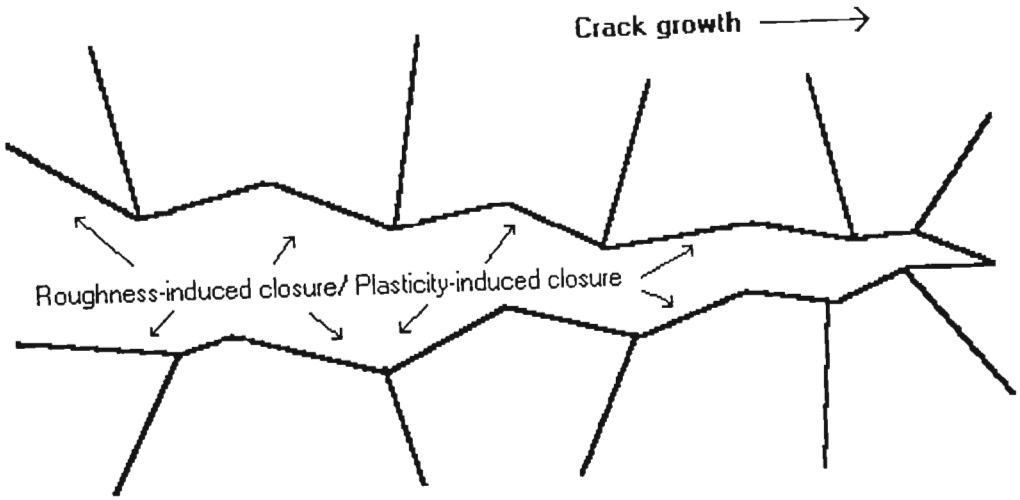

Figure 4.4 : Schematic model showing mechanisms influencing the fatigue crack growth rate of TIMETAL 21S in argon + 20% O_2 environment at 375°C

Figure 4.5 schematically shows the main fatigue crack growth rate influencing mechanisms operative in the argon + 20% O_2 environment at 450°C.

Retarded crack growth rates were again experienced in the argon + 20% O_2 environment at 550°C. The crack closure data suggested that an additional oxide-induced crack closure mechanism assisted in slowing the FCGR. Metallography also showed branched secondary cracking (evident only in the oxidizing environment) that contained a substantial amount of corrosion product. These cracks can further account for the slower crack growth rates in the argon + 20% O_2 environment. Changes in the crack propagation mode at 550°C was manifested by the smoother fracture surface appearance at lower ΔK in both the inert and oxidizing environments. This was attributed to the activation of other slip systems with increasing temperature, resulting in reduced crack closure loads and significantly less surface deformation. The effect of the environment was more noticeable at this temperature due to the presence of fine surface particles distributed over the fracture surface.

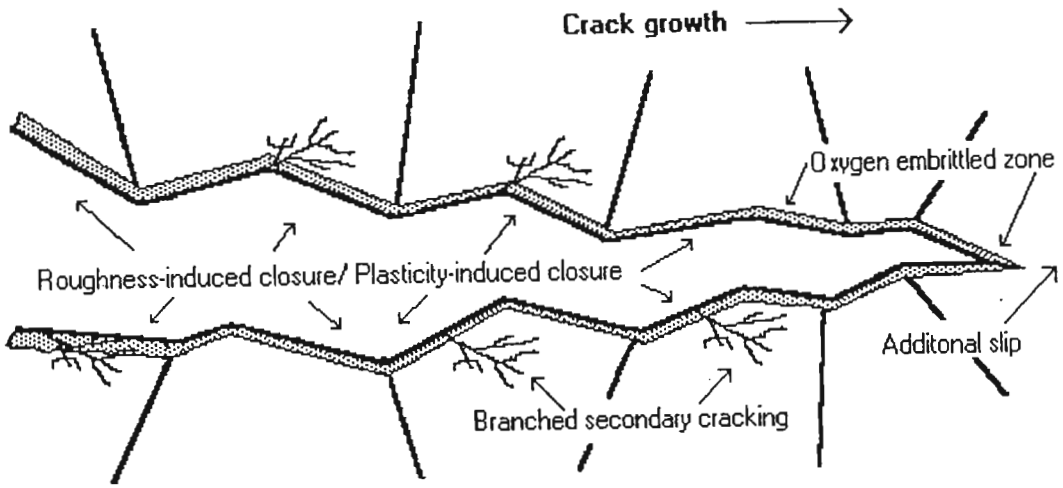

Figure 4.5 : Schematic model of synergistic mechanisms influencing the fatigue crack growth rate of TIMETAL 21S in argon + 20% O_2 environment at 450°C

At 620°C, the oxidizing environment produced a slower crack growth rate compared to the inert environment. Closure data was not available for this temperature, however it is believed that oxide-induced crack closure, along with the branched secondary cracking (again only experienced in the oxidizing environment) was accountable for the restrained crack growth. The interrupted tests showed a zigzag type of crack propagation that was obtained in the oxidizing environment as opposed to the straight crack experienced in the inert environment. Although the zigzag type of crack profile is mostly attributed to crystallographic orientation at low ΔK, the change in environment produced the different crack path profiles and hence substantiates the dependency of the fatigue crack path on the environment. The fatigue cracks growth rates found in both the inert and oxidizing environments at 550°C and 620°C were markedly accelerated over that obtained at the lower temperatures. This phenomena was attributed to the activation of additional slip systems in titanium alloys at higher temperatures. Figure 4.6 schematically models the active mechanisms that ultimately resulted in the distinct crack growth behaviour obtained at 550°C and 620°C in the oxidizing environment.

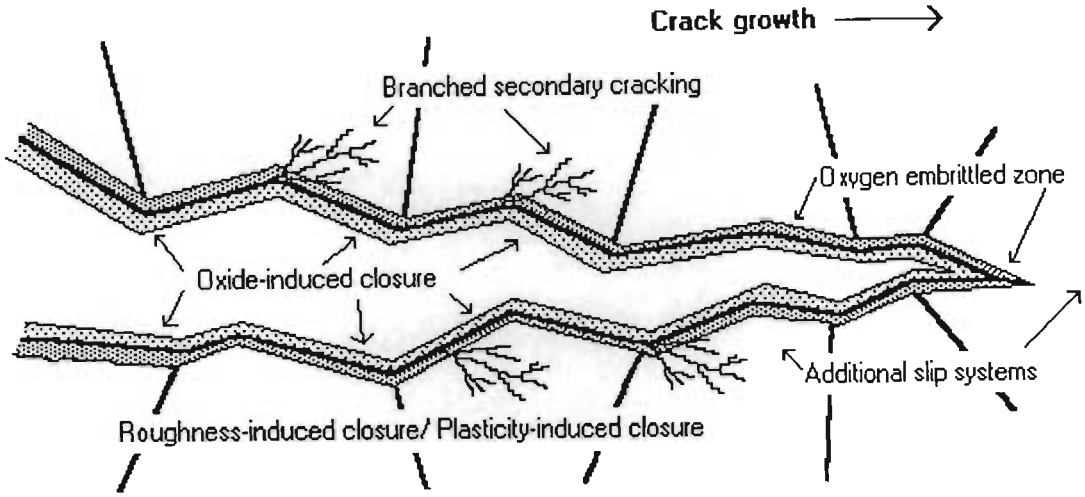

Figure 4.6 : Schematic model of synergistic mechanisms influencing the fatigue crack growth rates of TIMETAL 21S in argon + 20% O_2 environment at 550°C and 620°C

The behaviour in the inert environment at the different temperatures may effectively be modelled by figure 4.4, however, at higher temperatures, additional slip systems are presumed to be active and have to be included in the model.

4.3.3 Crack Closure and Consolidation Phenomena

Consolidation using the opening loads showed that the data obtained in the different environments at the different temperatures could not be collapsed into a singular region. While data from the 375°C and 450°C temperature tests in the respective environments could be collapsed into similar yet separate regions, the data from the 550°C tests could not be consolidated. In the inert environment, this showed that other mechanism(s) influenced the crack growth rates, and that in the oxidizing environment, the added effect of the material interaction with the environment at higher temperatures needs to be considered. For a similar effective crack driving force, the crack growth

rates in the argon + 20% O_2 environment was accelerated, showing the detrimental influence of the oxidizing environment. The consolidation process did prove to contribute to the explanation of the fatigue crack growth rates, however it could not entirely explain the crack growth behaviour.

Further observations of the closure-related data showed that the magnitude of the opening/closure loads decreased with increasing temperature and therefore illustrates the dependency of the crack growth rate on the effective closure loads viz. lower closure data → higher ΔK_{eff} → accelerated FCGR. The decreasing closure values were also attributed to the change in slip character at elevated temperatures. Additionally, a dependency of the closure loads on the applied P_{max} was shown.

Chapter 5

5. Conclusions

5.1 The Effect of the Oxidizing Atmosphere

The oxidizing environment influences the alpha phase precipitation kinetics, precipitation appearance and characteristics and provides more homogeneous precipitation sites that allows finer precipitation of the alpha phase at higher temperatures.

Although the combination of elements in TIMETAL 21S provides an improved oxidation resistant beta titanium alloy, oxygen dissolution at low temperatures is perceptible and the evolving oxide layer does not inhibit the oxygen dissolution, as manifested by the AES analysis and increased hardness at the centre of the alloy.

5.2 The Fatigue Crack Growth Characteristics

The load-line compliance test method used in this study provided the ability to accurately and precisely monitor fatigue crack growth rates at all temperatures when using an environmental chamber.

In this study, at temperatures higher than 375°C, the oxidizing environment retarded the crack growth rates, compared to that found in the inert environment.

At 375°C the factors controlling the fatigue crack growth rates were mainly roughness-induced crack closure and plasticity-induced crack closure. The fatigue crack growth rates at 375°C in the inert and oxidizing environments are essentially similar.

At 450°C the crack growth rate was retarded in the oxidizing environment due to the increased amount of secondary cracking experienced, as well as plasticity-induced closure and the roughness-induced crack closure effect. Branched secondary cracking

was found to have been environmentally induced and resulted in the crack branching and blunting phenomena which effectively reduced the stresses at the crack tip due to a mixed mode crack propagation mechanism.

At 550°C, the additional environmental effect of oxide-induced crack closure was found to retard the fatigue crack growth rate. Environmentally induced branched secondary cracking also contributed to the slower fatigue crack growth rates in the oxidizing environment.

At 620°C it is believed that oxide-induced crack closure, in addition to branched secondary cracking and the roughness and plasticity-induced crack closure, slowed the FCGR in the oxidizing environment. The existence of substantial surface oxide was manifested by the abundance of thermodynamically stable oxide-forming elements on the fracture surface.

There exists a marked acceleration of the FCGR at 550°C and 620°C due to a modification in slip character and lower closure levels.

Additional slips systems were activated at elevated temperatures and a correlation between the crack path, the environment and the test temperature can be established.

Closure-related data showed the irrepressible relationship between intrinsic crack closure loads and the fatigue crack growth rates as found at various temperatures. This is illustrated by the lower closure loads observed at increasing temperature.

Consolidation cannot account entirely for the TIMETAL 21S behaviour in the inert and oxidizing environment at the various temperatures. The data from the various tests could not be collapsed into a single region. Other synergistic mechanisms such as material embrittlement and characteristic behaviour through environmental interaction and secondary cracking leading to a crack tip blunting and branching effect can be incorporated to fully explain the final results.

5.3 Suggested topics for further research

A full characterization of TIMETAL 21S in various environments and at various temperatures has yet to be completed. Since the alloy is intended for, amongst others, high temperature, load bearing use, further research topics could include :

1. The effect of aging treatment on the FCGR of TIMETAL 21S and the microstructure required for optimal fatigue resistance

2. The effect of increasing R ratios on TIMETAL 21S to exclude the effects of the crack closure and further isolate the effect of an test environment on the alloy.

3. The effect of oxidization resistant coatings on the fatigue life of TIMETAL 21S

4. The role and characteristics of the various induced crack closure mechanisms should be further investigated, in particular, the effect of the environment on the near-threshold fatigue crack profile and crack propagation mechanism.

References

1. F H Froes, "Aerospace Materials for the Twenty-First Century", Aerospace Materials, Swiss Materials, 2(1990), no. 2, pp 23 - 36.

2. S A Meguid, "Engineering Fracture Mechanics", Elsevier Science Publishers, 1989.

3. N M Tallon, "Materials for Future Aerospace Systems", Materials Engineering Conference, Technion - Israel Institute Of Technology, Haifa, Israel, December 19-20, 1990

4. E Aghion, D Eliezer, N Comins, "Titanium Aluminides, A New Concept in Advanced Aerospace Materials", Technology SA, Mechanical Technology, March 1992, pp 3-7.

5. Earning it's Wings, Scientific American, June 1988, pp 12-13.

6. What's News, Popular Science, April 1986, pg 93.

7. "US Moves Towards Aerospace Plane Program", Aviation Week and Space Technology, December 16, 1985, pg 16.

8. L Kempfer, "Materials Take a Hypersonic Leap into Space", Mechanical Engineering, August 1990, pp 19-22.

9. J A Charles, F A A Crane, Selection and use of Engineering Materials, Second Edition, Butterworth and Co. Ltd, 1989.

10. E Aghion, "Environmental Effects on High Temperature Mechanical Behaviour of Advanced Aerospace Materials", Phase II Annual Report to CSIR, January 1994.

11. F H Froes, C Suryanarayana, D Eliezer, "Production, Characterization and Commercialization of Titanium Alloys", ISIJ International, Vol 31, 1991, no. 10, pp 1235 - 1248.

12. J M Larsen, K A Williams, S J Balstone, M A Stucke, "Titanium Aluminides for Aerospace Applications", Paper presented at the 1989 Symposium of High Temperature Aluminides and Intermetallics, Indiapolis, IN, October 1-5, 1989.

13. R G Rowe, S C Huang, "Recent Developments in Titanium Aluminide Alloys", Israel Journal Of Technology, Proc. of 4th Israel Materials Engineering Conference, Vol. 24, 1988, pp 255 - 260.

14. D J Duquette, N S Stoloff, "Aerospace Applications of Intermetallics", Rensseelaer Polytechnic Institute, Materials Engineering Department, Troy, N.Y..

15. E Aghion, "Environmental effects on high temperature mechanical behaviour of advanced aerospace materials", Phase I Annual Report to CSIR, January 1993.

16. "Titanium Takes on Nickel-Based Alloys", News at a Glance, Advanced Materials And Processes, no. 2, pg 9, 1993

17. T M F Ronald, "NASP Launches New Materials", Advanced Materials And Processes, 9/93, pp 24-28.

18. J Ferreira, E Aghion, N Comins, "Characteristics and applications of newly developed TIMETAL 21S titanium-based alloy", Technology SA, Mechanical Technology, July 1994, pp 18-21.

19. D Upadhyaya, D M Blackketter, C Suryanarayana, F H Froes, "Microstructure and Mechanical Characterization of BETA 21S Titanium-alloy", Proceedings of Titanium '92 : Science and Technology, Seventh World Conference, June 29 - July 2, 1992, San Diego, California, pp 447 - 454.

20. S S Joseph, F H Froes, "Titanium Metallurgy and Applications", Light Metals Age, December 1988, pp 5-12.

21. G Terlinde, H-J Rathjen and K-H Schwalbe, "Microstructure and Fracture Toughness of Aged Ti-10V-2Fe-3Al", Metallurgical Transactions, Vol 19A, April 1988, pp 1037 - 1049.

22. Metals Handbook, Ninth Edition, Volume 9, "Metallography and Microstructures", ASM.

23. M N Vijayshankar, S Ankem, "High Temperature Tensile Behaviour of β-Ti Alloys", Materials Science and Engineering, A129, 1990, pp 229-237.

24. E W Collings, "Physical Metallurgy of Titanium Alloys", American Society of Metals, Metals Park, OH, 1984.

25. H Ghonem, Y Wen, D Zheng, M Thompson, G Linsey, "Effects of Temperature and Frequency on Fatigue Crack Growth in Ti-β21S Monolithic Laminate", Materials Science and Engineering, A161, 1993, pp 45-53.

26. D L Moffat, U R Kattner, "The Stable and Metastable Ti-Nb Phase Diagrams", Metallurgical Transactions, Vol 19A, October 1988, pp 2389 - 2397.

27. E Breslauer, A Rosen, "Relationship between Microstructure and Mechanical Properties in Metastable β Titanium 15-3 Alloy", Materials Science and Technology, May 1991, Vol. 7, pp 441-446.

28. D Eylon, S Fujishiro, P J Postans and F H Froes, "High Temperature Titanium Alloys - A Review", Titanium Technology : Present Status and Future Trends, edited by F H Froes, D Eylon and H B Bomberger, published by Titanium Development Association, pp 87 - 94.

29. H G Suzuki and H Fuji, "Deformation Characteristics of Ti-15V-3Cr-3Sn-3Al at Elevated Temperature", ISIJ International, Vol. 31, 1991, pp 814 - 819.

30. R L Fleischer, R J Zabala, "Mechanical Properties of Ti-Cr-Nb Alloys and Prospects for High Temperature Applications", Metallurgical Transactions A, vol. 21A, August 1990, pp 2149 - 2154.

31. P J Bania, "Next Generation Titanium Alloys for Elevated Temperature Service", ISIJ International, Vol 31, no. 8, 1991, pp 840-847.

32. D Eylon, S Fujishiro, F H Froes, " Titanium Alloys for High Temperature Applications", High Temperature Materials and Processes, Vol 6, no. 1 & 2, 1984, pp 82 - 91.

33. J S Grauman, "Corrosion Behaviour of TIMETAL 21S for Non-aerospace Applications", Proceedings of Titanium '92 : Science and Technology, Seventh World Conference, June 29 - July 2, 1992, San Diego, California, pp 2737 - 2742.

34. H B Bomberger, Technical report WRDC-TR-89-4036 WPAFB, OH, 1989.

35. H Chuanxi, L Bingham, "Effects of Nb and W on the Mechanical Properties and Oxidation Resistance of High Temperature Titanium Alloys", Proceedings of Titanium '92 : Science and Technology, Seventh World Conference, June 29 - July 2, 1992, San Diego, California, pp 1891 - 1897.

36. T Khan, S Naka, P Veyssiere and P Costa, "Intermetallics for Structural Applications", Proceedings of High Temperature Materials for Power Engineering, Belgium, 24 - 27 Sept. 1990, pp 1533 - 1557.

37. "New Titanium-Niobium Alloy Solves Autoclave Problem", Tech Spotlight, Advanced Materials and Processes, Volume 145, no. 5, May 1994.

38. P J Bania, " Ti-1100: A New Elevated Temperature Titanium Alloy", Proceedings of 2nd International SAMPE Metals Conference, Aug. 2 - 4, 1988, pp 286 - 297.

39. S Ishiyama, S Hanada and O Izumi, "Effect of Zr, Sn and Al Additions on Deformation Mode and Beta Phase Stability of Metastable Beta Ti Alloys", ISIJ International, Vol 31, no. 8, 1991, pp 807 - 813.

40. S Ishiyama, S Hanada, "Effect of Zr, Sn and Al Addition on Mechanical Properties of Metastable β Titanium Alloys", Proceedings of Titanium '92 : Science and Technology, Seventh World Conference, June 29 - July 2, 1992, San Diego, California, pp 1947 - 1954.

41. C E Savrun, D H Polonis, "Precipitation and Reversion Processes in a β Titanium Alloy", Material Science and Engineering, A119, 1989, pp 153 - 144.

42. N Frey, T Buchillier, V-D Le and S G Steinemann, "Properties of Surface Oxides on Titanium and some Titanium Alloys", Proceedings of Titanium '92 : Science and Technology, Seventh World Conference, June 29 - July 2, 1992, San Diego, California, pp 2135 - 2142.

43. R W Judy, Jr, I L Caplan, F D Bogar, "Effects of Oxygen and Iron on the Environmental and Mechanical Properties of Unalloyed Titanium", Proceedings of Titanium '92 : Science and Technology, Seventh World Conference, June 29 - July 2, 1992, San Diego, California, pp 2073 - 2080.

44. J R Wood, D P Barbis, D Eylon, "Effect of Oxygen on the Microstructure and Properties of BETA-C™ (Ti-3Al-8V-6Cr-4Mo-4Zr) Investment Castings", Proceedings of Titanium '92 : Science and Technology, Seventh World Conference, June 29 - July 2, 1992, San Diego, California, pp 415 - 422.

45. W J Porter, R R Boyer, D Eylon, "Effects of Microstructure on the Mechanical Properties Ti-15V-3Cr-3Al-3Sn Castings", Proceedings of Titanium '92 : Science and Technology, Seventh World Conference, June 29 - July 2, 1992, San Diego, California, pp 1511 - 1518.

46. G T Gray III, C E Morris and A C Lawson, "Omega Phase Formation in Titanium and Titanium Alloys", Proceedings of Titanium '92 : Science and Technology, Seventh World Conference, June 29 - July 2, 1992, San Diego, California, pp 225 - 232.

47. S Hanada, O Izumi, "Transmission Electron Microscope Observations of Mechanical twinning in Metastable beta Titanium Alloys", Metallurgical Transactions, Vol 17A, Aug. 1986, pp 1409 - 1420.

48. L Wagner, J K Gregory, "Improving the Fatigue Life of Titanium Alloys: Part I", Advanced Materials and Processes, 3/94, pp 36u - 36z.

49. TIMETAL 21S DATA SHEET, Titanium Metals Corporation, Denver, Colorado, USA.

50. R R Boyer, "International Workshop on Beta Ti-Alloys", Journal of Materials, July 1994, pp 12 -13.

51. E S Huron, J A Miller, "Titanium Requirements for Current and Future Military Gas Turbine Engines", 2nd International SAMPE Metals Conference, August 2 - 4, 1988, pp 271 - 285.

52. P J Bania, "Beta Titanium Alloys and Their Role in the Titanium Industry", Journal of Materials, July, 1994, pp 16 - 19.

53. H Nakajima and M Koiwa, "Diffusion in Titanium", ISIJ International, Vol 31, no. 8, 1991, pp 757 - 766.

54. W M Parris, P J Bania, "Oxygen Effects on the Mechanical Properties of TIMETAL 21S", Proceedings of Titanium '92 : Science and Technology, Seventh World Conference, June 29 - July 2, 1992, San Diego, California, pp 153 - 160.

55. "Advanced Materials and their Uses", High-Tech Materials Alert, November 1994, Vol. 11, no. 11, pp 5 - 6.

56. M W Mahoney, P L Martin and D A Hardwick, "Microstructural stability of Beta 21S", Proceedings of Titanium '92 : Science and Technology, Seventh World Conference, June 29 - July 2, 1992, San Diego, California, pp 161 - 168.

57. S T Rolfe, J M Barsom, "Fracture and Fatigue Control in Structures, Applications of Fracture Mechanics", Published by Prentice-Hall Inc., 1977.

58. "Experimental Techniques in Fracture Mechanics", Society for experimental stress analysis monograph no.1, SESA, Published by Iowa State University Press, Iowa, 1975.

59. D Broek, "Elementary Engineering Fracture Mechanics", Published by Sijthoff and Noordhoff International Publishers, 1978.

60. T L Anderson, "Fracture Mechanics, Fundamentals & Applications", Published by CRC Press Inc., 1991.

61. K Hellan, "Introduction to Fracture Mechanics", McGraw-Hill Book Co., 1984.

62. D Broek, "Practical use of Fracture Mechanics", Published by Kluwer Academic Publishers, 1989.

63. H L Ewalds, R J H Wanhill, "Fracture Mechanics", Published by Edward Arnold (Publishers) Ltd, 1984.

64. 'Standard Test Method for Measurement of Fatigue Crack Growth Rates', ASTM Standards, Designation E 647 - 88a, Annual Book of ASTM Standards, 1983, SERIES 3, Vol. 03.01, Metals - Mechanical Testing; Elevated Temperature and Low-Temperature Tests, pp 710 - 730.

65. A P Parker, "The Mechanics of Fracture and Fatigue : An Introduction", Published by E & F N Spon in association with Methuen Inc., 1981

66. W F Brown, "Review of Developments in plane strain fracture toughness testing", ASTM Special Technical Publication 463, Published by the Society for Testing and Materials, 1970.

67. E E Gdoutos, "Fracture Mechanics Criteria and Applications", 1990, Kluwer Academic Publishers.

68. S Suresh, "Fatigue of Materials", Cambridge Solid State Science Series, Published by Press Syndicate of the University of Cambridge, 1991.

69. R H Dauskardt, R O Ritchie, B N Cox, "Fatigue of Advanced Materials, Part I", Advanced Materials and Processes, 7/93, pp 26 - 31

70. N N Au, "Application of the S_c Theory to Flightworthiness Evaluation of Space Launched Vehicles", Proceedings of the International Conference on the role of Fracture Mechanics in Modern Technology, Fukuoka, Japan, 2-6 June, 1986.

71. W F Deans, C E Richards, "A Simple and Sensitive Method of Monitoring Crack and Load in Compact Fracture Mechanics Specimens using Strain Gauges", Journal of testing and evaluation, Vol 7, no. 3, May 1979, pp 147 - 154.

72. M B Cortie, G G Garrett, "A New Look at an Old Technique for the Measurement of Fatigue Crack-Growth Rates", Experimental Mechanics, September 1989, pp 291 - 294

73. "Experimental techniques in Fracture mechanics, 2", Society for experimental stress analysis monograph no.2, 1975

74. M B Cortie, G G Garrett, "A Comparison of Fatigue-Crack Growth of Three Alloy Steels", Theoretical and Applied Fracture Mechanics, no. 11, 1989, pp 9 - 19.

75. W L Server, "Compliance correction for determining Load-Line Energies for Compact Fracture Toughness Specimens", Journal of testing and Evaluation, vol 7, no. 1, January 1979, pp 29 - 32.

76. G C Salivar, J E Heine, F K Haake, "The effect of Stress Ratio on the Near-Threshold Fatigue Crack Growth Behaviour of Ti-8Al-1Mo-1V at Elevated Temperature", Engineering Fracture Mechanics, vol. 32, no. 5, 1989, pp 807 - 817.

77. W J Mills, L A James and J A Williams, "A Technique for Measuring Load-Line Displacements of Compact Ductile Fracture Toughness Specimens at Elevated Temperatures", Journal of testing and Evaluation, vol 5, no. 6, Nov 1977, pp 446 - 451.

78. J K Donald, D W Schmidt, "Computer-controlled Stress Intensity Gradient Technique for High Rate Fatigue Crack Growth Testing", Journal of testing and Evaluation, vol 8, no. 1, Nov 1980, pp 19 - 24.

79. H I McHenry, "A Compliance Method for Crack Growth Studies at Elevated Temperature", Journal of Materials, JMLSA, vol. 6, no. 4, December 1971, pp 862 - 873.

80. A Cooley, T W Crooker, "Procedures for Precision Measurement of Fatigue Crack Growth Rate Using Crack-Opening Displacement Techniques", Fatigue Crack Growth Measurement and Data Analysis, ASTM STP 738, S J Hudak Jr and R J Bucci, Eds., American Society for testing and Materials, 1981, pp 85 - 102

81. Y-W Kim, "Ordered Intermetallic Alloys, Part III: Gamma Titanium Aluminides", Journal of Materials, July 1994, pp 30 - 39.

82. DATA SHEET, "Summary Table of Titanium Alloys", Advanced Materials and Processes, no. 6, 1994, pp 123 - 126.

83. "Titanium and its Alloys", Computer software, Sponsored by Titanium Developement Association, Boulder, Colorado. Developed by MATUS Databases - Engineering Information Co. Ltd (C) 1992.

84. S Z Bokshteyn, N P Zyulina and O V Markovich, "Phase Composition, Structure and Impurity Diffusion in Titanium Alloys", Phys. Met. Metall., vol 69, no. 4, 1990, pp 128 - 133.

85. R R Boyer, "Aerospace Applications of Beta Titanium Alloys", Journal of Materials, July, 1994, pp 20 - 23.

86. R W Schultz, "Environmental Behaviour of Beta Titanium Alloys", Journal of Materials, July, 1994, pp 24 - 29.

87. W T Donlon, J E Allison and J V Lasecki, "The Influence of Thermal Exposure and Microstructure of Elevated Temperature Titanium Alloys", Proceedings of Titanium '92 : Science and Technology, Seventh World Conference, June 29 - July 2, 1992, San Diego, California, pp 295 - 302.

88. N Niwa, T Demura and K Ito, "Effects of Chemical Composition on the Heat Treatment Response of Ti-15V-3Cr-3Sn-3Al Based Titanium Alloy", ISIJ International, Vol 30, 1990, no. 9, pp 773 - 779.

89. Y Kawabe and S Muneki, "Strengthening and Toughening of Titanium Alloys", ISIJ International, Vol. 31, 1991, no. 8, pp 785 - 791.

90. D Eylon, A Vassel, Y Combres, R R Boyer, P J Bania and R W Schultz, "Issues in the Development of Beta Titanium Alloys", Journal of Materials, July, 1994, pp 14 - 15.

91. Wang shihong, Shen quiqin, Liang youming,"Phase Transformations in Ti-15V-3Cr-3Sn-3Al Alloy", Proceedings of Titanium '92 : Science and Technology, Seventh World Conference, June 29 - July 2, 1992, San Diego, California, pp 761 - 767.

92. M A Imam, P K Poulose, B B Rath, "Effect of Cold Work and Heat Treatment in the Alpha Region on the Mechanical Properties of Ti 15-3", Proceedings of Titanium '92 : Science and Technology, Seventh World Conference, June 29 - July 2, 1992, San Diego, California, pp 177 - 184.

93. J Bechet, C Angelier, B Cormier, O Lacagne and M Lhermitte, "Phase Transformation in a Near β-Ti Alloy: Microstructure and Mechanical Properties ", Proceedings of Titanium '92 : Science and Technology, Seventh World Conference, June 29 - July 2, 1992, San Diego, California, pp 643 - 650.

94. H Ohyama, H Nakamori, Y Ashida and T Maki, "Effects of Cold Deformation on the Morphology of α Precipitates in β Titanium Alloys", ISIJ International, Vol. 32, 1992, pp 222 - 231.

95. S T Balsone, "The Effect of Elevated Temperature Exposure on the Tensile and Creep Properties of Ti-24Al-11Nb", Proceedings of the Workshop of Oxidation of High Temperature Intermetallics, Cleveland, Ohio, 22-23 September, 1988.

96. G A Young Jr and J R Sudly, "The Influence of Hydrogen on the Mechanical Properties of TIMETAL 21S", Proceedings of Titanium '92 : Science and Technology, Seventh World Conference, June 29 - July 2, 1992, San Diego, California, pp 2201 - 2208.

97. D Banerjee and V S Arunachalam, "On the α/β Interface Phase in Titanium Alloys", Acta Metallurgica, Vol. 29, 1981, pp 1685 - 1694.

98. H Ohyama, A Takemura and T Nishimura, "Effects of Deformation Temperature on As-forged and Post-aging Microstructures and Tensile Properties after Aging in Ti-15V-3Cr-3Sn-3Al", Proceedings of Titanium '92 : Science and Technology, Seventh World Conference, June 29 - July 2, 1992, San Diego, California, pp 481 - 488.

99. H Ohyama, Y Ashida T Nishimura and T Maki, "Effects of Deformation Temperature on Deformed and Aged Microstructures and Tensile Properties in Ti-15V-3Cr-3Sn-3Al Alloys", ISIJ International, Vol. 33, 1993, pp 889 - 897.

100. K E Weidemann, R K Bird, T A Wallace and R K Clark, "Mechanical Properties of Coated BETA-21S to Air at 700 and 800°C", Proceedings of Titanium '92 : Science and Technology, Seventh World Conference, June 29 - July 2, 1992, San Diego, California, pp 2185 - 2192.

101. K Maki, M Shioda, M Sayashi, T Shimizu and S Isobe, "Effect of Si and Niobium on the Oxidation Resistance of TiAl Intermetallics", Material Science and Engineering, A153, 1992, pp 591 - 596.

102. T J Johnson, M H Loretto, M W Kearns, "Oxidation of High Temperature Titanium Alloys", Proceedings of Titanium '92 : Science and Technology, Seventh World Conference, June 29 - July 2, 1992, San Diego, California, pp 2035 - 2042.

103. D L Moffat, U R Kattner, "The Stable and Metastable Ti-Nb Phase Diagrams", Metallurgical Transactions, Vol 19A, October 1988, pp 2389 - 2397.

104. Y Umakoshi, M Yamaguchi, T Sakagami and T Yamane, "Oxidation resistance of Intermetallic Compounds of Al_3Ti and TiAl", Journal of Material Science, 24, 1989, pp 1599 - 1603.

105. D V Ignatov, Z I Kornilova, E M Lazarev, V M Popova (Moscow), "Oxidisability of Titanium-Aluminide Alloys", UDC 669.295'71:669.046.42.001, source otherwise unknown.

106. "Bigger and Better titanium Forgings", Technical Spotlight, Advanced Materials and Processes, 3/94, pp 32 - 33.

107. M Peters, V Bachmann, K-H Trautman, H Schurman, Y T Lee and C H Ward, "Influence of Thermal Exposure on Properties and Microstructure of Elevated Temperature Titanium Alloys", Proceedings of Titanium '92 : Science and Technology, Seventh World Conference, June 29 - July 2, 1992, San Diego, California, pp 303 - 310.

108. K S Chan, "Fracture and Toughening Mechanisms in an α_2 Titanium Aluminide", Metallurgical Transactions, Vol. 21A, October 1990, pp 2687 - 2699.

109. R H Dauskardt, R O Ritchie, B N Cox, "Fatigue of Advanced Materials, Part II", Advanced Materials and Processes, 7/93, pp 30 - 35.

110. J M Larsen, J R Jira, "Small-crack Closure Measurements in Titanium Alloys", Experimental Mechanics, March 1991, pp 82 -87

111. K S Ravichandran, "Fatigue Crack Growth as Influenced by Microstructure in Ti-6Al-4V", Scripta Metallurgica et Materialia, vol. 24, 1990, pp 1559 - 1563.

112. S Mall, J A Perez, T Nicholas, "Influence of Loading History on Fatigue Threshold Behaviour in a Titanium Alloy", Engineering Fracture Mechanics, vol. 37, no. 1, 1990, pp 15 - 26.

113. C M Ward-Close, A F Blom, R O Ritchie, "Mechanisms Associated with Transient Fatigue Crack Growth under Variable-Amplitude Loading: an Experimental and Numerical Study", Engineering Fracture Mechanics, vol. 32, no.. 4, 1989, pp 613 - 638.

114. K J Miller, "Materials Science Perspective of Metal Fatigue Resistance", Materials Science and technology, June 1993, vol 9, pp 453 - 462.

115. G C Salivar, F K Haake, "A Comparison of Test Methods for the Determination of Fatigue Crack Growth Rate ThreshoLd in Titanium at Elevated Temperature", Engineering Fracture Mechanics, vol. 37, no.3, 1990, pp 505 - 517.

116. L S Vesier, D Antolovich, " Fatigue Crack Propagation in Ti-6242 as a Function of Temperature and Waveform", Engineering Fracture Mechanics, vol. 37, no. 4, 1990, pp 753 - 775.

117. G T Grey III, G Luetjering, J C Williams, "The Influence of Oxygen on the Structure, Fracture and Fatigue Crack Propagation Behaviour of Ti-8.6%Al", Metallurgical Transactions, vol. 21A, January 1990, pg 95 - 105.

118. L E Matokhnyuk, T Yu Yakovleva, "Influence of Loading Frequency on the Rules and Mechanisms of Fatigue Crack Growth in Titanium Alloys", Article translated from Problemy Prochnosti, no. 1, January 1988, pp 21 - 31.

119. W O Soboyejo, S M L Sastry, "An Investigation of the Effects of Heat Treatment on Microstructure and Fracture Behaviour of Extruded Ti-48Al-1.5Cr", Proceedings of Titanium '92 : Science and Technology, Seventh World Conference, June 29 - July 2, 1992, San Diego, California, pp 1049 - 1064.

120. T W Duerig, J E Allison, J C Williams, "Microstructural Influences on Fatigue Crack Propagation in Ti-10V-2Fe-3Al", Metallurgical Transactions, vol 16A, May 1985, pp 739 - 751.

121. D Buttinelli, F Felli, G B Festa, A J Querales, "Effect of Heat Treatment on the Fatigue Behaviour of the Beta-C Titanium Alloy", Proceedings of Titanium '92 : Science and Technology, Seventh World Conference, June 29 - July 2, 1992, San Diego, California, pp 505 - 512.

122. R R Boyer, J A Hall, "Microstructure - Property Relationships in Titanium Alloys (Critical Review)", Proceedings of Titanium '92 : Science and Technology, Seventh World Conference, June 29 - July 2, 1992, San Diego, California, pp 77 - 88.

123. J Petit, W Berata, B Bouchet, "Fatigue Crack Growth Behaviour of Ti-6Al-4V at Elevated Temperature", Proceedings of Titanium '92 : Science and Technology, Seventh World Conference, June 29 - July 2, 1992, San Diego, California, pp 1819 - 1826.

124. R Foerch, A Madsen, H Ghonem, "Environmental Influence on Fatigue Crack Growth Performance of Ti-1100 at Elevated Temperatures", Proceedings of Titanium '92 : Science and Technology, Seventh World Conference, June 29 - July 2, 1992, San Diego, California, pp 2043 - 2048.

125. R J T Penton, M T Cope, P Bowen, "Effects of Environment on Fatigue Crack Growth in a Ti_3Al based Aluminide", Proceedings of Titanium '92 : Science and Technology, Seventh World Conference, June 29 - July 2, 1992, San Diego, California, pp 1219 - 1226.

126. M Peters, V Bachmann, K-H Trautmann, H Schurman, Y T Lee, C H Ward, "Room and Elevated Temperature Properties of Ti-1100", Proceedings of Titanium '92 : Science and Technology, Seventh World Conference, June 29 - July 2, 1992, San Diego, California, pp 303 - 310.

127. J S Park, H Margolin, "The Role of Alpha and Beta Phases in the Fatigue Crack Propagation of Ti-Mn Alloys", Metallurgical Transactions, vol. 15A, January 1984, pp 155 - 171.

128. J L Mahon, "Computer Program for Stress, Strain Data Capture", Final year research and design project no. 19/53, Department of Mechanical Engineering, University of Natal, Durban, South Africa.

129. B London, D V Nelson, J C Shyne, "The Effect of Tempering Temperature on Near-Threshold Fatigue Crack Behaviour in Quenched and Tempered 4140 Steel", Metallurgical Transactions, vol. 19A, October 1988, pp 2497 - 2502.

130. H H Madden, "Chemical Information from Auger Electron Spectroscopy", J. Vac. Sci. Technol., 18(3), April 1981, pp 677 - 689.

131. J Gandon, J C Joud, "Analyse de Couches Minces D'Oxydes de Titane en Spectoscopie D'Electrons Auger", Journal of Less-Common Materials, 69(1980), pp 277 - 291.

132. BUEHLER DIALOG™ Microstructural Analysis Reference Manual - Titanium Alloys.

133. D A Jones, "Principles and Prevention of Corrosion", Macmillan Publishing Co., Edited by D Johnstone, 1991.

134. J H Ferreira, "Environmental Effect on HTLCF of Iron-Chromium Alloys at 600°C", 1989, MSc Thesis, University of Natal, Durban, South Africa.

135. E Aghion, M Bamberger, A Berkovits, "High-Temperature Low Cycle Fatigue of a Nickel-based MAR-M200 + Hf in Ar and Ar + 20% O_2 Environment", Journal of Material Science, 26, 1991, pp 1873 - 1881.

136. H H Smith, P S Kullen, D J Michel, "Fatigue Crack Propagation Behaviour of Titanium Alloys 6242S and 5621S at Elevated Temperature", Metallurgical Transactions A, Volume 19A, April, 1988, pp 881 - 885.

137. R O Ritchie, "Mechanisms of Fatigue Crack Propagation in Metals, Ceramics and Composities: Role of Crack Tip Shielding", Materials Science and Engineering A, 103, 1988, pp 15 - 28.

138. J K Shang, W Yu, R O Ritchie, "Role of Silicon Carbide Particles in Fatigue Crack Growth in SiC-particulate-reinforced Aluminium Alloy Composites", Materials Science and Engineering A, 102, 1988, pp 181 - 192.

139. H L Ewalds, F C van Doorn and W G Sloof, "Influence of Environment and Specimen Thickness on Fatigue Crack Growth Data Correlation by means of Elber-Type Equations", Corrosion Fatigue: Mechanics, Metallurgy, Electrochemistry and Engineering, ASTM STP 801, T W Crooker and B N Leis, Eds., American Society for Testing and Materials, 1983, pp 115 - 134.